6
CHAPTER 6
SSC MODEL: RLME SOURCES AND MMAX ZONES BRANCH

As discussed in Section 4.2, the two major branches of the master logic tree define two approaches to characterizing the spatial and temporal distribution of seismic sources: the Mmax zones approach and the seismotectonic zones approach. As discussed in Section 4.2.1, the "Mmax zones" model involves (1) the direct use of observed seismicity by spatial smoothing of distributed seismicity and (2) the inclusion of RLMEs that are defined primarily by paleoseismic evidence. The Mmax zones are defined solely by differences in the prior distribution of Mmax, using the Bayesian approach. In contrast, the "seismotectonic zones" model (described in Chapter 7), which also includes the RLMEs, involves the use of additional seismotectonic data to define the spatial variation in the characteristics of future earthquakes. This chapter defines both the RLME sources and the Mmax zones. Section 6.1 describes each of the RLME sources; Section 6.2 describes the alternative interpretations of the Mmax zones; Section 6.3 discusses the assessment of maximum magnitude for the Mmax zones; and Section 6.4 describes the spatial smoothing of recurrence parameters within the Mmax zones.

6.1 RLME Sources

By definition, RLME sources are the locations of repeated (more than one) large-magnitude (**M** $\geq$ 6.5) earthquakes in the historical or paleoearthquake record. Because of the rarity of RLMEs relative to the period of historical observation, evidence for these earthquakes comes largely from the paleoearthquake record. For example, paleoearthquakes identified by interpretations of paleoliquefaction features and fault displacement (paleoseismic) studies combined with those in the historical record result in the catalog of large-magnitude earthquakes in the central New Madrid region and at Charleston. At Charlevoix, RLMEs are observed in the historical record and are supplemented by the paleoearthquake record. For the Meers and Cheraw faults as well as the Wabash Valley source, there are no large-magnitude earthquakes in the historical record. The RLMEs for these sources are characterized by evaluating repeated surface-faulting displacements identified in trenches across the faults and, for the Wabash Valley source, by interpreting the geographic distribution of paleoliquefaction features.

The RLME sources considered for the CEUS SSC model are listed in Table 4.2.2-1 and shown on Figure 6.1-1, which is an overview map. Detailed maps of the RLME sources, along with their alternative geometries, are given in the individual subsections describing each of the 11 RLME sources (Sections 6.1.1 through 6.1.9). The relationship of the RLME sources to observed historical seismicity is enigmatic. Some of the RLME sources are associated with elevated

seismicity (Figures 6.1-2a and 6.1-2b), such as the central New Madrid faults (Figure 6.1-2b) and Charlevoix, but others occur within areas of moderate levels of seismicity (e.g., Charleston and Wabash Valley) or even relatively low levels of seismicity (e.g., Cheraw fault). Data evaluation tables for each of the 11 RLME sources are in Appendix C. Six data summary tables for the 11 sources are in Appendix D; a single data summary table (D-6.1.5) is provided for the combined New Madrid region sources described in Sections 6.1.5 to 6.1.8.

By identifying the RLME sources and including them in the SSC model, there is no implication that the set of RLME sources included is, in fact, the total set of RLME sources that might exist throughout the study region. This is because the presently available studies that have located and characterized the RLME sources have been concentrated in certain locations, not conducted systematically across the entire study region. If it were possible to identify all RLME sources throughout the study region, in much the same way that major faults are identified in a plate-boundary tectonic setting, then the earthquake potential of the remaining region might be assessed as being secondary to the RLME sources. This type of conclusion cannot be drawn in the CEUS, based on current knowledge. Therefore, the evidence for the existence of the RLME sources is included in the model, but the remaining parts of the study region are also assessed to have potentially significant earthquake potential, which is characterized using either Mmax zones (Section 6.2) or seismotectonic zones (Section 7.3).

The intent of the RLME sources is to model only the recurrence of repeated large earthquakes in a specific location. As such, the RLME sources represent a source of seismic hazard that is in addition to the hazard resulting from the occurrence of distributed seismicity modeled by the distributed seismicity sources—the Mmax zones. In essence, the RLME sources act as fault-like seismic sources embedded in large areal seismic source zones. They allow for a departure from the general truncated exponential recurrence behavior in specific locations. The expected magnitude of the RLMEs that occur in each RLME source is represented by an *epistemic* distribution assessed from the available information for each source. As described in Section 5.3.3.4, given a specific value for the expected RLME magnitude, the size of individual RLMEs is modeled by a uniform *aleatory* distribution over the range of ±0.25 magnitude units about the expected value. The assessment of the size and magnitude distribution for the RLME sources is independent of the assessment of the maximum magnitude distribution for the distributed seismicity sources. As a result, there is overlap in the magnitude ranges in most cases. This introduces a small degree of "double counting" in the area covered by the RLME sources. However, the earthquakes in the CEUS SSC earthquake catalog that are identified as RLMEs are not included in the calculation of earthquake recurrence rates for the distributed seismicity sources.

The assessment of RLME recurrence rates is based on paleoseismic data gathered at each location and the methodology described in Section 5.3.3. Table 6.1-1 presents a summary of the specific methods and data used for each RLME source. The descriptions of the data and the assessment of relative weights assigned to alternative data sets are discussed in the following sections.

6.1.1 Charlevoix

Repeated historical earthquakes have occurred within the Charlevoix region of the lower St. Lawrence (Figure 6.1-2a), including the February 5, 1663, **M** 7 (E[**M**] 7.00)[1]; December 6, 1791, **M** 5.8 (E[**M**] 5.50); October 17, 1860, **M** 6 (E[**M**] 6.08); October 20, 1870, **M** 6.5 (E[**M**] 6.55); and March 1, 1925, **M** 6.3 (E[**M**] 6.18) earthquakes (Lamontagne et al., 2008). Only two of these earthquakes, the 1663 and 1870 earthquakes, are considered RLME earthquakes. The rest are considered to be part of seismicity occurring in the distributed seismicity sources. In addition, paleoseismic investigations have identified evidence of paleoearthquakes throughout the Holocene (Tuttle and Atkinson, 2010; Doig, 1991; Filion et al., 1991) that are spatially restricted to the Charlevoix area (Tuttle and Atkinson, 2010).

Several explanations have been offered for why RLMEs occur within the Charlevoix seismic zone. Adams and Basham (1991) attribute seismicity of the SLR system to earthquakes occurring on rift structures in the regional stress field of southeast-to-east compression, recognizing that a Devonian impact structure also exists in the general area and may be related to the spatial concentration of seismicity in the Charlevoix area. The observation that seismicity continues beyond the impact structure (crater) with orientations indicative of reactivation of rift faults led Adams and Basham (1991) to de-emphasize the role of impact structures. Lamontagne and Ranalli (1997) correlate large-magnitude Charlevoix earthquakes to reactivation of rift faults in response to the regional stress field. They interpret variations in orientation and style of faulting for small-magnitude earthquakes to reactivation of impact-related faults and fractures in response to local stress and/or strength conditions. In another paper, Lamontagne and Ranalli (1996) attribute earthquakes in the Charlevoix seismic zone to some or all of the following circumstances:

- Fracturing above the brittle-ductile transition at depths of at least 25 km (15.5 mi.).
- High pore-fluid pressure at mid- to lower crustal depths where hydration reactions are not favored.
- Low coefficients of friction related to highly fractured zones at depth, as opposed to thick fault gouges made of clay minerals.

Results of two-dimensional stress modeling account for the spatial pattern of observed seismicity as stress concentration due to the interaction of the crater (local zone of weakness) and rift faults (large-scale weak zone) (Baird et al., 2009). Smaller-magnitude, more frequent seismicity occurs within the impact crater, and infrequent larger-magnitude earthquakes are localized along rift faults (Baird et al., 2009). Mazzotti and Adams (2005) have also observed that the discrepancy between modeled seismic moment and strain rates derived from earthquake statistics may represent a short-term process such as postglacial rebound.

A summary of the investigations evaluated for the Charlevoix seismic zone is provided in Appendix Table D-6.1.1, and information used in the CEUS SSC Project to characterize this

[1] Magnitudes are reported in the magnitude scale designated in the cited publication. E[**M**] denotes the value of the expected moment magnitude listed in the CEUS SSC catalog for the earthquake. It is reported to two decimal places to indicate that it is a calculated value. See the discussion in Section 3.3.1.

RLME zone is presented in Appendix Table C-6.1.1. The logic tree for the Charlevoix RLME source is shown on Figure 6.1.1-1.

6.1.1.1 Evidence for Temporal Clustering

The first node of the logic tree (Figure 6.1.1-1) addresses the issue of temporal clustering of earthquakes in the present tectonic stress regime (see Section 5.1.2). The historical earthquakes identified as RLMEs are the February 5, 1663, **M** 7 (E[**M**] 7.00), and the October 20, 1870, **M** 6.5 (E[**M**] 6.55), earthquakes. Recently, Tuttle and Atkinson (2010) reported evidence, based on a minimum magnitude to produce paleoliquefaction features, for three or more **M** ≥ 6.2 earthquakes during the past 10,000 years. These earthquakes include one historical earthquake possibly associated with either the 1663, 1870, or 1925 earthquake, and two prehistoric earthquakes occurring approximately 5,000 and 10,000 years ago. The available information on the size and location of these earthquakes and the geologic evidence for long-term slip rates or recurrence intervals are insufficient to evaluate whether the Charlevoix RLME source exhibits evidence for temporal clustering. Therefore, this node of the logic tree is not applicable to the Charlevoix RLME source.

6.1.1.2 Localizing Tectonic Features

The late Proterozoic–early Paleozoic SLR, which passes through the Charlevoix RLME source zone, is attributed to the opening of the Iapetus Ocean (Tremblay and Lemieux, 2001) and is characterized within the SLR seismotectonic zone in Section 7.3.1. The St-Laurent fault strikes N20-50E and dips 60–70 degrees to the southeast, forming a northeast-trending, southeast-dipping half graben oriented parallel to the main axis of the SLR system (Tremblay and Lemieux, 2001). High-resolution seismic profiles in the St. Lawrence estuary indicate that the Laurentian Channel trough transitions from a half graben to a graben structure from southwest to northeast (Tremblay et al., 2003).

Two major fault orientations (N40-70W and N20-40E) are found outside the Charlevoix impact zone, with minor fault sets trending east to west to N80W and north to south to N20E (Lemieux et al., 2003). Fault rocks consist of fault breccia, cataclastite, foliated gouge, and pseudotachylyte with a minimum thickness of 20 m (66 ft.) near Sault-au-Cochon (Tremblay and Lemieux, 2001). Fault rocks exposed at Cap-Tourmente consist of zones of protocataclasite, cataclasite, and fault breccia 10–15 m (33–49 ft.) thick (Tremblay and Lemieux, 2001). Changes in strain rate, pressure, temperature, and fluid conditions are required for formation of cataclastic rocks, pseudotachylytes, and fault gouge within the same environment, suggesting that a single, progressive tectonic event along the SLR resulted in this distribution of fault rocks (Lemieux et al., 2003). The St-Laurent fault crosses the Charlevoix impact crater without any major deflection in strike or without any fault offsets within or at the boundaries of the structure, indicating that impact-related faulting did not significantly alter the orientation of preexisting structures and that reactivation of the St-Laurent fault is younger than the impact structure (Tremblay and Lemieux, 2001).

Within the Charlevoix impact crater the St-Laurent fault is also characterized by a well-developed and extensive series of cataclastic rock, gouge, and pseudotachylyte, as well as polymictic clastic matrix breccias restricted to the impact crater (Tremblay and Lemieux, 2001). Fragments of cataclastic breccia are present, suggesting recurrent brecciation during incremental faulting events associated with the St-Laurent fault. Fault orientations are more scattered within the impact crater but are similar to the northwest- and northeast-trending faults of the entire rift system (Lemieux et al., 2003). The spread of orientations within the central portion of the crater is attributed to the impact-related polygonal pattern of normal faults, whereas the northwest and northeast fault sets represent the youngest reactivation of the SLR (Lemieux et al., 2003).

The SLR system has experienced multiple stages of reactivation. Stratigraphic evidence of Ordovician growth faulting during late stages of the Taconic orogeny in platform deposits near Charlevoix includes major variations in thickness laterally within the Ordovician section, the presence of slump deformation features induced by faulting in almost all stratigraphic units, the preservation of pseudotachylyte within synsedimentary breccias, and the occurrence of fault breccia clasts (Lemieux et al., 2003). Tremblay et al. (2003) speculate that additional episodes of reactivation of faulting in the SLR system are younger than the Devonian-age Charlevoix impact crater. Truncation of Devonian impact-related structures by northeast-southwest and northwest-southeast faults is consistent with Mesozoic fault reactivation due to rifting of the North Atlantic region (Lemieux et al., 2003). Tremblay et al. (2003) attribute some fault throw along the SLR system to the opening of the Central Atlantic in the Jurassic and/or seafloor spreading of the North Atlantic during the Cretaceous.

Because the occurrence of RLMEs in the Charlevoix zone cannot be associated with a specific feature, future RLMEs are modeled as occurring randomly within the RLME source zone, as indicated on the second node of the logic tree (Figure 6.1.1-1).

6.1.1.3 Geometry and Style of Faulting

The geometry of the Charlevoix RLME source, shown on Figure 6.1.1-2, is defined to encompass the locations of earthquakes with **M** > 6, mapped rift faults, and the Charlevoix impact crater. Gravity and magnetic data sets delineate Grenville and Appalachian crust (Figure 6.1.1-3) and were not used to constrain the geometry for the Charlevoix RLME source. Lamontagne (1999) observed that small to moderate earthquakes of the Charlevoix seismic zone occur between, not along, rift faults and extend northeast of the impact structure as a result of the asymmetric placement of rift faults through the crater (Baird et al., 2009). Large-magnitude earthquakes are thought to occur along weakened rift faults that concentrate stress into the crater (Baird et al., 2009). The geometry for the Charlevoix RLME source zone was modified from the Charlevoix source zone of the GSC H model (Adams et al., 1996; Adams and Halchuck, 2003). Tuttle and Atkinson (2010) consider a narrower geometry for the Charlevoix seismic zone that is more localized along rift faults. A single geometry for the Charlevoix RLME source that envelops both interpretations is used, as indicated by the third node of the logic tree shown on Figure 6.1.1-1.

The location of causative faults within the Charlevoix RLME source is uncertain. In addition, using a relationship between magnitude and rupture length (e.g., Leonard, 2010), the lengths of

ruptures that would be associated with the postulated RLMEs are in the range of 30–80 km (19–50 mi.), similar to the 30 by 85 km (19 by 53 mi.) dimensions of the RLME source. Given the small source size and uncertain fault locations, the boundaries of the Charlevoix RLME source are leaky, allowing ruptures to extend beyond the source boundary by 50 percent.

Hypocentral depths for earthquakes in the Charlevoix seismic zone occur as deep as 29 km (18 mi.), although most earthquakes occur between 8 and 15 km (5 and 9.5 mi.) (Lamontagne and Ranalli, 1996). Comparing this depth distribution to rheological models of the region, Lamontagne and Ranalli (1996) attribute earthquakes in the Charlevoix seismic zone to one or more of the following: faulting above the brittle-ductile transition at depths of at least 25 km (15.5 mi.); high pore-fluid pressure below the onset of ductility for hydrated feldspar at about 350°C; and a low coefficient of friction, possibly related to unhealed zones of intense fracturing. The distribution of spatially clustered earthquakes within the Charlevoix seismic zone indicates that very few earthquakes have occurred on the same fractures with similar focal mechanisms, implying that these fault zones occur in highly fractured rocks (Lamontagne and Ranalli, 1997). The thickness of seismogenic crust is modeled with equal weight on 25 and 30 km (16 and 19 mi.), as shown on the fourth node of the logic tree (Figure 6.1.1-1).

Tremblay et al. (2003) observe several orientations of faulting within the Charlevoix RLME source. Northeast-trending longitudinal faults parallel to the main axis of the rift show three trends (N25E, N40E, and N70E) and generally dip between 60 and 90 degrees to the southeast, although a minor number dip to the northwest. Crosscutting transverse faults show two trends (N70W and N50W) and dip to the northeast or southwest; these orientations are consistent with the horst-and-graben geometry of the SLR system. Both sets of faults are high-angle faults with dip angles averaging 75–80 degrees. The pitch of fault lineations is greater than 70 degrees, indicating that most structures are dip-slip faults (Tremblay et al., 2003). Lemieux et al. (2003) observed the largest variation in fault trends within the central portion of the impact crater, which still displayed a dominant northwest-southeast orientation.

Lamontagne (1999) observed that faulting style inferred from focal mechanisms within the Charlevoix RLME source indicates reverse to oblique-reverse faulting on fault planes with highly variable orientations, and he assumed that these ruptures occur on preexisting southeast-dipping faults. Adams and Basham (1991) report that structural complexity in the form of distributed fracturing and ring faulting within the impact crater may be responsible for more varied focal mechanisms within Charlevoix. Focal mechanisms for earthquakes of magnitude $\geq$3 show reverse faulting, whereas smaller-magnitude earthquakes indicate some strike-slip and normal faulting, suggesting that local stress conditions affect rupture style (Lamontagne and Ranalli, 1997). Fault-plane solutions for recent small earthquakes located within the Charlevoix seismic zone are predominantly reverse events on steeply dipping planes, but a number of events have a significant strike-slip component, some on northwest-striking planes and some on more shallowly dipping planes (Lamontagne, 1987; Adams et al., 1989; Wetmiller and Adams, 1990).

Analysis by Li et al. (1995) of rupture directions for two **M** 4 events indicates that focal mechanisms have east-dipping planes. Bent (1992) determined a reverse mechanism for the 1925 M_S 6.2 (E[**M**] 6.18) Charlevoix earthquake with a strike of N42° ± 7°E, dip of 53° ± 7°, and rake of 105° ± 10° and favors a southeast-dipping solution based on observed seismicity and mapped

faults. Dips for the January 11, 1986, M_N 4.0 (E[**M**] 3.40) and the March 18, 1987, M_N 3.3 (E[**M**] 2.79) earthquakes range between 42 and 59 degrees to the south (Lamontagne and Ranalli, 1997). Because of the variability exhibited in mapped structures and focal mechanisms, future ruptures for the Charlevoix RLME source are modeled as randomly oriented reverse events with dips between 45 and 60 degrees in either direction.

6.1.1.4 RLME Magnitude

The February 5, 1663, earthquake is the largest observed historical earthquake within the Charlevoix seismic zone. Lamontagne et al. (2008) use a best estimate for the magnitude of **M** 7. This estimate is based on felt effects in Quebec City, Trois-Rivières, Montreal, Boston, and New York and on reported landsliding along the St. Lawrence, Shipshaw, Betsiamites, Pentecote, Batiscan, and Saint-Maurice rivers (Lamontagne et al., 2008; Gouin, 2001). Using similar observations of intensity from felt reports and accounts of landsliding and liquefaction, Ebel (1996) assigned a magnitude of **M** ≥ 7.0 ± 0.5 to the 1663 Charlevoix earthquake and concluded that the magnitude of the 1663 event is somewhat larger than the 1925 Charlevoix earthquake. Ebel (2006b) later postulated that, if the total length of the Charlevoix seismic zone (70 km, or 43.5 mi.) produced a single rupture approaching **M** 7.5 during the 1663 event, all modern seismicity represents aftershocks from this event. Ebel (2009) notes that this rupture length could produce a main-shock magnitude of **M** 7.1–7.5. He interpreted MMI VI reports at Roxbury, Massachusetts, as a m_{bLg} 7.5 (**M** 7.8) using an intensity-attenuation relationship, and as a **M** 7.5 using recent ground-motion attenuation relationships. These lines of evidence led him to assign a magnitude of **M** 7.5 ± 0.3 to the 1663 Charlevoix event. Recent discussions with Ebel (pers. comm., 2009) indicate that he prefers a magnitude of 7.2–7.5.

Paleoliquefaction features occurring along the Gouffre, Malbaie, and Ouelle rivers (Figure 6.1.1-2) in the Charlevoix area (Appendix E, Section 1.2.8.1) provide evidence of three generations of earthquake-induced liquefaction within the last 10,000 years (Tuttle and Atkinson, 2010). The spatial distribution of these features and the lack of paleoliquefaction evidence to the south in the Trois Rivières area can be attributed to paleoearthquakes of **M** ≥ 6.2 in the Charlevoix seismic zone (Tuttle and Atkinson, 2010). The prehistoric earthquakes are considered RLMEs (**M** ≥ 6.5) given the range of magnitudes (M 6.2–7.0) capable of explaining the spatial distribution of observed liquefaction features (Tuttle and Atkinson, 2010). Recent work by Locat (2008) places the **M** 7 1663 earthquake near Saguenay, based on the distribution of largely undated landslide deposits throughout the region and subaqueous mass movements in the St. Lawrence estuary, Saguenay fjord, and nearby lakes. This work illustrates the role of landsliding, in addition to liquefaction, in recording paleoearthquakes in the region. However, better constraints on timing of events are required for correlating deformation with specific events and geotechnical studies of susceptibility are required for determining the location and magnitude of those events. Consequently, the results of the Locat (2008) study were not used in the characterization of the 1663 Charlevoix earthquake.

Based on the information above, the distribution for RLME magnitude tabulated below was developed. This magnitude distribution places most of the weight on the preferred magnitude from Lamontagne et al. (2008) and incorporates uncertainty from the paleoliquefaction record and recent estimates from Ebel (2009). Aleatory variability in the size of an individual

Charlevoix RLME is modeled as a uniform distribution of ±0.25 **M** units centered on the expected RLME magnitude value (Section 5.3.3.4).

Expected Charlevoix RLME Magnitude (M)	Weight
6.75	0.2
7.0	0.5
7.25	0.2
7.5	0.1

6.1.1.5 RLME Recurrence

The remaining nodes of the Charlevoix RLME logic tree address uncertainties in the specification of the annual frequency of RLMEs.

Recurrence Methods and Data

Paleoseismic investigations provide evidence of persistent earthquake activity through the Holocene. Filion et al. (1991) interpreted two earthquake-induced landslides by dating tree rings in the base of flow materials of dammed lakes along the Rivière du Gouffre, which is located within the Charlevoix seismic zone. Doig (1990) identified silt layers in lakes as recording earthquake-induced landslides and inferred a variable recurrence rate for the Charlevoix seismic zone: a recurrence interval of 120 years from 320 BC to AD 800; 270 years from AD 800 to 1500; and 75 years from AD 1500 to the present. Some silt layers in the section were correlated with historical earthquakes from 1638, 1663, 1791, 1870, and 1925 (Doig, 1990). These observations are difficult to quantitatively incorporate within earthquake recurrence calculations since silt layers may be due to nontectonically induced landslides; however, if the cause is tectonic, these silt layers can be attributed to either local moderate-sized earthquakes or distant large-magnitude earthquakes. Assigning a magnitude, location, and recurrence for the features identified by Doig (1990) would require a detailed chronology of regional landslide features and geotechnical assessments of their strength. Therefore, the recurrence for the Charlevoix RLME source is modeled from the 1663 and 1870 earthquakes and two prehistoric earthquakes identified by Tuttle and Atkinson (2010), which does include geotechnical assessments of liquefaction potential of host sediments in the evaluation of magnitude and location for these paleoearthquakes.

Tuttle and Atkinson (2010) provide evidence of at least three Holocene paleoearthquakes in Charlevoix with $\mathbf{M} \geq 6.2$, including one historical event with a bracketed age of at least 540 yr BP. Tuttle and Atkinson (2010) argue that the 540 yr BP features could be assigned to one of three historical Charlevoix earthquakes since 1660. This set of liquefaction features is therefore included in the recurrence assessment as either the 1663 or 1870 earthquake. Two prehistoric paleoearthquakes are included in the assessment of Charlevoix RLME recurrence. The oldest

generation of features interpreted as having been formed by paleoearthquakes includes pseudonodules and related folds along the Malbaie River, and pillars and convolute bedding along the Gouffre River formed between 10,120 and 9,410 yr BP (Tuttle and Atkinson, 2010). A paleoearthquake of intermediate age is identified by sand dikes and load casts formed since 5,040 yr BP (Tuttle and Atkinson, 2010). Dionne (2001) reports evidence of a sea-level lowstand of 10 m (33 ft.) along the south shore of the St. Lawrence estuary between 6 and 7 ka based on the elevations of intertidal or subtidal deposits overlying the erosional surface of marine clay and covered by emergent organic layers. This lowstand may have reduced the completeness of the paleoliquefaction record during that time, indicating that the three events observed by Tuttle and Atkinson (2010) in the past 10 kyr should be viewed as a minimum.

The available data suggest three possible alternatives for assessing the RLME recurrence rates: the historical record and the two alternative geologic records of 6–7 kyr and 9.5–10.2 kyr. The alternatives for the number of RLMEs in each time period are the 1870 and 1663 earthquakes in the historical period (data set 1); the 1870 and 1663 earthquakes with one paleoearthquake in 6–7 kyr (data set 2); and the 1870 and 1663 earthquakes with two paleoearthquakes in 9.5–10.2 kyr (data set 3). The assessment of RLME recurrence puts the greatest weight on the 6–7 kyr geologic record [0.6] because geologic conditions affecting the susceptibility of sediments are not likely to have changed since the sea level lowstand at 6–7 ka and thus the geological record is expected to be reasonably complete. The longer, 10 kyr, geologic record may be affected by incompleteness in the period before 6–7 ka, and is thus given lower weight [0.2], one-third of the weight assigned to the shorter geologic period. The historic period is also given lower weight [0.2] because it contains a small sample (two earthquakes) and the short recurrence interval between the 1663 and 1870 earthquakes could have occurred by chance (e.g., with approximately 10 percent probability for a Poisson process with the average return period based on the 6–7 kyr record).

The three alternative data sets represent two types of data. Data set 1 consists of earthquakes with known times of occurrence and is analyzed by the “Earthquake Recurrence Intervals” approach, while data sets 2 and 3 represent “Earthquake Counts in a Time Interval.” The common logic tree format used for the RLME sources includes a node for Recurrence Method and a node for Recurrence Data. The weights assigned to the three alternative data sets are used to assign the weights to the branches for these two nodes in the RLME logic tree. For the Recurrence Method node, the “Earthquake Recurrence Intervals” approach is assigned a weight of 0.2, the weight assigned to data set 1, and the “Earthquake Count in a Time Interval” approach is assigned a weight of 0.8, the sum of the weights assigned to data sets 2 and 3. For the Recurrence Data node on the “Earthquake Recurrence Intervals” branch, data set 1 then gets a conditional weight of 1.0. For the Recurrence Data node on the “Earthquake Count in a Time Interval” branch, data set 2 gets a conditional weight of 0.75 (= [0.6]/[0.8]) and data set 3 gets a conditional weight of 0.25 (= [0.2]/[0.8].

Earthquake Recurrence Model

As discussed in Section 5.3.3, the Poisson model is used as the default earthquake recurrence model, with a weight of 1.0 for the Charlevoix RLME source, as there are not sufficient data to justify including an alternative model.

RLME Annual Frequency

The final node of the logic tree addresses the uncertainty distributions for the annual frequency of RLMEs. These distributions were developed using the methodology described in Section 5.3.3.1. For data set 1 the relative likelihood of various values of the recurrence rate parameter was developed using Equation 5.3.3-4 and the observations of one closed recurrence interval between the 1663 and 1870 earthquakes and one open interval post the 1870 earthquake. The resulting relative-likelihood-based distribution was represented by the five-point discrete distribution listed in Table 6.1.1-1. For data set 2 the relative-likelihood-based distribution was developed using Equation 5.3.3-2, with N equal to three earthquakes and T uniformly distributed between 6 and 7 kyr. The distribution for data set 3 was also developed using Equation 5.3.3-2, with N equal to four earthquakes and T uniformly distributed between 9.5 and 10.2 kyr. The resulting distributions for RLME recurrence frequency are listed in Table 6.1.1-1.

6.1.2 Charleston

The September 1 (August 31 local time), 1886, E[**M**] 6.90, earthquake that occurred in the Charleston, South Carolina, area is the largest historical earthquake ever recorded in the Eastern United States. This earthquake produced modified Mercalli intensity (MMI) X shaking in the epicentral area near Charleston, and was felt as far away as Chicago (Johnston, 1996c). Strong ground shaking during the 1886 Charleston earthquake resulted in extensive liquefaction, which was expressed primarily as sand-blow craters at the ground surface (Dutton, 1889). Because no primary tectonic surface rupture has been identified as the causative structure for the 1886 earthquake, a combination of geologic, geophysical, geomorphic, and instrumental seismicity data have been used by multiple investigators to suggest several different faults as the potential source for Charleston-area seismicity (e.g., Behrendt et al., 1981; Talwani, 1982; Hamilton et al., 1983; Behrendt and Yuan, 1987; Marple and Talwani, 2000; Weems and Lewis, 2002; Talwani and Katuna, 2004; Dura-Gomez and Talwani, 2009; Talwani and Dura-Gomez, 2009; Chapman and Beale, 2008, 2010).

The existence of pre-1886 sand-blow craters and other paleoliquefaction features that occur throughout coastal South Carolina also provides evidence for prior strong ground motions during prehistoric large earthquakes in the region (e.g., Obermeier et al., 1989; Weems and Obermeier, 1990; Amick et al., 1990a, 1990b; Talwani and Schaeffer, 2001; Talwani et al., 2008). Paleoliquefaction studies conducted in coastal South Carolina since the 1980s provide evidence that the Charleston seismic source exhibits RLMEs and appears to be confined to the Charleston area. Based on the strong field evidence for RLMEs derived from the study of liquefaction and paleoliquefaction features, the Charleston seismic zone is characterized as an RLME source. Appendix Table D-6.1.2 (data summary table) lists the references that were reviewed to characterize the Charleston RLME source, and Appendix Table C-6.1.2 (data evaluation table) lists the data that were explicitly used to constrain the characterization of this RLME source. Neither the 1886 nor the prehistoric (i.e., pre-1886) earthquakes in the Charleston area can be definitively attributed to any specific fault or fault zone at the present time.

6.1.2.1 Evidence for Temporal Clustering

The first node of the logic tree (Figure 6.1.2-1) addresses the issue of temporal clustering of earthquakes in the present tectonic stress regime (see Section 5.1.2). The rates of deformation suggested by paleoliquefaction data and the lack of surface features that would be expected if those deformation rates persisted over the long term lead to the conclusion that either the recent sequence of earthquakes is an isolated occurrence in time, or such sequences occur as clusters with long intercluster periods of seismic quiescence. The recurrence behavior of the large earthquakes in the Charleston seismic zone therefore may be highly variable through time, such that periods of activity alternate with periods of quiescence. Section 5.1.2 provides a definition and discussion of the temporally clustered earthquake model.

Geologic and geomorphic observations suggest that inter-event times of large earthquakes in the Charleston seismic zone since the mid-Holocene (approximately hundreds to a few thousand years; see Section 6.1.2.5) are not characteristic of the region over longer-term periods. For example, based on reprocessed seismic reflection data, Chapman and Beale (2008, 2010) note evidence of a steeply dipping, down-to-the-east normal fault with approximately 200 m (656 ft.) of vertical offset in early Mesozoic sedimentary and volcanic rocks. They also report that overlying Cretaceous and Tertiary coastal plain sediments show approximately 10 m (33 ft.) of reverse up-to-the-east minor reverse displacement. Based on the minor amounts of Cretaceous-and-younger vertical separation associated with subsurface faults in the Charleston area, the mid-Holocene to modern seismicity rates inferred from the paleoliquefaction record are not interpreted to be indicative of the longer-term behavior of the Charleston seismic zone.

Additionally, geomorphic observations suggest that the high rate of recurrence of large earthquakes within the Charleston seismic zone inferred from mid-Holocene to modern seismicity is not indicative of the longer-term behavior of the Charleston seismic zone. A protracted period of large earthquakes recurring on the order of hundreds to a few thousand years apart would produce tectonic landforms with clear geomorphic expression, such as those present in regions of the world with comparably high rates of moderate to large earthquakes. For example, faults in the Eastern California shear zone with submillimeter-per-year slip rates and recurrence intervals on the order of about 5,000 years have clear expression in the landscape (Rockwell et al., 2000). The fact that such landforms are not evident in the Charleston area suggests that the Charleston source may have a recurrence rate that is highly variable through time. Therefore, sequences of earthquakes spaced about 500 to 1,000 years apart may be followed by quiescent intervals of many thousands of years.

Based on the geologic and geomorphic lines of evidence discussed above, the high rate of mid-Holocene to modern seismicity in the Charleston seismic zone is not interpreted to be a long-lived phenomenon. However, because no data definitively demonstrate whether the Charleston seismic zone is currently in or out of a temporal cluster, the Charleston RLME seismic source is modeled as “in” a temporal cluster with a weight of 0.9 and “out” of a temporal cluster with a weight of 0.1 in this study (Figure 6.1.2-1).

6.1.2.2 Localizing Feature

The second node of the Charleston RLME source logic tree indicates whether future earthquakes in the Charleston seismic zone will be associated with a specific localizing tectonic feature (Figure 6.1.2-1). As described in Section 6.1.2.3, numerous faults are postulated in the Charleston area, but there is no direct evidence that any structure is an active tectonic feature. Moreover, the 1886 earthquake is not definitively attributed to any particular fault or fault zone. Therefore, the "Random in Zone" option is given a 1.0 weight in the model. This modeling decision reflects the interpretation that future Charleston earthquakes will not necessarily occur on any known fault or fault zone, but rather somewhere within the alternative configurations for the Charleston RLME source shown on Figure 6.1.2-2.

6.1.2.3 Geometry and Style of Faulting

The third through fifth nodes of the Charleston RLME source logic tree address parameters that characterize source geometry, seismogenic crustal thickness, and rupture orientation for the Charleston RLME seismic source zones (Figure 6.1.2-1). The source characterization for Charleston comprises the following three alternative configurations (Figure 6.1.2-2):

- Charleston Local—The small "local" configuration includes the 1886 meizoseismal area (Bollinger, 1977); the preponderance of 1886 liquefaction features (e.g., Dutton, 1889; Talwani and Schaeffer, 2001); instrumentally located earthquakes in the Middleton Place–Summerville seismic zone (Madabhushi and Talwani, 1993); and numerous postulated faults (e.g., Weems and Lewis, 2002; Talwani and Katuna, 2004; Bartholomew and Rich, 2007; Talwani and Dura-Gomez, 2009).
- Charleston Narrow—The "narrow" configuration contains postulated north-northeast-striking structures, including the postulated Woodstock fault (Talwani, 1982); the southern segment of the postulated East Coast fault system (Marple and Talwani, 2000); and one interpretation of the location of Chapman and Beale's (2009) "fault C."
- Charleston Regional—The large "regional" configuration envelops most of coastal South Carolina, including the preponderance of pre-1886 paleoliquefaction features and postulated faults, and extends offshore to include the Helena Banks fault zone (Behrendt and Yuan, 1987).

For seismogenic crustal thickness, the fourth node of the logic tree (Figure 6.1.2-1), the three alternative Charleston source configurations adopt values and weights (shown in brackets) of 15 km (9 mi.) [0.2], 20 km (12 mi.) [0.4], and 25 km (16 mi.) [0.4]. Seismogenic crustal thickness in the Charleston area is not well constrained, but available data are consistent with these values. Bollinger (1983) indicates that seismogenic thickness in the Charleston area is poorly constrained, but he estimates a value of 12 km (7.5 mi.) for the 1886 earthquake on the basis of empirical scaling relations. Dura-Gomez and Talwani's (2009) relocated small-magnitude earthquakes in the Charleston area indicates depths to 16 km (10 mi.), with most hypocenters between 3 and 13 km (2 and 8 mi.) depth. Moreover, the CEUS SSC Project default values for seismogenic crustal thickness are consistent with those used in previous SSCs for Charleston. Bollinger (1992) adopts depths of 14 and 25 km (8.5 and 15.5 mi.) for his "Local Charleston"

and "SC Piedmont and Coastal Plain" zones, respectively. Chapman and Talwani (2002) adopt a value of 25 km (15.5 mi.) in their source characterization developed for the South Carolina Department of Transportation. Silva et al. (2003) adopt values of 16 and 20 km (10 and 12.5 mi.) depth, inferred from contemporary seismicity.

The remaining data used to constrain each of these three alternative configurations are summarized below and are shown on Figures 6.1.2-3, 6.1.2-4, 6.1.2-5a, and 6.1.2-5b. Additional descriptions of the data constraining the Charleston model are provided in Appendix Table C-6.1.2.

Charleston Local Source

The Charleston Local source configuration is an approximately 100 by 50 km (60 by 30 mi.) northeast-elongated zone centered on the 1886 Charleston meizoseismal area (area of greatest damage) (Figures 6.1.2-5a and 6.1.2-5b). The Charleston Local source completely incorporates the 1886 earthquake MMI X isoseismal (Bollinger, 1977); the majority of identified Charleston-area tectonic features and inferred fault intersections (e.g., Weems and Lewis, 2002; Talwani and Katuna, 2004; Bartholomew and Rich, 2007; Talwani and Dura-Gomez, 2009); and the majority of reported 1886 liquefaction features (e.g., Dutton, 1889; Talwani and Schaeffer, 2001). The Charleston Local source also envelops instrumentally located earthquakes in the Middleton Place–Summerville seismic zone (Tarr et al., 1981; Tarr and Rhea, 1983; Madabhushi and Talwani, 1993). The Charleston Local source excludes the northern extension of the southern segment of the postulated East Coast fault system (Marple and Talwani, 2000) because this system extends well north of the meizoseismal zone and is included in the Charleston Narrow source geometry. The Charleston Local source also excludes outlying liquefaction features, because liquefaction occurs as a result of strong ground shaking that may extend well beyond the extent of the causative fault.

In summary, the Charleston Local source configuration envelops (1) the meizoseismal area of the 1886 earthquake; (2) the area containing the majority of local tectonic features (although many have large uncertainties associated with their existence and activity); (3) the Middleton Place–Summerville seismic zone; and (4) the area of greatest density of 1886 liquefaction and prehistoric liquefaction. These four observations suggest that future earthquakes having magnitudes comparable to that of the 1888 Charleston earthquake most likely will occur within the volume of crust defined by the Charleston Local source configuration. Therefore, because a preponderance of evidence supports the interpretation that the seismic source for the 1886 Charleston earthquake is located in a relatively restricted area defined by the Charleston Local source, the Charleston Local source is given a relatively high weight of 0.50 in the model.

Future ruptures in the Charleston Local source are oriented northeast, parallel to the long axis of the zone and the regional structural grain of the Appalachian orogen. Future ruptures are modeled as occurring on vertical strike-slip faults. All boundaries of the Charleston Local source are strict, such that ruptures are not allowed to extend beyond the zone boundaries.

Charleston Narrow Source

The Charleston Narrow source configuration is an approximately 65 by 30 km (40 by 20 mi.), north-northeast-oriented source (Figures 6.1.2-5a and 6.1.2-5b). The geometry of the Charleston Narrow source is constrained on the basis of postulated faults and tectonic features in the Charleston area, including (1) the proposed Woodstock fault (Talwani, 1982); (2) the zone of river anomalies (Marple and Talwani, 1993) and the southernmost portion of the southern segment of the proposed East Coast fault system (Marple and Talwani, 2000); (3) the proposed Woodstock, Ashley River, Sawmill Branch, Lincolnville, and Charleston faults (Talwani and Dura-Gomez, 2009); and (4) one interpretation of the location of "fault C" by Chapman and Beale (2009), based on reprocessed seismic reflection lines. These postulated faults and tectonic features strike generally northeast and are located in the same narrowly constrained area. However, the Charleston Narrow source is not modeled as any particular fault, but rather as an area that represents the possibility that one or more of these features may exist and may be active. As described below in Section 6.1.2.5 (Recurrence), the Brownian Passage Time (BPT) renewal model is applied with low weight to the Charleston Narrow source configuration because it is the most "fault-like" of the alternative configurations.

The northeast and southwest extents of the narrow source are defined by fault mapping from Dura-Gomez and Talwani (2009) and Talwani and Dura-Gomez (2009). Marple and Talwani's (2000) depiction of the southern segment of the East Coast fault system extends northeast beyond the narrow source configuration. However, according to Dura-Gomez and Talwani (2009) and Talwani and Dura-Gomez (2009), evidence for the existence and activity of the East Coast fault system is greatest in the south (within the narrow source configuration) and decreases northeastward (beyond the narrow source configuration). The northeast and southwest boundaries of the Charleston Narrow source configuration are leaky, such that ruptures that initiate within the zone are allowed to extend beyond the zone boundaries in those directions, but by no more than 50 percent of the rupture length beyond the boundary.

The Charleston Narrow source configuration includes postulated faults with varying degrees of evidence of existence, none of which has clear evidence for Neogene activity. The Charleston Narrow source configuration is given a 0.30 weight in the CEUS SSC model.

Future ruptures in the Charleston Narrow source are oriented north-northeast, parallel to the long axis of the zone. Future ruptures are modeled as occurring on vertical strike-slip faults. As described above, the northeast and southwest boundaries of the Charleston Narrow source are leaky, whereas the northwest and southeast boundaries of the Charleston Narrow source are strict, and ruptures are not allowed to extend beyond the zone boundaries to the northwest and southeast.

Charleston Regional Source

The Charleston Regional source configuration is an approximately 260 by 150 km (160 by 95 mi.) source that entirely envelops both the local and narrow zones. The regional source extends to the northeast and southwest to capture the preponderance of prehistoric paleoliquefaction features; to the southeast to include the offshore Helena Banks fault zone (Behrendt and Yuan,

1987); and inland to capture earthquakes in the Bowman seismic zone (Tarr et al., 1981; Tarr and Rhea, 1983; Smith and Talwani, 1985). The elongation and orientation of the Charleston Regional source is roughly parallel to the regional structural grain of the Appalachian orogen as well as to the elongation of 1886 isoseismals (Bollinger, 1977; Figures 6.1.2-5a and 6.1.2-5b).

The large area covered by the Charleston Regional source reflects the uncertainty associated with the seismic source or sources that produced the 1886 and prehistoric earthquakes. The size of the regional source configuration is based partially on consideration of the liquefaction magnitude-bound relation developed for the CEUS (Olson et al., 2005b; Olson, 2009) and the mapped extent of paleoliquefaction features. The inlandmost paleoliquefaction features are found along the Edisto River, approximately 80 km (50 mi.) from the coast (Figures 6.1.2-3 and 6.1.2-5a; Obermeier, 1996, figure 7.6) and typically are smaller than those found nearer the coast. The regional source extends inland of these features, however, in recognition of the fact that liquefaction susceptibility generally decreases further inland due to material properties and saturation level. The regional source extends offshore because, based on the distribution of liquefaction and paleoliquefaction features, the possibility of an offshore seismic source cannot be precluded. Moreover, the regional source extends offshore to include the northeast-striking Helena Banks fault system, as is clearly shown by multiple seismic reflection profiles, and is interpreted to exhibit Late Miocene offset (Behrendt et al., 1983). Furthermore, the occurrence of at least one light-magnitude earthquake in 2002 (November 11, E[**M**] 3.98) suggests a possible spatial association of seismicity with the mapped trace of the Helena Banks fault system.

The preponderance of evidence supports the interpretation that the seismic source for Charleston RLMEs is located in a relatively restricted area defined by either the Charleston Local or Narrow source configurations. The larger volume of crust represented by the Charleston Regional source configuration allows for the possibility that Charleston RLMEs are produced by a fault of faults beyond the 1886 meizoseismal zone and beyond the area containing the majority of postulated Charleston faults. The Charleston Regional source configuration is given a 0.20 weight in the CEUS SSC model.

For future rupture orientations in the Charleston Regional source configuration, two alternatives exist: (1) future ruptures oriented parallel to the long axis of the source (northeast) with 0.80 weight, and (2) future ruptures oriented parallel to the short axis of the source (northwest) with 0.20 weight. In these and all cases for Charleston, future ruptures are modeled as occurring on vertical strike-slip faults. All boundaries of the Charleston Regional source are strict, such that ruptures are not allowed to extend beyond the zone boundaries.

6.1.2.4 RLME Magnitude

The sixth node of the Charleston RLME source logic tree defines the magnitude of future large earthquakes in the Charleston RLME source, and assigned weights (Figure 6.1.2-1). Estimates for magnitude are based on estimates of magnitude for the 1886 Charleston earthquake and on geotechnical estimates of magnitudes of prehistoric earthquakes in coastal South Carolina.

Estimates of 1886 Earthquake Magnitude

Estimates for the magnitude of the 1886 Charleston earthquake typically are in the high-6 to mid-7 range, with more modern estimates generally nearer the low end of this range. For example, a geotechnical assessment of 1886 liquefaction data led Martin and Clough (1994) to estimate **M** 7–7.5 for the 1886 Charleston earthquake. Johnston (1996c) estimates **M** 7.3 ± 0.26 for the earthquake, based on isoseismal area regressions accounting for eastern North America anelastic attenuation. The best estimate by Bakun and Hopper (2004) is **M** 6.9, with a 95 percent confidence level corresponding to a range of **M** 6.4–7.1, based on isoseismal area regression, including empirical site corrections. Most recently, Talwani (2009) studied empirical fault length–magnitude relationships and geotechnical assessments of the 1886 and prehistoric Charleston earthquakes and derives a best estimate of **M** 7.0 for the 1886 earthquake. The CEUS SSC earthquake catalog assigns E[**M**] 6.90 to the 1886 Charleston earthquake.

Geotechnical Estimates of Prehistoric Earthquake Magnitudes

Geotechnical estimates for the magnitudes of prehistoric earthquakes typically are based on one or more of the following factors: (1) empirical relations between size of paleoliquefaction features (e.g., dike width) and magnitude; (2) characterization of in situ sediment properties and the degree of strong ground motion required to liquefy those sediments; (3) distance separating the most distal paleoliquefaction feature from a known or assumed earthquake location; and (4) areal extent of the paleoliquefaction field produced by a single earthquake. Dike widths and other paleoliquefaction-feature dimensional data are lacking for the Charleston region, so magnitude estimates for prehistoric Charleston earthquakes are based on in situ soil properties and the spatial distribution of paleoliquefaction features. Geotechnical estimates for the magnitudes of prehistoric earthquakes in the Charleston seismic zone vary widely, but typically are in the high-5 to high-7 range. These widely varying magnitude estimates reflect the uncertainties associated with the use of paleoliquefaction data (see Appendix E, CEUS Paleoliquefaction Database, Uncertainties Associated with Paleoliquefaction Data, and Guidance for Seismic Source Characterization).

Hu et al. (2002a, 2002b) describe methodologies and provide estimates for the magnitudes of prehistoric Charleston earthquakes based on geotechnical estimates of in situ soil properties. They report magnitude estimates ranging from **M** 6.8 to 7.8 for "large" regional Charleston earthquakes, and from **M** 5.5 to 7.0 for possible "moderate" local earthquakes at Georgetown, South Carolina. A subsequent study by Leon et al. (2005), which includes two of the same three coauthors as Hu et al. (2002a, 2002b), presents lower magnitude estimates for prehistoric Charleston earthquakes. Leon (2003) and Leon et al. (2005) present geotechnical assessments of magnitude for Charleston prehistoric earthquakes that account for the effects of sediment aging. Their magnitude estimates range from **M** 5.5 to 7.2 for "large" regional Charleston earthquakes and from **M** 4.3 to 6.4 for possible "moderate" local earthquakes at Bluffton and Georgetown, South Carolina. Using standard penetration test, cone penetration test, and shear-wave velocity data, Gassman et al. (2009) suggest a preferred magnitude range of **M** 6.7–7.0 for prehistoric, historic, and future earthquakes in the Charleston seismic zone. Based on the interpretation of prehistoric Charleston earthquakes developed as part of the CEUS SSC Project (see Section 6.1.2.5—Recurrence), paleoliquefaction fields are similar to the 1886 earthquake liquefaction

field in location and extent. As such, the prehistoric earthquakes that formed these fields likely had magnitudes similar to the 1886 earthquake.

Charleston RLME Magnitude

The Charleston RLME source magnitude distribution for future large earthquakes is based on assessment of the currently available data, interpretations of the range of magnitude estimates for the 1886 and prehistoric Charleston earthquakes, and the assumption that future large earthquakes will have magnitudes similar to these earthquakes. The magnitude distribution includes a total of five discrete magnitude values from **M** 6.7 to 7.5, each separated by 0.2 **M** units (Figure 6.1.2-1). It includes a discrete value of **M** 7.3 to represent Johnston's (1996c) mean estimate for the 1886 earthquake, as well as a higher value of **M** 7.5 to capture a low probability that future large earthquakes in the Charleston seismic source will be greater than **M** 7.3. To represent Bakun and Hopper's (2004) best estimate of the 1886 Charleston earthquake magnitude, the Charleston RLME source magnitude distribution includes a discrete value of **M** 6.9. The magnitude distribution also includes a lower value of **M** 6.7 to capture a low probability that future large earthquakes in the Charleston seismic source will be less than **M** 6.9.

The resulting RLME magnitude distribution is tabulated below. This distribution results in a weighted mean magnitude of **M** 7.1 for the Charleston RLME seismic source. Aleatory variability in the size of an individual Charleston RLME is modeled as a uniform distribution of ±0.25 **M** units centered on the expected RLME magnitude value (Section 5.3.3.4).

Expected Charleston RLME Magnitude (M)	Weight
6.7	0.1
6.9	0.25
7.1	0.3
7.3	0.25
7.5	0.1

6.1.2.5 RLME Recurrence

The remaining nodes of the Charleston RLME source logic tree (i.e., nodes seven through twelve) address the uncertainty modeling of the of Charleston RLMEs (Figure 6.1.2-1). Section 1.2.6 of Appendix E provides additional information on paleoliquefaction features in coastal South Carolina.

Recurrence Method

The recurrence data for the Charleston RLME source consists of ages of past RLMEs estimated from the paleoliquefaction record. Therefore, node seven of the logic tree indicates that recurrence for the Charleston RLME source is based solely on the "Earthquake Recurrence Intervals" approach.

Time Period

The eighth node of the Charleston RLME source logic tree assesses length and completeness of the paleoliquefaction record, which are sources of epistemic uncertainty in the CEUS SSC (Figure 6.1.2-1). The paleoliquefaction record along the South Carolina coast extends from 1886 to the mid-Holocene, approximately 5,500 yr BP (Talwani and Schaeffer, 2001). The consensus of scientists who have evaluated these data is that the paleoliquefaction record of earthquakes is complete only for approximately the past 2,000 years and that liquefaction events likely are missing from the older portions of the record (Talwani and Schaeffer, 2001). For this reason, this study places more weight on the paleoseismic record from the most recent 2,000 years of record. The perception that the paleoseismic record may be incomplete from 2,000 to 5,500 yr BP is based on the argument that past fluctuations in sea level have produced intervals of low water table conditions, and thus low liquefaction susceptibility, during which large earthquakes may not be represented in the paleoliquefaction record (Talwani and Schaeffer, 2001). While this assertion may be true, it is also possible that the paleoliquefaction record may be complete back to the mid-Holocene (Talwani and Schaeffer, 2001). Based on these arguments, the approximately 2,000-year record of Charleston earthquakes is given a 0.80 weight in the model, and the approximately 5,500-year record is given a 0.20 weight.

Earthquake Count

The ninth node of the Charleston logic tree addresses the uncertainty in the number of RLMEs that have occurred in the Charleston RLME source (Figure 6.1.2-1). Alternative interpretations of the distribution of paleoliquefaction features include a total of four large earthquakes in the past approximately 2,000 years and between four and six large earthquakes in the past approximately 5,500 years. The alternative characterizations represented in the logic tree are based on (1) interpreted length of the paleoliquefaction record, (2) interpreted types of constraining ages, and (3) evaluations of the area distribution and interpretations of which of the prehistoric liquefaction features were caused by large-magnitude earthquakes centered in the Charleston area and which were caused by moderate-magnitude local earthquakes.

Talwani and Schaeffer (2001) combine previously published data with their own studies of paleoliquefaction features in the South Carolina coastal region to derive possible earthquake recurrence histories for the region. They estimate recurrence intervals of approximately 550 to 1,000 years and interpret the possibility of both moderate- and large-magnitude earthquakes (roughly **M** 6+ and 7+, respectively). The CEUS SSC Project supplements Talwani and Schaeffer's (2001) compilation of Charleston paleoliquefaction data with data from other studies (e.g., Noller and Forman, 1998; Talwani et al., 2008) (see Section 1.2.6 of Appendix E).

Talwani and Schaeffer (2001) identify individual earthquake episodes based on regional correlations of prehistoric sand-blow craters with overlapping calibrated radiocarbon ages having 1-sigma (68.3 percent confidence interval) error bands. The standard in paleoseismology, however, is to use calibrated radiocarbon ages with 2-sigma (95.4 percent confidence interval) error bands (e.g., Grant and Sieh, 1994). Likewise, in paleoliquefaction studies, to more accurately reflect the uncertainties in radiocarbon dating and age estimates of paleoliquefaction features, Tuttle (2001) advises the use of calibrated radiocarbon dates with 2-sigma error bands (as opposed to narrower 1-sigma error bands). On Tuttle's (2001) recommendation, the CEUS SSC Project recalibrated and reported the conventional radiocarbon ages presented in Talwani and Schaeffer (2001) with 2-sigma error bands (see Appendix E and the CEUS SSC paleoliquefaction database). This recalibration was performed with the radiocarbon calibration program OxCal version 4.1 (Bronk Ramsey, 2009) using the radiocarbon calibration curve of Stuiver et al. (1998). The recalibrated 2-sigma radiocarbon ages form the basis of the CEUS SSC Project analyses of the timing, location, and magnitude of paleoearthquakes that induced liquefaction in the vicinity of Charleston, South Carolina.

For the Charleston data set, two types of radiocarbon ages are used to constrain the timing of formation of prehistoric sand-blow craters, namely contemporary (or "con") radiocarbon ages, and radiocarbon ages that provide maximum or minimum age constraints on a sand-blow crater (Figure 6.1.2-6). Contemporary ages are those ages interpreted by Talwani and Schaeffer (2001) as closely approximating the time of formation of the sand-blow crater. The data for determining contemporary ages include fragile twigs or stems that became entrained in fine-grained deposits within crater deposits during or very soon after crater formation, and that are thus approximately equivalent in age with time of formation of the feature. Maximum and minimum ages are provided by carbon samples collected from stratigraphic positions below and above a paleoliquefaction feature, respectively. Typically, the estimated ages of paleoliquefaction features from maximum/minimum pairs of radiocarbon samples are broader than those provided by contemporary radiocarbon ages. For this reason, contemporary ages are preferred.

Another reason for preferring contemporary age constraints concerns the specific geologic environment in which the Charleston region sand-blow craters are found. The vast majority of the sand-blow craters are located on the crests of beach ridges in geologic units that are tens to hundreds of thousands of years old or more (McCartan et al., 1984; Obermeier, 1996). Moreover, LiDAR data indicate that the vast majority of these sand-blow craters features are located on local topographic highs, representing areas removed from active deposition that are characterized by ongoing soil formation, stripping, and reworking processes. Considering the geologic environment where the sand-blow craters occur, it is unclear exactly what radiocarbon ages from maximum/minimum samples collected from stratigraphic positions above and below the paleoliquefaction features may mean. However, as described below, the timing of prehistoric earthquakes in the Charleston region is largely constrained by contemporary ages, with the maximum/minimum ages primarily used as possible evidence for constraining spatial extent, and thus the magnitude, of some of the prehistoric liquefaction fields.

Figures 6.1.2-7 and 6.1.2-8 are space-time diagrams showing the 2-sigma radiocarbon age constraints on paleoliquefaction features in the Charleston region as vertical lines, and interpreted earthquakes as colored horizontal bars. Age constraints from samples, or pairs of

samples, used to define each earthquake are shown as vertical colored bars. Appendix E provides a detailed description of the methodologies and uncertainties associated with interpreting prehistoric earthquakes from paleoliquefaction data.

Figure 6.1.2-7 shows the prehistoric earthquake scenario based on contemporary age constraints only. Figures 6.1.2-9 through 6.1.2-13 show in map view the spatial distribution of paleoliquefaction features associated with each interpreted earthquake in the "contemporary ages only" scenario. In this scenario, four large-magnitude regional earthquakes (1886, A, B, and C) have occurred in the past approximately 2,000 years. Two additional earthquakes (D and E) occurred in the past approximately 5,500 years. Yet, based on the possibly limited spatial extent of the liquefaction fields associated with earthquakes D and E, it is unclear from the "contemporary ages only" scenario whether earthquakes D and E were large-magnitude regional earthquakes with liquefaction fields similar to that produced by the 1886 earthquake, or whether they were moderate-magnitude local earthquakes. Table 6.1.2-1 summarizes the age constraints and sizes (regional or local) of interpreted prehistoric Charleston earthquakes A through E from the "contemporary ages only" scenario.

Figure 6.1.2-8 shows the prehistoric earthquake scenario based on contemporary and maximum/minimum age constraints (the "all ages" scenario). In this figure, the maximum/minimum age constraints are shown as vertical dashed lines to differentiate them from the solid vertical lines that represent contemporary age constraints. Unpaired maximum or minimum age constraints are shown as up or down arrows, respectively, and typically are not useful for interpreting prehistoric earthquakes. Figures 6.1.2-14 through 6.1.2-18 show in map view the spatial distribution of paleoliquefaction features associated with each interpreted earthquake in the "all ages" scenario. The results of the "contemporary ages only" and "all ages" scenarios are nearly identical in terms of the timing of past earthquakes in coastal South Carolina.

However, there are potentially important differences between the two scenarios with respect to the interpreted geographic extent of liquefaction in prehistoric earthquakes D and E. Specifically, earthquakes D and E in the "contemporary ages only" scenario may have produced localized liquefaction fields (Figures 6.1.2-13 and 6.1.2-14) and therefore may have been moderate-magnitude earthquakes. The "all ages" scenario, however, indicates that earthquake D and possibly earthquake E produced regional liquefaction fields (Figures 6.1.2-17 and 6.1.2-18) and, therefore, likely were large magnitude. Table 6.1.2-2 summarizes the age constraints and sizes (regional or local) of interpreted prehistoric Charleston earthquakes A through E.

The ninth node of the Charleston logic tree shows weights for the possible combinations of prehistoric large earthquakes for the approximately 2,000-year and 5,500-year records (Figure 6.1.2-1). Earthquake chronologies based on the "contemporary ages only" scenario are assigned a weight of 0.80 because, as discussed above, contemporary ages provide the best approximations of the timing of formation of Charleston area sand-blow craters. Earthquake chronologies based on the "all ages" scenario are assigned a weight of 0.20 because, as discussed above, it is unclear exactly what radiocarbon ages from maximum/minimum samples collected from stratigraphic positions above and below the paleoliquefaction features may mean.

Earthquake Recurrence Model

The tenth node of the Charleston RLME source logic tree defines the earthquake recurrence models used for the regional, local, and narrow source zones (Figure 6.1.2-1). For the regional and local sources, only the Poisson model is used. For the more "fault-like" narrow source zone, the Poisson model is assigned 0.90 weight, and the BPT renewal model is assigned 0.10 weight. Use of the BPT renewal model requires specification of the coefficient of variation of the repeat time for RLMEs, parameter α. As discussed in Section 5.3.3, the uncertainty distribution for α developed by Working Group (2003) was adopted. This distribution is shown on the eleventh node of the Charleston RLME source logic tree (Figure 6.1.2-1). Section 5.3.3 provides additional information regarding the use of the earthquake recurrence models.

RLME Annual Frequency

The final (twelfth) node of the logic tree addresses the uncertainty distributions for the annual frequency of RLMEs (Figure 6.1.2-1). These distributions were developed using the methodology described in Sections 5.3.3.1 and 5.3.3.2. For the Poisson model, the relative likelihood of various values of the recurrence rate parameter was developed using Equation 5.3.3-4 and the observations of the time intervals between the selected paleoearthquakes and the open interval post the 1886 earthquake. For the renewal model, the relative likelihoods of various values of the mean recurrence interval for RLMEs were developed using Equations 5.3.3-7, 5.3.3-8, and 5.3.3-9 for each set of past RLMEs and specified value of coefficient of variation. The resulting parameters were then used to compute the equivalent annual frequency of RLMEs using Equations 5.3.3-10 and 5.3.3-11.

The data used for the recurrence rate calculations are the time intervals between individual RLMEs for the renewal model case, and the age of the oldest RLME for the Poisson case. These are calculated from the age estimates for each past RLME. With the exception of the 1886 earthquake, these ages are estimated from two types of data, as described above, and are subject to uncertainty. One type of data consists of age dates for samples whose ages are considered to be contemporary with the earthquake occurrence, denoted as CON ages. Each sample has its own age estimate with associated uncertainty. Table 6.1.2-3 lists the sample age data used for each prehistoric earthquake. These data are shown on Figures 6.1.2-7 and 6.1.2-8. For this analysis, the range in CON ages of the samples listed in Table 6.1.2-3 was treated as a two-sigma uncertainty estimate. The uncertainty was approximated by a normal distribution with mean equal to the center of the age range and standard deviation equal to ¼ of the uncertainty range. For the i^{th} sample associated with RLME A, the probability distribution for the true age of earthquake A is then given by the normal probability distribution:

$$f(A|A_i) = \exp\left(-\frac{(A-\mu_{A_i})}{2\sigma_{A_i}^2}\right) \qquad (6.1.2\text{-}1)$$

where μ_{A_i} and $\sigma_{A_i}^2$ are the mean and variance of the age of sample A_i, respectively. The likelihood for the age of A, given all of the associated sample ages, then becomes

$$L(A|A_{1..n}) = \prod_{i=1}^{n} f(A|A_i) \qquad (6.1.2\text{-}2)$$

Equation 6.1.2-2 was used to compute the relative likelihood of possible ages for each RLME using the associated liquefaction feature age data in Table 6.1.2-2. These relative likelihoods were then normalized by their sum to produce the uncertainty distributions for the age of each RLME shown on Figure 6.1.2-19 with the label "Con Ages."

The second type of data associated with the Charleston RLMEs is samples that provide constraints on the event age in terms of representing points in time either before or after each earthquake occurrence. These additional age data, labeled in Table 6.1.2-2 as either "B" for before the earthquake or "A" for after the earthquake, were used to modify the CON age distributions by simulating ages from the CON age distributions shown on Figure 6.1.2-19 and from a normal distribution for the constraining feature age, and rejecting those simulations that violate the age constraints. The process was repeated until 10,000 possible ages were obtained for each RLME; these were then ranked to produce the cumulative distributions labeled "All Ages" on Figure 6.1.2-19.

The uncertainty distributions for RLME annual frequency were then computed by repeatedly simulating samples of RLME dates from the age distributions shown on Figure 6.1.2-19 and computing a relative likelihood distribution for RLME rate from each sample. The resulting distributions were then combined to produce a composite distribution for RLME rate, assigning 0.8 weight to RLME ages sampled from the Con Ages distributions and 0.2 weight to ages from the All Ages distributions. These composite distributions were then represented by five-point discrete approximations. The resulting distributions for RLME recurrence frequency are listed in Tables 6.1.2-4 and 6.1.2-5 for the Poisson and Renewal models, respectively.

6.1.3 Cheraw Fault

The Cheraw fault trends northeast and is located on the High Plains in southeastern Colorado, approximately 140 km (85 mi.) east of the Rocky Mountain range front (Crone and Machette, 1995; Crone, Machette, Bradley, et al., 1997; Crone and Wheeler, 2000; Figure 6.1-1). The fault, which has a down-to-the-northwest throw, lies on the western side of the Las Animas arch, a relatively low-relief, 300 km (183 mi.) long, positive structural feature in southeastern Colorado (Curtis, 1988). The crest of the arch lies approximately 20–40 km (12–24 mi.) east of the Cheraw fault.

Crone, Machette, Bradley, et al. (1997) note that the total throw of the fault is not substantial (only tens of meters are demonstrable) and that the fault does not appear to have a long history of recurrent movement. From interpretation of a structure-contour map of the top of the Lower Cretaceous Dakota Sandstone presented by Sharps (1976), Crone, Machette, Bradley, et al. (1997) estimate 6–8 m (20–26 ft.) of down-to-the-northwest throw, which is comparable to the amount of throw on early Quaternary alluvial deposits.

The Cheraw fault, which is mapped for a distance of 46 km (28 mi.), forms a subtle, northwest-facing scarp that can be traced for at least 30 km (18 mi.; Kirkham and Rogers, 1981; Crone,

Machette, Bradley, et al., 1997). Based on the following, Kirkham and Rogers (1981) concluded that the Cheraw fault has been active in the Quaternary: the presence of this scarp, vegetation lineaments, linear ponds, sinkholes, and dissolution pits along the fault trace; the apparent ponding of alluvium against the scarp where the scarp interrupts the gradient of local drainages; and the apparent displacement of the middle Rocky Flats Alluvium.

The fault was first recognized during regional geologic mapping by the USGS (Scott, 1970; Sharps, 1976; Kirkham and Rogers, 1981; Scott et al., 1978). Further paleoseismic field investigations of the Cheraw fault conducted by the USGS provided evidence for multiple surface-faulting earthquakes during the late Pleistocene and Holocene (Crone and Machette, 1995; Crone, Machette, Bradley, et al., 1997). Based on the results of these studies, the Cheraw fault is characterized as an RLME fault source.

Characterization of the Cheraw fault is based on references cited in the following subsections and in Appendix Tables C-6.1.3 Data Evaluation and D-6.1.3 Data Summary. The logic tree for the Cheraw RLME source is shown on Figure 6.1.3-1. Locations of tectonic features and key localities where detailed paleoseismic investigations have been conducted to evaluate the location and activity of the Cheraw fault are shown on Figure 6.1.3-2. The location of the Cheraw fault relative to total magnetic anomaly and residual isostatic gravity data is shown on Figure 6.1.3-3.

6.1.3.1 Evidence for Temporal Clustering

The first node of the logic tree (Figure 6.1.3-1) addresses the issue of temporal clustering of earthquakes in the present tectonic stress regime (see Section 5.1.2). The Cheraw fault lies within a seismically quiescent region of eastern Colorado, but has evidence for two to three surface ruptures in the past 20–25 kyr (Crone, Machette, Bradley, et al., 1997). Crone, Machette, Bradley, et al. (1997) concluded that three surface-rupturing earthquakes (at about 8, 12, and 20–25 ka) are recorded in a trench excavated across the Cheraw fault. The evidence for the penultimate earthquake as presented by Crone, Machette, Bradley, et al. (1997) is not as definitive as the evidence for the earliest and latest earthquakes (Dr. A. Crone, USGS, electronic comm., April 21, 2010). Based on both review of the trench logs and data used to support the interpretation of three earthquakes reported by Crone, Machette, Bradley, et al. (1997) and communications with Dr. A. Crone, the likelihood that the latest Pleistocene displacement on the Cheraw fault is the result of two surface ruptures is given a weight of 0.4, and the published interpretation of three earthquakes is given a slightly higher weight (0.6).

Crone, Machette, Bradley, et al. (1997) speculate that earthquakes older than about 25 kyr must have occurred before about 100 ka because of the time needed to incise, widen, and backfill the paleo-stream channel that is now filled with latest Pleistocene deposits (Crone and Wheeler, 2000). The cumulative vertical offset on the Cretaceous shale is 3.2–4.1 m (10.5–13.5 ft.), which is the total offset of the two or three late Quaternary earthquakes (Crone, Machette, Bradley, et al., 1997). Crone and others (Crone, Machette, and Bowman, 1997; Crone, Machette, Bradley, et al., 1997) suggest that these earthquakes may be part of a pattern of temporal clustering of earthquakes in which one or more earthquakes occur in a short period of time (10–15 kyr) and that the interval of high activity is bounded by longer intervals (>100 kyr) of inactivity.

Based on the geomorphic and geologic lines of evidence described above, the within-cluster branch of the logic tree is given a weight of 0.9, and the out-of-cluster branch is given a weight of 0.1 (Figure 6.1.3-1). There is no evidence to suggest the Cheraw fault is out of a cluster based on the fact that the time elapsed since the last Holocene earthquake (approximately 8,000 years; Crone, Machette, Bradley, et al., 1997) is not longer than the mean intracluster recurrence rate for two or three earthquakes in 20–25 kyr (approximately 13,158 or 8,333 years). This weighting is consistent with the weightings for other RLMEs that exhibit clustered behavior (e.g., New Madrid seismic zone, Meers fault).

6.1.3.2 Geometry and Style of Faulting

The Cheraw fault is well expressed as a topographic feature on the Shuttle Radar Topography Mission (SRTM) topographic data along its entire 46 km (28 mi.) long mapped extent; a subtle northwest-facing scarp is present along at least 30 km (18 mi.; Crone, Machette, Bradley, et al., 1997). Dan Clark (Geoscience Australia) recently suggested that the fault may extend farther to the northeast, based on review of the Shuttle Radar Topographic Mission (SRTM) data, but no field investigation of this possible extension has been conducted (Dr. A. Crone, USGS, electronic comm., March 3, 2010). The possible northeast extension (approximately 16 km [10 mi.]) parallels and appears to coincide in part with a railway line. Thus, it is not certain if the feature is a culture feature or a culturally modified tectonic feature.

The second and third branches of the logic tree indicate that the Cheraw RLME source is modeled as a fault source and that two alternative total lengths of the fault are considered. The topographically well-expressed 46 km (28 mi.) long fault is given highest weight (0.8); the longer (extended) length of 62 km (38 mi.), which is based solely on interpretation of SRTM topographic data, is given much lower weight (0.2) pending confirmation by field investigations.

Based on the paleoseismic evidence for multiple surface ruptures on the Cheraw fault, it likely extends to seismogenic depths. There is little seismicity within the vicinity of the Cheraw fault from which to assess the thickness of seismogenic crust. The generic distribution of 13 km (weight of 0.4), 17 km (weight of 0.4), and 22 km (weight of 0.2) is used.

The downdip geometry of the Cheraw fault is not well known. In the near-surface trench exposures, the main fault dips steeply (70–80 degrees) to the northwest. The dip at depth, however, is uncertain. Crone and Wheeler (2000) give an average dip of 66 degrees based on the average dip of the main fault as mapped by Crone, Machette, Bradley, et al. (1997) in the only exposure of the fault, a 3–4 m (10–13 ft.) deep trench. The USGS characterization of the fault for use in the National Seismic Hazard Maps uses a dip of 60 degrees (2002 National Seismic Hazards—Fault Parameters database). Based on the observation of a steeply dipping main fault near the ground surface and analogy to well-documented seismogenic normal faults with dips of approximately 50 degrees at seismogenic depth in the Western United States, the following dip values and associated weights are used in this study to characterize the Cheraw fault: 50°NW (0.6), 65°NW (0.4).

The sense of motion on the Cheraw fault is not well known, but it is inferred to be a down-to-the-northwest normal fault based on the attitude of the faults exposed in the trench across the scarp

(Crone, Machette, Bradley, et al., 1997). No compelling evidence of lateral slip was observed on the Cheraw fault, and normal displacement is consistent with the attitude (steeply dipping to the northwest) and orientation (northeast-southwest strike) of the fault scarp in the prevailing stress field of the Midcontinent (east-northeast to northeast maximum horizontal stress direction) (Dr. A. Crone, USGS, electronic comm., January 11, 2010).

6.1.3.3 RLME Magnitude

The magnitude distribution for the Cheraw RLME source is defined using magnitude estimates from empirical relationships relating earthquake magnitude to fault rupture characteristics. Potential rupture lengths, rupture areas, and displacement-per-event data from trenching investigations are considered. The following relationships are used:

- Wells and Coppersmith (1994)—surface rupture length, subsurface rupture length, maximum displacement, average displacement, and rupture area for all faults.
- Somerville et al. (2001)—rupture area.

The rupture characteristics that were used in these relationships were defined as described below.

Rupture Length

Two alternative rupture lengths are considered: 46 km (28.5 mi.), the total length of the well documented Quaternary faulting, and 30 km (18.5), the length of the fault with geomorphic expression of recent faulting.

Average and Maximum Displacement

Paleoseismic trenching investigations provide data for estimating a cumulative post-25 ka vertical displacement of approximately 3.2–4.1 m (10.5–13.5 ft.) (similar to the 3.3 m [10.8 ft.] estimated from the drilling results at this site [Crone and Machette, 1995]) and displacement per event of approximately 1.5 m (5 ft.); 1.1–1.6 m (3.6–5.2 ft.); and 0.5–1.1 m (1.6–3.6 ft.), respectively, for the three most recent earthquakes (oldest to youngest) (Crone, Machette, Bradley, et al., 1997). However, as discussed in Section 6.1.3.4, the evidence for the penultimate earthquake is not conclusive, and the displacements measured for this earthquake and the younger earthquake may have occurred in a single earthquake. Based on these observations, the average slip per earthquake at this site would range from 1.1 to 2.1 m (3.6 to 6.9 ft.); the maximum slip during a single earthquake would range from 1.6 m (5.2 ft.) to as much as 2.6 m (8.5 ft.).

The trench site was selected because it is along a part of the fault where a prominent scarp is present on deposits incised into and therefore, younger than Rocky Flats Alluvium. Given the location of the site along the central part of the Quaternary fault and the prominence of the scarp at this locality, it is likely that these measured vertical offsets represent maximum rather than average displacements. However, since there is insufficient information to judge whether the

displacements per earthquake measured at the sole trench site along the Cheraw fault represent average or maximum values, both relationships are considered.

Rupture Area

Potential rupture area for the Cheraw fault rupture was estimated using rupture length, fault dip, and downdip fault width estimates for the Cheraw fault. Empirical relationships defined by Wells and Coppersmith (1994) for all slip types and by Somerville et al. (2001) for CEUS earthquakes are used to estimate magnitude from fault area.

Based on the resulting magnitudes from these parameters (rupture length, displacement per event, and rupture area; see Table 6.1.3-1), the maximum magnitude distribution tabulated below was assigned to the Cheraw fault.

Expected Cheraw RLME Magnitude (M)	Weight
6.8	0.3
7.0	0.3
7.2	0.3
7.4	0.1

6.1.3.4 RLME Recurrence

The remaining nodes of the Cheraw RLME logic tree address the uncertainties in modeling the recurrence rate of Cheraw RLMEs

Recurrence Method

Two types of data are available for assessing the recurrence frequency of Cheraw RLMEs. The first is the average slip rate of the fault and the second is the number and timing of previous RLMEs, allowing application of the “Earthquake Recurrence Intervals” approach. These two approaches are considered equally viable for assessing RLME annual frequency and are given equal weight in the Cheraw RLME source logic tree (Figure 6.1.3-1).

Recurrence Data

The average latest Pleistocene to Holocene slip rate on the Cheraw fault is on the order of 0.14–0.18 mm/yr; more rigorous calculations based on timing and displacement data inferred from the trench excavation allow for a range of values between 0.23 and 0.09 mm/yr (Crone and Wheeler, 2000). These slip rate values apply to periods of time when the fault is in an active phase. During that time, two or three surface rupturing earthquakes have occurred, with the oldest occurring

20-25 ka. As outlined above in Section 6.1.3.1, the evidence for the penultimate earthquake reported by Crone, Machette, Bradley, et al. (1997) is less definitive than the evidence for the earliest and latest earthquakes, but the three-event scenario is still slightly favored by Dr. Crone, one of the principal investigators for the trenching investigation. Based on review of the data and discussions with Dr. Crone, the published interpretation of three earthquakes is therefore slightly favored (weight of 0.6) over two (weight of 0.4).

A long-term average slip rate can be estimated for the Cheraw fault. Drilling results from the USGS investigations show that about 7–8 m (23–26 ft.) of throw has occurred on the Cheraw fault since deposition of an alluvial deposit tentatively correlated with the early Pleistocene Rocky Flats Alluvium estimated to be 1.2 Ma (Crone and Wheeler, 2000). These data yield a best-estimate long-term slip rate of ≤0.007 mm/yr (Crone and Wheeler, 2000). It is noted, however, that subsequent work on the Rocky Flats Alluvium along the Colorado Front Range using terrestrial cosmogenic nuclide dating techniques has shown that the age of Rocky Flats Alluvium ranges between about 400 ka and 2 Ma, with age increasing with distance from the range front (Riihimaki et al., 2006). The long-term average slip rate thus could be a factor of two higher or lower than the best-estimate rate if a broader age uncertainty is considered.

Because of the temporal clustering of earthquakes, it may not be appropriate to characterize the rate of movement on the fault using the long-term average. If it is assumed that the total displacement occurred in two intervals of clustered behavior comparable to the recent one from approximately 25 to 8 ka, the interval of time between the clusters could be several hundred thousand years.

Earthquake Recurrence Model

As discussed in Section 5.3.3, the Poisson model is used as the default earthquake recurrence model with weight 1.0 for the Cheraw RLME source as there are not sufficient data to justify including an alternative model.

RLME Annual Frequency

The final node of the logic tree addresses the uncertainty distributions for the annual frequency of RLMEs. These distributions were developed using the methodology described in Section 5.3.3.1.

For the “in-cluster” case and the “Earthquake Recurrence Intervals” approach, the relative likelihood of various values of the recurrence rate parameter was developed using Equation 5.3.3-4 and the observation of one or two closed recurrence intervals and one open interval post the 20-25 ka earthquake. Thus the value of $\sum_{i=1}^{N} t_i + t_0$ was assumed to be uniformly distributed between 20 and 25 ka with N either 1 or 2. The resulting discrete uncertainty distributions for RLME annual frequency are listed in Table 6.1.3-2.

For the in-cluster slip-rate case, the fault slip rates were assessed by dividing the late Quaternary vertical offset by the age of the oldest earthquake in the trench. Uncertainty in the offset was incorporated by sampling from a uniform distribution between 3.2 and 4.1 m (10.5 and 13.5 ft.), and uncertainty in the age was incorporated by sampling from a uniform distribution between 20 and 25 ka. The results of 10,000 simulations were ranked to produce a cumulative distribution for slip rate. Because the range of results was narrow (0.13 to 0.20 mm/year), the three-point approximation developed by Keefer and Bodily (1983) was used to define the discrete distribution for recurrence rate listed in Table 6.1.3-3.

"Out-of-cluster" RLME recurrence rates for the Cheraw fault are based on the estimated elapsed time between the Holocene/late Pleistocene earthquakes and the penultimate earthquake cluster. Longer recurrence intervals of either 200, 350, or 500 kyr are expected based on the geomorphic evidence for a minimum period of at least 100 kyr between the oldest earthquake recorded in the trench and the previous earthquake, and the observation that only two or three surface-rupturing earthquakes (similar in size to the recent surface-rupturing earthquakes) have occurred. These values are assigned equal weight and were inverted to produce RLME frequencies. The resulting distribution for out-of-cluster RLME frequency is listed in Table 6.1.3-4.

The out-of-cluster slip rate for the Cheraw fault was assessed by dividing the total offset of the Rocky Flats Alluvium by its estimated age. The total offset is assumed to be uniformly distributed between 7 and 8 m (23 and 26 ft.). The age of the alluvium is most likely between 1.2 and 2 Ma, but could be as young as 0.4 Ma. A trapezodial probability density function with uniform probability between 1.2 and 2 Ma, tapering to zero at 0.4 Ma, was used to represent this uncertainty. A distribution for long-term slip rate was developed by repeatedly sampling from the offset and age distributions and ranking the resulting values of slip rate. The results were then approximated using the Miller and Rice (1983) five-point discrete approximation to produce the out-of-cluster slip-rate distribution listed in Table 6.1.3-5.

6.1.4 Meers Fault

The Meers fault in southwestern Oklahoma (Figure 6.1.4-1) is the southern boundary of the Wichita frontal fault system, which separates the early Paleozoic Anadarko basin to the northeast from the late Paleozoic (Carboniferous) Arbuckle-Wichita-Amarillo uplift of the Ouachita orogeny to the southwest (Jones-Cecil, 1995; McConnell, 1989). During the Carboniferous, predominately oblique, left-lateral, and reverse slip along the Wichita frontal fault system uplifted the Wichita and related mountains and generated about 10 km (6 mi.) of total structural relief. Slip on the Meers fault contributed to approximately 2 km (1 mi.) of down-to-the-north vertical offset (Jones-Cecil, 1995).

Paleoseismic studies of the Meers fault conducted in the late 1980s and the 1990s documented late Cenozoic reactivation of the Meers fault, including two Holocene surface-rupturing events with left-lateral reverse slip (Crone and Luza, 1990; Kelson and Swan, 1990; Swan et al., 1993). Based on the evidence for RLMEs, the Meers fault is characterized as an RLME source. Appendix Table D-6.1.4 lists the references that were reviewed in developing the characterization of the Meers RLME source, and Appendix Table C-6.1.4 lists the data that were

explicitly used in constraining the characterization. Figure 6.1.4-2 shows the Meers RLME source logic tree.

6.1.4.1 Evidence for Temporal Clustering

The first node of the logic tree (Figure 6.1.4-2) addresses the issue of temporal clustering of earthquakes in the present tectonic stress regime (see Section 5.1.2). Based on stratigraphic relations observed within trenches, soil pits, and hand auger samples, Swan et al. (1993) demonstrated that the Meers fault experienced two surface-rupturing earthquakes within the last approximately 3,000–4,000 years. However, based on observations of offset ridge crests across the fault, it is also apparent that there have been previous earthquakes on the fault (Crone and Luza, 1990; Ramelli and Slemmons, 1986; Swan et al., 1993). Swan et al. (1993) used correlations between soils observed along the Meers fault and more distant, dated soils to argue that any previous earthquakes along the Meers fault occurred prior to 200–500 ka. Based on these observations, the Meers fault appears to exhibit clustered earthquake behavior. Accordingly, the Meers fault can be classified currently as either "in" or "out" of an earthquake cluster.

The in-cluster branch of the logic tree is given a weight of 0.8 and the out-of-cluster branch a weight of 0.2. The weights reflect that there is no evidence to suggest the Meers fault is out of a cluster, based on the fact that the time elapsed since the last Holocene event (approximately 1,500 years) (Swan et al., 1993) is shorter than the weighted mean intracluster recurrence rate (approximately 2,300 years); see discussion of recurrence rates below. The weights also reflect that there is no evidence of current activity along the fault (i.e., seismicity).

6.1.4.2 Localizing Feature

The second branch of the logic tree (Figure 6.1.4-2) describes whether future earthquakes associated with the Meers fault structure are expected to be localized along the Meers fault scarp ("Fault" on the logic tree), or whether they may occur along other structures within the Oklahoma aulacogen with the same rates as observed on the Meers ("Random in Zone" on the logic tree). The inclusion of this branch on the logic tree represents the interpretation that, while none of the other faults associated with the Oklahoma aulacogen and Arbuckle-Wichita-Amarillo uplift have observed Quaternary faulting (e.g., Crone and Wheeler, 2000; Ham et al., 1964; Hanson et al., 1997; Swan et al., 1993; Wheeler and Crone, 2001; Williamson, 1996), there is the possibility that Meers-like earthquakes (e.g., similar magnitudes and recurrence rates) could occur on other faults within the aulacogen.

Meers-like ruptures within the aulacogen are allowed only on the out-of-cluster branch of the logic tree, reflecting the interpretation that the spatial migration of Meers-like earthquakes will occur only if the Meers fault is out of a cluster (i.e., there can be only one Meers-like structure active within the aulacogen at any given time). This interpretation is based on the fact that there is no evidence of Quaternary activity on other faults within the aulacogen. On the out-of-cluster branch we give a low weight of 0.1 to the possibility of migrating Meers-like earthquakes

because there are no observations supporting the existence of other active faults within the aulacogen.

6.1.4.3 Geometry and Style of Faulting

The third through fifth branches of the logic tree describe the source geometry and style of faulting (Figure 6.1.4-2).

The surface trace of the Meers fault is easily identified on aerial photographs for a total distance of approximately 26 km (16 mi.) as a south-down topographic escarpment (Ramelli et al., 1987; Crone, 1994). The scarp over much of this distance has been visited by various researchers and is attributed to Holocene rupture along the Meers fault (e.g., Crone and Luza, 1990; Kelson and Swan, 1990; Ramelli and Slemmons, 1990; Ramelli et al., 1987; Swan et al., 1993; Crone, 1994). In addition to this prominent scarp along the Meers fault, an approximately 11 km (6.8 mi.) southeast extension of the Meers fault scarp (Figure 6.1.4-1) was identified by Ramelli et al. (1987) and Ramelli and Slemmons (1990) by analyzing low-sun-angle aerial photography. The southeast extension is more subtle and discontinuous than the originally identified 26 km (16 mi.) long scarp. Ramelli and Slemmons (1990) argue that the southeastern continuation of the scarp shares the same history of events on the Meers fault, judging by its alignment with the original scarp, the consistent down-to-south separation across the scarp, its proximity to the original scarp, and the presence of a small drainage channel aligned parallel to the scarp and across the pattern of local drainage networks. However, Ramelli and Slemmons (1990) also acknowledge uncertainty in the structural relationship between the northwest and southeast scarps due to a left step in the scarp near the junction of the two scarp strands, and due to the absence of a scarp across East Cache Creek (Figure 6.1.4-1). In addition, field evaluation of the southeast extension of the scarp has not been possible because the scarp traverses the Fort Sill Military Reservation, where access is restricted (Ramelli and Slemmons, 1990; Ramelli et al., 1987; Crone, 1994).

One researcher (Cetin, 2003) has suggested that the Meers fault scarp also extends 30 km (19 mi.) to the northwest of the prominent scarp described above (Figure 6.1.4-1). Cetin (2003) proposed this extension based on what he describes as “displaced terrace deposits of Pleistocene age, displaced, buried and/or overthickened soil horizons, fault-related colluvium deposits (colluvial wedges) found near and only on the downthrown side of the fault, active seepage near the fault, deflection of stream alignments and the land use pattern along the fault.” However, as summarized by Wheeler and Crone (2003), the evidence presented by Cetin (2003) for Quaternary faulting is not conclusive.

To account for the potential northwest extension, the characterization of the Meers fault used here includes two alternate interpretations of the extent of the active Meers fault trace (third branch on logic tree). The alternate interpretations for fault length are (1) the approximately 37 km (23 mi.) trace as defined by Ramelli and Slemmons (1990) and Ramelli et al. (1987); and (2) an extended trace that includes the approximately 30 km (19 mi.) extension defined by Cetin (2003). The interpretations are given weights of 0.9 and 0.1, respectively. The low weight for the extended trace reflects that Cetin’s (2003) hypothesized northwest extension is not supported by robust, well-documented evidence and not widely supported by the expert community.

When Meers-like earthquakes are allowed to migrate off the fault on the out-of-cluster branch, the earthquakes are limited to occurring within the Oklahoma aulacogen.

The seismogenic thickness for the Meers fault is modeled as either 15 km or 20 km (9.3 mi. or 12 mi.) with equal weights. These depths are based on the depth distribution of seismicity within Oklahoma (Luza and Lawson, 1993).

The Meers fault is well recognized as a down-to-the-south oblique fault dominated by left-lateral slip (e.g., Swan et al., 1993; Wheeler and Crone, 2003). Based on trench exposures and a shallow seismic reflection survey, the Meers fault in the shallow subsurface (to over 150 m [490 ft.] depth) is thought to be near-vertical to slightly northeastward-dipping (Crone and Luza, 1990; Miller et al., 1990; Ramelli and Slemmons, 1990; Swan et al., 1993). However, regional well data, seismic reflection data, and comparison of the Meers fault to other faults in the Wichita frontal fault system suggest that at depth the Meers fault dips approximately 40 degrees to the southwest (Good et al., 1983; McConnell, 1989). Given the uncertainty as to what the best single dip is to characterize the Meers for future earthquake ruptures, a vertical and 40-degree southwest dip are given equal weights for earthquakes on the Meers fault. When Meers-like earthquakes are allowed for the out-of-cluster branch of the logic tree, they are characterized with a strike of N60W (i.e., approximately parallel to the faults of the Amarillo-Wichita-Arbuckle uplifts) and a random dip between 90 and 40 degrees to the southwest.

The uncertainty in the Meers fault dip also drives uncertainty as to whether the fault is best characterized as an oblique normal or reverse fault. An oblique-reverse interpretation is preferred based on the observations in the shallow subsurface (Swan et al., 1993). The obliquity of slip along the fault is not well constrained because of the lack of robust horizontal and vertical control points in the same trenches that can be used to estimate net slip. Published estimates of horizontal-to-vertical slip ratios have ranged from 1.3:1 (Kelson and Swan, 1990; Swan et al., 1993) to greater than 5:1 (Crone and Luza, 1990).

6.1.4.4 RLME Magnitude

The sixth branch of the logic tree describes the earthquake magnitudes for the Meers RLME (Figure 6.1.4-2).

The Meers fault RLME source is modeled using a maximum moment earthquake model where the earthquake magnitude is characterized using a distribution of characteristic magnitudes representing epistemic uncertainty in the potential magnitude of future earthquakes. The magnitude distribution was defined using magnitude estimates from empirical relationships relating earthquake magnitude to fault rupture characteristics. The following relationships were used:

- Wells and Coppersmith (1994)—rupture length, maximum displacement, average displacement, and rupture area for strike-slip, reverse, and all faults.
- Hanks and Bakun (2002)—rupture area.
- Ellsworth (2003)—rupture area.

- Somerville et al. (2001, 2005)—rupture area.

The rupture characteristics that were used in these relationships were defined as described below.

Rupture Length

Three rupture lengths for the Meers fault were used to estimate earthquake: 26 km, 37 km and 67 km (16 mi., 23 mi., and 42 mi.). The 26 km (16 mi.) length is based on the widely accepted extent of Holocene rupture along the Meers fault. The 37 km (23 mi.) length includes the southeast extension to the Meers fault that was mapped by Ramelli and Slemmons (1990) and Ramelli et al. (1987) using low-sun angle photography (see Section 6.1.4.1). The 67 km (42 mi.) extent takes into account the approximately 30 km (19 mi.) long northwest extension of the fault proposed by Cetin (2003).

Average and Maximum Displacement

Only the study by Swan et al. (1993) is used to constrain displacement estimates because it is the only study to have recognized and explicitly measured displacements for the two Holocene events. Based on the results of their investigations, Swan et al. (1993) estimated that the average net slip per event along the fault is between 1.75 and 3 m (5.74 and 9.8 ft.), and the maximum net displacement is 3.5 to 5.25 m (12 and 17.2 ft.). These estimates are poorly constrained because Swan et al. (1993) were able to measure displacement at only a few locations; they measured only one net displacement (as opposed to just vertical or horizontal) and based most of the estimates on stratigraphic offsets of alluvial and colluvial material as well as paleochannel thalwegs exhumed in trenches, both of which can be difficult to use in developing accurate displacement estimates.

Rupture Area

Potential rupture area for the Meers fault rupture was estimated using rupture length, fault dip, and downdip fault width estimates for the Meers fault. A lower-bound rupture area of 390 km^2 (151 $mi.^2$) was calculated using the 26 km (16 mi.) estimate of Holocene rupture length (Ramelli and Slemmons, 1990; Ramelli et al., 1987), a fault dip of 90 degrees, and a downdip fault width of 15 km (9.3 mi.) based on the depth distribution of observed seismicity in the Oklahoma region (Luza and Lawson, 1993). The fault dip of 90 degrees was used for the minimum-bound estimate for the following reasons:

- There have been no studies that have reconciled the discrepancy between the shallow, near-vertical northeast dip of the fault and the deeper, moderate southwest dip of the fault (Crone and Luza, 1990; McConnell, 1989; Miller et al., 1990; Ramelli and Slemmons, 1990; Swan et al., 1993).
- There are few direct measurements of the Meers fault dip at depth (Crone, 1994; McConnell, 1989).
- This estimate is meant to be a minimum bound. An upper-bound rupture area of 1,150 km^2 was calculated using the 37 km (23 mi.) estimate of Holocene rupture length (Ramelli and

Slemmons, 1990; Ramelli et al., 1987); a fault dip of 40 degrees southwest; and a downdip fault width of 20 km (12 mi.), based on the depth distribution of observed seismicity in the Oklahoma region (Luza and Lawson, 1993).

Estimated magnitude ranges from these relationships and fault characteristics are presented in Table 6.1.4-1. Note that the Wells and Coppersmith (1994) displacement relationships for reverse faults were not used because they are reported as not significant at the 95 percent probability level. Based on these estimates, the following distribution for the expected RLME magnitude for the Meers fault was developed:

Expected Meers RLME Magnitude (M)	Weight
6.6	0.1
6.7	0.45
6.9	0.3
7.3	0.1
7.4	0.05

The above distribution reflects the following preferences.

- Magnitudes from the 26 km (16 mi.) rupture length estimate were given the highest weight because (1) the scarp is best expressed along the 26 km (16 mi.) long segment, potentially suggesting that Holocene ruptures were restricted to this length; and (2) rupture length is the most robust directly measurable characteristic of the Holocene ruptures compared to estimates of displacement and area, which require more assumptions to derive.
- Magnitudes from the 37 km (23 mi.) rupture length estimate were given moderate weight because (1) future earthquakes may extend along the entire 37 km of the scarp, and (2) there is no available information on the timing of events along the extended scarp.
- Magnitudes from the 67 km (42 mi.) rupture length estimate were given the lowest weight because there is no evidence that a rupture has occurred along this entire length.
- Magnitudes from the 390 km^2 (151 $mi.^2$) rupture area are given low to moderate weight because they reflect a reasonable interpretation of the potential rupture area of the Holocene earthquakes yet are a less direct measure of the Holocene events than the rupture length.
- Magnitudes from the 1,150 km^2 (444 $mi.^2$) rupture area are given low weight because it is unlikely that any of the Holocene ruptures have the maximum bound area (i.e., maximum length, maximum depth, and shallow dip).
- Magnitudes from the displacement estimates are given low weights because the displacements are poorly constrained by the data collected by Swan et al. (1993).

6.1.4.5 RLME Recurrence

The remaining branches of the logic tree describe the assessment of RLME recurrence rates.

Recurrence Method

The data available for assessing the recurrence rate of the Meers RLMEs provide assessments of the timing of past earthquakes. Thus the "Earthquake Recurrence Intervals" approach is used with weight 1.0 (Figure 6.1.4-2).

Recurrence Data

Recurrence rates are determined using inter-event times from the Holocene ruptures for (1) the out-of-cluster branch when earthquakes occur randomly within the OKA zone, and (2) the in-cluster branch when earthquakes occur on the Meers fault trace. For the out-of-cluster branch when the earthquakes occur on the Meers fault trace, the time elapsed between the last pre-Holocene earthquake and the Holocene earthquake cluster is used to define the recurrence rate. All recurrence rates are determined from the results of the Swan et al. (1993) study because it is both the most detailed study and the only study to have recognized and dated two Holocene earthquakes on the Meers fault.

Out-of-cluster recurrence rates for the Meers fault are based on the estimated elapsed time between the Holocene earthquakes and the penultimate earthquake cluster. Swan et al. (1993) estimated that the elapsed time between the Holocene cluster and the next most recent earthquake was between 200 and 500 kyr.

Intracluster recurrence rates for the Meers fault are based on estimates of the time elapsed since the first Holocene earthquake and the number of observed events in the Holocene. The date of the first Holocene earthquake is constrained by eight radiocarbon ages presented by Swan et al. (1993). From this suite of ages, the tightest constraining minimum and maximum ages are used to define the uncertainty in the date of the first Holocene earthquake. For example, four radiocarbon ages between approximately 7,000 and 3,000 yr BP constrain the maximum age of the earthquake, but only the tightest constraining age (2,918 calibrated years BP) is used.

The maximum age of the earthquake is constrained by sample PITT-0478 of Swan et al. (1993). This sample was collected at the "Valley" site of Swan et al. (1993; Figure 6.1.4-1) from an alluvial deposit near the bottom of the trench that was clearly offset by the fault. The calibrated radiocarbon age for this sample is 2,918 yr BP. The minimum age of the earthquake is constrained by sample PITT-0478 of Swan et al. (1993). This sample was collected at the "Southeast Ponded Alluvium" site of Swan et al. (1993; Figure 6.1.4-1) from an alluvial deposit interpreted to have ponded against the fault scarp after the first Holocene earthquake. The calibrated radiocarbon age for this sample is 2,093 yr BP.

Earthquake Recurrence Model

As discussed in Section 5.3.3, the Poisson model is used as the default earthquake recurrence model with weight 1.0 for the Meers RLME source as there are not sufficient data to justify including an alternative model.

RLME Annual Frequency

The final node of the logic tree addresses the uncertainty distributions for the annual frequency of RLMEs (Figure 6.1.4-2). These distributions were developed using the methodology described in Section 5.3.3.1. For the in-cluster case, the relative likelihood of various values of the recurrence rate parameter was developed using Equation 5.3.3-4 and the observations of one closed recurrence interval between the ~1,500 ka and the ~2,900 ka earthquakes and one open interval post the ~1,500 ka earthquake. The value of $\sum_{i=1}^{N} t_i + t_0$ was assessed to be uniformly distributed between 2,153 and 2,968 years, with N equal to 1. The resulting relative-likelihood-based distribution was represented by the five-point discrete distribution listed in Table 6.1.4-2.

For the out-of-cluster case, the range of return periods for clusters of 200–500 kyr was represented by three equally likely values of 200, 350, and 500 kyr. These return periods are inverted to produce the distribution for out-of-cluster RLME frequency listed in Table 6.1.4-3. The weighting reflects the evaluation that there is no evidence to support a preferred return period.

6.1.5 Reelfoot Rift–New Madrid Fault System

The New Madrid region is the source of the 1811-1812 New Madrid earthquake sequence, which includes the three largest earthquakes to have occurred in historical time in the CEUS. Extensive geologic, geophysical, and seismologic studies have been conducted to characterize the location and extent of the likely causative faults of each of these earthquakes and to assess the maximum magnitude and recurrence of earthquakes in this region. Appendix Table D-6.1.5 provides a summary of recent publications pertinent to the identification and characterization of seismic sources in this region. Based on the results of these studies, a system of faults within the New Madrid seismic zone (NMSZ) in the northern Reelfoot rift has been identified as an RLME source (herein referred to as the New Madrid fault system [NMFS] RLME source). Appendix Table C-6.1.5 lists the data that were explicitly used to constrain the characterization of this RLME source. The logic tree showing the characterization of the NMFS RLME sources is shown on Figure 6.1.5-1.

Models that have been proposed to explain the origin of stresses driving active deformation in the CEUS and specifically in the NMSZ are summarized in Appendix Table D-6.1.5. Several of these provide explanations for localization of seismicity and recurrence of large-magnitude earthquakes in the NMSZ, as follows:

- The presence of a rift pillow underlying the Reelfoot rift (Mooney et al., 1983) causes local stress concentration (Grana and Richardson, 1996).
- A weak subhorizontal detachment fault exists in the lower crust above the rift pillow that causes local stress concentration (Stuart et al., 1997).
- High local heat flow creates high ductile strain rates in the upper mantle and lower crust, causing seismicity in the upper crust (Liu and Zoback, 1997).
- Glacial unloading north of the NMSZ at the close of the Wisconsinan increased seismic strain rates in the NMSZ and initiated the Holocene seismicity (Grollimund and Zoback, 2001). Modeling studies by Grollimund and Zoback (2001) show that the removal of the Laurentide ice sheet approximately 20,000 years ago (ka) changed the stress field in the vicinity of New Madrid, causing seismic strain rates to increase by about three orders of magnitude. The modeling predicts that the high rate of seismic energy release observed during late Holocene time is likely to continue for the next few thousand years (Grollimund and Zoback, 2001).
- Some local or regional perturbation of the stress field, pore pressure, or thermal state is responsible for triggering viscous relaxation of a weak lower-crustal zone within an elastic lithosphere. This may cause a sequence of fault ruptures in short recurrence intervals. A likely explanation for this perturbation is recession of the Laurentian ice sheet approximately 14 ka (Kenner and Segall, 2000; Kenner, 2003). Kenner and Segall (2000) and Kenner (2003) suggest that this model explains the apparently contradictory observations of the Holocene increase in seismic strain rate in the NMSZ relative to long-term geologic and geomorphic observations that do not support steady-state deformation at these rates. Model predictions mostly are consistent with earthquake magnitude, coseismic slip, recurrence intervals, cumulative offset, and surface deformation rates in the NMSZ. In particular, the computed interseismic strain rates may be undetectable with available geodetic data, implying that low observed rates of strain accumulation cannot rule out future large-magnitude earthquakes.
- Low-permeability seals form around the fault zone as stress accumulates, raising the pore pressure until an earthquake happens. Temporal clustering may reflect the evolution of pore fluid pressure in a fault zone (Crone et al., 2003).
- Accelerated late Wisconsinan and Holocene denudation above the NMSZ due to the confluence of the Mississippi and Ohio rivers stepping north to Thebes Gap, perhaps in combination with the retreating Laurentide forebulge, may have been sufficient to initiate Holocene seismicity by causing a perturbation in the local stress field (the Kenner and Segall model [2000]; Van Arsdale et al., 2007).
- Descent of the ancient Farallon slab into the deep mantle beneath central North America as inferred from high-resolution seismic tomography induces a highly localized flow and stresses directly below the NMSZ. This localization arises because of structural variability in the Farallon slab and the low viscosity of the sublithospheric upper mantle. It is hypothesized that the mantle-flow-induced surface depression and associated local focusing of bending stresses in the upper crust may operate analogously to previous crustal loading scenarios, with one difference being that the slab-related loads reside in the mantle (Forte et al., 2007).

- Fault weakening can lead to repeated earthquakes on intraplate faults (Lyakhovsky et al., 2001). The predicted patterns vary with the weakening history. Clusters of large intraplate earthquakes can result from fault weakening and healing, and the clusters can be separated by long periods of quiescence. Stress triggering and migration cause spatiotemporal clustering of earthquakes (Li et al., 2009).
- Strain in the NMSZ over the past several years has accumulated too slowly to account for seismicity over the past approximately 5,000 years, hence excluding steady-state fault behavior. Fault loading, strength, or both may vary with time in the plate interior. Time variations in stress could be due to local loading and unloading from ice sheets or sediments or to earthquakes on other faults (Calais and Stein, 2009).
- The NMSZ is associated with a local, northeast-southwest-trending, low-velocity anomaly in the lower crust and upper mantle, instead of a high-velocity intrusive body as proposed in previous studies. The low-velocity anomaly is on the edge of a high-velocity lithospheric block, consistent with the notion of stress concentration near rheological boundaries. This lithospheric weak zone may shift stress to the upper crust when loaded, thus leading to repeated shallow earthquakes (Zhang et al., 2009b).
- Stress changes are caused by the Quaternary denudation/sedimentation history of the Mississippi valley. Flexural stresses are sufficient to trigger earthquakes in a continental crust at failure equilibrium. The resulting viscoelastic relaxation leads to failure again on the main fault (lower-strength threshold) and neighboring faults. In the absence of significant far-field loading, this process can only maintain seismic activity for a few thousand years (Calais et al., 2009).

The principal seismic activity within the upper Mississippi embayment is interior to the Reelfoot rift along the NMSZ. The NMSZ consists of three principal trends of seismicity: two northeast-trending arms and a connecting northwest-trending arm (Figure 6.1.5-2). This seismicity pattern has been interpreted as a northeast-trending right-lateral strike-slip fault system with a compressional left-stepover zone (Russ, 1982; Chiu et al., 1992; Schweig and Ellis, 1994), referred to as the NMFS. The south arm is coincident with the subcrop Blytheville arch; the central arm is coincident with the subcrop Pascola arch and surface Lake Country uplift; and the north arm trends at a low angle to the western margin of the Reelfoot rift (Figures 6.1.5-2 and 6.1.5-3). Johnston and Schweig (1996) identify the following fault segments within the central fault system of the NMSZ: Blytheville arch (BA); Blytheville fault zone (BFZ); Bootheel lineament (BL); New Madrid West (NW); New Madrid North (NN); Reelfoot fault (RF); Reelfoot South (RS; Figure 6.1.5-4). They outline three rupture scenarios associating each of the three 1811-1812 earthquakes with fault segments (individually or in various combinations) using historical accounts and geologic evidence. Their interpretation is consistent with the spatial distribution and source characteristics of contemporary NMSZ seismicity (Hough and Martin, 2002).

The December 16, 1811, earthquake (referred to variously by different authors as the D1, D16, or NM1 earthquake) is believed to have occurred on the south arm of seismicity (possibly the Cottonwood Grove–Ridgley fault system) associated with the BA, a major crustal transpressional fault structure identified from seismic reflection data (Figure 6.1.5-2). Mueller et al. (2004) and Bakun and Hopper (2004a) infer a location for this earthquake on the northern end of the BA

(just south of the intersection of the BL and the BFZ (also referred to as the Cottonwood Grove fault). Two alternative geometries for the main fault rupture are outlined by Johnston and Schweig (1996): BA/BL (preferred) or BA/BFZ (Figure 6.1.5-4). More recent studies by Guccione et al. (2005) have documented evidence for multiple faulting earthquakes along the central part of the BL, and it is recommended that the BL be renamed the Bootheel fault (Figure 6.1.5-3). Along the central part of the BL, a less than 10.2 ka Pleistocene braidstream sand has been displaced vertically approximately 3 m (10 ft.) and an approximately 2.4 ka Holocene paleochannel has been displaced horizontally at least 13 m (43 ft.; Guccione et al., 2005).

The causative fault for the January 23, 1812, earthquake (referred to variously by different authors as the J1, J23, or NM2 earthquake) is generally inferred to be the northern seismicity arm of the NMSZ (segment NN; Figure 6.1.5-4). Baldwin et al. (2002) suggest that the North Farrenburg lineament may be associated with NN and represent the surface expression of coseismic rupture from the January 23, 1812, earthquake. Johnston and Schweig (1996) also consider an alternative scenario in which the source for the January 23, 1812, earthquake is the west-trending zone of seismicity that lies along the trend of the RF (S#3 on Figure 6.1.5-4b). In this alternative model, both the NN and RF ruptured in the February 7, 1812, earthquake.

Microearthquake data from the northeastern NMSZ show three alignments that extend from New Madrid, Missouri, into western Kentucky and southern Illinois that may represent extensions of the NMSZ and therefore alternative locations for the NM2 rupture (Braile et al., 1986; Wheeler, 1997; Woolery and Street, 2002; Shumway, 2008) (Figure 6.1.5-2). Braile et al. (1997) identified two parallel trends of concentrated seismicity approximately 70 and 90 km (43.5 and 56 mi.) long that extend north-northeast from the central NMSZ to within 14.4 km (9 mi.) of the Illinois/Kentucky border (Wheeler, 1997; Woolery and Street, 2002). Shumway (2008) identifies these two parallel trends and a third, shorter alignment (approximately 40 km [25 mi.] long) running east-northeast from just south of Charleston, Missouri, to just north of Bardwell, Kentucky.

Mueller et al. (2004) and Hough et al. (2005) infer that the J23 (NM2) main shock may have been a remotely triggered earthquake with a location some 200–250 km (124–155 mi.) north of the New Madrid earthquake in the Wabash Valley of southern Illinois and Indiana. Bakun and Hopper (2004a) discount more northerly locations, based on the absence of 1811-1812 liquefaction features that would indicate a source in that region. They follow Johnston and Schweig (1996) in assigning the NM2 earthquake to the NN segment. Cramer et al. (2006) suggest that unilateral rupture within the New Madrid fault zone could have led to extraordinary strong ground motions to the east.

The February 7, 1812, earthquake (referred to variously by different authors as the F1, F7, or NM3 earthquake) occurred on the RF, which connects the two other fault zones through the stepover region (Johnston and Schweig, 1996). The Reelfoot scarp is the surface expression of a west-dipping reverse fault that lies within the left-stepping restraining bend between two dextral strike-slip arms of the NMSZ (Russ, 1982; Sexton and Jones, 1986; Kelson et al., 1992, 1996; Schweig and Ellis, 1994) (Figure 6.1.5-3). The fault and associated fold are defined by microearthquakes (Pujol et al., 1997); seismic reflection profiles (Sexton and Jones, 1986; Odum et al., 1998; Van Arsdale et al., 1999); surface topography; shallow trench excavations (Russ,

1982; Kelson et al., 1992, 1996; Mueller et al., 1999); and borehole data (Mihills and Van Arsdale, 1999; Champion et al., 2001). Using the constraints on fault geometry derived from interpretation of microearthquakes and seismic reflection profiles and the amounts of surface deformation based on geomorphic and trenching investigations, the slip rate for the RF is estimated (Mueller et al., 1999; Van Arsdale, 2000; Champion et al., 2001) (Appendix Table D-6.1.5). Mueller and Pujol (2001) use these constraints on geometry, slip rate, and displacement during historical and prehistoric earthquakes to estimate the rate of late Holocene moment release and the magnitudes of earthquakes for the two most recent strain cycles.

Maximum magnitudes in the New Madrid region are based largely on the analysis of intensity data from the 1811-1812 earthquake sequence (Johnston, 1996b; Johnston and Schweig, 1996; Hough et al., 2000; Mueller et al., 2004; Bakun and Hopper, 2004a; Hough and Page, 2011) and, to a lesser degree, on magnitude assessments inferred from paleoliquefaction features (Tuttle, Schweig, et al., 2002) (Appendix Table D-6.1.5). Cramer (2001) calculates the range of magnitudes (M 6.5–7.8) for fault segments that capture the range of uncertainty in the dimensions of the segment rupture (length and width (≤19 km [11.8 mi.]) of the seismogenic crust) and choice of magnitude/area relationship (Wells and Coppersmith [1994] or Somerville and Saikia [2000] area-magnitude relationships). Mueller and Pujol (2001) provide an additional assessment of past earthquake magnitudes through detailed mapping of the geometry and area of the RF, combined with estimates of fault slip rate, recurrence, and displacement in individual earthquakes to estimate the rate of late Holocene moment release(Appendix Table D-6.1.5).

Constraints on the recurrence of large-magnitude earthquakes in the NMSZ come from paleoliquefaction studies (Saucier, 1991; Tuttle, 1999, 2001; Craven, 1995a; Li et al., 1998; Tuttle and Schweig, 1996, 2000, 2001; Tuttle, Lafferty, and Schweig, 1998; Tuttle, Collier, et al., 1999; Tuttle et al., 2000; Tuttle, Schweig, et al., 2002; and Tuttle and Wolf, 2003; Appendix E) and from evaluation of fault-related deformation along the Reelfoot scarp (Kelson et al., 1992, 1996). The age constraints for these earthquakes are summarized in Table 6.1.5-1. Findings from these studies indicate that major earthquakes occurred in the New Madrid region in ~AD 900 (900–1,200 yr BP relative to AD 1950) and ~AD 1450 (350–650 yr BP relative to AD 1950) (Figures 6.1.5-5 and 6.1.5-6; Tuttle and Schweig, 2001; Tuttle, Schweig, et al., 2002).

Saucier (1991) presents evidence for a significant earthquake in the northern part of the New Madrid region in AD 489 (1461 yr BP) ± 50 yr (Appendix E). Tuttle et al. (2005) recognized a New Madrid event about 2350 BC ± 200 yr that included several large, closely timed earthquakes, but state that the paleoearthquake record may be incomplete before AD 300 and that additional research is needed to assess whether the rate of earthquakes during the past 1,200 years is typical of the longer-term behavior. Tuttle, Schweig, et al. (2002) note that, given uncertainties in dating liquefaction events, the recurrence time between the three most recent New Madrid earthquakes (AD 900, AD 1450, and 1811-1812) may have been as short as 200 years or as long as 800, with an average of 500 years. Tuttle (2001) notes that similarities in the size and spatial distributions of historical (1811-1812) and paleoliquefaction features indicate that the NMSZ was the likely source of the two paleoearthquakes that are recognized regionally. Saucier (1989) first recognized compound sand blows that formed during the 1811-1812 earthquake sequence. Tuttle, Schweig, et al. (2002) document evidence that prehistoric sand blows, like those formed during the 1811-1812 earthquakes, probably are compound structures

resulting from multiple earthquakes closely clustered in time (i.e., earthquake sequences). The current preferred age estimates of earthquakes from 2-sigma radiocarbon maximum and minimum age constraints and, in some instances, archeological data as outlined in Appendix E are given in Table 6.1.5-1.

6.1.5.1 Evidence for Temporal Clustering

The first node of the logic tree (Figure 6.1.5-1) addresses the issue of temporal clustering of earthquakes in the present tectonic stress regime (see Section 5.1.2).

Various observations suggest that the high rate of seismicity within the NMSZ in the Holocene is not characteristic of the region over longer-term periods. Schweig and Ellis (1994) note that extensive seismic reflection data in the New Madrid seismic zone show relatively small cumulative fault offsets in the post-Cretaceous Mississippi embayment sediments (e.g., Hamilton and Zoback, 1982). Van Arsdale (2000) concluded based on seismic reflection and trench data that slip rates on the RF during the Holocene are at least four orders of magnitude higher than during the Pleistocene.

Other geomorphic observations also suggest that the NMSZ became more active within the past few thousand years and that this activity is part of the most recent cluster of large earthquakes. Longer-term geomorphic records suggest that periods of clustered activity within the NMSZ are interspersed with longer intervals of inactivity (Holbrook et al., 2006). The concept that the locus of seismicity and active faulting may shift or migrate within the Reelfoot rift region was suggested by McBride, Nelson, and Stephenson (2002) to explain the changes in rates of activity for faults of the Fluorspar Area fault complex within the northern Reelfoot rift, and more recently by others to explain the apparent discrepancies between long-term deformation rates on faults within the NMSZ (McKenna et al., 2007) and the evidence for possible temporally clustered earthquakes in the southern part of the rift near Marianna, Arkansas (Tuttle, 2009).

Geodetic data suggest that present strain accumulation across the NMSZ is near zero (Calais et al., 2005; Smalley et al. 2005) and that strain has accumulated too slowly to account for the paleoseismicity recorded over the past approximately 5,000 years, thereby ruling out steady-state fault behavior (Newman et al., 1999; Calais and Stein, 2009; Calais et al., 2009; Li et al., 2007, 2009; McKenna et al., 2007).

Alternative interpretations of geodetic strain in the region of the NMSZ have been reported in the literature. Using analysis of geodetic measurements from a permanent GPS array in mid-America that was installed in the mid- to late 1990s, Smalley et al. (2005) suggest relatively rapid rates of strain of the order of 10^{-7} per year, comparable in magnitude to those across active plate boundaries, and consistent with known active faults in the region. Relative convergence across the RF estimated from this study is ~2.7 ± 1.6 mm/year. Relative fault-parallel, right-lateral motion of ~1 mm/year was measured across the southern right-lateral strike-slip fault zone, which is highlighted by a prominent northeast-trending and vertical zone of microseismicity and right-lateral focal mechanisms. Surface velocities at distances beyond a few fault dimensions (far-field) from active faults, however, do not differ significantly from zero. According to Smalley et al. (2005), it is not certain whether the driving force behind the current

surface velocities is related to post-1811-1812 seismic processes or to the accumulation of a locally sourced strain. Others speculate that the recent small earthquakes in the NMSZ are aftershocks of the large earthquakes of 1811-1812 (Ebel et al., 2000; Stein and Newman, 2004; McKenna et al., 2007). The geodetic data indicate, however, that aseismic slip is almost certainly required across faults (or shear zones) within the upper few kilometers of the surface (Smalley et al., 2005).

More recent interpretation of geodetic results in the NMSZ shows motions between 0 and 1.4 mm/yr, and two opposing interpretations of these data are suggested (Calais and Stein, 2009). As outlined by Calais and Stein, the upper bound is consistent with steady-state behavior, in which strain accumulates at a rate consistent with a repeat time for M ~ 7 earthquakes of about 600–1,500 years, as seen in the earthquake record. The lower bound cannot be reconciled with this record, which implies that the recent cluster of large-magnitude earthquakes does not reflect long-term fault behavior and may be ending. New analysis suggests strain rates lower than 1.3×10^{-9}/yr, less than predicted by a model in which large earthquakes occur because the NMSZ continues to be loaded as a deeper weak zone relaxes (e.g., Kenner and Segall, 2000). At a steady state, a rate of 0.2 mm/yr implies a minimum repeat time of 10 kyr for low M = 7 earthquakes having approximately 2 m (6.5 ft.) of coseismic slip and a repeat time of longer than 100 kyr for M = 8 earthquakes.

In summary, geodetic and geologic observations suggest that both temporal clustering and spatial migration of seismicity occurs within the Reelfoot rift, and various researchers have argued that the NMSZ faults are not presently accumulating strain at a rate consistent with that recorded by the late Holocene paleoliquefaction record and that they may be entering a less active period (e.g., Calais and Stein, 2009; McKenna et al., 2007). A recent review by the Independent Expert Panel on New Madrid Seismic Zone Earthquake Hazards of the current national seismic hazard maps in the region of the NMSZ considered claims that the apparent lack of current deformation may indicate that the process driving NMSZ earthquakes has ceased, but members of the panel and other experts consider such claims unlikely (NMSZ Expert Panel, 2011). This possibility is acknowledged but is given relatively low weight in the source model for several reasons: the relatively short geodetic record, uncertainties in the potential variability in strain accumulation over such short periods, and gaps in the state of knowledge regarding the relationship between the crustal motion measured by space geodesy and the elastic strain that is released by earthquakes. The NMSZ Expert Panel (2011) notes that the integration of GPS data in NMSZ seismic hazard analysis is limited by two main factors: (1) limitations of the existing GPS data and (2) lack of physical understanding of how stress accumulation on faults is related to surface deformation in intracontinential regions. Three options are considered in the CEUS SSC source characterization (Figure 6.1.5-1):

- The recent behavior of all three of the faults in the NMFS as inferred from paleoliquefaction studies (in a period of clustered earthquakes) is interpreted to be representative of the rate of future earthquakes (i.e., the recent period of activity for the three faults will continue into the future at the same rate; weight of 0.9).
- The NMSZ is shutting down as suggested by geodetic observations that show little or none of the interseismic motion expected before a future large earthquake (i.e., out of a period of clustered earthquakes; Newman et al., 1999; Calais et al., 2005). In this case, the hazard is

modeled by the underlying seismotectonic zone (Reelfoot rift zone) on the seismotectonic branch of the master logic tree or by global spatial smoothing of seismicity on the Mmax branch of the logic tree (weight of 0.05).

- Only the Reelfoot thrust (RFT) fault, which shows geomorphic evidence of an earlier phase of activity inferred from fluvial geomorphology (Holbrook et al., 2006), is considered to be in an active phase. In this case, the RFT is currently producing RLMEs at a lower rate (weight of 0.05).

6.1.5.2 Geometry and Style of Faulting

Fault sources included in the characterization of the NMFS RLME source are (1) the New Madrid South (NMS) fault; (2) the New Madrid North (NMN) fault; and (3) the RFT (Figure 6.1.5-4c). The first two levels of the logic tree (Figure 6.1.5-1) for these sources address the uncertainty in the technical community regarding the location and extent of the causative faults that ruptured during the 1811-1812 earthquake sequence. This uncertainty is represented by alternative geometries for the NMS, NMN, and RFT faults. The locations of the faults that make up the New Madrid characteristic earthquake sources are shown on Figures 6.1-2b, 6.1.5-3, and 6.1.5-4.

For the NMS fault source, two alternatives are considered, as described by Johnston and Schweig (1996): (1) the BA-BL (Blytheville arch-Bootheel lineament), and (2) the BA-BFZ (Blytheville arch-Blytheville fault zone). Although modern seismicity is occurring primarily along the BFZ, Johnston and Schweig (1996) present arguments suggesting that the BA-BL is the most likely location for the main NM1(D1) earthquake and that major NM1(D1) aftershocks occurred on the BFZ (the northeast extension of the Cottonwood Grove fault). Recent studies by Guccione et al. (2005) document that the presence of recent surface deformation and an offset Holocene channel across the BL (Bootheel fault). Therefore, slightly greater weight is given to BA/BL (weight of 0.6) (total length of 133 km [82.5 mi.]) than to BA-BFZ (weight of 0.4) (total length of 115 km [72 mi.]).

Two alternative total lengths are considered for the NMN fault source: NMN-S and NMN-L. The first, which is given the highest weight (0.7), allows for rupture of the 56.4 km (35 mi.) fault segment (NN; Figure 6.1.5-4) as defined by Johnston and Schweig (1996). Cramer (2001) uses a similar value (59 km [36.7 mi.]) as the length of this fault source. The alternative, NMN-L, which has a total length of 95 km (59 mi.), allows for the fault to extend north, including the westernmost of two trends of northeast-aligned seismicity noted by Wheeler (1997) and Shumway (2008; Figure 6.1.5-2). McBride et al. (2003) observe evidence in seismic profiles for reactivation of northeast-trending structures near Olmstead, Illinois, along the trend of the westernmost seismicity alignment. They conclude that the graben structure in this area has been reactivated as a fault-propagation fold that apparently affects Holocene sediments near the ground surface. Wheeler et al. (1997) and other researchers argue for a structural northern boundary to the rift in this region (see Appendix Table D-6.1.5). The northern extension (NMN-L; Figure 6.1.5-4c) is not as well defined by seismicity as the NMN-S segment is. Also, the recurrence interval of large-magnitude earthquakes in the northern Mississippi embayment appears significantly longer than the recurrence interval for NMSZ earthquakes based on

paleoliquefaction studies. Given these observations, the longer (97 km [60.3 mi.]) fault length (NMN-L) is given less weight (0.3) than the shorter (60 km [37.3 mi.]) fault length (NMN-S).

Johnston and Schweig (1996) conclude from historical accounts that the NM3 (F1) earthquake occurred on the RF, and they identify three possible segments of the fault: a central 32 km (19.9 mi.) long reverse fault defined by the RF scarp between the two northeast-trending strike-slip faults; a 35 km (21.7 mi.) long segment, Reelfoot South (RS), that extends to the southeast; and a 40 km (24 mi.) long segment west of the New Madrid North fault (Figure 6.1.5-4a). Seismicity and geomorphic data indicate that the southeast segment is slightly shorter (25–28 km [15.5–17.4 mi.]) than indicated by Johnston and Schweig (Van Arsdale et al., 1999; Mueller and Pujol, 2001). Cramer (2001) uses a total length of 60 km (37.3 mi.) for the RF. The alternative fault rupture scenarios of Johnston and Schweig (1996) include rupture of a 40 km (24 mi.) long northwest fault segment (Figure 6.1.5-4b).

Cramer (2001) assigns a length of 33 km (20.5 mi.) to this segment, which he refers to as the west arm. Mueller and Pujol (2001) note that this westerly arm is imaged as a vertical fault that terminates the RFT. They interpret the westerly arm as a left-lateral strike-slip fault kinematically linked to the RFT. Bakun and Hopper (2004) suggest a preferred epicenter location at the northern end of the RS segment. Hough and Martin (2002) show a slightly different geometry for the northwestern portion of the fault and do not interpret the historical 1811-1812 earthquake ruptures to have extended to the rift margin on the southeast. Van Arsdale et al. (1999) and Mueller and Pujol (2001) argue that the RF is continuous from New Madrid southeast to near Dyersburg, Tennessee. Alternatively, Csontos and Van Arsdale (2008) conclude that two segments of the fault, which they refer to as the Reelfoot North and Reelfoot South faults, are discrete segments that may not rupture as one fault. These two faults differ in strike, dip, depth, area, and basement displacement; further, the Reelfoot South fault does not have a surface scarp. Csontos and Van Arsdale (2008) note that the Reelfoot North fault is symmetric from its maximum fold amplitude of 11 m (36 ft.) northwest of Reelfoot Lake (Champion et al., 2001). They believe that the fold amplitude (scarp height) diminishes to near zero at the eastern edge of the Mississippi River floodplain, and that this is not consistent with what would be expected if the RF had ruptured over its entire 70 km (43.5 mi.) of mapped bedrock length as one plane during its Holocene history.

Two alternative fault geometries are included in this study: (1) the RFT-S fault that is based on the observed length of concentrated seismicity that is consistent with a reverse fault geometry (i.e., Chiu et al. 1992; Mueller and Pujol, 2001; Hough and Martin, 2002; Csontos and Van Arsdale, 2008); and (2) a longer fault (RFT-L) that allows for extensions to the northwest (the northwest segment of Johnston and Schweig [1996] and Cramer [2001]) and to the southeast to the margin of the Reelfoot rift. The shorter length (46.2 km [28.6 mi.]), which has geomorphic and seismologic evidence for reverse slip is given higher weight (0.7) than the alternative, longer fault (RFT-L; 82.8 km [51.3 mi.]) (weight of 0.3), which also includes the western fault segment that shows evidence for strike-slip movement.

Recent analysis and relocation of 19 earthquakes ($\mathbf{M} \leq 3.6$) in the northeastern part of the NMSZ, using a velocity model of the Mississippi embayment with appropriate depths to bedrock beneath seismic stations, shows that only 2 of the earthquakes occurred at depths between 13 and

15 km (8.1 and 9.3 mi.; Shumway, 2008). Herrmann and Ammon (1997) show depths of up to 16 km (10 mi.) for earthquakes in the Reelfoot rift. Based on these data, the following distribution for seismogenic crustal thickness is used to characterize the New Madrid fault system RLME sources: 13 km (8.1 mi.; weight of 0.3), 15 km (9.3 mi.; weight of 0.5), and 17 km (10.6 mi.; weight of 0.2).

The style of faulting for each of the fault sources is based on geologic and seismologic observations. The NMS fault is modeled as an oblique right-lateral strike-slip fault based on the following: focal mechanisms (Herrmann and Canas, 1978; Chiu et al., 1992); geologic evidence for a right-laterally offset Holocene channel along the Bootheel fault (Guccione et al., 2005); and the near-surface expression of flower structures associated with strike-slip and oblique movement of deeper, reactivated boundary faults as interpreted from seismic profile data (Odum et al., 1995). The RFT fault is modeled as a reverse fault dipping an average of 40 degrees southwest (the average being measured from near the surface to seismogenic depth) (Herrmann and Canas, 1978; Chiu et al., 1992, Mueller and Pujol, 2001; Van Arsdale, 2009). It is noted that the western end of the RFT-L may be steeper and more strike-slip, but for this regional assessment that has not been explicitly modeled. The NMN fault is modeled as a right-lateral strike-slip fault based on focal mechanisms (Shumway, 2008) and apparent right-lateral deflections of drainages and geophysical anomalies (Baldwin et al., 2002).

6.1.5.3 RLME Magnitude

Seismic source characterizations of the New Madrid seismic source zone typically consider the 1811-1812 earthquakes to represent the maximum earthquake for this source. Table 6.1.5-2 summarizes recent estimates of the magnitude of the New Madrid 1811-1812 main shocks.

Bakun and Hopper (2004b) provide preferred estimates of the locations and moment magnitudes and their uncertainties for the three largest earthquakes in the 1811-1812 sequence near New Madrid. Their preferred intensity magnitude M_I, which is their preferred estimate of **M**, is 7.6 (6.8–7.9 at the 95 percent confidence interval) for the December 16, 1811, earthquake (NM1); 7.5 (6.8–7.8 at the 95 percent confidence interval) for the January 23, 1812, earthquake (NM2); and 7.8 (7.0–8.1 at the 95 percent confidence interval) for the February 7, 1812, earthquake (NM3). The intensity magnitude M_I is the mean of the intensity magnitudes estimated from individual MMI assignments. In their analysis, Bakun and Hopper (2004b) consider two alternative eastern North America (ENA) intensity attenuation models, which they refer to as models 1 and 3. As indicated in Table 6.1.5-2, these two models give significantly different results for larger-magnitude earthquakes. Bakun and Hopper state that because these models are empirical relations based almost exclusively on **M** < 6 calibration earthquakes, "there is no way to confidently predict which relation better represents the MMI distance data for **M** 7 earthquakes in ENA" (Bakun and Hopper, 2004b, p. 66). They present arguments supporting their preference for model 3, but do not discount the results based on model 1.

Dr. Susan Hough (written comm., August 23, 2004) concluded that there are insufficient data regarding the calibration of ENA earthquakes larger than **M** > 7 to rely strictly on ENA models as was done in Bakun and Hopper (2004b). She offered arguments to support **M** 7.6 (her preferred estimate of the size of the 2003 Bhuj earthquake) as a reasonable upper bound for the

largest of the earthquakes in the 1811-1812 New Madrid earthquake sequence, which is consistent with the estimates cited by Hough et al. (2000) and Mueller et al. (2004).

More recently, Hough has conducted new analyses and has revisited the intensity assignments, developing a set of "consensus intensities" for the four largest earthquakes in the New Madrid earthquake sequence (the three main shocks and a fourth large aftershock) based on independent assignments from four experts with experience in analysis of historical earthquakes: Duncan Agnew, Paola Albini, Kenneth Burke, and Stacey Martin (Hough and Page, 2011). The consensus intensity values are systematically (almost universally) lower than those estimated by Hough et al. (2000). Using the method developed by Bakun and Wentworth (1997) and two CEUS attenuation relations developed by Bakun et al. (2003) and Bakun and Hopper (2004), Hough and Page (2011) estimate magnitudes using the consensus values as well as the independent assignments by the four experts. The magnitude values are lower than those estimated by Hough et al. (2000).

Tuttle, Hengesh, et al. (2002) discuss the M_w 7.7 Bhuj earthquake in the Kachchh region of India as a potential analog for the New Madrid earthquakes based on similarities in the tectonic and geologic settings between the two regions as well as on the extent and scale of paleoliquefaction that occurred in the Bhuj earthquake relative to the paleoliquefaction features in the NMSZ region. Tuttle, Hengesh, et al. (2002) note that if the Ambraseys (1988) relationship between magnitude and distance to the farthest liquefaction formed during an earthquake reflects intraplate earthquakes, then the Bhuj earthquake, which has a slightly shorter maximum distance to liquefaction than the NMSZ earthquakes, supports an estimate of $M_w \geq 7.6$ for the size of the 1811-1812 earthquakes.

Mueller et al. (2004) use instrumentally recorded locations of recent earthquakes (assumed by Mueller et al. to be aftershocks of the 1811-1812 sequence) and models of elastic stress change to develop a kinematically consistent rupture scenario for the main-shock earthquakes of the 1811-1812 New Madrid sequence. In general, the estimated magnitudes for NM1 and NM3 used in their analysis ($M = 7.3$ and $M = 7.5$, respectively) are consistent with those previously published by Hough et al. (2000). Mueller et al.'s results (2004) suggest that the NM1 and NM3 main shocks occurred on two contiguous faults: the strike-slip Cottonwood Grove fault and the RFT, respectively. The locations of the NM1 and NM3 earthquakes on the Cottonwood Grove and RFT, respectively, are relatively well constrained. In contrast to the earlier Hough et al. study (2000) that located the NM2 earthquake on the NN, Mueller et al. (2004) suggest a more northerly location for the NM2 earthquake, possibly as much as 200 km (124.3 mi.) to the north in the Wabash Valley of southern Indiana and Illinois. Hough et al. (2005) also infer a similar more northerly location.

Using Bakun and Wentworth's method (1997), Mueller et al. (2004) obtain an optimal location for the NM2 main shock at 88.43°W, 36.95°N and a magnitude of **M** 6.8. They note that the location is not well constrained and could be fit almost as well by locations up to 100 km (62 mi.) northwest or northeast of the optimal location. Mueller et al. (2004) conclude that the three earthquakes on the contiguous faults increased stress near fault intersections and end points, in areas where present-day microearthquakes have been interpreted as evidence of primary main-shock rupture. They suggest that their interpretation is consistent with established

magnitude/fault area results, and does not require exceptionally large fault areas or stress drop values for the New Madrid main shocks.

With respect to the location of the NM2 earthquake, Bakun and Hopper (2004b) also discuss the paucity of MMI assignments available for this earthquake to the west of the NMSZ and the resulting uncertainty in its location. They note that the two MMI sites closest to the NMSZ provide nearly all of the control on the location of this earthquake and that, based on these two sites, a location northeast of their preferred site is indicated. They indicate, however, that the lack of 1811-1812 liquefaction observations in western Kentucky, southern Illinois, and southern Indiana precludes an NM2 location in those areas. Bakun and Hopper (2004b) follow Johnston and Schweig (1996) in selecting a preferred location on the NMN fault. Dr. Steve Obermeier confirmed that liquefaction features in the Wabash Valley region that would support the more northerly location preferred by Mueller et al. (2004) are absent (S. Obermeier, pers. comm., August 24, 2004). He noted that he had looked specifically in the area mentioned in the Yearby Land account that was cited by Mueller et al. (2004) and observed evidence for only small sand blows and dune sands, but did not see features of the size and origin described in that account.

Dr. Arch Johnston (written comm., August 31, 2004) indicated that the earlier estimates of Johnston (1996b) are likely to be high by about 0.2–0.3 magnitude units. More recently, Johnston expressed concerns regarding the estimation of magnitude for the 1811-1812 earthquakes from intensity data and indicated that he is working on developing revised estimates based on the assumption that the seismicity represents aftershocks from the 1811-1812 earthquakes (pers. comm., February 16, 2010). This analysis is not yet complete.

A review of published estimates (e.g., Bakun and Hopper, 2004b; Mueller et al., 2004; Hough and Page, 2011) indicates that uncertainty and differing views remain within the research community regarding the size and location of the 1811-1812 earthquakes. Based on review of the publications described in the preceding paragraphs and on communications with Drs. Bakun, Hough, and Johnston, the maximum magnitude for the NMFS faults (NMN, NMS, and RFT faults) is assessed as follows.

- Equal weight (one-third) is given to estimates based on Bakun and Hopper (2004b), Hough and Page (2011), and the Johnston revisions (written comm., August 31, 2004) to Johnston (1996b).
- Results from both intensity attenuation relations (models 1 and 3) in the Bakun and Hopper estimate (2004b) are used. Based on Bakun and Hopper's preference for model 3, weights of 0.75 and 0.25 are assigned to model 3 and model 1, respectively.
- In the case of the Hough and Page estimates (2011), which also use the Bakun and Hopper (2004b) attenuation models, similar weights of 0.75 and 0.25, are assigned to values based on model 3 and model 1, respectively.

The resulting RLME magnitude distribution for each of the three faults is given in the table below. Rupture sets 1 and 2 correspond to the revised Johnston estimates (1996b); rupture sets 3 and 4 correspond to the Bakun and Hopper estimates (2004b); and rupture sets 5 and 6 correspond to the Hough and Page estimates (2011).

As discussed in the following section, the present interpretation of the paleoearthquake data is that the two prehistoric earthquake ruptures that occurred before the 1811-1812 sequence also consisted of multiple large-magnitude earthquakes. Therefore, for this assessment, the modeled earthquake scenario includes rupture of multiple (two to three) fault sources. Furthermore, the arguments for the high- versus low-magnitude assessments for the individual faults are considered to be highly correlated. Therefore, six alternative sets of ruptures were produced from the distributions developed previously for each fault, as shown in the logic tree on Figure 6.1.5-1 and tabulated below.

Rupture Set	Expected NMFS RLME Magnitude for:			Weight
	NMS	RFT	NMN	
1	7.9	7.8	7.6	0.167
2	7.8	7.7	7.5	0.167
3	7.6	7.8	7.5	0.25
4	7.2	7.4	7.2	0.083
5	6.9	7.3	7.0	0.25
6	6.7	7.1	6.8	0.083

The magnitudes tabulated above represent the uncertainty distribution for the expected magnitude for the RLME for each fault within the NMFS. The size of the next RLME is assumed to vary randomly about the expected value following a uniform distribution over the range of ±0.25 magnitude units (Section 5.3.3.4).

6.1.5.4 RLME Recurrence

The remaining nodes of the NMFS RLME source logic tree address the assessment of earthquake recurrence rates.

Recurrence Method

The data available for assessing the recurrence rate of the NMFS RLMEs provide assessments of the timing of past earthquakes. Thus the “Earthquake Recurrence Intervals” approach is used with weight 1.0 (Figure 6.1.5-1).

Recurrence Data

The best constraints on recurrence of NMFS RLME sources derive from paleoliquefaction studies throughout the New Madrid region and from paleoseismic investigations of the RF scarp and associated fold. Using studies of hundreds of earthquake-induced paleoliquefaction features at more than 250 sites, Tuttle, Schweig, et al. (2002, 2005) concluded that (1) the fault system

responsible for the New Madrid seismicity generated sequences of two to three very large earthquakes in ~2350 BC, ~AD 900, ~AD 1450, as well as in 1811 and 1812; (2) given uncertainties in dating liquefaction features, the time between the past three earthquakes may be as short as 200 years or as long as 800 years, with an average of 500 years; (3) the paleoliquefaction record between 2350 BC and AD 900 is probably incomplete; and (4) some of the prehistoric sand blows are compound structures, resulting from multiple earthquakes (i.e., earthquake sequences) occurring closely spaced in time.

Out-of-cluster recurrence rates for the NMFS are based on dates presented in Holbrook et al. (2006). Holbrook et al. (2006) present a reconstruction of Holocene Mississippi River channels from maps of floodplain strata to identify channel perturbations reflective of major displacements on the RFT. This evaluation, in combination with the paleoliquefaction chronology developed by Tuttle et al. (2002, 2005), provides evidence of temporal clustering of earthquakes in a compressive Midcontinent intraplate on short-term cycles (months), as well as evidence for longer-term reactivation cycles (10^4–10^6). The study makes a case for a ~1,000-year cluster of earthquakes with 10^2 year spacing on the RF, beginning with a coseismic slip event near the end of the middle Holocene at ~2200 to ~1600 BC. This Holocene cluster appears separated from the modern episode of seismicity (beginning ~AD 900) by at least 1,700 years of tectonic quiescence.

Earthquake Recurrence Model

The Poisson and renewal recurrence models are given weights of 0.75 and 0.25, respectively (Figure 6.1.5-1). As discussed in Section 5.1.2, the renewal model is considered more appropriate on a physical basis if a fault is responding to quasi-steady-state loading, producing more periodic occurrences of large earthquakes. This would suggest that a weight of 0.5 or larger be applied to the renewal model. However, it is not clear that such a physical process applies to the NMFS, even though there is evidence for periodic occurrence of large earthquakes. Therefore, the weight assigned to the renewal model is reduced to 0.25.

RLME Annual Frequency

The final node of the logic tree addresses the uncertainty distributions for the annual frequency of RLMEs (Figure 6.1.5-1). These distributions were developed using the methodology described in Sections 5.3.3.1 and 5.3.3.2. For the Poisson model, the relative likelihood of various values of the recurrence rate parameter was developed using Equation 5.3.3-4 and the observations of the time intervals between the selected paleoearthquakes and the open interval post the 1812 earthquakes. For the renewal model, the relative likelihoods of various values of the mean recurrence interval for RLMEs were developed using Equations 5.3.3-7, 5.3.3-8, and 5.3.3-9 for each set of past RLMEs and specified value of coefficient of variation. The resulting parameters were then used to compute the equivalent annual frequency of RLMEs using Equations 5.3.3-10 and 5.3.3-11.

The data used for the recurrence rate calculations are the time intervals between individual RLMEs for the renewal model case and the age of the oldest RLME for the Poisson case. These are calculated from the age estimates for each past RLME. With the exception of the 1811-1812

earthquakes, these ages are estimated from two types of data, as described above. Uncertainty distributions for the ages of the two previous RLME sequences were developed from age dating of liquefaction features. Tables 6.1.5-3 and 6.1.5-4 list liquefaction features associated with the AD 900 and 1450 RLMEs, respectively (see the CEUS SSC Project paleoliquefaction database, Appendix E). The second and third columns list the minimum and maximum ages for these features defined as time before January 1, 2011. The ages were chosen based on the age range for the liquefaction features. The remaining columns of each table list possible ages for the two RLME sequences. The cells in each row contain an "X" when the age range for the liquefaction feature is in conflict with the RLME age at the top of the column. For example, the second feature in Table 6.1.5-3, "MarkedT01-01," has an age range of 511–591 years before January 1, 2011. Those columns of the table with RLME ages outside of this range are marked with an "X." The first feature, "Tyr01-01" has an age range of 211–711 years, which allows all of the possible ages listed in the column headings. Thus, no cells are marked with an "X" for this feature.

The last row of Tables 6.1.5-3 and 6.1-5-4 lists the number of liquefaction features whose age estimates are inconsistent with the specified RLME ages. As indicated, there are no RLME ages that do not conflict with at least one liquefaction feature age range. However, there are possible RLME ages where the number of liquefaction feature age conflicts is small compared to the total number of features. For example, age estimates for the AD 1450 RLME in the range of 511–590 years are in conflict with the ages for 2–4 liquefaction features, while age estimates outside this range are in confict with 6–8 features. Similarly, age estimates for the AD 900 RLME in the range of 1,011–1,211 years are in conflict with the ages for 1–4 liquefaction features, while age estimates outside this range are in conflict with the ages for 7 or more liquefaction features.

The data listed in Tables 6.1.5-3 and 6.1.5-4 were used to construct distributions for the age of the two RLMEs. The limits of possible ages were defined based on the age limits that are inconsistent with the ages of four or fewer liquefaction features. This age range was chosen because the number of feature age inconsistencies grows quickly outside this range. A trapezoidal probability density function was constructed using these age limits and assigning equal probability to ages that were in conflict with the ages of fewer features. The assigned probability density functions and the resulting cumulative distribution functions for RLME age are shown on Figure 6.1.5-7.

The uncertainty distributions for in-cluster RLME annual frequency were then computed by repeatedly simulating samples of RLME dates from the age distributions shown on Figure 6.1.5-7 and computing a relative likelihood distribution for RLME rate from each sample. The resulting distributions were then combined to produce a composite distribution for RLME rate. These composite distributions were then represented by five-point discrete approximations. The resulting distributions for RLME recurrence frequency are listed in Tables 6.1.2-5 and 6.1.2-6 for the Poisson and Renewal models, respectively.

The out-of-cluster RLME rate for the NMFS was estimated from the data presented in Holbrook et al. (2006), who indicate initiation of NMFS clusters of large earthquakes 1,000 years ago (the start of the current cluster) and 4,000 years ago (the start of the previous cluster). These data correspond to one closed interval and one open interval. Using the likelihood formulation of

Equation 5.3.3.4, the distribution for out-of-cluster RLME frequency listed in Table 6.1.5-7 was developed.

The paleoliquefaction data gathered in the New Madrid region indicates that the prehistoric earthquakes have occurred in sequences closely spaced in time that are similar to the 1811-1812 sequence. Figure 6.1.5-8 shows the estimated earthquake sizes and locations for the 1811-1812 sequence (from Johnston and Schweig, 1996) and the two previous sequences. These data indicate that the RF has ruptured in all three sequences, but the NMN and NMS sources may not have produced large earthquakes in all three sequences. The available data allow for the possibility that the third earthquakes on the NMN and NMS sources may have been dependent earthquakes, on the order of a unit magnitude smaller than the main earthquakes. However, it is also possible that the paleoliquefaction record is not completely known for these earthquakes and they may have been comparable in size to the larger historical earthquakes. These observations were used to construct two alternative scenarios for the relative frequency of earthquake sequences on the central New Madrid fault sources, one in which all three components produce large earthquakes in each RLME sequence and one in which the NN component ruptures in two out of three RLME sequences. During preliminary model development, it was found that these two alternatives produced minimal difference in computed hazard. Therefore, the recurrence model presented here only includes the alternative of all three components.

6.1.6 Reelfoot Rift—Eastern Rift Margin Fault

Several studies have concluded that the eastern Reelfoot rift margin is a fault zone characterized by recurrent movement in the Quaternary, with the most recent earthquake at some localities occurring within the Holocene (e.g., Crone, 1992; Luzietti et al., 1992; Crone and Schweig, 1994; Cox et al., 2006). Based on the results of these studies and preliminary results of seismic surveys along the Mississippi River that show evidence for near-surface faulting (Dr. B. Magnani, Center for Earthquake Research and Information, U. of Memphis, pers. comm., May 29, 2009), two independent sources of RLMEs, referred to as the Eastern Rift Margin South (ERM-S) and North (ERM-N) RLME sources, are included in the seismic source model. Uncertainties in the location, rate, and size of earthquakes that may occur on these two RLME sources are outlined in logic trees (Figures 6.1.6-1a and 6.1.6-1b). Locations of tectonic features and key localities where detailed geophysical surveys and subsurface explorations have been conducted to evaluate the location and activity of faults and paleoliquefaction features along the eastern margin of the Reelfoot rift zone are shown on Figure 6.1.6-2 and discussed below. Additional information used to identify and characterize RLME sources along the eastern margin of the Reelfoot rift zone is summarized in Appendix Tables C-6.1.6 and D-6.1.5.

The Crittenden County fault zone (CCFZ), located in northeastern Arkansas about 25 km (15.5 mi.) northwest of Memphis, Tennessee, is a northeast-trending zone of high-angle (up-to-the-northwest throw) reverse faulting that extends at least 32 km (20 mi.; Crone, 1992). The CCFZ, which has no known surface expression, was one of the first structures along the southeastern Reelfoot rift margin to be identified from interpretation of seismic profiles as a potential source of damaging earthquakes (Crone, 1992; Luzietti et al., 1992; Williams et al., 1995). The CCFZ roughly coincides with the southeastern margin of the northeast-trending Reelfoot rift (Figure 6.1.6-2). Based on this coincidence, Crone (1992) suggests that preexisting, west-dipping normal

faults within the rift may have been reactivated as reverse faults with up-to-the-west movement during the Late Miocene and Tertiary.

A history of recurrent fault movement from the Mesozoic into the Quaternary is interpreted by Williams et al. (1995) using seismic data (Vibroseis, Mini-Sosie, shotgun, and weight drop) and drillhole data. High-resolution seismic-reflection and refraction data show deformed and faulted beds of Pleistocene (and possibly Holocene) age above the deeper, well-imaged CCFZ in Eocene and older strata. The possible association of these shallow deformation features with the CCFZ suggests that recurrent movement may have occurred on the fault zone in the Quaternary (Williams et al., 1995). However, the lack of a clear connection between the near-surface faults that disrupt the Quaternary section and the main flexure and faults at depth leads to some uncertainty in the interpretation of the shallow faults. The sense of vertical offset in Quaternary deposits is opposite to the net structural relief in the underlying rift and on the deeper structure. Reflections from the Quaternary-Eocene unconformity show warping, dip, or interruptions in places over the CCFZ that suggest a length of at least 16 km (10 mi.) of near-surface deformation; this deformation may represent Quaternary or Holocene movement (Luzietti et al., 1992).

Williams et al. (1995) interpret one seismic profile to show that the unconformity between Eocene and overlying Quaternary deposits (referred to as the QE unconformity) has 5 m (16.5 ft.) of relief and is faulted approximately 2 m (6.5 ft.), both down to the west across one trace of the CCFZ. A second profile shows a fault with approximately 1 m (3.3 ft.) of down-to-the-east throw. The deformation extends into the overlying deposits, and a Holocene reflector is deformed by a rootless, second-order structure that is interpreted to be a bending-moment fault formed in response to the monoclinal bulge caused by the subjacent main reverse fault or an oblique-slip component in a strike-slip regime (Williams et al., 1995). Mihills and Van Arsdale (1999) also suggest that Holocene uplift may be associated with the CCFZ.

Chiu et al. (1997) report a distinct seismicity lineation that appears to be associated with the southeastern Reelfoot rift margin approximately 25 km (15.5 mi.) to the northeast of the CCFZ. They noted that focal mechanisms suggest that minor faulting on this margin is characterized by right-lateral strike-slip with high-angle thrust faulting. The faulting is generally consistent with an east-west-oriented, maximal, horizontal, compressional stress, similar to the regional stress regime. Based on analysis of intensity data, Hough and Martin (2002) conclude that a large aftershock of the December 11, 1811, New Madrid earthquake (M 6.1 ± 0.2) occurred within the southwestern one-third to one-half of this band of seismicity.

Paleoseismic and geomorphic investigations along the eastern margin of the Reelfoot rift from Meeman-Shelby Forest State Park (approximately 25 km [15.5 mi.] north of Memphis) to the Tennessee-Kentucky border are presented by Cox and others (Cox, Van Arsdale, and Harris, 2001; Cox, Van Arsdale, et al., 2001; Cox, Van Arsdale, and Larsen, 2002; Cox et al., 2006) (Figure 6.1.6-2). The results of these investigations show that the southeastern rift margin coincides with a 150 km (93 mi.) long linear topographic scarp from near Memphis to the Tennessee-Kentucky line; S-wave reflection profiles, auger data, and trench excavations reveal late Wisconsinan-Holocene surface faulting and late Holocene liquefaction associated with this fault-line scarp (Cox, Van Arsdale, and Harris, 2001; Cox, Van Arsdale, et al., 2001; Cox, Van

Arsdale, and Larsen, 2002; Cox et al., 2006). Cox, Van Arsdale, and Harris (2001), following Fisk (1944), refer to this fault as the Big Creek fault. Cox, Van Arsdale, et al. (2001) and other researchers (e.g., Csontos et al., 2008) subsequently refer to this zone of faults as the southeastern or eastern Reelfoot rift margin fault system. Based on variation in sense of throw along strike and flower-structure geometry observed in seismic profiles, Cox and others (Cox, Van Arsdale, et al. 2001; Cox, Van Arsdale, and Larsen, 2002) conclude that this fault is a strike-slip fault and is currently accommodating right-lateral strain along the boundary of the hanging wall of the RFT. Significant right-lateral offset (8–15 m [26.2–49.2 ft.) and vertical (≥3 m [9.8 ft.] of up-to-the-west throw) displacement of a late Pleistocene fluvial channel (approximately 20 ka) is inferred from stratigraphic and structural relationships observed in paleoseismic trenches at the Porter Gap locality (Cox, Van Arsdale, and Larsen, 2002). This offset is the result of multiple (at least two) surface faulting earthquakes, the most recent being between 2,000 and 2,500 years ago (Cox, Van Arsdale, and Larsen, 2002; Cox et al., 2006).

Evidence for Holocene faulting also is observed in paleoseismic trenches at the Meeman-Shelby Forest paleoseismic site, and constraints on timing of the most recent earthquakes at this site and the Porter Gap site allow for the possibility of a single late Holocene rupture of ≥80 km (50 mi.) (Cox et al., 2006; Figure 6.1.6-2). Paleoliquefaction surveys along the Hatchie and Obion rivers near Covington and Dyersburg, Tennessee, to date have not identified paleoliquefaction features of this age, but the ages of some prehistoric liquefaction features along the two rivers have not yet been constrained (Dr. M. Tuttle, pers. comm., March 5, 2010). Along the northern part of the fault zone at the Union City site, seismic profiling and push-core transect data suggest only 1.5 m (5 ft.) of down-to-the-northwest faulting of early Wisconsinan Roxana Loess, with no discernable deformation of late Wisconsinan Peoria Loess (Cox et al., 2006). Cox et al. (2006) speculate that this segment turned off (or activity decelerated significantly) in the late Pleistocene-Holocene on the northeastern part of the fault zone north of the intersection of the RFT and the eastern margin of the rift.

One of the key structures identified in seismic data in the vicinity of the Meeman-Shelby Forest paleoseismic trenching locality is a high-angle (about 75 degrees), west-dipping reverse fault that Williams et al. (2001) identified and named the Meeman Shelby fault (MSF; Figure 6.1.6-3a). Cox and others (Cox, Van Arsdale, and Larsen, 2002; Cox et al., 2006) correlate this fault pick with a northeast-trending fault along the bluff escarpment. As imaged in a high-resolution Mini-Sosie seismic reflection line, the MSF displaces Paleozoic and Cretaceous units 70 and 40 m (230 and 131 ft.), respectively; deformation of the overlying Eocene strata is expressed primarily as an up-to-the-west fold with amplitude of about 50 m (164 ft.) at the base (Williams et al., 2001). Similar structures (i.e., having up-to-the-west folding) are observed in seismic profiles along the CCFZ, which lies approximately 18 km (11 mi.) to the west at its northernmost mapped location, and along a N33°E trend, approximately 33 km (20.5 mi.) northeast of the Meeman-Shelby vibroseis line (Williams et al., 2001). In a more recent paper, Odum et al. (2010) reevaluated the Mini-Sosie seismic reflection line and now suggest that the MSF is a N13°W trending fault that correlates with the eastern boundary fault of Joiner Ridge, a 10–15 km (6.2–9.3 mi.) wide by approximately 50 km (31 mi.) long structure defined by the uplift of the Pliocene-Pleistocene unconformity surface (Csontos et al., 2008).

The westernmost pick of the MSF as imaged on the Mini-Sosie line also lines up with a series of three fault picks identified in a high-resolution seismic survey conducted along the Mississippi River from Caruthersville, Missouri, to Helena, Arkansas (Dr. B. Magnani, CERI, U. of Memphis, pers. comm., May 29, 2009) (Figure 6.1.6-2). A line drawn through these fault picks (ERM-RP) projects along an approximately N30°E trend through the original Meeman-Shelby fault pick identified by Williams et al. (2001). Although there is currently no independent evidence that a fault of this trend is present at this location, a similar N30°E trend is exhibited by the postulated Memphis and Ellendale faults, which Van Arsdale et al. (2002) describe as possible Quaternary (and Holocene in the case of the Ellendale fault) active structures.

6.1.6.1 Evidence for Temporal Clustering

The first node of the logic tree addresses the issue of temporal clustering of earthquakes in the present tectonic stress regime (Figure 6.1.6-1). The available data regarding number and timing of recent earthquakes and long-term slip rates for the ERM sources are not sufficient to evaluate whether the ERM RLME sources exhibit evidence for temporal clustering. Therefore, this branch of the tree is not applicable to the Reelfoot rift ERM-S and ERM-N RLME sources.

6.1.6.2 Geometry and Style of Faulting

The primary basis for characterizing two independent RLME sources along the eastern margin of the rift is the apparent differences in the timing and recency of late Pleistocene and Holocene surface deformation inferred from paleoseismic investigations (Cox, Van Arsdale, and Harris, 2001; Cox, Van Arsdale, et al., 2001; Cox, Van Arsdale, and Larsen, 2002; Cox et al., 2006). Based on the evidence for cumulative slip, as well as on the timing and recency of faulting along the rift margin, Cox, Van Arsdale, and Harris (2001) suggest that lateral slip on the southeastern rift margin (ERM-S) is greatest southwest of the restraining bend (adjacent to the Reelfoot thrust hanging wall). In this area, 25 m (82 ft.) of reverse separation underlies the bluff along the southern part of the margin. On the northern segment (ERM-N), the rift margin is characterized by a less prominent scarp (9 m [29.5 ft.] high) and a lack of seismicity.

The location of late Quaternary faulting has been identified at only a few localities where detailed paleoseismic trenches, geophysical surveys, and drilling have been conducted (Figure 6.1.6-2). The zone of bedrock faulting associated with the Reelfoot rift margin, however, is considerably wider. In the vicinity of the CCFZ, the zone of basement faults may be on the order of 4–8 km (2.5–5 mi.) wide (Hildenbrand, 1982; Crone, 1992). Csontos and Van Arsdale (2008) show the zone to be as much as 10–12 km (6.2–7.5 mi.) wide north of Memphis (Figure 6.1.6-2 inset). Uncertainty in the width of the zone of faulting and location of future ruptures along this margin is therefore represented by a zone rather than a single fault.

The location, and extent, of the ERM-N is based primarily on Cox, Van Arsdale, et al. (2001). The ERM-N source zone is centered on the pronounced topographic escarpment and lineament identified by Cox, Van Arsdale, et al. (2001; Figure 6.1.6-3b). The basis for the dashed extension of the ERM-N into Kentucky as shown by Cox et al. (2006) is not discussed in that publication, and this feature is not topographically expressed in the digital elevation model data. Cox, Van

Arsdale, and Harris (2001) speculate that a basement fault may have controlled the emplacement of the Big Foot pluton that appears to coincide with a boundary between two drainage basin asymmetry domains to the north of Union City. There is no supporting data to demonstrate that a Quaternary fault is present; thus in the absence of topographic evidence for the extension of the fault to the north, the dashed extension is not included directly in the characterization of the ERM-N RLME source. However, the northern end of the ERM-N is treated as a leaky boundary (i.e., it is not a barrier to future fault ruptures) allowing ruptures to propagate further to the northeast along the dashed extension.

The location of the ERM-S segment is based on faults observed in paleoseismic trenches, geophysical surveys, and alignments of geomorphic features (Cox et al., 2006). Based on the orientation of the ERM fault in the current stress field, on the linear geometry of the fault system inferred from geomorphology, and on focal mechanisms of minor faulting along the margin, the predominant sense of slip for this fault system is considered to be right-lateral strike-slip with a component of reverse slip. Cox et al. (2006) interpret Holocene right-lateral slip on the basis of focal plane mechanisms of contemporary seismicity and evidence for right-lateral offset of late Pleistocene channel deposits.

To the south of the Meeman-Shelby Forest State Park area, evidence for latest Pleistocene to Holocene activity is noted for the CCFZ (Williams et al., 1995) and possibly for a N30°E trend defined by the fault picks identified in the recent river seismic survey (ERM-RP) (Dr. B. Magnani, Center for Earthquake Research and Information, U. of Memphis, pers. comm., May 29, 2009). These two alternatives are included as the southern extension of the ERM-S (Figure 6.1-2b). The validity and continuity of the ERM-RP as a continuous fault have not been confirmed. For this reason, this alternative (ERM-SRP) is given less weight (0.4) than the ERM-SCC (weight of 0.6), which is a known fault having Quaternary and possible Holocene activity.

Within the zones associated with the ERM-N, the ERM-SCC and ERM-SRP faults are distributed uniformly throughout the zone subparallel to the preferred fault traces; the faults are modeled as vertical strike-slip faults. Both the northeastern and southwestern ends of the zones are modeled as leaky to allow for uncertainty in the extent of possible reactivated faults along the rift margin.

The probability distribution used to model seismogenic thickness for the NMFS RLME source (Section 6.1.5.2), which is consistent with analysis of focal mechanisms along the ERM (Chiu et al., 1997), is used to model the ERM RLME sources: 13 km (8 mi.; weight of 0.3), 15 km (9.3 mi.; weight of 0.5), and 17 km (10.6 mi.; weight of 0.2).

6.1.6.3 RLME Magnitude

There are little (ERM-S) or no (ERM-N) data except for possible fault length that provide direct constraints on the magnitude of prehistoric earthquakes along the southeastern margin of the Reelfoot rift.

The ERM-S source extends for a distance of approximately 114 km (71 mi.). The fault is similar in length and style of faulting to the New Madrid South fault (discussed in Section 6.1.5). There

are only limited paleoseismic data from which to identify the length of fault ruptures or the size of individual displacements for prehistoric earthquakes on this fault zone. Information on timing of earthquakes shown on Figure 6.1.6-4, which is discussed below in Section 6.1.6.4, allows for the possibility of a ≥80 km (50 mi.) long rupture between the Porter Gap and Meeman-Shelby Forest sites, but does not preclude shorter ruptures (Cox et al., 2006). Vertical displacement of 0.5 m (1.6 ft.) and right-lateral offset of 0–2 m (0–6.6 ft.) during the most recent earthquake at the Porter Gap site are reported by Cox et al. (2006).

Ruptures of ≤80 or 114 km (≤50 or 71 mi.), assuming seismogenic depths ranging from 13 to 17 km (8.1 to 10.5 mi.), yield magnitude estimates ranging from ≤**M** 7.0/ **M** 7.4 (Wells and Coppersmith [1994] magnitude-length and magnitude-area relationships) to ≤**M** 7.4/**M** 7.6 (Somerville et al. [2001] magnitude-area relationship, median) (Table 6.1.6-1). Displacements of 0.5 or 2.1 m (1.5 or 6.9 ft.) (calculated oblique slip) would suggest magnitudes of **M** 6.5–7.1 to as much as **M** 6.7–7.3 based on empirical relationships for magnitude from maximum or average displacement, respectively (Table 6.1.6-1).

Given the uncertainty in the dimensions of paleoruptures, a wide range of values that capture the range in RLME magnitude estimates suggested by limited fault-specific data and analogy to the NMS fault is used to characterize the southern segments of the ERM south of the intersection with the Reelfoot rift. The resulting distribution for the expected RLME magnitude is tabulated below.

Expected ERM-S RLME Magnitude (M)	Weight
6.7	0.15
6.9	0.2
7.1	0.2
7.3	0.2
7.5	0.2
7.7	0.05

The ERM-N segment is approximately 73 km (45.5 mi.) long, which is more comparable in length to the New Madrid North (NMN) fault. There are no data on paleoearthquake rupture dimensions that can be used to estimate magnitude. Ruptures of 73 km (45.5 mi.), assuming a seismogenic depth ranging from 13 to 17 km (8 to 10.6 mi.), yield magnitude estimates ranging from **M** 7.0 (Wells and Coppersmith [1994] magnitude-area relationship) to **M** 7.4 (Somerville et al. [2001] magnitude-area relationship, median) (Table 6.1.6-2). A distribution similar to that used for the ERM-S, but with a lower maximum value based on the shorter total length, is used to characterize the ERM-N. The distribution is tabulated below.

Expected ERM-N RLME Magnitude (M)	Weight
6.7	0.3
6.9	0.3
7.1	0.3
7.4	0.1

6.1.6.4 RLME Recurrence

The remaining nodes of the ERM RLME logic trees address the estimation of recurrence rate of RLMEs.

Recurrence Method

The data available for assessing the recurrence frequency of ERM RLMEs consist of the number of earthquakes that postdate a specific geologic stratum. Therefore, the "Earthquake Count in a Time Interval" approach is used to assess RLME recurrence frequency.

Recurrence Data

Paleoseismic investigations indicate that several paleoearthquakes have occurred along and within the southeastern part of the Reelfoot rift. Figure 6.1.6-4 is a summary diagram showing the relative timing and slip information inferred from paleoseismic investigations at the Porter Gap and Meeman-Shelby Forest localities on the ERM-S. The youngest calibrated radiocarbon ages of sediments predating the latest faulting earthquake (~0.5 m [1.6 ft.] vertical displacement) are 4,100–3,900 yr BP at Shelby County and 2,790–2,740 yr BP at Porter Gap (Cox et al., 2006). Radiocarbon ages from sediments postdating the latest faulting are 2,120–1,800 yr BP at Shelby County and 945–765 yr BP at Porter Gap. Minor liquefaction adjacent to the fault observed at the Porter Gap site is similar in age to widespread liquefaction features in the New Madrid region that are associated with an earthquake that occurred 2,750 yr BP ± 150 yr (Appendix E). An interpreted offset Wisconsinan paleochannel at Porter Gap records an unknown number of surface faulting earthquakes. It is assumed that at least two and possibly four earthquakes of a size similar to the recent earthquake have occurred at this locality in the past approximately 20 kyr. The infrared stimulated luminescence analysis ages of samples from the offset channel fill are 19,600 yr BP ± 1,900 yr and 19,900 yr BP ± 1,740 yr (Cox et al., 2006).

The recurrence data for the ERM RLME sources are more limited than for the NMFS RLME source. Except for the Porter Gap locality along the ERM-S segment that has a reported slip rate based on an offset channel, the recurrence data for the other segments of the ERM RLME source consists of an estimated number of earthquakes within a time period (inter-earthquake intervals or elapsed time intervals are not well constrained). There is no specific information regarding the timing of recent earthquakes on the CCFZ or inferred ERM-RP faults.

The northern segment of the southeastern rift margin fault system (ERM-N) appears to be less active than the segment to the south. Paleoseismic data from the Union City site are insufficient to estimate the timing or number of earthquakes that formed the 9 m (29.5 ft.) high scarp. The most recent faulting at a site near Union City along the northern segment of the fault appears to postdate Sangamon–early Wisconsinan terrace deposits (60–35 ka), but predate late Wisconsinan Peoria Loess (?) (ca. 24–12 ka; Cox, Van Arsdale, et al., 2001). Paleoliquefaction features in Kentucky dated at 11,300 yr BP ± 200 years (Appendix E) could be related to an earthquake on the ERM-N. However, these features are approximately 40 km (25 mi.) north of the northeastern end of the ERM-N source, and their correlation to the most recent earthquake recorded at the Union City site is uncertain. Based on these observations, one or possibly two earthquakes have occurred on the ERM-N fault source since 12–35 ka. Due to uncertainty in what fault produced the paleoliquefaction features in western Kentucky, highest weight (0.9) is given to the evidence for a single earthquake on the ERM-N at the Union City site since 12–35 ka.

Earthquake Recurrence Model

As discussed in Section 5.3.3, the Poisson model is used as the default earthquake recurrence model with weight 1.0 for the ERM-S and ERM-N RLME sources as there are not sufficient data to justify including an alternative model.

RLME Annual Frequency

The final node of the logic tree addresses the uncertainty distributions for the annual frequency of RLMEs (Figure 6.1.6-1). These distributions were developed using the methodology described in Section 5.3.3.1. The relative-likelihood-based distribution was developed using Equation 5.3.3-2.

For the ERM-S RLME source, the number of past earthquakes, *N*, was set at two, three, or four. The interpretation of the data does not favor one of these three values, so they are given equal weight in the RLME logic tree (Figure 6.1.6-1a). The time period *T* is treated as uniformly distributed over the range of 17.7–21.7 kyr. The resulting distributions for RLME recurrence frequency are listed in Table 6.1.6-3.

For the ERM-N RLME source, the number of past earthquakes, *N*, was set at one or two, with weights of 0.9 and 0.1, respectively, as indicated above (Figure 6.1.6-1b). The time period *T* is treated as uniformly distributed over the range of 12–35 kyr. The resulting distributions for RLME recurrence frequency are listed in Table 6.1.6-4.

6.1.7 Reelfoot Rift—Marianna

Earthquake-induced liquefaction features, including large sand blows comparable in size to the NMSZ sand blows, have been identified near Marianna, Arkansas, about 75 km (46.5 mi.) southwest of Memphis, Tennessee (Tuttle et al., 2006; Al-Shukri et al., 2005, 2006, 2009). These sand blows, which are located 80 km (50 mi.) south of the southwestern end of the NMSZ, formed between about 5 and 10 ka and predate paleoearthquakes attributed to the NMSZ. The

presence of the features suggest a nearby source of Holocene RLMEs in the southeastern part of the Reelfoot rift outside of the NMSZ, which is herein referred to as the Marianna (MAR) RLME source. Paleoliquefaction features used to define the MAR source zone also are at least 30 km (19 mi.) south of the southern limits of the ERM RLME sources (Figures 6.1-2b and 6.1.6-2). The possibility that some of the earthquakes that triggered paleoliquefaction in the Marianna area originated on faults associated with the ERM RLME sources is considered as discussed below. A logic tree outlining the source characterization parameters for the MAR RLME source is shown on Figure 6.1.7-1. Data and observations used to characterize the MAR RLME source are summarized in Appendix Tables C-6.1.7 and D-6.1.7. Figures 6.1.7-2 and 6.1.7-3 show the locations of paleoliquefaction sites and structural features in the Marianna region in the southern part of the Reelfoot rift.

Tuttle et al. (2006) observed that a large sand blow at the Daytona Beach site near Marianna, which formed about 3500 BC (5,500 yr BP), may correlate with smaller sand blows to the northeast and southwest up to 175 km (108.7 mi.) away. Al Shukri et al. (2005) identified an earthquake at the Nancy 1 site near Marianna that occurred shortly after 4,850–4,800 yr BP. Al-Shukri et al. (2009) identified additional older paleoliquefaction features at the Daytona Beach Southeast site: those that formed about 10 ka and others that possibly predate 10 ka. A compound sand blow that formed about 4800 BC (6,800 yr BP) at the St. Francis 500 site may have formed as the result of several very large, closely timed earthquakes.

The location(s) of the earthquake source(s) responsible for these paleoliquefaction features is not known, but the size of the sand blows implies strong ground shaking at Marianna (Al-Shukri et al., 2005). A fault zone associated with the eastern Reelfoot rift margin is judged as a likely source for several reasons: its great length (approximately 300 km [186.5 mi.]); history of seismic activity; late Wisconsinan–early Holocene fault movement in western Tennessee; and structural relationship to the New Madrid fault system (Tuttle et al., 2006). Other potential fault sources in the vicinity of Marianna include the Big Creek fault zone and the White River fault zone.

A northwest-trending lineament defined by sand blows extends from the Daytona Beach locality to the northwest and southeast; the lineament initially defined to be approximately 10 km (6 mi.) in length (Tuttle et al., 2006) has been extended to a total length of 17 km (10.5 mi.) based on additional trenching and ground-penetrating radar surveys (Al Shukri et al., 2009; Al Quadi, 2010) (Figures 6.1.7-2 and 6.1.7-3). Its length, linear morphology, and parallelism to the nearby White River fault zone support the interpretation that the lineament may be fault controlled rather than related solely to lateral spreading (Al-Shukri et al., 2009). Al-Shukri et al. (2009) also identified a fracture in a trench exposure with a strike of N50°W (subparallel to the lineament) that crosscuts the sand blows. Although suggestive of being structurally controlled, further work is needed to verify by geologic and/or geophysical studies that strata below the sand layer that liquefied are faulted.

6.1.7.1 Evidence for Temporal Clustering

The first node of the logic tree for the MAR RLME source (Figure 6.1.7-1) addresses the issue of temporal clustering of earthquakes in the present tectonic stress regime. Available published and

unpublished information on the timing of paleoearthquakes in the Marianna region that is compiled in the paleoliquefaction database (Section 6.1.7.4) indicates that four earthquakes occurred during the time period from approximately 10 to 4.8 ka and that no late Holocene paleoliquefaction features have been identified to date. Tuttle (2009) cites the absence of late Holocene earthquakes in the southern rift as possible evidence that the locus of activity within the Reelfoot rift migrates over periods of 5–15 kyr. The data, while suggestive of possible temporal clustering, do not clearly demonstrate that the causative structures are in a period of inactivity. It also is unclear whether some of the paleoliquefaction features are due to earthquakes that originated on the Eastern Rift Margin (ERM) RLME source described above in Section 6.1.6. These uncertainties are represented by the equal weight assigned to the "in" versus "out" of a cluster models. In the case of the "out-of-a-cluster" model, the characterization defaults to the background (either the Mesozoic-and-younger Mmax zone or the Reelfoot rift seismotectonic zone).

6.1.7.2 Geometry and Style of Faulting

The location of the causative structure(s) for the earthquakes that produced the Marianna paleoliquefaction features is not well constrained based on the present state of knowledge, but there is evidence to indicate that at least some of the features are related to earthquakes on a local fault. The MAR RLME zone used for this study encompasses the paleoliquefaction sites that have been used to define the northwest-trending Daytona Beach lineament as well as the more distant Nancy and St. Francis sites near Marianna and Marianna Gap, respectively. The zone includes structures that have been considered as possible sources of the earthquakes that produced the paleoliquefaction, including the ERM RLME faults, Big Creek fault, and White River fault (Tuttle et al., 2006).

Northeast-trending faults, including possible structures related to the ERM faults and the subparallel Big Creek fault, are likely to be reactivated as predominantly strike-slip faults with a reverse component, based on focal mechanisms recorded in the southern Reelfoot rift (Chiu et al., 1997) and general orientation within the present north-northeast-directed maximum horizontal stress field (Zoback, 1992b). The eastern Reelfoot rift margin affects the regional drainage pattern in both the St. Francis basin and the Western Lowlands (Spitz and Schumm, 1997). The Big Creek fault zone parallels the Reelfoot rift margin and marks the boundary between south-trending Wisconsinan valley-train deposits and southwest-trending Holocene meander-belt deposits (Fisk, 1944; Krinitzsky, 1950).

The northwest-trending White River fault zone (WRFZ) is characterized as a steeply dipping, predominantly strike-slip fault with a small up-to-the-southwest component of reverse slip (Fisk, 1944; Krinitsky, 1950). Schumm and Spitz (1996) and Spitz and Schumm (1997) show the WRFZ as a left-lateral strike-slip fault. Schumm and Spitz (1996) note that the WRFZ is defined by numerous geologic and topographic features, which include a northwest-trending magnetic lineament, northwest-trending basement faults within the Western Lowlands, northwest-trending Paleozoic faults in the Ozark Uplands, extremely angular northwest-trending salients in the valley margins, tributaries to the L'Anguille River that form a drainage pattern parallel to the WRFZ, and the breach and offset of the southern end of Crowley's Ridge that may be structurally controlled. Schumm and Spitz (1996) observe that many of the anomalous features

are located on Pleistocene and Holocene deposits, indicating that much of the suggested deformation may be as young as Holocene in age. Csontos et al. (2008) describe the WRFZ as an up-to-the-south fault, based on gravity, magnetic (Hildenbrand and Hendricks, 1995; Langenheim and Hildenbrand, 1997), and seismic reflection data (Howe, 1985).

Based on these observations, two equally weighted orientations that subparallel the sides of the MAR zone are used to model fault ruptures: vertical, northeast-trending strike-slip faults and vertical northwest-trending strike-slip faults. The faults suggested as possible sources for the earthquakes that generated the Marianna paleoliquefaction features extend beyond the boundaries of the MAR zone. Uncertainties in the location of the epicenters and extent of paleoearthquakes in this region are accounted for by assuming that all boundaries to the MAR zone are leaky.

The probability distribution used to model seismogenic thickness for the Reelfoot rift as a whole (see Section 7.3.6) and other RLME sources in the Reelfoot rift (e.g., the New Madrid fault system and the ERM RLME sources [Sections 6.1.5.2 and 6.1.6.2]) is used to model the MAR RLME zone: 13 km (8 mi.; weight of 0.3), 15 km (9.3 mi.; weight of 0.5), and 17 km (10.5 mi.; weight of 0.2). This distribution also is consistent with seismogenic depths of between 14 and 16 km (8.7 and 10 mi.) for well-located earthquakes along the southeastern margin of the rift.

6.1.7.3 RLME Magnitude

The magnitudes of RLMEs in the MAR zone are not well constrained. The size of the largest paleoliquefaction features observed in trenches and imaged by ground penetrating radar surveys are comparable to the largest paleoliquefaction features observed in the NMSZ.

The maximum magnitude probability distribution for the MAR RLME magnitude gives relatively equal weight to a range of values estimated for the New Madrid South (NMS) fault based on the estimated size of the December 16, 1811, earthquake. The resulting distribution is tabulated below.

Expected Marianna RLME Magnitude (M)	Weight
6.7	0.15
6.9	0.2
7.1	0.2
7.3	0.2
7.5	0.2
7.7	0.05

6.1.7.4 RLME Recurrence

The remaining branches of the logic tree describe the assessment of RLME recurrence rates.

Recurrence Method

The data available for assessing the recurrence rate of the Marianna RLMEs provide assessments of the timing of past earthquakes. Thus the "Earthquake Recurrence Intervals" approach is used with weight 1.0 (Figure 6.1.7-1).

Recurrence Data

Four ages of paleoliquefaction features are known from paleoliquefaction studies to date (Appendix E). Estimated event ages (BP = before 1950) are as follows:

Nancy1— 4,825 yr BP ± 25 yr (4.8 ka)
Nancy2—5,460 yr BP ± 130 yr and 5,620 yr BP ± 40 yr (5.5 ka and 5.6 ka)
Daytona Beach—5,440 yr BP ± 130 yr (5.4 ka)
Daytona Beach SE2—9,855 yr BP ± 295 yr and one event before that (9.9 ka and before 9.9 ka)
St. Francis 500—6,805 yr BP ± 95 yr (6.8 ka)

Sand blows of similar age (5.5 ka) at Nancy2 and Daytona Beach probably formed during the same earthquake. Slightly older sand blows at Nancy2 (5.6 ka) could also have formed during the same earthquake. Because the age estimates of these sand blows are based on close maximum age constraints, the 4.8 and 5.5 ka sand blows could not have formed during the 6.8 ka earthquake (recorded at St. Francis 500). It also seems unlikely that the 9.9 ka sand blow formed during the 6.8 ka earthquake.

The most likely sequence of earthquakes along the Daytona Beach lineament includes earthquakes at 4.8 ka, 5.5 ka, and 9.9 ka, and another earthquake before that during the late Wisconsinan. The 6.8 ka earthquake recorded at the St. Francis site looks like an additional earthquake and may be related to an earthquake sequence resulting from multiple ruptures near the intersection of the ERM and the WRFZ. The two equally weighted data sets consist of either three or four earthquakes, with the oldest occurring approximately 9.9 ka.

Earthquake Recurrence Model

As discussed in Section 5.3.3, the Poisson model is used as the default earthquake recurrence model with weight 1.0 for the Marianna RLME source as there are not sufficient data to justify including an alternative model.

RLME Annual Frequency

The final node of the logic tree addresses the uncertainty distributions for the annual frequency of RLMEs. These distributions were developed using the methodology described in Section 5.3.3.1. The relative likelihood of various values of the recurrence rate parameter was developed using Equation 5.3.3-4 and the observations of two or three closed recurrence intervals and one open interval post the 9.9 ka earthquake. The value of $\sum_{i=1}^{N} t_i + t_0$ was assumed to be uniformly distributed between 9.6 kyr and 10.2 kyr with N equal to either 2 or 3. The resulting relative-likelihood-based distributions were represented by the five-point discrete distribution listed in Table 6.1.7-1.

6.1.8 Reelfoot Rift—Commerce Fault Zone

The Commerce geophysical lineament (CGL) is a 600 km long (373 mi.), 5–10 km (3–6 mi.) wide, northeast-trending gravity and magnetic anomaly that trends subparallel to and west of the Reelfoot rift (Hildenbrand and Hendricks, 1995). Recent studies have identified surface geomorphic anomalies, paleoseismic evidence for latest Pleistocene to Holocene tectonic deformation, and geologic structures coincident with the vertical surface projection of the CGL in southeastern Missouri along what is referred to as the Commerce section of the CGL (Baldwin et al., 2006). The following lines of evidence, both direct and indirect, for Quaternary fault activity along the Commerce section of the CGL in southeast Missouri, have been reported in the published literature as outlined by Baldwin et al. (2006) and Givler and Baldwin (2009).

- Anomalous west-flowing drainages on Crowley's Ridge (Cox, 1988; Fischer-Boyd and Schumm, 1995).
- Displacement of late Tertiary and Pleistocene to Holocene deposits (Harrison and Schultz, 1994; Harrison et al., 1999, 2002) along northeast-striking faults favorably oriented to be reactivated in the present-day stress field.
- Paleoliquefaction features within the Western Lowlands of southeastern Missouri that, in part, coincide with the CGL (Vaughn, 1991, 1992, 1994).
- Presence of diffuse contemporary seismicity in partial alignment with the CGL (Harrison and Schultz, 1994; Langenheim and Hildenbrand, 1997).
- Geophysical evidence of Tertiary and Quaternary deformation coincident with the surface traces of previously mapped bedrock faults in the Bloomfield Hills and Benton Hills (Stephenson et al., 1999; Odum et al., 2002).

- Evidence of late Pleistocene to early Holocene deformation on the Idalia Hill fault zone based on geomorphic mapping, acquisition of seismic reflection, and ground-penetrating radar data, coupled with paleoseismic trenching and borehole information collected at the South Holly Ridge site, near Idalia, Missouri (Baldwin et al., 2006).
- Preliminary results of ongoing investigations of the Penitentiary fault, an apparent en echelon continuation of the Commerce fault to the northeast into southern Illinois, also provide evidence in multiple seismic lines of interpreted latest Pleistocene and possible early Holocene (?) faulting. The continuation of the Penitentiary fault to the northeast is poorly constrained; the geomorphic expression of a reactivated fault-line scarp is not apparent to the north (Odum et al., 2002; Baldwin et al., 2008; Givler and Baldwin; 2009).

Based on these observations, an RLME fault source that encompasses faults and probable fault-related geomorphic features exhibiting evidence of repeated late Pleistocene and Holocene activity is included in the source model. A logic tree summarizing the characterization of this RLME source, referred to as the Commerce Fault Zone RLME source, is shown on Figure 6.1.8-1. The Commerce Fault Zone RLME source is modeled as a strike-slip fault zone extending south from the northern limit of the mapped Penitentiary fault (Tamms, Illinois) to the southern end of the paleoseismic sites near Qulin Ridge (Qulin, Missouri), where evidence for Quaternary activity (paleoliquefaction and anomalous stream deflections) has been documented (approximately at the Missouri-Arkansas border), a distance of about 120 km (75 mi.; Figure 6.1.8-2). Evidence for late Quaternary deformation and repeated latest Pleistocene to Holocene faulting along the CGL also is observed to the north in southern Illinois and Indiana. This deformation is considered in the characterization of the Wabash Valley RLME source (discussed in Section 6.1.9).

Locations of tectonic features and key localities where detailed geophysical surveys and subsurface explorations have been conducted to evaluate the location and activity of faults and paleoliquefaction features along the Commerce Fault Zone RLME source are shown on Figure 6.1.8-2 and are discussed below. Additional information used to identify and characterize an RLME source along the Commerce section of the CGL is summarized in Appendix Tables C-6.1.8 and D-6.1.8.

6.1.8.1 Evidence for Temporal Clustering

The first node of the logic tree for the Commerce Fault Zone RLME source (Figure 6.1.8-1) addresses the issue of temporal clustering of earthquakes. Early studies (Vaughn, 1994; Harrison et al., 2002) near Qulin Ridge and the English Hills, respectively, suggested that there may be evidence for two late Holocene earthquakes on structures related to the CGL, which could imply that the fault/fault zone is in a more active period of deformation. However, as noted below in Section 6.1.8.4, the liquefaction and secondary faulting used to document these Holocene earthquakes may be related to strong ground motion from earthquakes occurring elsewhere in the Reelfoot rift. There is no evidence to support large-magnitude earthquakes along the Idalia Hill or Penitentiary faults directly southwest and northeast of the English Hills as would be expected if large-magnitude earthquakes had ruptured the fault zone in the late Holocene. The available data regarding number and timing of recent earthquakes and long-term slip rates for the

Commerce Fault Zone RLME source are not sufficient to evaluate whether this RLME source exhibits evidence for temporal clustering. Therefore, this branch of the tree is not applicable to this source.

6.1.8.2 Geometry and Style of Faulting

The Commerce Fault Zone RLME source is modeled as a fault zone that encompasses late Pleistocene and possible Holocene active faults identified from geophysical, geomorphologic, and geologic data that are coincident with CGL defined by gravity and magnetic anomalies (Hildenbrand and Hendricks, 1995; Figure 6.1.8-3). Specific features used to define this RLME source are the Penitentiary fault (Givler and Baldwin, 2009; Baldwin et al., 2008); the Commerce fault (Palmer, Hoffman, et al., 1997; Palmer, Shoemaker, et al., 1997; Harrison and Schultz, 1994; Harrison et al., 2002); the Idalia Hill fault zone (Baldwin et al., 2006); and faults imaged in seismic data near Qulin Ridge (Stephenson et al., 1999) that align with an anomalous deflection of the St. Francis River (Fischer-Boyd and Schumm, 1995; Figure 6.1.8-2).

At most of the sites where detailed geophysical and subsurface paleoseismic studies have been conducted, deformation occurs across a broad zone up to a kilometer or slightly more in width. In some areas, such as in the English Hills where north-northeast-striking faults at Thebes Gap appear to splay north from the Commerce fault, the zone of Quaternary faulting encompasses the entire width of the CGL (e.g., Harrison et al., 1999; Figure 6.1.8-2). A zone the width of the entire CGL is therefore used to capture the uncertainty in the location of deformation that may be related to the Commerce Fault Zone RLME source. In the hazard analysis, future ruptures are distributed uniformly within this zone.

Recent analysis and relocation of 19 earthquakes ($\mathbf{M} \leq 3.6$) in the northeastern part of the NMSZ, using a velocity model of the Mississippi embayment with appropriate depths to bedrock beneath seismic stations, show that 2 of the earthquakes occurred at depths between 13 and 15 km (8 and 9.3 mi.; Shumway, 2008). Herrmann and Ammon (1997) show depths of up to 16 km (10 mi.) for earthquakes in the Reelfoot rift. Based on these data, the following distribution for seismogenic crustal thickness is used to characterize the Commerce Fault Zone RLME source: 13 km (8 mi.; weight of 0.3), 15 km (9.3 mi.; weight of 0.5), and 17 km (10.6 mi.; weight of 0.2).

The Commerce Fault Zone RLME source is modeled as a zone of vertical strike-slip faulting based on the following geologic and seismologic observations:

- The style of neotectonic and older deformation in the Thebes Gap area is consistent with strike-slip deformation along near-vertical structures (Harrison et al., 1999).
- Near-vertical faults and complex flower-like structures are observed in seismic data at multiple locations along the CGL (Stephenson et al., 1999; Harrison et al., 1999; Baldwin et al., 2006, 2008).
- The regional northeast strike of the faulting is favorably oriented for right-lateral transpressive slip in the present north-northeast-directed maximum horizontal stress field (Zoback, 1992).

- Focal mechanism analysis of a **M** 3.85 (E[**M**] 3.83) earthquake (February 5, 1994) along the northward-projected trend of the Commerce fault zone shows motion was primarily right-lateral strike-slip along a north-northeast azimuth (Herrmann and Ammon, 1997).

Ruptures within the Commerce Fault Zone RLME source are modeled as striking N47°E, subparallel to the Commerce and Penitentiary faults within the zone. The northwest and southeast boundaries are fixed based on the width of the CGL as defined from geophysical data and mapped faults. The northeast and southwest boundaries of the zone are considered leaky boundaries to allow for ruptures to extend along the trend of the CGL into adjacent less well studied areas where there is not a sufficient paleoseismic record to demonstrate or preclude recent activity along a similar rheological boundary.

6.1.8.3 RLME Magnitude

The Commerce Fault Zone RLME source extends for a distance of approximately 120 km (75 mi.). There are only limited paleoseismic data from which to identify the length of fault ruptures or the size of individual displacements for prehistoric earthquakes on this fault zone. Information on timing of earthquakes shown on Figure 6.1.8-4, which is discussed below in Section 6.1.8.4, allows for the possibility of a rupture involving the entire fault source (120 km [75 mi.]) in a single earthquake or possibly two or more smaller earthquakes. A late Pleistocene earthquake may have ruptured the southern half (55–63 km [34–39 mi.]). Baldwin et al. (2006) cite evidence for 2.0–2.2 m (6.6–7.2 ft.) of separation of a late Pleistocene–early Holocene colluvium/paleosol in trenches across the Idalia Hill fault zone; this separation may represent tectonic slip (possibly combined vertical and horizontal slip) during the most recent surface faulting earthquake at that site.

Ruptures of 55–65 km (37–40 mi.) or 120 km (75 mi.)—the southern half or entire length, respectively—assuming a seismogenic depth ranging from 13–17 km (8–10.5 mi.), yield magnitude estimates ranging from **M** 6.9–**M** 7.5 (Wells and Coppersmith, 1994) for a magnitude-area and magnitude-length relationships to **M** 7.2–**M** 7.7 (Somerville et al., 2001) for magnitude-area relationship, median. A displacement of 2.0–2.2 m (6.6–7.2 ft.) would suggest magnitudes of **M** 7.0–7.1 and **M** 7.2–7.3 based on empirical relationships for magnitude from maximum or average displacement, respectively (Wells and Coppersmith, 1994; Table 6.1.8-1). Smaller ruptures, however, cannot be precluded, based on the available data.

Given the uncertainty in the dimensions of paleo-ruptures, and the broad range of uncertainty considered even for 1811-1812 earthquakes, of which the NMN (NM2 earthquake) may be an analog for the Commerce source (see Table 6.1.5-2), the distribution tabulated below that captures a wide range in RLME magnitude estimates is used.

Expected Commerce Fault Zone RLME Magnitude (M)	Weight
6.7	0.15
6.9	0.2
7.1	0.2
7.3	0.2
7.5	0.2
7.7	0.05

6.1.8.4 RLME Recurrence

The remaining branches of the logic tree describe the assessment of RLME recurrence rates.

Recurrence Method

The data available for assessing the recurrence rate of the Commerce Fault Zone RLME provides assessments of the timing of past earthquakes. Thus the "Earthquake Recurrence Intervals" approach is used with weight 1.0 (Figure 6.1.8-1).

Recurrence Data

The ages of earthquakes interpreted from stratigraphic and structural relations observed in trenches and from paleoliquefaction earthquakes at sites along the Commerce section of the CGL are shown on Figure 6.1.8-4. The colored bars show possible rupture scenarios (i.e., ruptures that are permitted by the timing of earthquakes documented at the four paleoseismic localities). The paleoseismic investigation localities are ordered from south to north.

Paleoliquefaction studies in the Western Lowlands along the southern part of the Commerce section of the CGL provide evidence for at least four poorly constrained prehistoric earthquakes, which are related to the NMSZ and/or structures associated with the CGL (Vaughn, 1994; Tuttle, Lafferty, and Schweig, 1998; Tuttle, Chester, et al., 1999) (Figure 6.1.8-2). Vaughn (1994) estimates the timing of four prehistoric earthquakes that, from oldest to youngest, occurred at about (1) 23,000–17,000 yr BP; (2) 13,400–9,000 yr BP, (3) AD 240–1020; and (4) AD 1440–1540. In the CEUS SSC paleoliquefaction database, these are assigned the following ages: 22,750 yr BP ± 650 yr; 12,600 yr BP ± 200 yr; 1,050 yr BP ± 150 yr; and 500 yr BP ± 150 yr. The two most recent earthquakes of Vaughn (1994) likely are related to paleoearthquakes associated with seismic sources within the NMSZ (Tuttle, Schweig, et al., 2002). Baldwin et al. (2006) note that the two earlier paleoliquefaction earthquakes may correlate to earthquakes on nearby CGL structures, based on the earthquake's apparent older age and greater size. The timing of these earthquakes is compatible with the timing of poorly constrained earthquakes

interpreted at the South Holly Ridge site on the Idalia fault, approximately 30 km (19 mi.) to the northeast.

At the South Holly Ridge site, analysis of trench, borehole, and ground-penetrating radar data constrains the timing of the most recent earthquake on the Idalia fault to between the latest Pleistocene —about18 ka—and early Holocene (pre-7.7 ka). Evidence for a penultimate earthquake predates 23–18 ka (Baldwin et al., 2006).

Evidence of Quaternary and probable Holocene deformation involving near-surface faults in the Benton Hills and Thebes Gap areas has been documented by Harrison and Schultz (1994); Harrison et al. (1999); Palmer, Hoffman, et al. (1997); Palmer, Shoemaker, et al. (1997); Stephenson et al. (1999); and Odum et al. (2002) (see Data Summary table D-6.1.5; Figure 6.1.8-2). Harrison et al. (1999) document evidence for four episodes of Quaternary faulting: one in late- to post-Sangamon, pre- to early Roxana time (between 60 and 50 ka); one in syn- or post-Roxana, pre-Peoria time (between 35 and 25 ka); and two to possibly three in post-Peoria time (<17 ka). At least two earthquakes may have occurred in the latest Holocene (just after 2-sigma calibrated calendar ages of 3747–3369 BC and AD 639–968) (Harrison et al., 2002). The youngest in the Benton Hills may represent secondary tectonic deformation correlative with a NMSZ earthquake (Harrison et al., 1999).

The timing of recent earthquakes on the Penitentiary fault are not well constrained at this time; preliminary analysis of data from paleoseismic investigations indicates latest Pleistocene and possible early Holocene faulting (Givler and Baldwin, 2009).

The possibility that most or the entire Commerce Fault Zone RLME source ruptured during an earthquake approximately 23,000 yr BP is permitted, but not required by the available data. The syn- or post-Roxana period of deformation observed on structures in the English Hills broadly overlaps with earthquakes recorded at the South Holly Ridge site on the Idalia Hill fault (Baldwin et al., 2006), with paleoliquefaction in the Western Lowlands near Qulin (Vaughn, 1994), and possibly with poorly constrained earthquakes on the Penitentiary fault (Baldwin et al., 2008). The available data also suggest the possibility of an earthquake involving only the southern part of the fault; the latest Pleistocene earthquake observed at the South Holly Ridge site (18,500–7,600 yr BP) broadly overlaps with the paleoliquefaction in the Western Lowlands (Vaughn, 1994).

The middle to late Holocene deformation earthquakes observed in the English Hills, however, are not evident on the easternmost fault strands of the Idalia Hill fault at the South Holly Ridge site, approximately 30 km (19 mi.) to the south or at the Penitentiary site about 19 km (12 mi.) to the north (Baldwin et al., 2006, 2008). Thus it is not clear that the middle to late Holocene earthquakes recorded on faults within the English Hills and by paleoliquefaction in the Western Lowlands near Qulin are related to large-magnitude earthquakes on faults within the Commerce Fault Zone RLME source. The preferred interpretation (weight 0.75) is that two earthquakes have occurred in the past 23 kyr with the possibility (weight 0.25) that the count is three earthquakes.

Earthquake Recurrence Model

As discussed in Section 5.3.3, the Poisson model is used as the default earthquake recurrence model with weight 1.0 for the Commerce Fault Zone RLME source as there are not sufficient data to justify including an alternative model.

RLME Annual Frequency

The final node of the logic tree addresses the uncertainty distributions for the annual frequency of RLMEs (Figure 6.1.8-1). These distributions were developed using the methodology described in Section 5.3.3.1. The relative likelihood of various values of the recurrence rate parameter was developed using Equation 5.3.3-4 and the observations of one or two closed recurrence intervals and one open interval. The value of $\sum_{i=1}^{N} t_i + t_0$ was assumed to be uniformly distributed between 18.9 and 23.6 kyr with N equal to either 1 or 2. The resulting relative-likelihood-based distributions were represented by the five-point discrete distribution listed in Table 6.1.8-2.

6.1.9 Wabash Valley

Mapping and dating of liquefaction features throughout most of the southern Illinois basin and in parts of Indiana, Illinois, and Missouri have identified energy centers for at least eight Holocene and latest Pleistocene earthquakes having estimated moment magnitudes of **M** 6 to ~7.8 (Obermeier et al., 1991; Munson et al., 1997; Pond and Martin, 1997; Obermeier, 1998; McNulty and Obermeier, 1999; Tuttle, Chester, et al., 1999) (Table 6.1.9-1). The proximity of the energy centers for the two largest earthquakes inferred from the paleoliquefaction data (referred to as the Vincennes and Skelton paleoearthquakes), both of which are located within 25–40 km (15.5–25 mi.) of Vincennes, Indiana, suggests that there is a source of RLMEs (~**M** = 6.7–7.8) in the Wabash Valley region. These two paleoearthquakes are located in the general vicinity of the most numerous and strongest historical earthquakes (**M** 4–5.5) in the lower Wabash Valley of Indiana and Illinois (Obermeier, 1998). A logic tree outlining the characterization of the Wabash Valley RLME source for this study is presented on Figure 6.1.9-1. Other prehistoric earthquakes identified from paleoliquefaction studies in southern Illinois and southern Indiana are considered in the characterization of the Illinois basin-extended basement seismotectonic zone (Section 7.3.5) and the modification of the Mmax priors.

The locations of tectonic features and the key localities in the Wabash Valley region of southern Illinois and southern Indiana where studies have been conducted to evaluate evidence for tectonic surface deformation, the location and activity of faults, and extent of paleoliquefaction features are shown on Figure 6.1.9-2 and are discussed below. Figure 6.1.9-3 shows the Wabash RLME source relative to total magnetic anomaly and residual isostatic gravity data. Additional information used to identify and characterize the Wabash Valley RLME source is summarized in Appendix Tables C-6.1.9 and D-6.1.9).

6.1.9.1 Evidence for Temporal Clustering

The first node of the logic tree for the Wabash Valley RLME source considers the issue of temporal clustering of earthquakes in the present tectonic stress regime (Figure 6.1.9-1). The paleoliquefaction evidence used to identify the Wabash Valley RLME source, which is discussed in Section 6.1.9.4, includes two earthquakes in the latest Pleistocene to Holocene. The record is not sufficient to recognize periods of temporal clustering (i.e., faster or slower rates of activity). Therefore, this branch of the tree is not applicable to the Wabash Valley RLME source.

6.1.9.2 Geometry and Style of Faulting

The geometry of the Wabash Valley RLME source zone is based on consideration of a variety of structural, geologic, geomorphic, and paleoseismologic observations and hypotheses as outlined below.

- A broad flexure (bend or stepover) in bedrock structure has been postulated to concentrate stress in this region (Hildenbrand and Ravat, 1997). This bend or stepover lies near the northern terminus of an approximately 600 km (375 mi.) long magnetic and gravity lineament, referred to as the Commerce geophysical lineament (CGL), which extends from Vincennes, Indiana, far into Arkansas. Late Quaternary faulting recently has been identified near this lineament, close to the Missouri-Illinois border (Langenheim and Hildenbrand, 1997) (see discussion of the Commerce Fault Zone RLME source, Section 6.1.8). Wheeler and Cramer (2002) discuss the concept of a left stepover functioning as a restraining bend if the CGL is acting as a right-lateral strike-slip fault in the current tectonic environment.
- McBride and Kolata (1999) note a possible relationship between the most deformed region of the Precambrian basement yet to be identified beneath the Illinois basin (the Enterprise subsequence) and some of the largest twentieth-century earthquakes in the central Midcontinent. This region roughly coincides with the area of the broad flexure in the CGL.
- Morphometric analysis of the land surface, detailed geologic mapping, and structural analysis of bedrock in the Wabash Valley generally indicate westward tilting of the modern land surface, preferred channel migration to the west side of the valley (see inset on Figure 6.1.9-2), a convex longitudinal profile of the Wabash River where it crosses the La Salle anticlinal belt, and increased river incision into the floodplain downstream of the anticlinal belt. These geomorphic anomalies occur along the western edge of the CGL in the restraining bend region (Fraser et al., 1997).
- Evaluation of recently acquired industry seismic-reflection profile data from southern Illinois provides additional insights as to the causative structures for recent earthquakes. McBride et al. (1997) and McBride, Hildenbrand, et al. (2002) report a northeast-trending zone of dipping reflectors and diffractions that they interpret as a zone of intrusions or a zone of deformation, or both. McBride, Kolata, et al. (2002) suggest that the zone, which lies along the CGL, may represent thrust faults deep within crystalline basement, faults that may be subject to reactivation. The largest instrumentally recorded earthquake in the Illinois basin, which occurred on November 9, 1968, had a moment magnitude of **M** 5.4 (Johnston, 1996a) or m_{bLg} 5.5 (McBride, Hildenbrand, et al., 2002) (E[**M**] 5.32). Its focal mechanism has a nodal plane that is subparallel to the zone of dipping reflections, a midcrustal hypocenter that

is located within the zone, and a seismic moment that corresponds to a rupture zone approximately the same size as one of the reflectors. McBride et al. (1997) and McBride, Hildenbrand, et al., (2002) note that earthquakes may be nucleating along compressional structures in crystalline basement and thus may occur in parts of the basin where there are no obvious surface faults or folds. They conclude that shallow Paleozoic structures are "decoupled" from deeper, possibly seismogenic, structures. The results of their study suggest that a seismogenic source just north of the New Madrid seismic zone in the Wabash Valley area consists, in part, of thrusts in the basement localized along igneous intrusions that are locally coincident with the CGL.

- McBride et al. (2007) further evaluate major structures within the Illinois basin, including the Wabash Valley fault system (WVFS) and the La Salle anticlinal belt (LSA). Based on results of reprocessing seismic reflection profiles, combined with earthquake hypocenter parameters, three distinct seismotectonic environments are defined in the upper crust in the southern portion of the Illinois basin. First, a fault pattern that appears to correspond to the steep nodal plane of a strike-slip mechanism earthquake (April 3, 1974, m_b4.7, E[**M**] 4.29) is interpreted to be a deeply buried rift zone or zone of intense normal faulting underpinning a major Paleozoic depocenter of the Illinois basin (Fairfield basin). Second, a similar earthquake (June 10, 1987, m_b 5.2, E[**M**] 4.95) and its well-located aftershocks define a narrow zone of deformation that occurs along and parallel to the frontal thrust of the LSA. Third, the hypocenter of the largest earthquake in the study area (November 9, 1968, m_b 5.5, E[**M**] 5.32) as outlined above may be spatially associated with a prominent zone of dipping middle crustal reflections, just west of the WVFS, which have been interpreted as a deeply buried blind thrust.

- Holocene activity is evidenced on faults within the WVFS. The WVFS is a linear northeast-southwest band of narrow graben structures that lie within the southern part of the Illinois basin (Bristol and Treworgy, 1979; Treworgy, 1981; Sexton et al., 1986; Kolata and Nelson, 1991; Rene and Stanonis, 1995; Bear et al., 1997; Hildenbrand and Ravat, 1997; Woolery, 2005). The WVFS consists of a series of high-angle normal faults and strike-slip faults with trends between N15°E and N50°E. These faults lie within and form the borders of the northeast-trending Grayville graben. The Grayville graben (~20 km [~12.5 mi.] wide, ~0.7 km [~0.4 mi.] maximum basement relief, and <40 km [25 mi.] long) underlying the Wabash Valley developed during late Precambrian-Cambrian (Iapetan) rifting, perhaps in response to stress concentrations generated by a bend in the Reelfoot–Rough Creek–Rome rift system (Hildenbrand and Ravat, 1997). Although some workers (e.g., Sexton et al., 1986) have suggested that the WVFS may be a northward extension of the Reelfoot rift, others have noted that both the dike pattern and mapped WVFS terminate near the Reelfoot–Rough Creek–Rome rift system (Hildenbrand and Ravat, 1997) and that fault displacements of the WVFS decrease southward in the direction of the NMSZ (Bear et al., 1997). The WVFS offsets the Pennsylvanian and older units with vertical offsets of as much as 145 m (480 ft.) along the faults (Nelson, 1995; Bristol and Treworgy, 1979). Woolery (2005) describes high-angle deformation associated with one of the faults in the WVFS, the Hovey Lake fault, extending above the Paleozoic bedrock and into upper Quaternary sediment. Time-displacement calculations from the data show approximately 10.5 m (34.4 ft.) of offset on the top-of-bedrock horizon, located 7.7 m (25.3 ft.) below ground surface, suggesting fault movement at this site as late as ~37 ka. More recent Holocene deformation is evidenced by

folding and faulting of sediments across the Uniontown scarp, a prominent scarp on the floodplain of the Ohio River that is interpreted to be associated with the Hovey Lake fault (Counts et al., 2009a, 2009b; Van Arsdale et al., 2009).

- Analysis of the June 18, 2002, M_w 4.6 (E[**M**] 4.38) earthquake, which occurred on a steeply dipping fault within the WVFS at a depth of about 18 km (11 mi.), may suggest that buried faults associated with a possible Precambrian rift system are being reactivated by the contemporary east/east-northeast-trending regional horizontal compressive stress (Kim, 2003). The source mechanism determined from regional waveform analysis is predominantly strike-slip along near-vertical nodal planes (dips 82 and 84 degrees), striking 28 and 297 degrees. The close proximity of the epicenter to the trace of the Caborn fault (WVFS) and good agreement between the strike and dip of that fault and source mechanism for the June 2002 earthquake suggest that the earthquake occurred on that fault.
- Analysis of geodetic data in the southern Illinois basin suggests systematic northwestward motion of about 0.5–0.7 mm/yr (0.02–0.03 in.) with respect to the Stable North American Reference Frame. Block models, which assume boundaries along the Cottonwood Grove fault system–Rough Creek graben and the WVFS, indicate marginal block velocities with possible strike-slip motion along the WVFS, and east-west motions along the CGRCG (Hamburger et al., 2008).

The causative structures for the paleoearthquakes are not known. The Wabash Valley RLME source zone encompasses the structural features, postulated neotectonic deformation, and locations of the inferred energy centers for the Vincennes and Skelton earthquakes described above (Figure 6.1.9-2). Characteristics for future earthquake ruptures in the WV RLME source zone are given in Table 5.4-2.

Given the uncertainty in the location of the causative faults, the boundaries of the Wabash Valley RLME source zone are modeled as leaky.

Two alternative depths are used to estimate the seismogenic thickness of the crust in the Wabash Valley RLME source zone: 17 km (10.6 mi.; weight of 0.7) and 22 km (13.7 mi.; weight of 0.3). Higher weight is assigned to the shallower depth based on the evidence for reactivations of structures in the upper 15–17 km (9.3–10.6 mi.) of crust as inferred from recent seismicity (McBride et al., 2007). This depth is more likely to represent the average depth of seismogenic crust throughout the RLME source zone. The greater seismogenic thickness is consistent with the focal depth of the 1968 earthquake, which is postulated to have ruptured a reverse fault in the basement in the Fairfield basin, a localized basin within the southern Illinois basin.

Earthquakes in the in the Wabash Valley RLME source zone are modeled as a mixture of vertical strike-slip and reverse (with a random dip in the range of 40–60 degrees) based on the focal mechanisms for recent earthquakes (Figure 6.1.9-2). Due to the wide range in style, orientation, and focal depth of recent earthquakes and variability of structural trends within the zone, the aleatory variability in future earthquakes within the Wabash Valley RLME source is expected to be as follows:

strike—parallel to the long axis of the zone [0.8]
2/3 strike-slip, 90 degrees
1/3 reverse, uniform 40–60 degrees to the west
N50°W [0.1] strike-slip, 90 degrees
N20°W [0.1] reverse, uniform 40–60 degrees to the west

6.1.9.3 RLME Magnitude

The magnitude assessments for the Wabash Valley RLME source are based on recent analysis of paleoliquefaction features associated with the Vincennes and Skelton energy centers in the vicinity of the lower Wabash Valley of southern Illinois and Indiana. The magnitude of the largest paleoearthquake in the lower Wabash Valley (the Vincennes-Bridgeport earthquake), which occurred 6,011 ± 200 yr BP, was estimated to be ≥ **M** 7.5 using the magnitude-bound method (Obermeier, 1998). Use of a more recently developed magnitude-bound curve for the CEUS based on a value of **M** ~ 7.6–7.7 for the largest of the 1811-1812 New Madrid earthquakes (reduced from the higher **M** 8 used in the older curve) gives a lower estimate of **M** 7.1–7.3 depending on the minimum (115 km [71.5 mi.]) and maximum (153 km [95 mi.]) distance, respectively, of distal paleoliquefaction features related to this paleoearthquake (Olson et al., 2005b). The lower-bound relationship developed by Castilla and Audemard (2007) from a worldwide database gives a range of **M** 7.0–7.3 for the same minimum and maximum distance values.

Estimates based on a suite of geotechnical analyses (cyclic stress and energy stress methods) range from **M** 7.5 to 7.8 (summarized in Obermeier et al., 1993). The highest value of **M** 7.8 is based on geotechnical studies using the energy-acceleration method (a possibly flawed energy method, see Table 6.1.9-1) (Pond and Martin, 1997). A reanalysis of this earthquake has been done by Green et al. (2004a, 2004b; Green et al., 2005) using more recent ground-motion attenuation relationships for the central United States, review of approximately 50 boring logs presented by Pond and Martin (1996) to select appropriate standard penetration test values for the reanalysis, and the most recent magnitude scaling factors suggested by Youd et al. (2001). Using the cyclic stress method, the best estimate of the magnitude for the Vincennes-Bridgeport earthquake based on all these solutions ranges from **M** 7+ to 7.5. The energy-based solution developed by Green (2001) that circumvents the use of the magnitude scaling factor, which is a significant, questionable factor in the use of the cyclic stress method in the central United States, gives a value of **M** ~ 7.5 for each of the four newer ground-motion attenuation relationships (Green et al., 2004b). The more recent evaluations by Green et al. (2005) have considered the influence of aging effects on liquefaction susceptibility and concluded that for moderately susceptible sites like those in southern Illinois, the small changes expected given the types of sediments would have little influence on the interpretation of paleomagnitude (Obermeier et al., 2001; Obermeier, pers. comm., August 2003).

The next largest earthquake, the Skelton paleoearthquake, occurred 12,000 ± 1,000 yr BP (Hajic et al., 1995; Munson et al., 1997; Obermeier, 1998). The magnitude of this earthquake is estimated to be **M** 7.1–7.3 by Munson et al. (1997; using a magnitude-bound approach) or **M** 7.3 by Pond and Martin (1997; using a possibly flawed energy-stress method; see Table 6.1.9-1). Olson et al. (2005b) gives an estimate of **M** 6.7 for this paleoearthquake, and the lower-bound relationship of Castilla and Audemard (2007) would yield a value of **M** 6.3. The estimated values of the size of the epicentral area of this paleoearthquake are clearly minimums, as deposits of an age that would preserve a record of this earthquake are not widespread.

The difference in the estimated sizes of the Vincennes and Skelton paleoearthquakes is on the order of 0.5 to 1 magnitude units. This probably represents a combination of the aleatory variability in the size of individual Wabash RLMEs and epistemic uncertainties in the approaches and data used to estimate the magnitudes of the prehistoric earthquakes. Therefore, a broad probability distribution is used to capture the range in uncertainty in the magnitude of earthquakes in the Wabash Valley RLME. This distribution is tabulated below.

Expected Wabash Valley RLME Magnitude (M)	Weight
6.75	0.05
7.0	0.25
7.25	0.35
7.5	0.35

6.1.9.4 RLME Recurrence

The remaining branches of the logic tree describe the assessment of RLME recurrence rates.

Recurrence Method

The data available for assessing the recurrence rate of the Wabash Valley RLMEs provide assessments of the timing of past earthquakes. Thus the "Earthquake Recurrence Intervals" approach is used with weight 1.0 (Figure 6.1.9-1).

Recurrence Data

The available data for characterizing the recurrence rate of Wabash Valley RLMEs are the estimated ages for the Vincennes-Bridgeport and Skelton paleoearthquakes described above.

Earthquake Recurrence Model

As discussed in Section 5.3.3, the Poisson model is used as the default earthquake recurrence model with weight 1.0 for the Wabash Valley RLME source as there are not sufficient data to justify including an alternative model.

RLME Annual Frequency

The final node of the logic tree addresses the uncertainty distributions for the annual frequency of RLMEs. These distributions were developed using the methodology described in Section 5.3.3.1. The relative likelihood of various values of the recurrence rate parameter was developed using Equation 5.3.3-4 and the observations of one closed recurrence interval between the Vincennes-Bridgeport and Skelton paleoearthquakes and one open interval post the Vincennes-Bridgeport paleoearthquake. The value of $\sum_{i=1}^{N} t_i + t_0$ was assumed to be uniformly distributed between 11 and 13 kyr with N equal to 1. The resulting relative-likelihood-based distributions were represented by the five-point discrete distribution listed in Table 6.1.9-2.

6.2 Mmax Distributed Seismicity Source Zones

In the Mmax zones branch of the master logic tree, the two components of the SSC model are the RLME sources and the Mmax distributed seismicity sources or, simply, Mmax zones. As discussed in the criteria for identifying seismic sources (Section 4.1.3.3), after earthquake recurrence rate, the most important criterion for identifying a seismic source is potential differences in Mmax. The Mmax zones branch considers only this parameter in defining alternative zonation models.

6.2.1 Definition of Mmax Zones

The Bayesian approach to estimating Mmax, described in Section 5.2.1.1, uses a prior distribution that is defined based on a statistical analysis of the global SCR database. The statistical analyses carried out for the CEUS SSC Project indicate only a marginally significant difference in prior distributions between Mesozoic-and-younger extended crust (MESE) and non-Mesozoic-and-younger crust (NMESE). For example, the *p*-value associated with the separation of these two data sets is 0.14 (see Section 5.2), which indicates that there is a 14 percent chance that the two data sets were derived from the same population, such that they would be expected to have the same mean value. To account for the uncertainty in whether the SCR database can be separated with confidence into two prior distributions, two alternatives are considered in the Mmax zones model: (1) two Mmax zones that are defined by two prior distributions (MESE and NMESE), and (2) a single Mmax zone that represents a single prior distribution. The first model is assigned slightly higher weight (0.6) than the single zone model (0.4). Preference is given to the first model because there is marginal statistical significance for the separation of the SCR database into the two parts, but there is also a reasonable likelihood that there is no reliable separation of the SCR database with confidence.

Alternative configurations for the two Mmax zones are shown on Figures 6.2-1 and 6.2-2. The separation reflects the assessment of those parts of the study region that show evidence of Mesozoic-and-younger extension (MESE) and those parts that do not (NMESE). Criteria used to make this assessment are described in Section 6.2.2. The uncertainty in that assessment is represented by the two alternatives: (1) the "narrow" MESE that is distinguished by clear major Mesozoic-and-younger extensional features, and (2) the "wide" MESE whose western boundary is drawn to include more questionable evidence for such features. Because of the more technically defensible evidence for the narrow interpretation, it is assigned a weight of 0.8, and the wide interpretation is assigned a weight of 0.2.

6.2.2 Criteria for Defining the MESE/NMESE Boundary

The breakup of the supercontinent of Pangaea into Laurasia to the north and Gondwana to the south resulted in Mesozoic extension of the crust and consequent development of the Atlantic Ocean (Triassic), the passive Atlantic margin (Jurassic), and the Gulf of Mexico (from Triassic to Jurassic). As a result of this extension, both the Atlantic and Gulf Coast margins generally consist of three crustal domains. For the Atlantic margin, the domains comprise rifted continental crust of Appalachian origin lying principally beneath the Coastal Plain and continental shelf, oceanic crust underlying the continental rise, and the intervening 50–100 km (30–60 mi.) wide zone of transitional, or rift-stage, crust (Klitgord et al., 1988; Holbrook, Reiter, et al., 1994). Crustal domains in the Gulf of Mexico region consist of thick transitional crust, thin transitional crust, and newly formed oceanic crust (Buffler and Sawyer, 1985; Marton and Buffler, 1994; Salvador, 1991a, 1991b; Sawyer et al., 1991). Mesozoic extension associated with opening of the Atlantic Ocean and Gulf of Mexico also resulted in extensional reactivation of Paleozoic structures within the St. Lawrence rift, Reelfoot rift, and Northern Appalachians (Tremblay et al., 2003; Lemieux et al., 2003; Wheeler, 1997; Faure et al., 2006). Lesser amounts of Mesozoic extension may have occurred within the Rough Creek and Grayville grabens (Wheeler, 1997; Wheeler and Cramer, 2002). The extent of possible Mesozoic reactivation of older Iapetan rift structures inferred to be present in basement rock beneath the Appalachian detachment or older basement structures cratonward of the well-defined Mesozoic rifts is not well constrained.

Cretaceous-and-younger extension also occurred in response to thermal processes and related uplift in the northeastern United States and eastern Canada as portions of the North American Plate rode over Cretaceous hotspots (McHone, 1996; Cox and Van Arsdale, 1997, 2002; Morgan, 1983; Crough, 1981; Sleep, 1990).

The cratonward limit of significant Mesozoic-and-younger extension is inferred from a variety of geologic, geophysical, and seismologic data. Criteria used to define this boundary are listed below, ordered from most diagnostic to least definitive for identifying Mesozoic-and-younger extension.

1. Grabens and sedimentary rift basins of Mesozoic age.
2. Mesozoic-and-younger plutons.
3. Extensive distributed brittle normal faults and basaltic (thoeliitic) dikes of Mesozoic-and-younger age.

4. Evidence for Mesozoic-and-younger regional uplift and unroofing with associated normal faulting or fault reactivation.
5. Localized extensional reactivation of pre-Mesozoic structures.
6. Favorably oriented older extensional faults (e.g., Iapetan rift faults proximal to regions of Mesozoic rifting).

Regions that generally meet the first three to four criteria are included in the MESE-narrow (MESE-N) zone. This zone includes the ECC-AM, ECC-GC, AHEX, GHEX, RR, SLR, NAP, GMH, and PEZ-N seismotectonic zones described in Section 7.0 (Table 6.2-1). A description of the geologic observations and data that demonstrate Mesozoic-and-younger extension in these zones, and the basis for the definition of the cratonward limit (boundary) of the respective units used to define the MESE-N boundary are provided in Section 7.0.

The MESE-wide (MESE-W) boundary encompasses regions that have less definitive evidence for significant Mesozoic-and-younger extension. These regions include areas that have known or possible Iapetan-rift faults that may have been reactivated during the Mesozoic (e.g., the Rough Creek and Grayville grabens, Rome Trough-Kentucky River fault system) and older Precambrian compressional structures, such as the Clarendon-Linden fault and Central Metasedimentary Belt boundary structure in western New York and Ontario, Canada, that have evidence of extensional reactivation during latest Precambrian/early Paleozoic Iapetan rifting, but have less definitive evidence for Mesozoic reactivation. The MESE-W zone differs from the MESE-N in that it adopts the wide alternative geometries for the Paleozoic Extended Zone (PEZ-W); Reelfoot rift (with Rough Creek graben, RR-RCG); and the Illinois Basin Extended Basement (IBEB) zone (Table 6.2-1). Due to the limited Mesozoic deformation or lack of clear evidence of significant Mesozoic extension in these regions, low weight (0.2) is assigned to this alternative boundary. The boundaries of these zones are discussed in the descriptions of these seismotectonic source zones in Section 7.0.

6.3 Maximum Magnitude Distributions for Mmax Distributed Seismicity Sources

This section presents the Mmax distributions for the Mmax distributed seismicity sources. The methodology used to develop these distributions is presented in Section 5.2.1. The steps involved are identification of the maximum observed earthquake in each distributed seismicity source (described in Section 6.3.1) and then application of the quantitative approaches developed in Section 5.2.1 to produce the composite Mmax distributions (described in Section 6.3.2).

6.3.1 Maximum Observed Earthquake Magnitude

The maximum observed earthquake magnitude, $m_{\max-obs}$, represents the size of the largest non-RLME observed to have occurred within each source. The value of this magnitude is used in developing the likelihood function for the Bayesian Mmax approach (Section 5.2.1.1) and is a parameter of the Kijko approach (Section 5.2.1.2). Two sources are used to assess $m_{\max-obs}$. One is the CEUS SSC earthquake catalog developed for this study (Section 3); the other is the

compilation of identified paleoearthquakes that are not associated with RLME sources. The latter consists of the four non-RLMEs that have been identified in southern Illinois/southern Indiana. These earthquakes are discussed in Section 7.3.5. These earthquakes have estimated magnitudes of **M** 6.2–6.3 and represent the largest non-RLMEs in the study region.

The largest historical non-RLMEs identified in the project catalog are listed below by Mmax zone.

Mmax Distributed Source	Largest Historical Earthquake	
	Date	E[M]
Study Region	September 16, 1732	6.25
MESE-N	September 16, 1732	6.25
MESE-W	September 16, 1732	6.25
NMESE-N	May 31, 1897	5.91
NMESE-W	May 16, 1909	5.72

The 1732 earthquake occurred in the St. Lawrence region; the 1897 earthquake occurred in Giles County, Virginia; and the 1909 earthquake occurred at the border of North Dakota, Montana, and Canada.

Uncertainty in $m_{\max-obs}$ was incorporated into the Mmax assessment using the procedure described in Section 5.2.1.1.6. The uncertainties in the magnitudes for the catalog of historical earthquakes or paleoearthquakes for each source were used to develop simulated catalogs of earthquake magnitudes. The largest values for each simulation were then used to develop a distribution for $m_{\max-obs}$. Figure 6.3.1-1 shows the resulting distributions for $m_{\max-obs}$. The blue curve on each plot shows the distribution developed for $m_{\max-obs}$, and the red vertical line indicates the nominal observed magnitude. The phrase "paleo" in the plot legend indicates that the set of paleoearthquakes is the controlling set for determining $m_{\max-obs}$ and was the set used to develop the Mmax distributions. The 1882 E[**M**] 5.58 earthquake, which is discussed in Section 7.3, occurred very near the boundary between the ECC-GC and OKA seismotectonic zones, and the uncertainty in its location is addressed by including alternative locations. To be consistent with the assessments for the seismotectonic zones, the 1882 earthquake is considered to have occurred in either the MESE zones or the NMESE zones. However, because this earthquake is not the largest historical earthquake in either zone, the alternative locations have only a small effect on the distributions for $m_{\max-obs}$.

6.3.2 Mmax Distributions

Mmax distributions were developed for each Mmax distributed seismicity source using the Bayesian and Kijko methods. For the Bayesian Mmax approach, the alternative priors described

in Section 5.2.1.1 were used. For the study region, only the composite prior is used, as the single source zone model is based on no difference between Mesozoic extended and non-extended crust. The remaining Mmax zones are assigned the composite prior with weight 0.4, and either the MESE or NMESE prior with weight 0.6. Figures 6.3.2-1 through 6.3.2-5 show the resulting Mmax distributions obtained by each method. Indicated in the legend of each figure are the weights assigned to the individual Mmax methods following the weighting approach described in Section 5.2.1.1. The final weighted composite distributions are indicated by the thick red bars on each plot.

The Mmax distributions for the study region and the MESE-W and NMESE-N Mmax zones utilize the paleoearthquake record to define the distribution for $m_{\max-obs}$. Because the number of paleoearthquakes is small, the Kijko method is assigned zero weight in these cases. The Kijko method is given appreciable weight (0.23) only for the NMESE-W Mmax zone.

The continuous distributions shown on Figures 6.3.2-1 through 6.3.2-5 were used to construct five-point discrete approximations for use in hazard analyses. These distributions are listed in Table 6.3.2-1. The differences in the distributions for NMESE-N and NMESE-W reflect the presence or absence of the Wabash Valley paleoearthquakes within the boundary of the source zone.

6.4 Recurrence Parameters

The recurrence parameters (i.e., rate and *b*-values) for the Mmax zones were calculated using the methodology and parameters described in Section 5.3.2. Briefly, this methodology divides the source zone into cells of dimensions a quarter or half degree and then calculates the rate and *b*-value in each cell using the likelihood function of the data in that cell, together with penalty functions that tend to smooth the cell-to-cell variation in the rate or the *b*-value. In addition, this procedure characterizes epistemic uncertainty in the recurrence parameters by generating eight alternative maps of the recurrence parameters.

6.4.1 Rate and b-Value Maps for Single Zone and Two Zones

Figures 6.4.1-1 through 6.4.1-9 show the mean recurrence maps for the three alternative configurations of the Mmax zones distributed seismicity source zones and the three choices of magnitude weights (i.e., Cases A, B, and E). Maps of the calculated uncertainties in recurrence parameters, as well as alternative recurrence maps that represent that uncertainty (eight alternative maps for each source-zone configuration), are shown in Appendix J.

The maps in this section show more pixelation than the maps in Section 7. This is because the cell size had to be increased to half a degree to overcome computer run-time limitations.

6.4.2 Comparison of Recurrence Parameters to Catalog

Figures 6.4.2-1 through 6.4.2-15 compare the expected counts from the recurrence maps for each source zone to the observed earthquake counts within the zone. The error bars on the data represent the 16–84 percent range of statistical uncertainty in the counts and are calculated using the approach by Weichert (1980). Each of the eight curves represents expected counts (i.e., rate times equivalent period of completeness) for one of the eight equally weighted alternative maps, taking Mmax into account.

These comparisons indicate a good agreement between predicted and observed rates. The only exception is the MESE-N source zone, for which the recurrence model has a slight tendency to underestimate the rates for magnitude 5.7 and higher. This is the result of deviations of the data from the exponential magnitude distribution. The actual discrepancy is smaller than it appears in the figures. If one were to consider the effect of uncertainty in Mmax on the recurrence curves, the curves would spread out at these higher magnitudes, with some of the curves coming closer to the data.

Table 6.1-1
Summary of Data Used to Assess RLME Recurrence Frequencies

RLME Source	Recurrence Method	Recurrence Data
Charlevoix	Earthquake recurrence intervals Equation 5.3.3-4	Data Set 1 $N = 1, \sum_{i=1}^{N} t_i + t_0$ = 348 yr
	Earthquake count in a time interval Equation 5.3.3-2	Data Set 2 $N = 3$, T uniformly distributed between 6 and 7 kyr Data Set 3 $N = 4$, T uniformly distributed between 9.5 and10.2 kyr
Charleston	Earthquake recurrence intervals Equation 5.3.3-4 for Poisson case Equation 5.3.3-9 for renewal model case	Earthquake data defining intervals 1886 Earthquake Earthquake A: 95% interval on Con age 523 to 618 yr BP 95% interval on All age 523 to 617 yr BP Earthquake B: 95% interval on Con age 910 to 1,063 yr BP 95% interval on All age 920 to 1,065 yr BP Earthquake C: 95% interval on Con age 1,569 to 1,854 yr BP 95% interval on All age 1,637 to 1,888 yr BP Earthquake D: 95% interval on Con age 3,338 to 3,684 yr BP 95% interval on All age 3,334 to 3,642 yr BP Earthquake E: 95% interval on Con age 4,868 to 5,277 yr BP 95% interval on All age 4,924 to 5,320 yr BP

RLME Source	Recurrence Method	Recurrence Data
Cheraw Fault	Earthquake recurrence intervals Equation 5.3.3-4	In-cluster data N = 1 or 2, $\sum_{i=1}^{N} t_i + t_0$ uniformly distributed between 20 and 25 kyr Out-of-cluster assessment 200, 350, or 500 kyr cluster recurrence interval
	Slip rate Equation 5.3.3-5	In-cluster data *D* uniformly distributed between 3.2 and 4 m; *T* uniformly distributed between 20 and 25 kyr Out-of-cluster data *D* uniformly distributed between 3.2 and 8 m; *T* between 0.4 and 2 Myr (uniformly distributed between 1.2 and 2.0 Myr, tapering to 0 at 0.4 Myr)
Meers Fault	Earthquake recurrence intervals Equation 5.3.3-4	In-cluster data N = 1, $\sum_{i=1}^{N} t_i + t_0$ uniformly distributed between 2,153 and 2,968 yr Out-of-cluster assessment 200, 350, or 500 kyr cluster recurrence interval
New Madrid Fault System	Earthquake recurrence intervals Equation 5.3.3-4 for Poisson case Equation 5.3.3-9 for renewal model case	Earthquake data defining in-cluster intervals 1811-1812 earthquake sequence AD 1450 earthquake sequence: 95% interval on age 461 to 523 yr BP AD 900 earthquake sequence: 95% interval on age 979 to 1,147 yr BP Out-of-cluster data N = 1, $\sum_{i=1}^{N} t_i + t_0$ = 4,000 yr

RLME Source	Recurrence Method	Recurrence Data
Eastern Rift Margin—South	Earthquake count in a time interval Equation 5.3.3-2	N = 1, 2, or 3, T uniformly distributed between 17.7 and 21.7 kyr
Eastern Rift Margin—North	Earthquake count in a time interval Equation 5.3.3-2	N = 1 or 2, T uniformly distributed between 12 and 35 kyr
Marianna	Earthquake recurrence intervals Equation 5.3.3-4	N = 2 or 3, $\sum_{i=1}^{N} t_i + t_0$ uniformly distributed between 9.6 and 10.2 kyr
Commerce Fault Zone	Earthquake recurrence intervals Equation 5.3.3-4	N = 1 or 2, $\sum_{i=1}^{N} t_i + t_0$ uniformly distributed between 18.9 and 23.6 kyr
Wabash Valley	Earthquake recurrence intervals Equation 5.3.3-4	N = 1, $\sum_{i=1}^{N} t_i + t_0$ uniformly distributed between 11 and 13 kyr

Table 6.1.1-1
Charlevoix RLME Recurrence Frequency

RLME Frequency (earthquakes/year)			
Data Set 1	**Data Set 2**	**Data Set 3**	**Weight**
9.3E-03	1.3E-03	9.8E-04	0.101
6.7E-03	8.4E-04	6.7E-04	0.244
4.2E-03	5.7E-04	4.7E-04	0.310
2.2E-03	3.7E-04	3.2E-04	0.244
7.7E-04	1.9E-04	1.8E-04	0.101

Table 6.1.2-1
Summary of Interpreted Charleston Earthquake Ages and Sizes from "Contemporary Ages Only" Scenario

Earthquake	Age (years BP)	No. of Constraining Features	No. of Constraining Ages	SW-NE Extent (km)	Dist. to Energy Center (km)*	Assessment: Regional or Local?
1886	64	—		200	100	Regional
A	536–655	6	7	190	110	Regional
B	982–1,046	7	12	175	110	Regional
C	1,524–1,867	5	5	160	150	Regional
D	*3,472–3,559*	*5*	*7*	*100*	*100*	*Local?*
E	*4,864–5,281*	*1*	*1*	—	*90*	*Local?*

* Assumes approximate center of 1886 Charleston meizoseismal area as energy center.

Table 6.1.2-2
Summary of Interpreted Charleston Earthquake Ages and Sizes from "All Ages" Scenario

Earthquake	Age (years BP)	No. of Constraining Features	No. of Constraining Ages	SW-NE Extent (km)	Dist. to Energy Center (km)*	Assessment: Regional or Local?
1886	64	—	—	200	100	Regional
A	536–655	6	7	190	110	Regional
B	982–1,046	8	14	175	110	Regional
C	1,569–1,867	6	7	250	150	Regional
D	3,472–3,559	6	9	190	100	Regional
E	*4,821–5,281*	*2*	*3*	*80?*	*90*	*Local?*

* Assumes approximate center of 1886 Charleston meizoseismal area as energy center.

Table 6.1.2-3
Charleston Liquefaction Feature Ages Used to Assess Ages of Prehistoric Earthquakes

Prehistoric Earthquake	Site ID	Age Type*	Minimum Age (yr BP)	Maximum Age (yr BP)
A	BLUF-C-11	CON	316	680
A	BLUF-B-8	CON	475	655
A	BLUF-A-4	CON	307	905
A	BLUF-A-7	CON	316	678
A	HLYD-125	CON	536	680
A	SP-SPN	CON	317	667
B	CG-1	CON	796	1174
B	HLYD-XVII	CON	662	1356
B	HLYD-XIV	CON	982	1291
B	SP-SPMR-1	CON	690	1056
B	SP-SPMR-2	CON	687	1691
B	SP-BWL	CON	741	1049
B	GTWN-A	CON	663	1315
B	SP-BWR	A	766	1053
B	SP-BWR	B	1141	1383
C	FHS-1	CON	1524	1867
C	SP-SPS	CON	1178	2148
C	OLN-A	CON	794	2679
C	MM-1	CON	1400	2303
C	MB-3	CON	1145	2306
C	BLUF-A-5	A	1569	1969
C	BLUF-A-5	B	2001	2331
D	BLUF-D-14	CON	2880	3835
D	BLUF-D-15	CON	2965	3680
D	TMH-A	CON	2045	4416
D	TMH-C	CON	3415	4075
D	TMH-ARP	CON	3215	3845
D	GPWY-A	A	1870	2152
D	GPWY-A	B	3450	3827
E	GPWY-D	CON	4864	5281
E	TMH-D	A	4821	6176
E	TMH-D	B	5045	8189

* CON = Contemporary with earthquake; B = before earthquake; A = after earthquake

Table 6.1.2-4
Charleston RLME Recurrence Frequency for Poisson Model

RLME Frequency (earthquakes/year)					Weight
Post-2,000 yrs Earthquakes 1886, A, B, and C	**Post-5,500 yrs Earthquakes 1886, A, B, and C**	**Post-5,500 yrs Earthquakes 1886, A, B, C, and D**	**Post-5,500 yrs Earthquakes 1886, A, B, C, and E**	**Post-5,500 yrs Earthquakes 1886, A, B, C, D, and E**	
4.7E-03	4.7E-03	2.7E-03	1.9E-03	2.2E-03	0.101
3.1E-03	3.1E-03	1.9E-03	1.3E-03	1.5E-03	0.244
2.1E-03	2.1E-03	1.3E-03	9.2E-04	1.1E-03	0.310
1.3E-03	1.3E-03	8.8E-04	6.4E-04	7.8E-04	0.244
6.8E-04	6.8E-04	5.0E-04	3.4E-04	4.6E-04	0.101

Table 6.1.2-5
Charleston RLME Recurrence Frequency for Renewal Model

RLME Frequency (earthquakes/year)					
Post-2,000 yrs Earthquakes 1886, A, B, and C	**Post-5,500 yrs Earthquakes 1886, A, B, and C**	**Post-5,500 yrs Earthquakes 1886, A, B, C, and D**	**Post-5,500 yrs Earthquakes 1886, A, B, C, and E**	**Post-5,500 yrs Earthquakes 1886, A, B, C, D, and E**	**Weight**
α = 0.3					
6.4E-05	6.8E-05	3.5E-07	4.5E-09	1.5E-08	0.101
7.6E-06	8.0E-06	2.5E-08	2.0E-10	8.7E-10	0.244
9.5E-07	1.0E-06	2.2E-09	1.2E-11	7.0E-11	0.310
8.5E-08	9.2E-08	1.4E-10	5.4E-13	4.4E-12	0.244
2.3E-09	2.5E-09	2.7E-12	6.4E-15	8.2E-14	0.101
α = 0.5					
1.4E-03	1.4E-03	2.2E-04	5.2E-05	7.0E-05	0.101
3.8E-04	3.9E-04	4.5E-05	8.2E-06	1.3E-05	0.244
9.5E-05	9.8E-05	9.3E-06	1.4E-06	2.5E-06	0.310
1.7E-05	1.7E-05	1.4E-06	1.7E-07	3.7E-07	0.244
1.0E-06	1.1E-06	7.6E-08	7.0E-09	2.1E-08	0.101
α = 0.7					
2.6E-03	2.7E-03	1.0E-03	5.2E-04	5.7E-04	0.101
9.8E-04	9.9E-04	3.3E-04	1.4E-04	1.6E-04	0.244
3.2E-04	3.3E-04	9.5E-05	3.4E-05	4.5E-05	0.310
7.1E-05	7.3E-05	2.0E-05	6.1E-06	9.2E-06	0.244
5.6E-06	5.8E-06	1.5E-06	3.9E-07	7.6E-07	0.101

Table 6.1.3-1
Range of Cheraw Fault Estimated Magnitudes (M)

Approach	Rupture Length[1]		Max. Displacement[2]		Average Displacement[3]		Rupture Area[4]			Rupture Area[5]		
Parameter Value	30 km (18.5 mi.)	46 km (28.5 mi.)	1.6 m (5.2 ft.)	2.6 m (8.5 ft.)	1.1 m (3.6 ft.)	2.1 m (6.9 ft.)	430 km^2 (L = 30 km SD = 13 km Dip = 65°)	1,020 km^2 (L = 46 km SD = 17 km Dip = 50°)	1,321 km^2 (L = 46 km SD = 22 km Dip = 50°)	430 km^2 (30 km × 14.3 km) (assumes 65° dip)	1,020 km^2 (L = 46 km SD = 17 km Dip = 50°)	1,321 km^2 (L = 46 km SD = 22 km Dip = 50°)
Estimated Magnitude (M)	6.6/6.6	6.9/6.9	6.8/6.8	6.9/7.0	6.8/7.0	7.0/7.2	6.6/6.7	7.0/7.0	7.1/7.1	7.0	7.4	7.5

[1] Wells and Coppersmith (1994)—Subsurface rupture length (km) to magnitude (M), normal fault/all types

[2] Wells and Coppersmith (1994)—Maximum displacement (m) to magnitude (M), normal fault/all types

[3] Wells and Coppersmith (1994)—Average displacement (m) to magnitude (M), normal fault/all types

[4] Wells and Coppersmith (1994)—Area (km2) to magnitude, normal fault/all types

[5] Somerville et al. (2001)—Area (km2) to magnitude

Table 6.1.3-2
Cheraw RLME In-Cluster Recurrence Frequency

RLME Frequency (earthquakes/year)		
2 Earthquakes in 20–25 ka	**3 Earthquakes in 20–25 ka**	**Weight**
2.4E-04	3.1E-04	0.101
1.3E-04	1.9E-04	0.244
7.6E-05	1.2E-04	0.310
3.8E-05	7.2E-05	0.244
1.4E-05	3.2E-05	0.101

Table 6.1.3-3
Cheraw RLME In-Cluster Slip Rates

RLME Fault Slip Rate (mm/year)	Weight
0.14	0.185
0.16	0.630
0.19	0.185

Table 6.1.3-4
Cheraw RLME Out-of-Cluster Recurrence Frequency

RLME Frequency (earthquakes/year)	Weight
5.0E-06	0.333
2.9E-06	0.334
2.0E-06	0.333

Table 6.1.3-5
Cheraw RLME Out-of-Cluster Slip Rates

RLME Fault Slip Rate (mm/year)	Weight
0.0038	0.101
0.0043	0.244
0.0054	0.310
0.0072	0.244
0.011	0.101

Table 6.1.4-1
Range of Estimated Meers Fault Earthquake Magnitudes (M)

Approach	Rupture Length			Max. Displacement		Average Displacement		Rupture Area	
Parameter Value	26 km (16 mi.)	37 km (23 mi.)	67 km (42 mi.)	3.5 m (12 ft.)	5.25 m (17.2 ft.)	1.75 m (5.74 ft.)	3.0 m (9.8 ft.)	390 km^2 (151 $mi.^2$)	1,150 km^2 (444 $mi.^2$)
Estimated Magnitude (M)	~6.7	~6.9	~7.1	7.1–7.2	7.2–7.4	7.1–7.3	7.3–7.5	6.6–7.0	7.1–7.4

Table 6.1.4-2
Meers RLME In-Cluster Recurrence Frequency

RLME Frequency (earthquakes/year)	Weight
2.1E-03	0.101
1.2E-03	0.244
6.7E-04	0.310
3.4E-04	0.244
1.2E-04	0.101

Table 6.1.4-3
Meers RLME Out-of-Cluster Recurrence Frequency

RLME Frequency (earthquakes/year)	Weight
5.0E-06	0.333
2.9E-06	0.334
2.0E-06	0.333

Table 6.1.5-1
Preferred Ages for Paleoearthquakes in the New Madrid Region[1]

AD 1811-1812
500 yr BP ± 150 yr (350–650 yr BP)
1,050 yr BP ± 150 yr (900–1,200 yr BP)
2,750 yr BP ± 150 yr; sand blow of this age at only one site (Eaker 2); sand dike at Porter Gap (2,600–2,900 yr BP)
2,902 yr BP ± 2,138 yr; possibly same as Holbrook's event ~1000 BC or 2,514–3,560 yr BP
4,300 yr BP ± 150 yr (4,150–4,450 yr BP)

[1] Age in years BP, relative to AD 1950 (see Appendix E)

Table 6.1.5-2
Magnitude Comparisons for New Madrid 1811-1812 Earthquake Sequence

Study	NM1	NM2	NM3
Johnston (1996b)	M 8.1 ± 0.3	M 7.8 ± 0.3	M 8.0 ± 0.3
Johnston (pers. comm., Aug. 31, 2004)	M 7.8–7.9	M 7.5–7.6	M 7.7–7.8
Johnston (pers. comm., Feb. 16, 2010)	Currently has no new information that would change his previous estimates. He noted that he is disillusioned with using intensity data to estimate moment magnitude and thinks that overinterpretation of the data using site correction, etc. is a problem.		
Bakun and Hopper (2004b)	M_I 7.6 (**M** 7.2–7.9) (preferred model 3)	M_I 7.5 (**M** 7.1–7.8) (preferred model 3)	M_I 7.8 (**M** 7.4–8.1) (preferred model 3)
	M_I 7.2 (**M** 6.8–7.9) (model 1)	M_I 7.2 (**M** 6.8–7.8) (model 1)	M_I 7.4 (**M** 7.0–8.1) (model 1)
Bakun (electronic comm., Feb. 3, 2010—no change, use entire range of uncertainty cited in Bakun and Hopper, 2004b)	M 6.8–7.9	M 6.8–7.8	M 7.0–8.1
Hough et al. (2000)	**M** 7.2–7.3 (using isoseismal method of Johnston, 1996) **M** 7.0–7.3(using method of Bakun and Wentworth, 1997)[1]	**M** ~ 7.01[2] (located on the New Madrid North fault) (using isoseismal method of Johnston, 1996)	**M** 7.4–7.5 (using isoseismal method of Johnston, 1996)
Mueller and Pujol (2001)	–	–	**M** 7.2–7.4 (preferred **M** 7.2–7.3)
Mueller et al. (2004)	**M** 7.3	**M** 6.8 (located within the Wabash Valley of southern Illinois/ southern Indiana)	**M** 7.5
Hough and Page (2011)	**M** 6.69/6.85 (min) to **M** 6.85/7.08 (max) (full range of experts) **M** 6.7 (model 1)/6.9 (model 3)[3]	**M** 6.72/6.86 (min) to **M** 6.91/7.09 (max) (full range of experts) **M** 6.8 (model 1)/7.0 (model 3) (NM location)[3] **M** 6.5 (model 1)/6.7 (model 3) (IL location near 1968 event)[3]	**M** 6.83/7.02 (min) to **M** 7.21/7.50 (max) (full range of experts) **M** 7.1 (model 1)/7.3 (model 3)[3] Scaling relationships **M** 6.8 (assume 35 km length, 15 km width, 1 m slip)

[1] Based on intensity values reported in Hough et al. (2000) and Bakun and Wentworth (1997) method as noted in Hough and Page (2011).

[2] The estimated location and magnitude of this earthquake are revised in Mueller et al. (2004).

[3] Using method of Bakun and Wentworth (1997) and published attenution models; following Bakun et al. (2003) and Bakun and Hopper (2004) these are referred to as models 1 and 3.

Table 6.1.5-3
Liquefaction Constraints on Age of AD 1450 NMFS RLME

Liquefaction Feature	Maximum Age (years before 1/1/2011)	Minimum Age (years before 1/1/2011)	Age of AD 1450 RLME (years before 1/1/2011)*							
			351	471	511	556	561	571	590	601
Tyr01-01	711	211								
MarkedT01-01	591	511	X	X						X
MarkedT01-03	591	511	X	X						X
HatchieR31-02	1551	221								
Nodena01-01	561	341						X	X	X
KochD01-01	1021	351								
LittleR09-02	696	466	X							
Eaker01-01	601	271								
Yarbro01-01	591	341								X
Yarbro03-03	591	341								X
Crav01-01	601	331								
ObionR216-02	811	611	X	X	X	X	X	X	X	X
Dodd01-01	721	556	X	X	X					
Cagle01-01	591	321								X
ObionR200-02	711	591	X	X	X	X	X	X	X	
CurrentR02-01	701	561	X	X	X	X				
Wilhelmina01-05	571	471	X						X	X
No. of Samples with Age Range Outside of Specific Age			8	6	4	3	2	3	4	8

* X indicates sample age range does not include specified date.

Table 6.1.5-4
Liquefaction Constraints on Age of AD 900 NMFS RLME

Liquefaction Feature	Maximum Age (years before 1/1/2011)	Minimum Age (years before 1/1/2011)	Age of AD 900 RLME (years before 1/1/2011)*					
			801	1011	1021	1131	1211	1221
CentralD01-01	1221	771						
Eaker03-01	1211	611						X
Eaker03-03	1211	611						X
Eaker02-01	1541	1011	X					
Bugg01-01	1211	1011	X					X
Hueys01-01	1211	1011	X					X
Haynes01-02	1211	611						X
Arch01-01	1351	801						
Dill01-01	1101	521				X	X	X
NewFrnk03-01	1221	1021	X	X				
NewFrnk04-01	1371	1131	X	X	X			
Johnson05-01	1211	1011	X					X
Wilhelmina01-03	1236	1106	X	X	X			
Tow01-01	1472	1020	X	X				
HillH01-01	1221	1011	X					
No. of Samples with Age Range Outside of Specific Age			9	4	2	1	1	7

* X indicates sample age range does not include specified date.

Table 6.1.5-5
NMFS In-Cluster RLME Recurrence Frequency—Poisson Model

RLME Frequency (earthquakes/year)	Weight
6.0E-03	0.101
3.7E-03	0.244
2.4E-03	0.310
1.4E-03	0.244
6.2E-04	0.101

Table 6.1.5-6
NMFS In-Cluster RLME Recurrence Frequency—Renewal Model

RLME Frequency (earthquakes/year)			
$\alpha = 0.3$	$\alpha = 0.5$	$\alpha = 0.7$	Weight
3.5E-03	4.8E-03	4.4E-03	0.101
1.1E-03	2.2E-03	2.2E-03	0.244
3.2E-04	8.9E-04	1.0E-03	0.310
6.4E-05	2.6E-04	3.4E-04	0.244
4.7E-06	3.1E-05	4.7E-05	0.101

Table 6.1.5-7
NMFS Out-of-Cluster RLME Recurrence Frequency—Poisson Model

RLME Frequency (earthquakes/year)	Weight
1.3E-03	0.101
7.2E-04	0.244
4.2E-04	0.310
2.2E-04	0.244
8.0E-05	0.101

Table 6.1.6-1
Range of ERM-S Estimated Magnitudes (M)

Approach	Rupture Length[1]		Max. Displacement[2]		Average Displacement[3]		Rupture Area[4]			Rupture Area[5]		
Parameter Value	≤80 km (50 mi.)	114 km (71 mi.)	0.5 m (1.5 ft.)	2.1 m (6.9 ft.)	0.5 m (1.5 ft.)	2.1 m (6.9 ft.)	≤1,040 km^2 (L ≤ 80 km SD = 13 km)	1,215 km^2 (L = 80 km SD = 15 km)	1,938 km^2 (L = 114 km, SD = 17 km)	≤1,040 km^2 (L ≤ 80 km SD = 13 km)	1,215 km^2 (L = 80 km SD = 15 km)	1,938 km^2 (L= 114 km, SD = 17 km)
Estimated Magnitude (M)	≤7.2/7.2	7.4/7.4	6.6/6.5	7.1/6.9	6.8/6.7	7.3/7.2	≤7.1/7.0	7.1/7.1	7.3/7.3	≤7.4	7.4	7.6

[1] Wells and Coppersmith (1994)—Subsurface rupture length (km) to magnitude (M), strike-slip/all types

[2] Wells and Coppersmith (1994)—Maximum displacement (m) to magnitude (M), strike-slip/all types

[3] Wells and Coppersmith (1994)—Average displacement (m) to magnitude (M), strike-slip/all types

[4] Wells and Coppersmith (1994)—Area (km^2) to magnitude, strike-slip/all types

[5] Somerville et al. (2001)—Area (km^2) to magnitude

Table 6.1.6-2
Range of ERM-N Estimated Magnitudes (M)

Approach	Rupture Length[1]	Rupture Area[2]			Rupture Area[3]		
Parameter Value	≤73 km (45.5 mi.)	≤949 km^2 (L = 73 km, SD = 13 km)	1,095 km^2 (L = 73 km, SD = 15 km)	1,241 km^2 (L = 73 km, SD = 17 km)	≤949 km^2 (L = 73 km, SD = 13 km)	1,095 km^2 (L = 73 km, SD = 15 km)	1,241 km^2 (L = 73 km, SD = 17 km)
Estimated Magnitude (M)	≤7.1/7.2	≤7.0/7.0	7.1/7.1	7.1/7.1	≤7.3	7.4	7.4

[1] Wells and Coppersmith (1994)—Subsurface rupture length (km) to magnitude (M), strike-slip/all types

[2] Wells and Coppersmith (1994)—Area (km^2) to magnitude, strike-slip/all types

[3] Somerville et al. (2001)—Area (km^2) to magnitude

Table 6.1.6-3
ERM-S RLME Recurrence Frequency

RLME Frequency (earthquakes/year)			
2 Earthquakes in 17.7–21.7 kyr	**3 Earthquakes in 17.7–21.7 kyr**	**4 Earthquakes in 17.7–21.7 kyr**	**Weight**
3.5E-04	4.3E-04	5.0E-04	0.101
2.1E-04	2.8E-04	3.4E-04	0.244
1.4E-04	1.9E-04	2.4E-04	0.310
8.0E-05	1.2E-04	1.6E-04	0.244
3.6E-05	6.2E-05	9.0E-05	0.101

Table 6.1.6-4
ERM-N RLME Recurrence Frequency

RLME Frequency (earthquakes/year)		
1 Earthquake in 12–35 kyr	**2 Earthquakes in 12–35 kyr**	**Weight**
2.9E-04	3.9E-04	0.101
1.5E-04	2.2E-04	0.244
8.0E-05	1.3E-04	0.310
4.0E-05	7.2E-05	0.244
1.4E-05	3.2E-05	0.101

Table 6.1.7-1
Marianna RLME Recurrence Frequency

RLME Frequency (earthquakes/year)		
3 Earthquakes in 9.6–10.2 kyr	**4 Earthquakes in 9.6–10.2 kyr**	**Weight**
6.9E-04	8.4E-04	0.101
4.2E-04	5.5E-04	0.244
2.7E-04	3.7E-04	0.310
1.6E-04	2.4E-04	0.244
7.2E-05	1.2E-04	0.101

Table 6.1.8-1
Range of Commerce Fault Zone RLME Estimated Magnitudes (M)

Approach	Rupture Length[1]		Max. Displacement[2]		Average Displacement[3]		Rupture Area[4]			Rupture Area[5]		
Parameter Value	≤55 km (34 mi.)	120 km (75 mi.)	2.0 m (6.6 ft.)	2.2 m (6.9 ft.)	2.0 m (6.6 ft.)	2.2 m (6.9 ft.)	≤715 km^2 (L ≤ 55 km, SD = 13 km)	975 km^2 (L = 65 km, SD = 15 km)	2.040 km^2 (L = 120 km, SD = 17 km)	≤715 km^2 (L ≤ 55 km, SD = 13 km)	975 km^2 (L = 65 km, SD = 15 km)	2,040 km^2 (L = 120 km, SD = 17 km)
Estimated Magnitude (M)	≤6.9/7.0	7.4/7.5	7.0/6.9	7.1/6.9	7.3/7.2	7.3/7.2	≤6.9/6.9	7.0/7.0	7.4/7.3	≤7.2	7.3	7.7

[1] Wells and Coppersmith (1994)—Subsurface rupture length (km) to magnitude (M), strike-slip/all types

[2] Wells and Coppersmith (1994)—Maximum displacement (m) to magnitude (M), strike-slip/all types

[3] Wells and Coppersmith (1994)—Average displacement (m) to magnitude (M), strike-slip/all types

[4] Wells and Coppersmith (1994)—Area (km^2) to magnitude, strike-slip/all types

[5] Somerville et al. (2001)—Area (km^2) to magnitude

Table 6.1.8-2
Commerce Fault Zone RLME Recurrence Frequency

RLME Frequency (earthquakes/year)		
2 Earthquakes in 18.9–23.6 kyr	**3 Earthquakes in 18.9–23.6 kyr**	**Weight**
2.5E-04	3.3E-04	0.101
1.4E-04	2.0E-04	0.244
8.0E-05	1.3E-04	0.310
4.0E-05	7.6E-05	0.244
1.4E-05	3.4E-05	0.101

Table 6.1.9-1
Liquefaction Evidence for Prehistoric Earthquakes in the Southern Illinois Basin

Inferred Energy Center for Earthquake(s)	Location	Size and Distribution of Features	Age[1]	Estimated Magnitude	Reference(s)
Lower Wabash Valley					
Vincennes-Bridgeport	~25 km (~15 mi.) west of Vincennes, Indiana	≥0.5 m (≥1.6 ft.) dike width; 115 km (71.5 mi.) minimum to 153 km (95 mi.) maximum distance from inferred energy center	~6,100 ± 200 yr BP	≥ **M** 7.5–7.8 (magnitude-bound, cyclic stress, and energy stress methods)	Munson et al. (1997) Obermeier (1998) Obermeier et al. (1993)
				M 7.8 (energy-stress)[2]	Pond and Martin (1997)
				M 7.1–7.3 (updated magnitude-bound curve)	Olson et al. (2005b)
				M ~ 7.5 (back-calculated ground motion characteristics from paleoliquefaction effects)	Green et al. (2005)
				M 7.99 ± 0.27 (preliminary results—probabilistic approach using magnitude bounds and back-calculations to address uncertainties).	Olson et al. (2007)

Table 6.1.9-1 *(continued)*

Inferred Energy Center for Earthquake(s)	Location	Size and Distribution of Features	Age[1]	Estimated Magnitude	Reference(s)
				M ~ 7.5 ± 0.3 Prior distribution from magnitude-bound method combined with likelihood function from sites of observed liquefaction (or no liquefaction) to yield posterior distribution. Considers uncertainties in back-calculation analyses.	Olson (2009)
				≥M 7.0 (115 km epicentral distance); **≥M** 7.3 (153 km epicentral distance); (minimum magnitude-bound curve)	Castilla and Audemard (2007)
Skelton	~40 km (~25 mi.) SW of Vincennes, Indiana	≥0.5 m (≥1.6 ft.) dike width; 50–60 km (31–37 mi.) maximum distance from inferred energy center	~12,000 ± 1,000 yr BP	**M** ~ 7.1 (summary of magnitude-bound and geotechnical analysis results)	Hajic and Wiant (1997) Obermeier (1998)
				M 7.1–7.3 (magnitude bound)	Munson et al. (1997)
				M 7.3 (energy stress)[2]	Pond and Martin (1997)
				M 6.7 (updated magnitude bound)	Olson et al. (2005b
				≥ M 6.3 (63 km epicentral distance); (minimum magnitude-bound curve)	Castilla and Audemard (2007)
Single site near	35 km (22 mi.)	Very small and restricted	4,000 ± 500 yr	Near threshold	Munson et al.

Table 6.1.9-1 *(continued)*

Inferred Energy Center for Earthquake(s)	Location	Size and Distribution of Features	Age[1]	Estimated Magnitude	Reference(s)
Iona, Indiana	SE of Vincennes, Indiana, near Iona	(probably limited to 5 km [3.1 mi.])	BP	(**M** ~ 5.5–6.0 to <6.7)	(1997) Obermeier (1998)
Central and Southern Indiana					
Vallonia	East Fork valley ~100 km (~62 mi.) east of the Wabash Valley seismic zone	≥0.5 m (1.5 ft.); 36 km (22.5 mi.) maximum distance from inferred energy center	3,950 ± 250 yr BP	**M** ≥ 6.9 (magnitude bound)	Munson et al. (1997) Obermeier (1998)
				M 7.1 (energy stress)[2]	Pond and Martin (1997)
				M 6.3 (updated magnitude bound)	Olson et al. (2005b)
				≥ M 5.7 (36 km epicentral distance); (minimum magnitude-bound curve)	Castilla and Audemard (2007)
Martinsville-Waverly	~30–50 km (~18–30 mi.) SW of Indianapolis, Indiana (location poorly constrained)	≥0.15 to ≤0.5 m (≥5 to ≤1.6 ft.); 28 km (17.5 mi.) maximum distance from inferred energy center Geotechnical analyses demonstrate that these features are not associated with the **M** ~ 7.5 Vincennes	Between 8,500 and 3,500 yr BP	**M** 6.8 (magnitude bound)	Munson et al. (1997) Obermeier (1998)
				M 6.9 (energy stress)[2]	Pond and Martin (1997)
				M 6.2 (updated magnitude bound)	Olson et al. (2005b)

Table 6.1.9-1 *(continued)*

Inferred Energy Center for Earthquake(s)	Location	Size and Distribution of Features	Age[1]	Estimated Magnitude	Reference(s)
		earthquake		**≥ M** 5.5 (28 km epicentral distance); (minimum magnitude-bound curve)	Castilla and Audemard (2007)
Single site near Elnora, Indiana	60 km (37 mi.) E-NE of Vincennes	Limited areal extent	2,000 ± 500 yr BP	**M** ≥ 5.5–6.0	Munson et al. (1997) Obermeier (1998)
Single site along Indian Creek, Indiana	~50 km (~31 mi.) S-SW of Indianapolis	Single site	~20,000 yr BP	Unknown	Munson et al. (1997) Obermeier (1998)
Ohio River region—Absence of paleoliquefaction in Ohio River sediments along the Indiana-Kentucky and Illinois-Kentucky borders suggests that this area has not experienced severe ground shaking in the past 4,500 years (Munson et al., 1997). However, Munson et al. (1997) suggest that a 5–6 m (16.4–19.7 ft.) thick clay cap may have kept sand dikes from penetrating to levels above the current maintained water level of the Ohio River.					
Central and Southern Illinois					
Springfield	~35 km (~22 mi.) NE of Springfield, Illinois	Maximum dike width 0.4 m (1.3 ft.); 35 km (22 mi.) maximum distance from inferred energy center	One, possibly two, events between 5,960 ± 60 yr BP and 7,380 ± 90 yr BP	**M** 6.2–6.8 **M** 5.5 (second event)	Hajic et al. (1995) McNulty and Obermeier (1999)
				M 6.2 (updated magnitude bound)	Olson et al. (2005b)
				≥ M 5.7 (35 km epicentral distance); (minimum magnitude-bound curve)	Castilla and Audemard (2007)

Table 6.1.9-1 *(continued)*

Inferred Energy Center for Earthquake(s)	Location	Size and Distribution of Features	Age[1]	Estimated Magnitude	Reference(s)
Shoal Creek (Germantown, Illinois)	Centered in vicinity of lower Shoal Creek near its confluence with Kaskaskia River: ~65 km (~40 mi.) E-SE of St. Louis, Missouri. Alternative location: Centralia fault (Du Quoin monocline)	Maximum dike width 1.55 m (5 ft.); 35 km (22 mi.) maximum distance from inferred energy center	~5,670 ± 80 yr BP 4520 BC ± 200 yr	**M** 6.5 (lower limit)	McNulty and Obermeier (1999)
				M 6.2 (updated magnitude bound)	Olson et al. (2005b)
				≥ M 5.7 (35 km epicentral distance); (minimum magnitude-bound curve)	Castilla and Audemard (2007)
				Alternative scenarios: **M** 7.0 (Shoal Creek) **M** 7.5 (Centralia/Du Quoin)	Tuttle, Chester, et al. (1999)
Cache River	Cache River from Sandusky to the Mississippi River	Dike width 1–9 cm (0.4–3.5 in.)	Two ages: maximum age AD 1020–1250 for younger and possibly older event(s) Age estimates of Middle Holocene liquefaction features are of poor quality (cannot preclude they could be associated with	Unknown Middle Holocene events could have formed as a result of a very large earthquake originating from a distant source such as the NMSZ or a smaller-magnitude earthquake from a closer source such as the Commerce geophysical lineament.	Chester and Tuttle (2000) Tuttle (2005b)

Table 6.1.9-1 *(continued)*

Inferred Energy Center for Earthquake(s)	Location	Size and Distribution of Features	Age[1]	Estimated Magnitude	Reference(s)
			the 4520 BC ± 200 yr (Shoal Creek) event).		
n/a	Big Muddy River	No new sites identified. Geologic conditions not favorable for liquefaction.	n/a	All paleoliquefaction dikes in the region could possibly be induced by paleoearthquakes that occurred near the potential seismogenic sources identified by reanalysis of seismic reflection data. Maximum possible magnitude for a basement-involved fault in the region is between M 6 and just above M 7.	Su and McBride (1999)
Southeastern Missouri					
Big Muddy and Meramec rivers	~30 km (~20 mi.) SW of St. Louis, Missouri	Dikes 0.1–1 cm (.04–.4 in.) wide; maximum dike at MR25W site is 20 cm (7.9 in.) wide	Big Muddy River: post-9070 BC and possibly prior to 4240 BC Meramec River: post-13,210 BC. Several features are estimated to have formed during the late Holocene and Holocene. No	Three scenarios: Local, **M** > 5.2–6.0 Shoal Creek, **M** 7.0 Centralia fault, **M** 7.5 Results of liquefaction potential analysis (cyclic stress method using in situ geotechnical testing results for three possible source layers) showed that a local (**M** > 5.25–6.0) earthquake would induce liquefaction for the upper and middle layer; a **M** 6.75 earthquake in Germantown, Illinois (~80 km [~50 mi.] from site) would not induce liquefaction in any layer; a **M** 7.5 along Centralia fault–Du Quoin monocline (~100 km [~62 mi.] from site) would	Tuttle, Chester, et al. (1999) Tuttle (2005b)

Table 6.1.9-1 *(continued)*

Inferred Energy Center for Earthquake(s)	Location	Size and Distribution of Features	Age[1]	Estimated Magnitude	Reference(s)
			liquefaction features have yet been attributed to the 4,520 ± 200 yr BP (Shoal Creek) earthquake. Maximum age of 20 cm (7.9 in.) wide dike at MR 25W site is 4340–3990 BC. Stratigraphic relations suggest it might be as young as 800 BC.	induce liquefaction in the upper and middle layers; a **M** 7.8 along the same structure would induce liquefaction in all three layers; a **M** 8 earthquake produced by northern New Madrid fault would not induce liquefaction.	

[1] Ages given in yr BP are uncorrected radiocarbon ages.

[2] The energy-stress method used by Pond and Martin (1997) is flawed (energy attenuation relations used should not be used for liquefaction analysis and the results are not reliable [S. Obermeier, pers. comm., May 13, 2003]).

Table 6.1.9-2
Wabash RLME Recurrence Frequency

RLME Frequency (earthquakes/year)	Weight
4.4E-04	0.101
2.5E-04	0.244
1.4E-04	0.310
7.2E-05	0.244
2.4E-05	0.101

Table 6.2-1
Alternative Mmax Zonation Models

Mesozoic Extended—Narrow Model		Mesozoic Extended—Wide Model	
MESE-N	**NMESE-N**	**MESE-W**	**NMESE-W**
AHEX	MidC-A	AHEX	MidC-D
ECC-AM	IBEB	ECC-AM	OKA
ECC-GM	OKA	ECC-GM	
GHEX		GHEX	
RR		RR-RCG	
SLR		SLR	
NAP		NAP	
GMH		GMH	
PEZ-N		IBEB	
		PEZ-W	

Table 6.3.2-1
Maximum Magnitude Distributions for Mmax Distributed Seismicity Sources

Weight Assigned to Mmax	Maximum Magnitude for:				
	Study Region	MESE-N	NMESE-N	MESE-W	NMESE-W
0.101	6.5	6.4	6.4	6.5	5.7
0.244	6.9	6.8	6.8	6.9	6.1
0.310	7.2	7.2	7.1	7.3	6.6
0.244	7.7	7.7	7.5	7.7	7.2
0.101	8.1	8.1	8.0	8.1	7.9

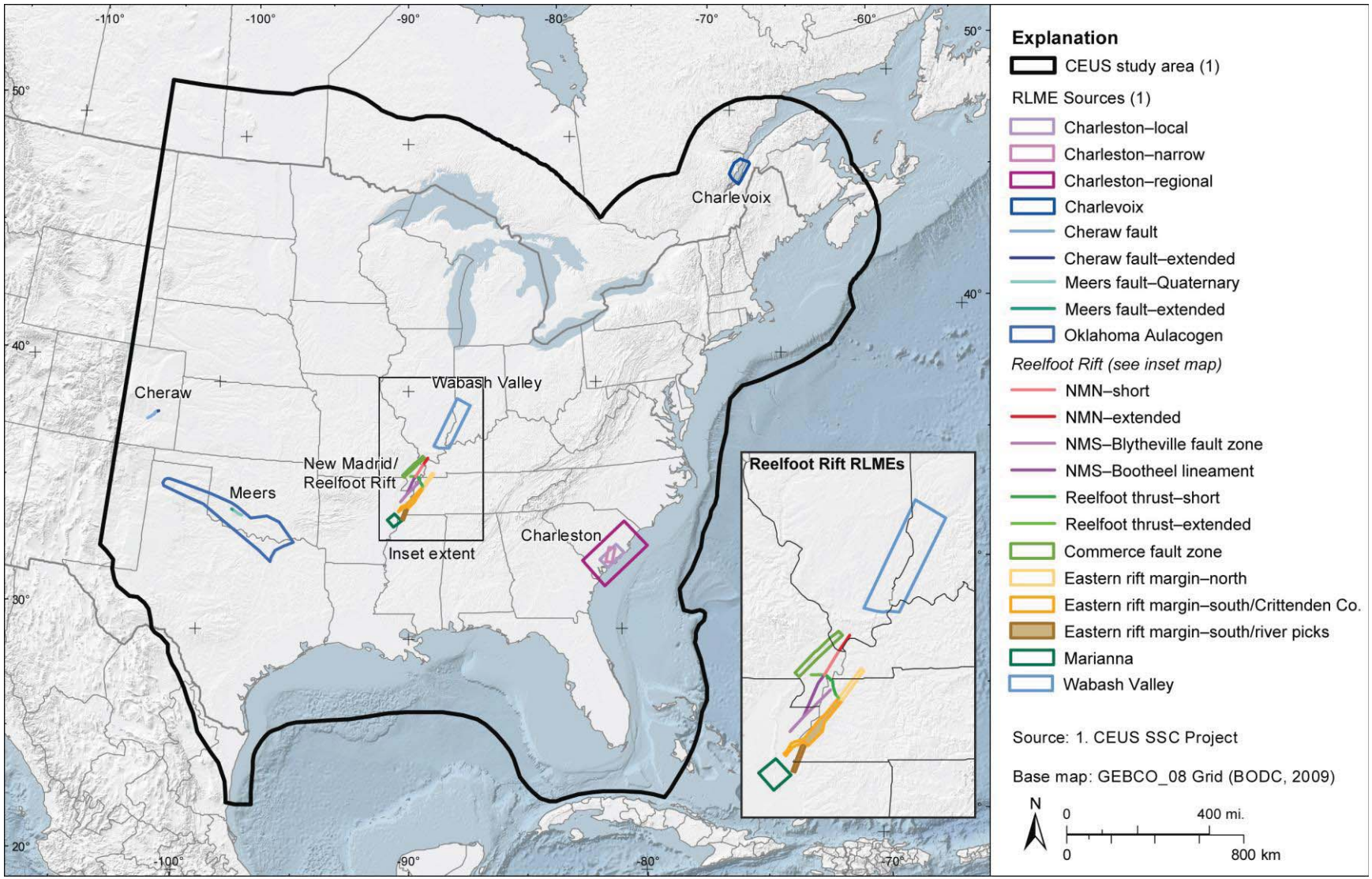

Figure 6.1-1
Map showing the RLME sources characterized in the CEUS SSC model. Detailed alternatives to the source geometries are shown on figures associated with each RLME discussion.

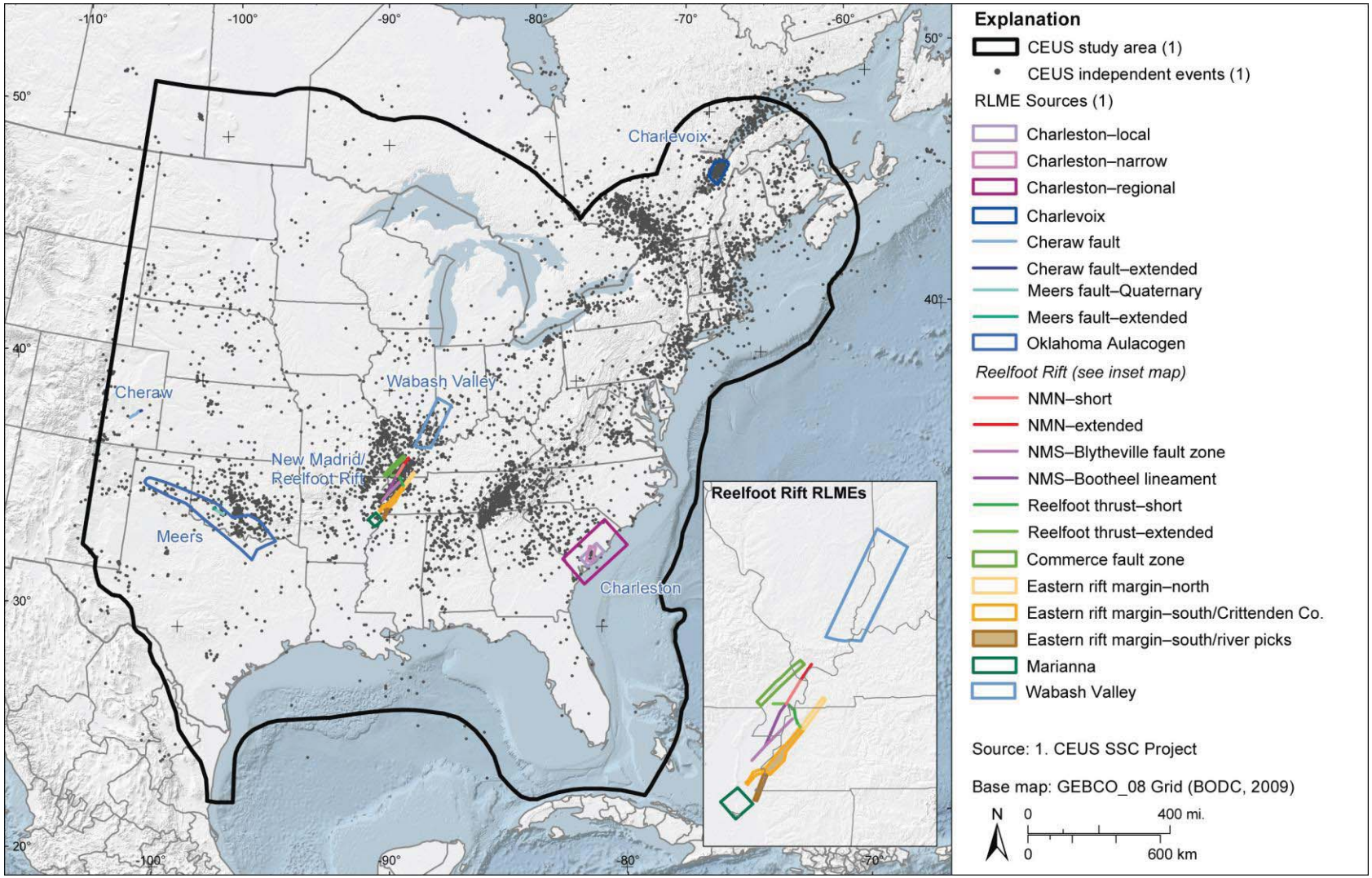

Figure 6.1-2a
Map showing the RLME sources and seismicity from the CEUS SSC earthquake catalog. Some of the RLMEs occur in regions of elevated seismicity, but others do not.

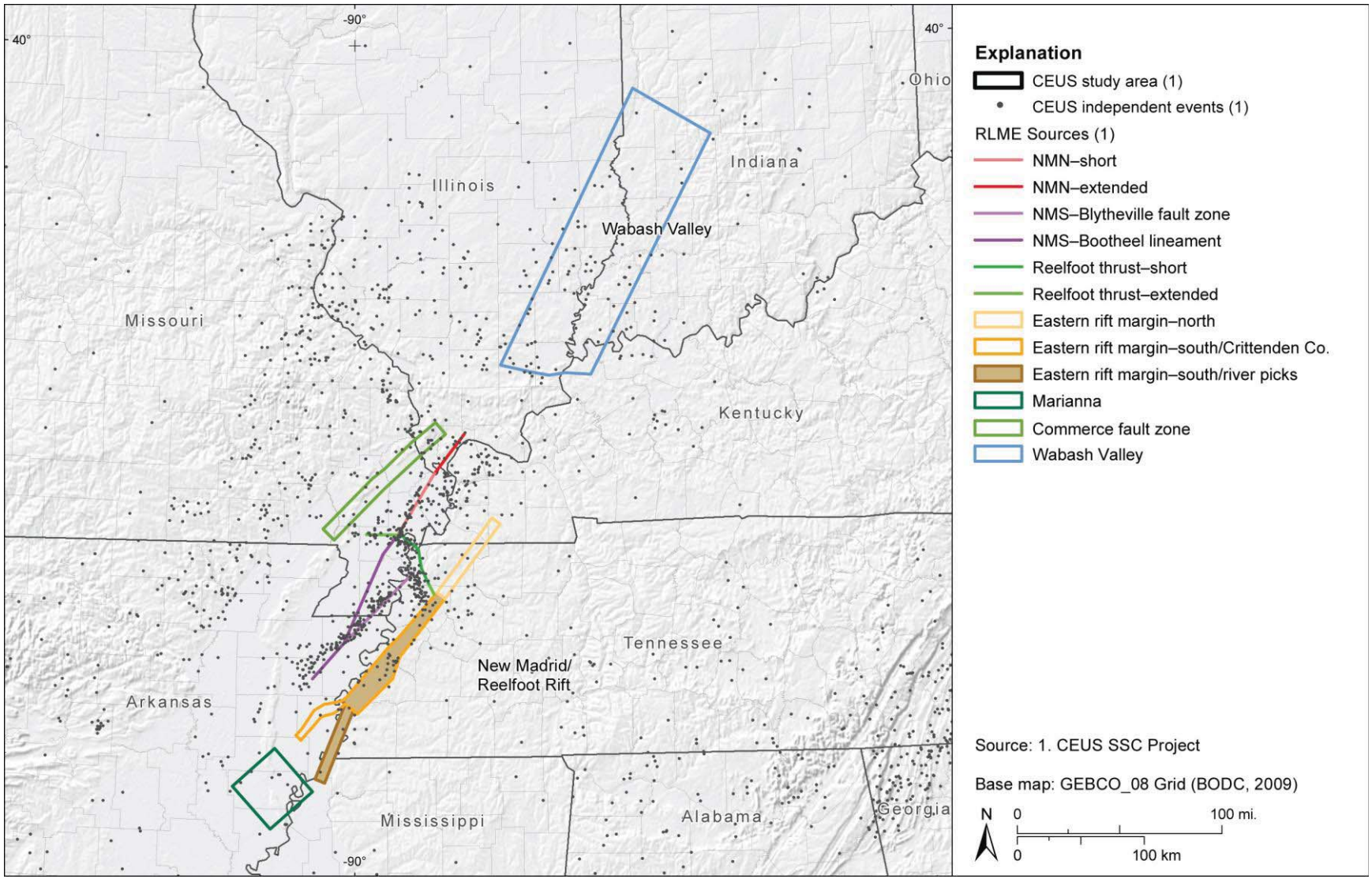

Figure 6.1-2b
Close-up of the Wabash Valley and New Madrid/Reelfoot Rift RLME sources and seismicity from the CEUS SSC earthquake catalog. Some of the RLMEs occur in regions of elevated seismicity, but others do not.

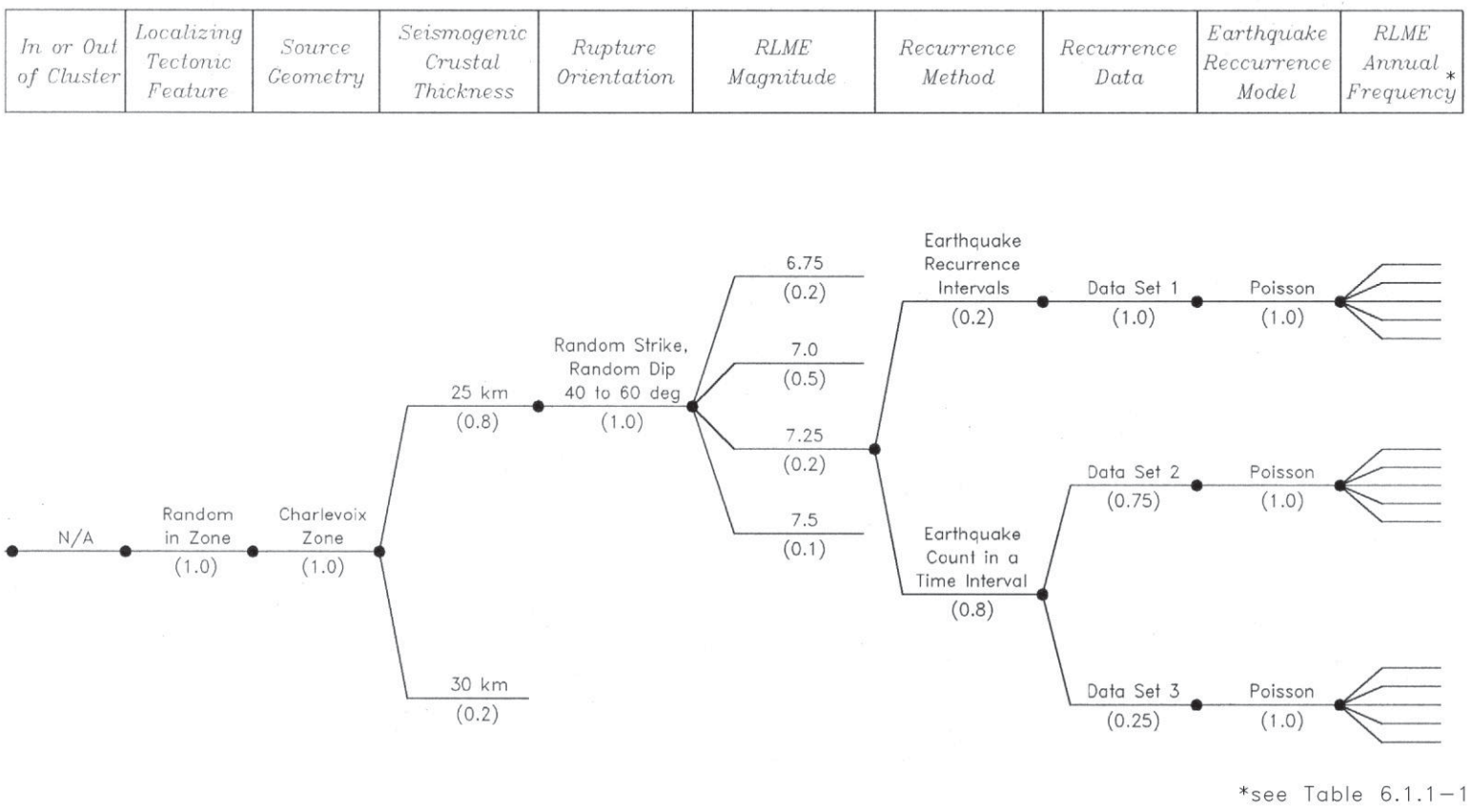

Figure 6.1.1-1
Logic tree for the Charlevoix RLME source

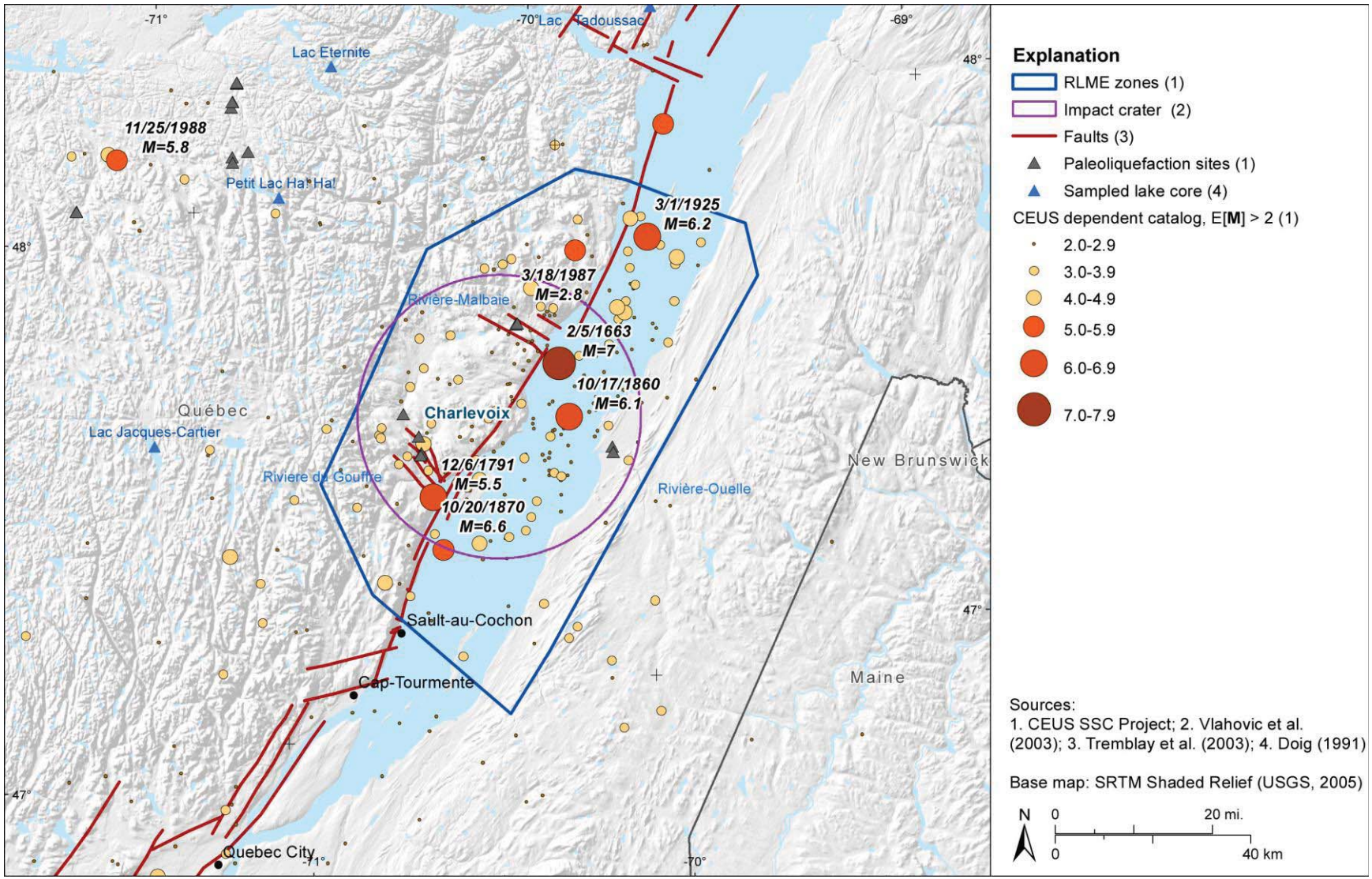

Figure 6.1.1-2
Seismicity and tectonic features of the Charlevoix RLME

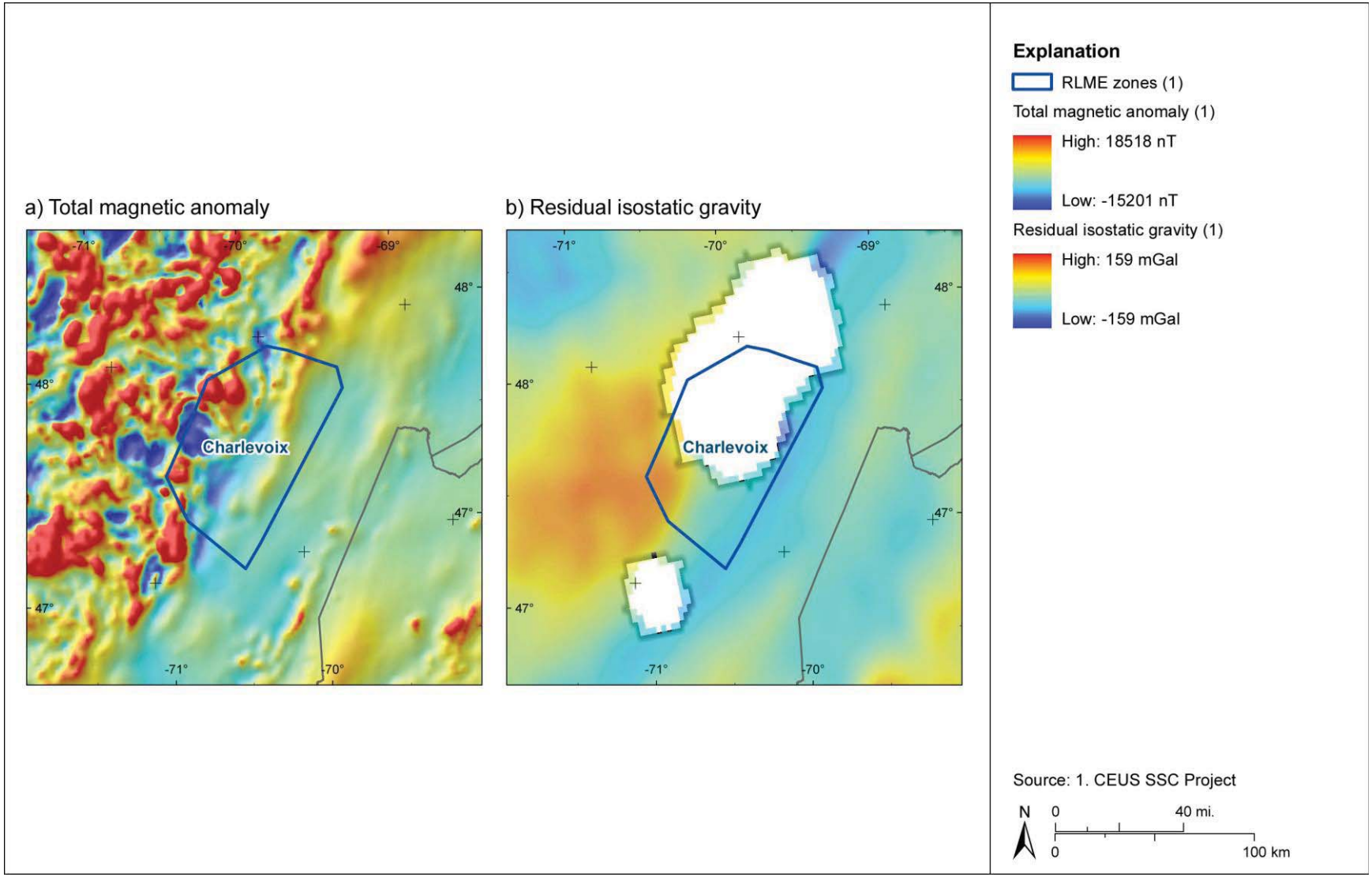

Figure 6.1.1-3
Magnetic and gravity anomaly maps of the Charlevoix RLME

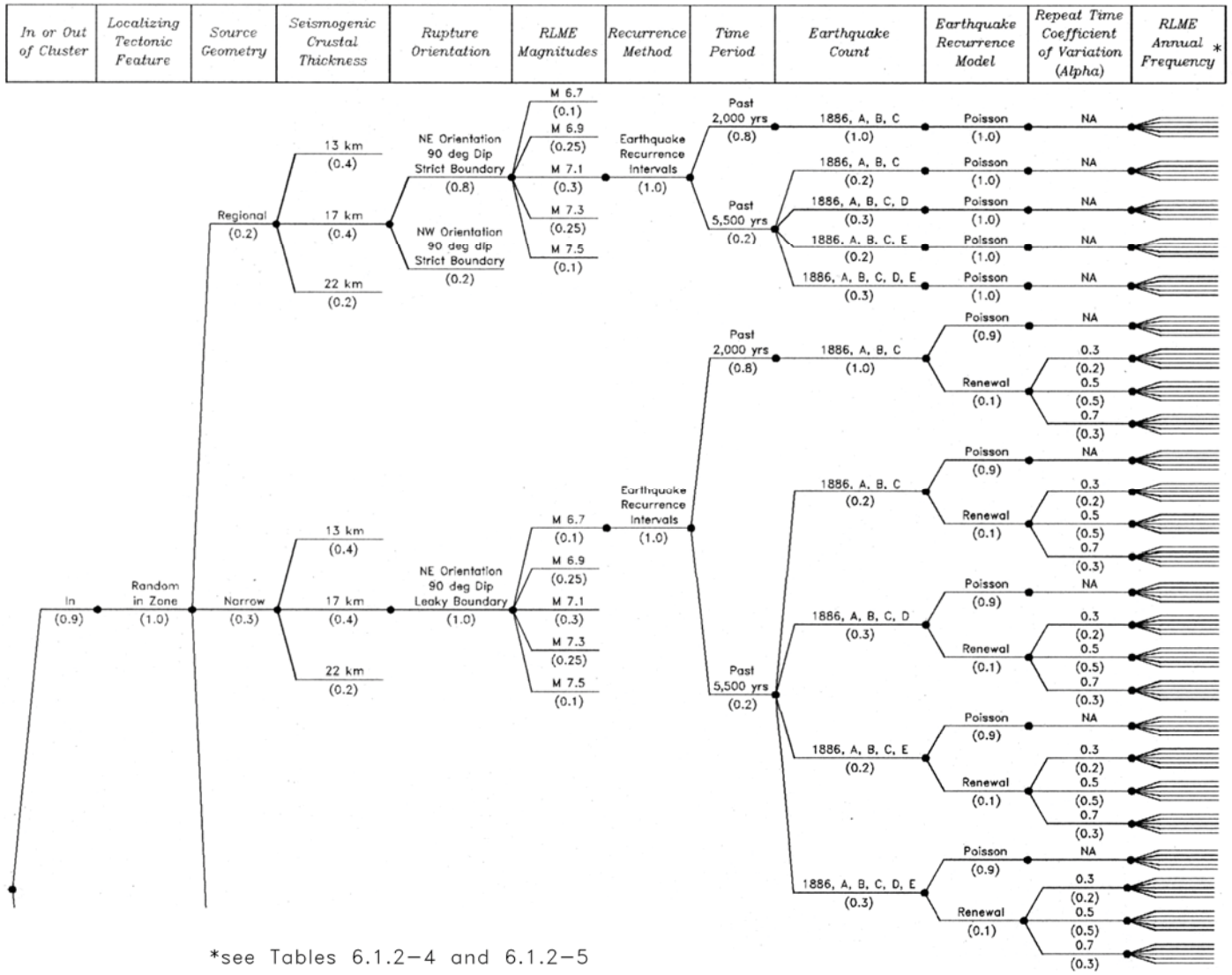

Figure 6.1.2-1a
Logic tree for the Charleston RLME source

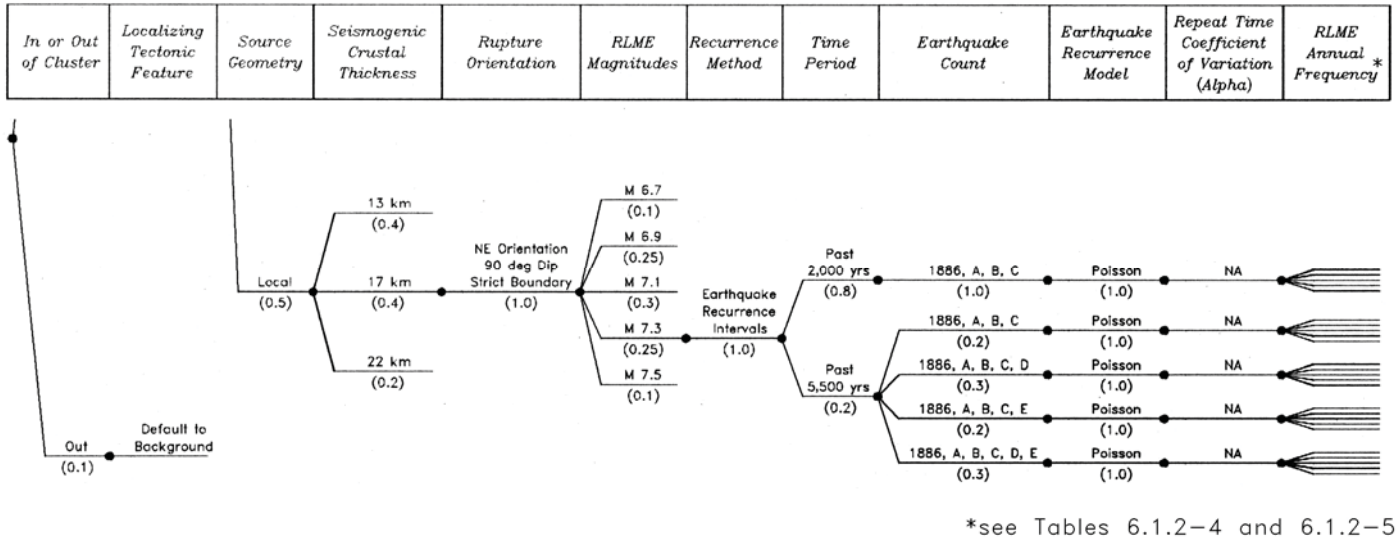

Figure 6.1.2-1b
Logic tree for the Charleston RLME source

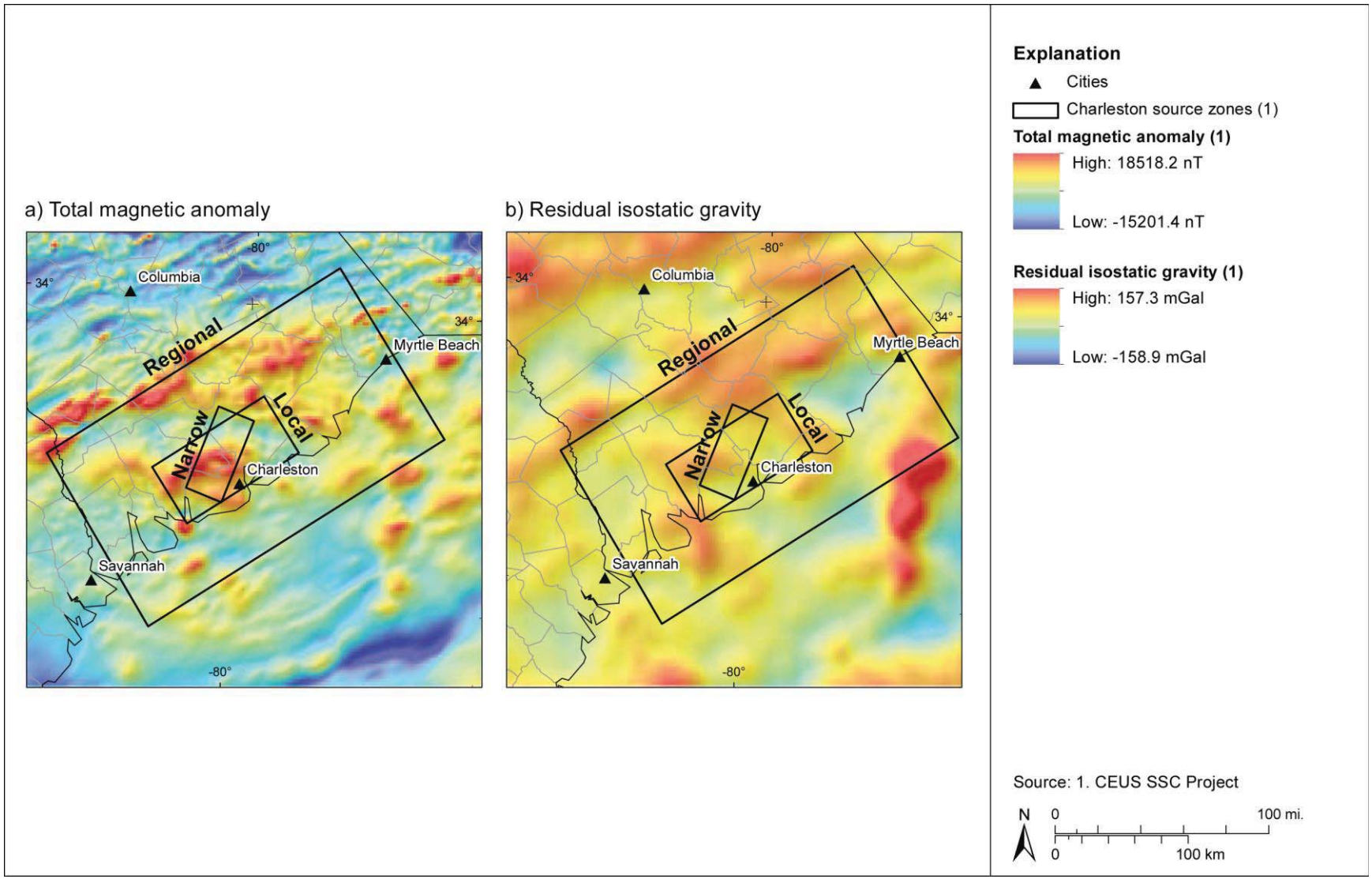

Figure 6.1.2-2
Charleston RLME source zones with (a) total magnetic anomaly and (b) residual isostatic gravity data

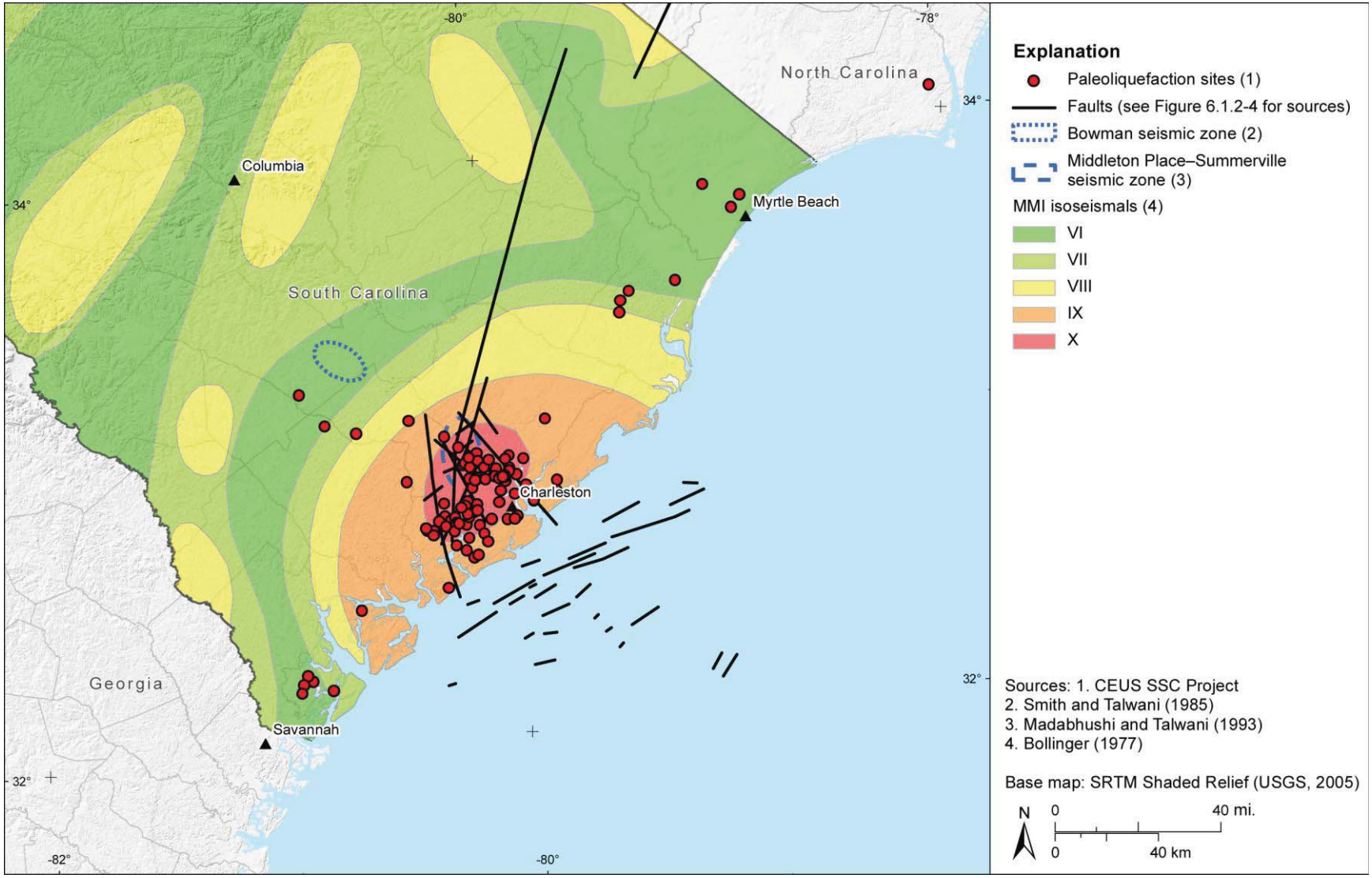

Figure 6.1.2-3
Postulated faults and tectonic features in the Charleston region

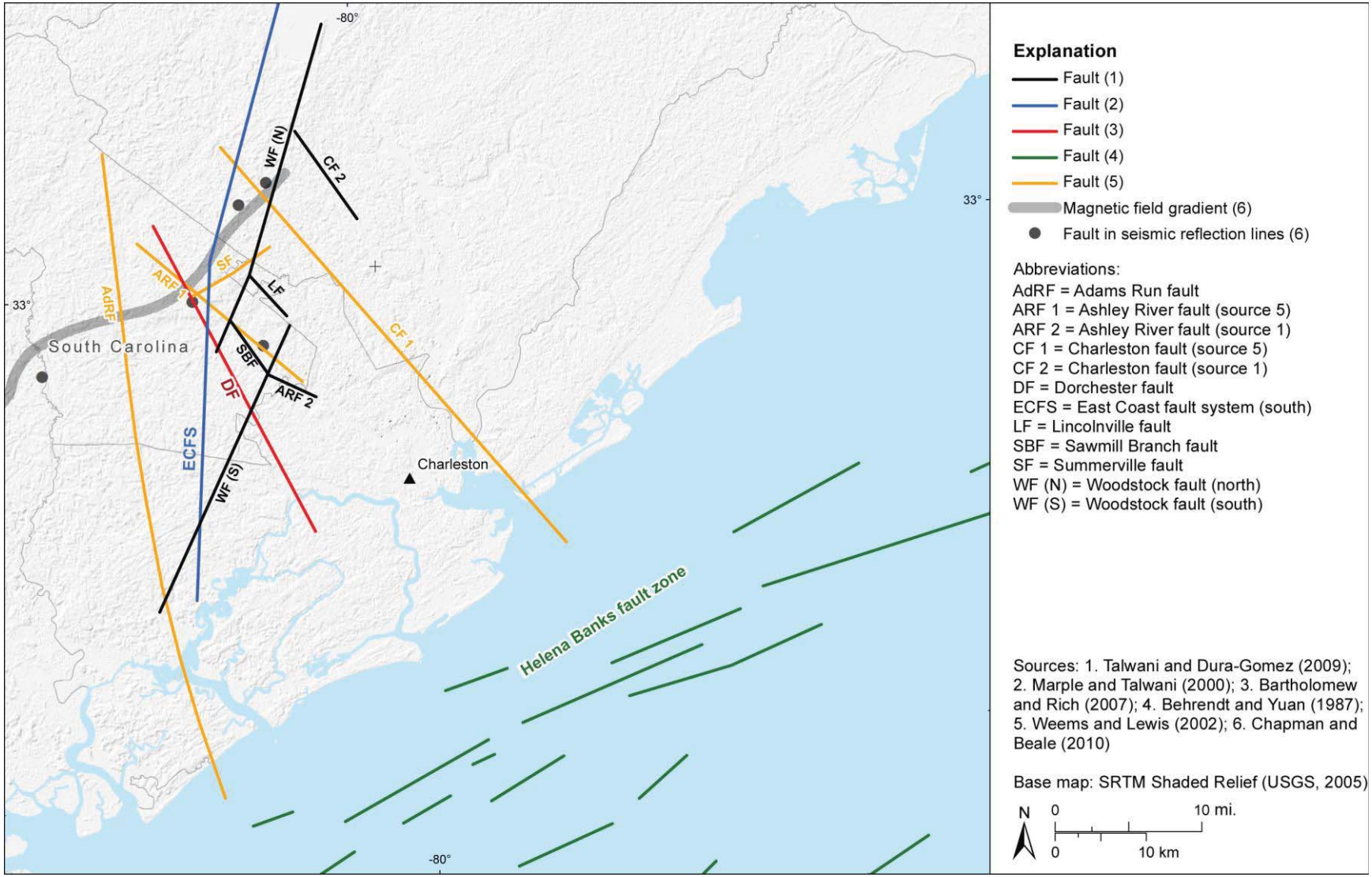

Figure 6.1.2-4
Postulated faults and tectonic features in the local Charleston area

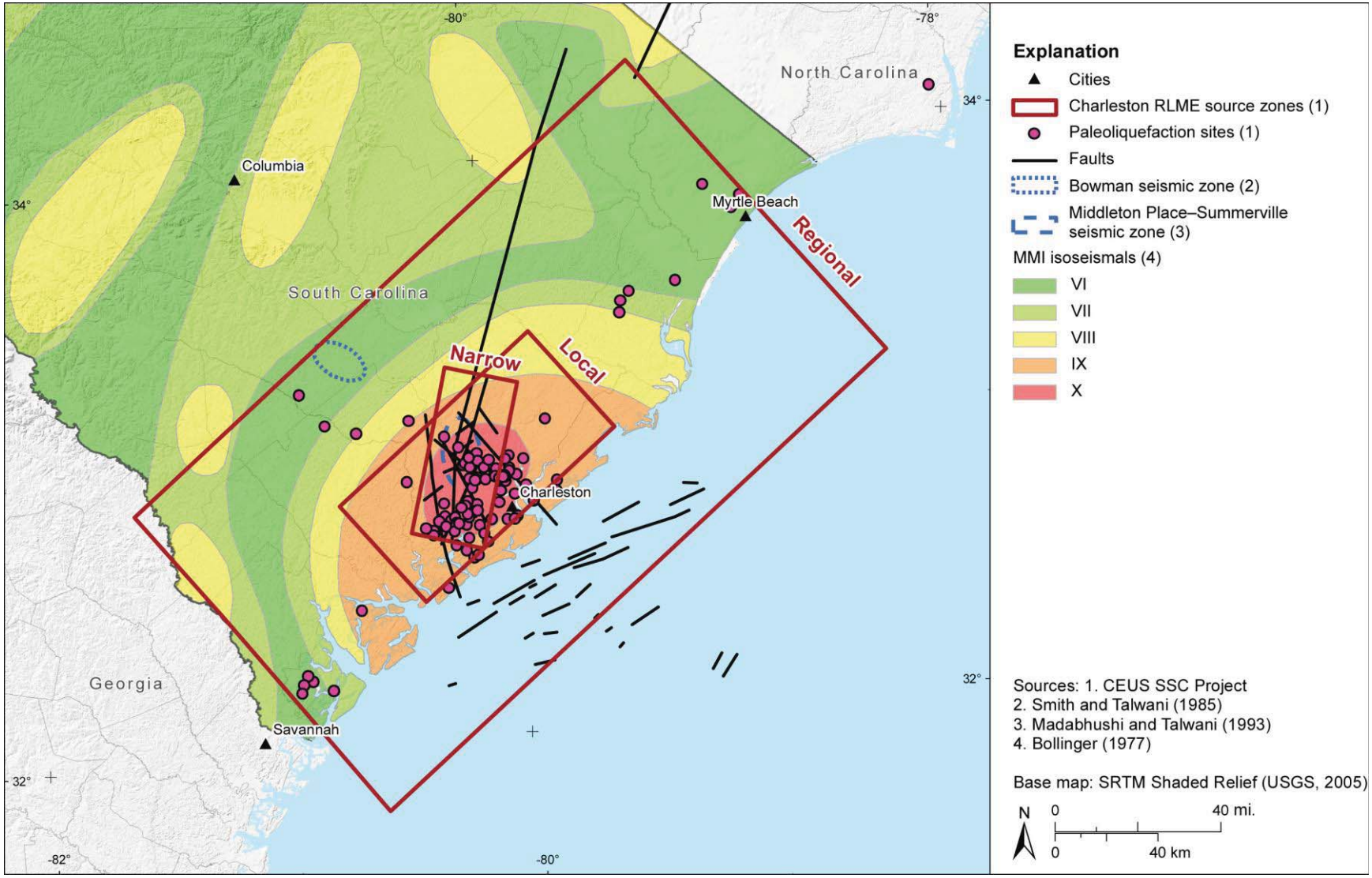

Figure 6.1.2-5a
Postulated faults and tectonic features in the Charleston region with Charleston RLME source zones

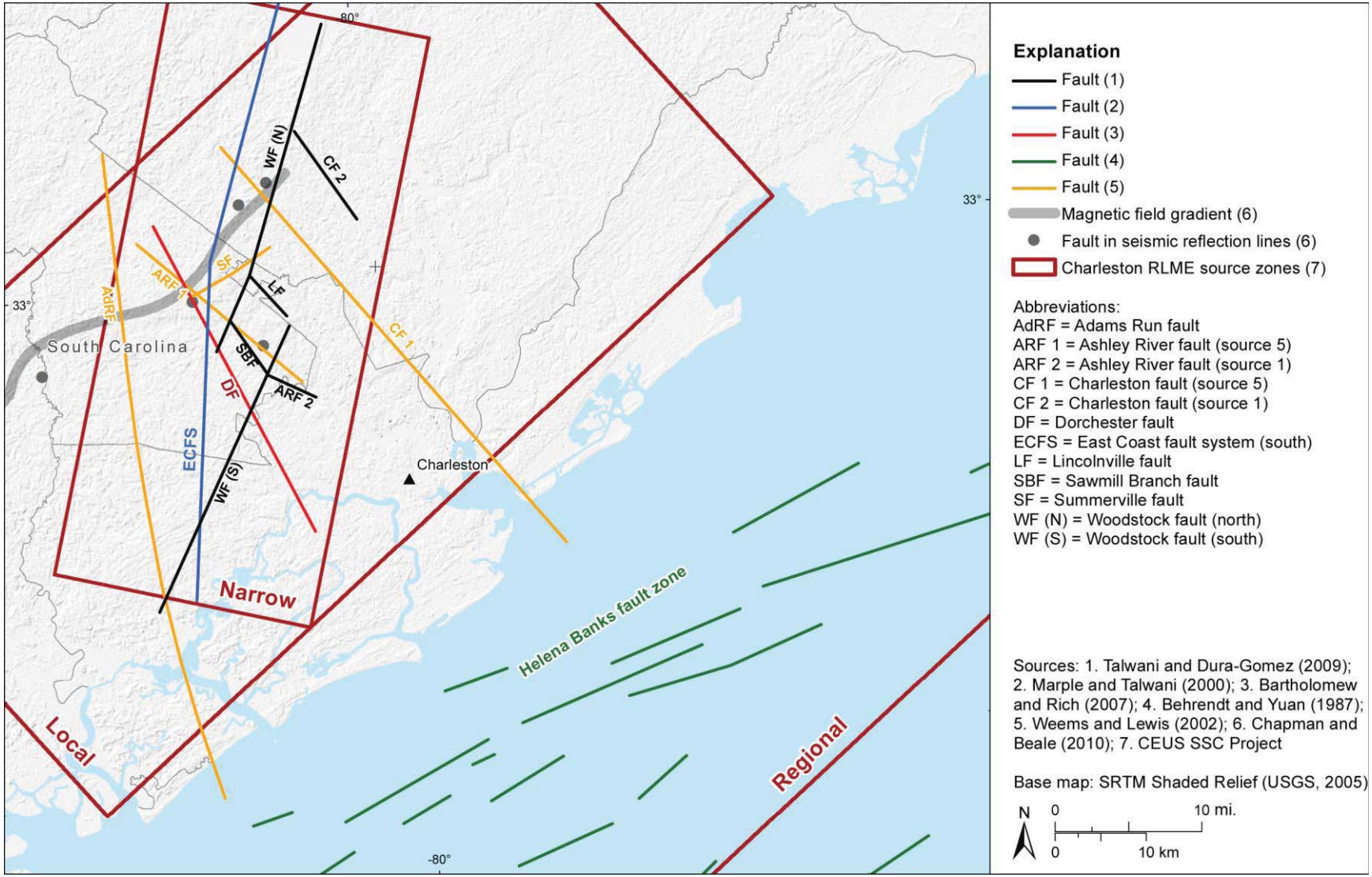

Figure 6.1.2-5b
Postulated faults and tectonic features in the local Charleston area with Charleston RLME source zones

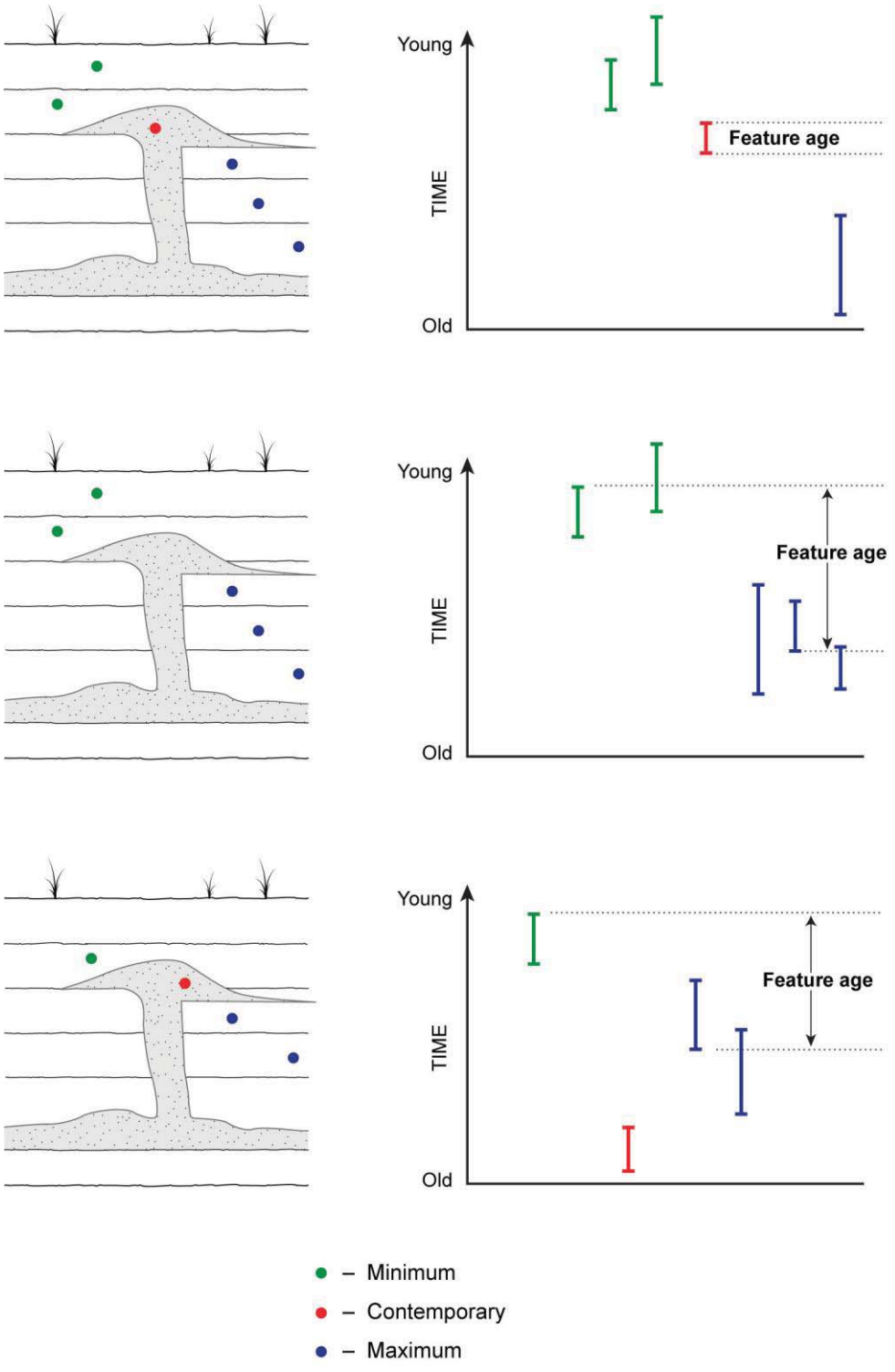

Figure 6.1.2-6
Schematic diagram showing contemporary, maximum, and minimum constraining age sample locations

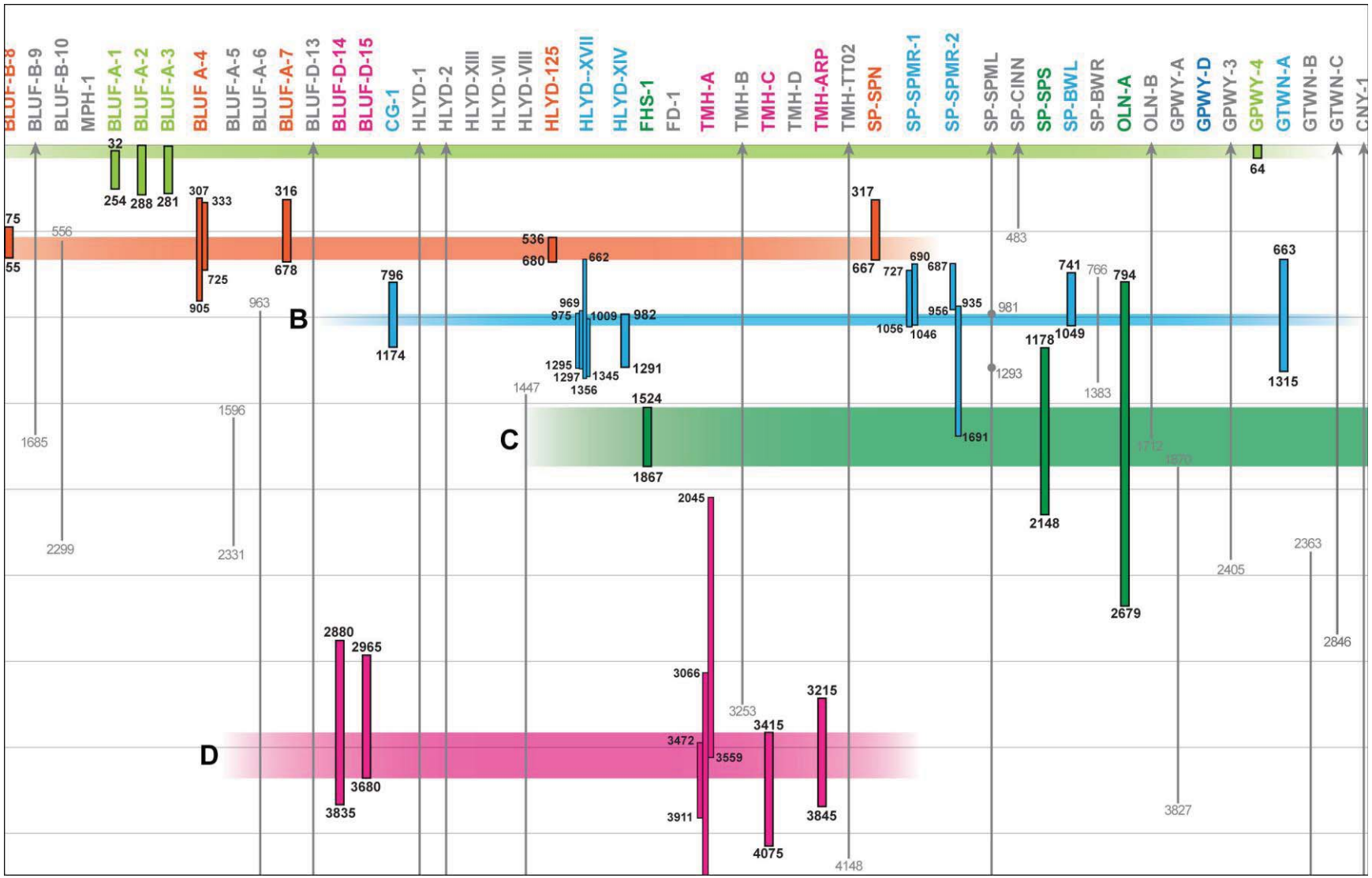

Figure 6.1.2-7
Charleston space-time diagram of earthquakes interpreted from paleoliquefaction, contemporary-ages-only scenario

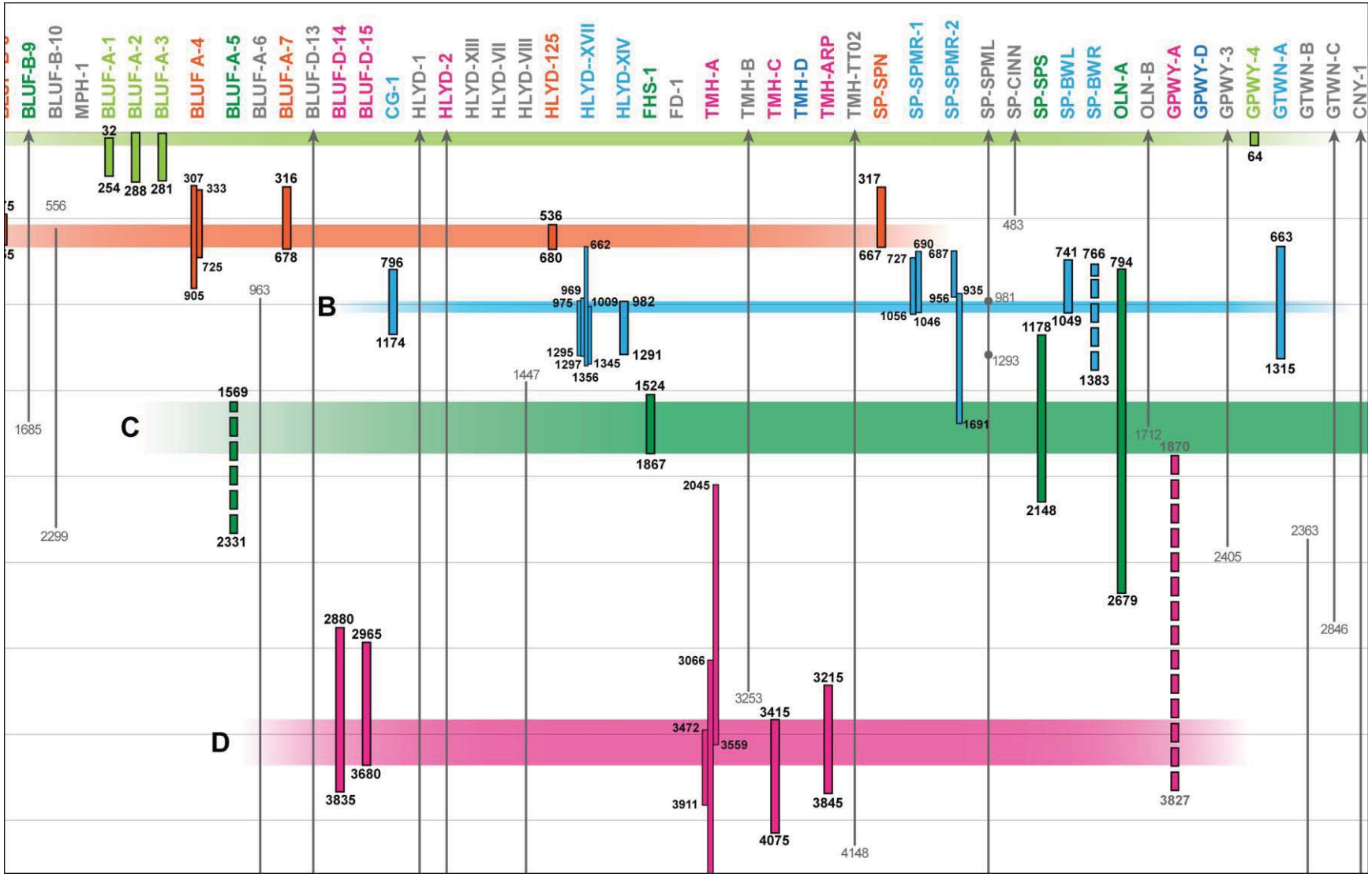

Figure 6.1.2-8
Charleston space-time diagram of earthquakes interpreted from paleoliquefaction, all-ages scenario

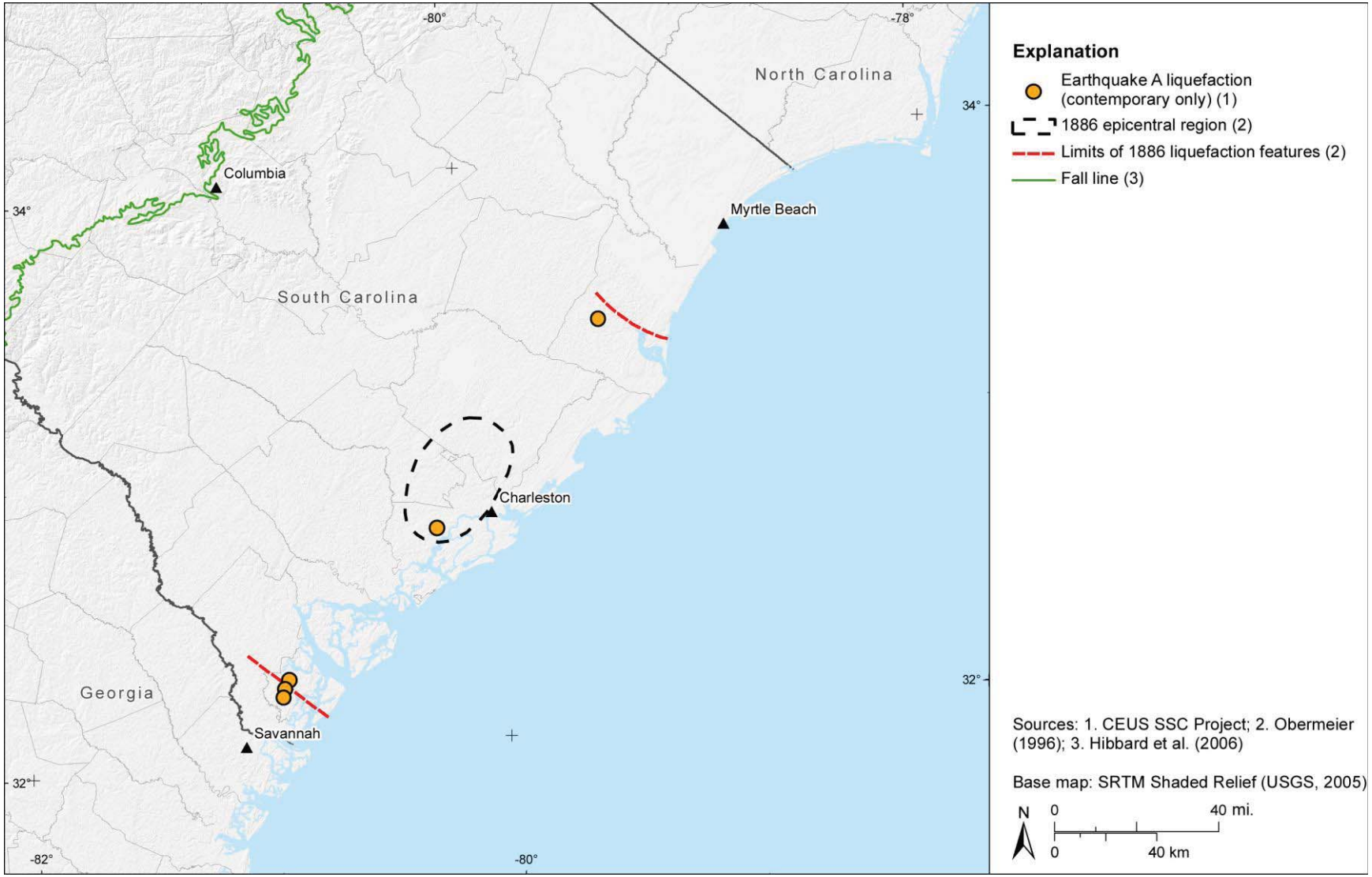

Figure 6.1.2-9
Distribution of liquefaction from earthquake A, contemporary-ages-only scenario

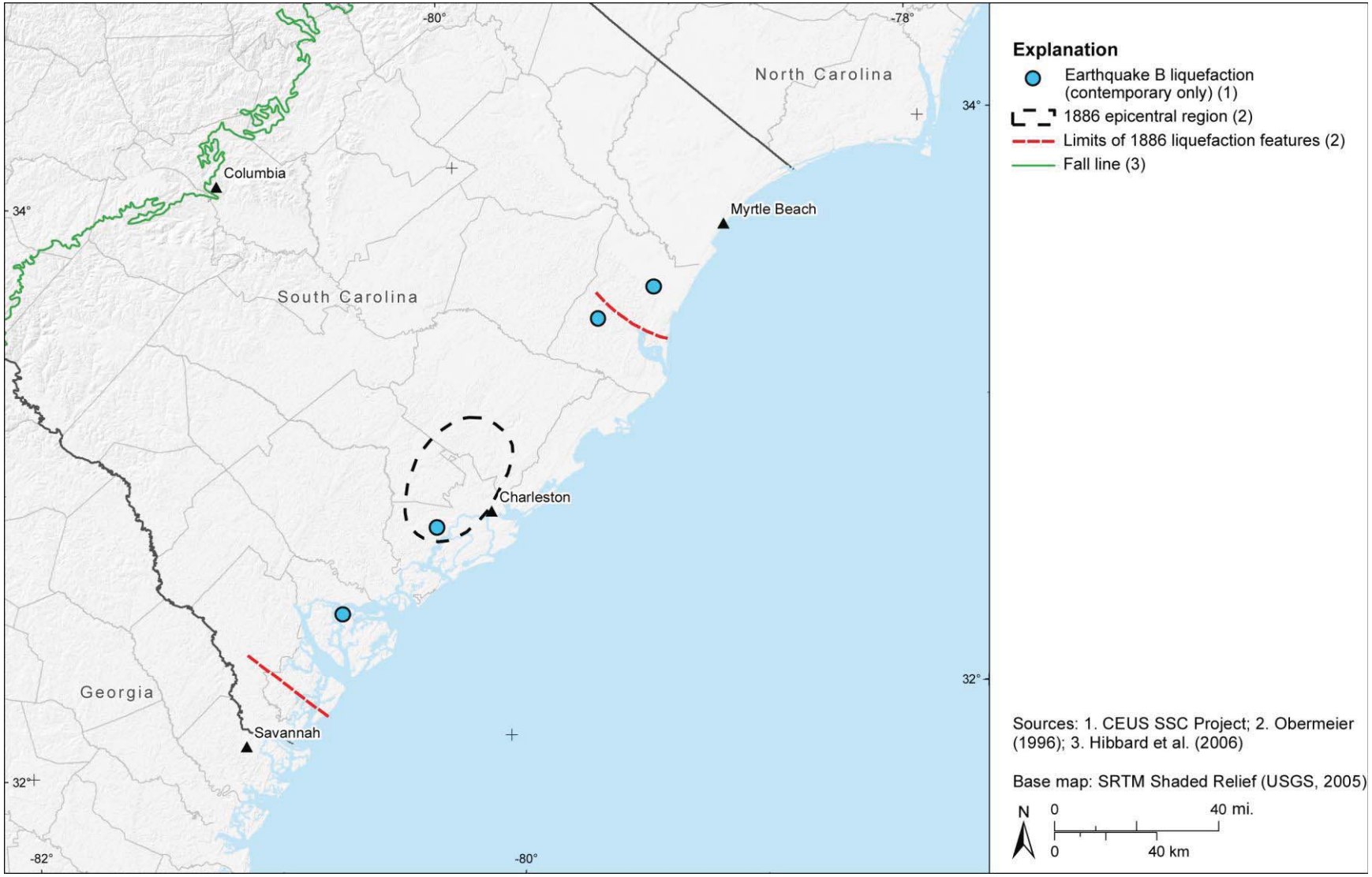

Figure 6.1.2-10
Distribution of liquefaction from earthquake B, contemporary-ages-only scenario

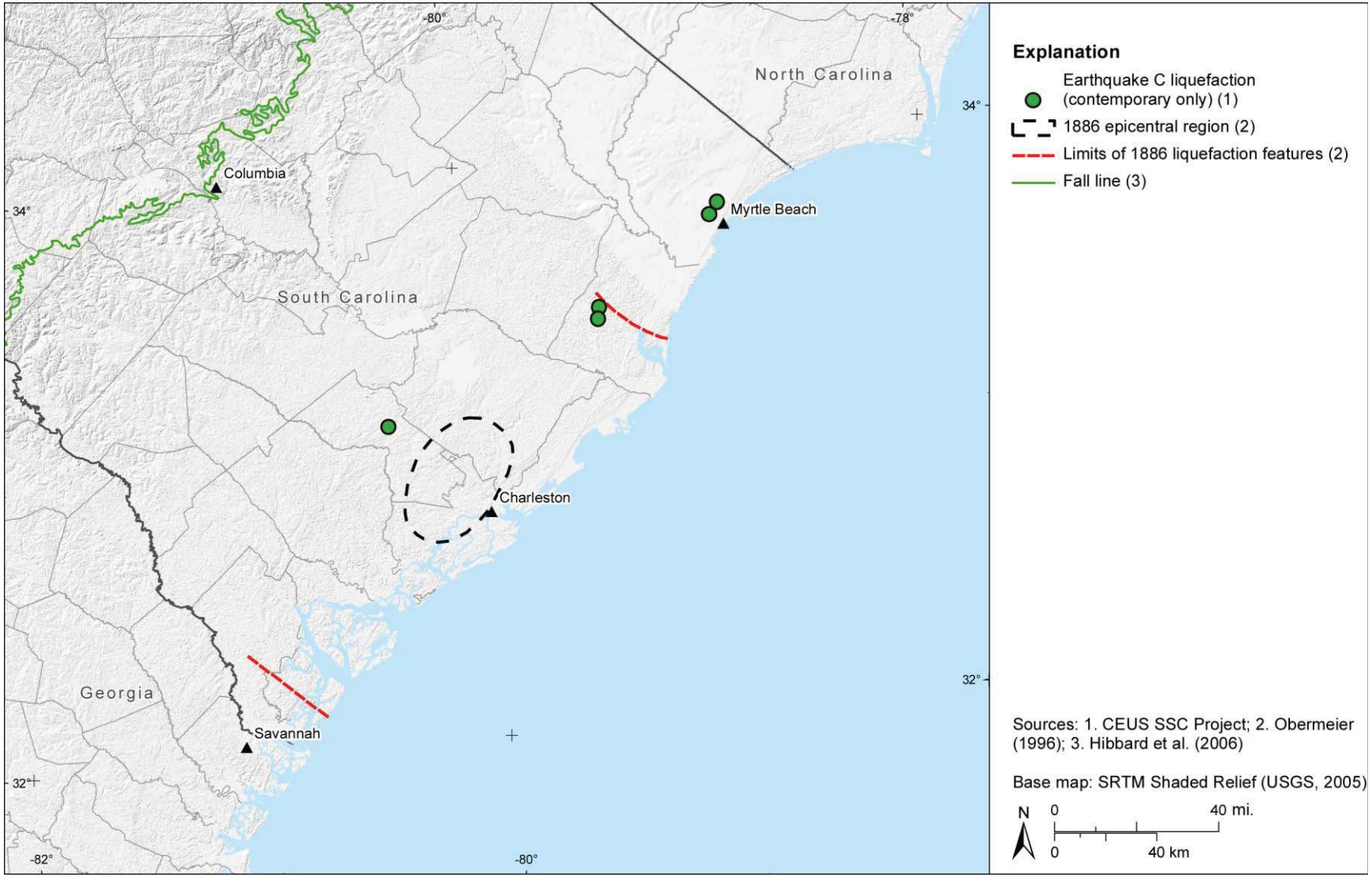

Figure 6.1.2-11
Distribution of liquefaction from earthquake C, contemporary-ages-only scenario

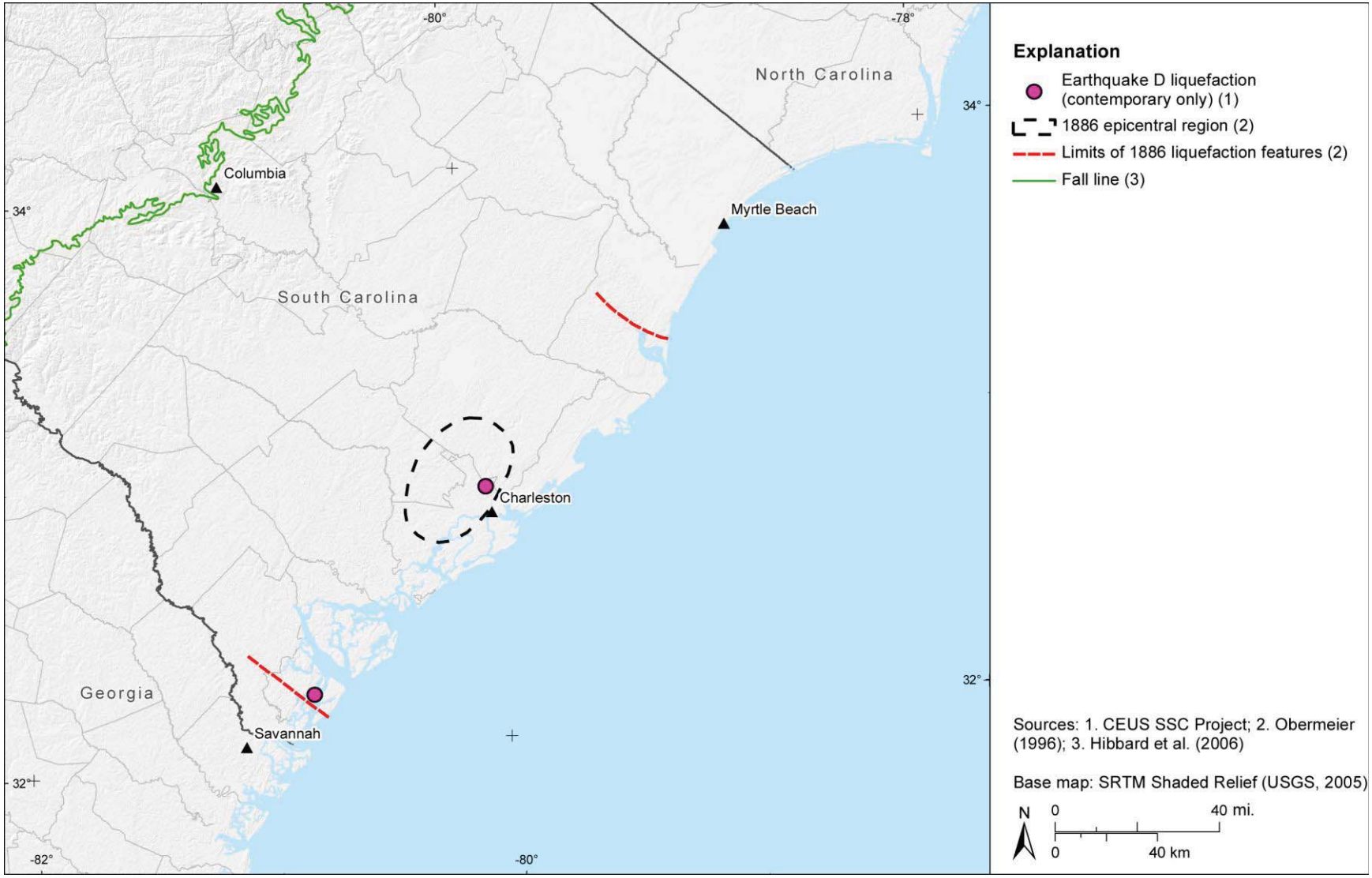

Figure 6.1.2-12
Distribution of liquefaction from earthquake D, contemporary-ages-only scenario

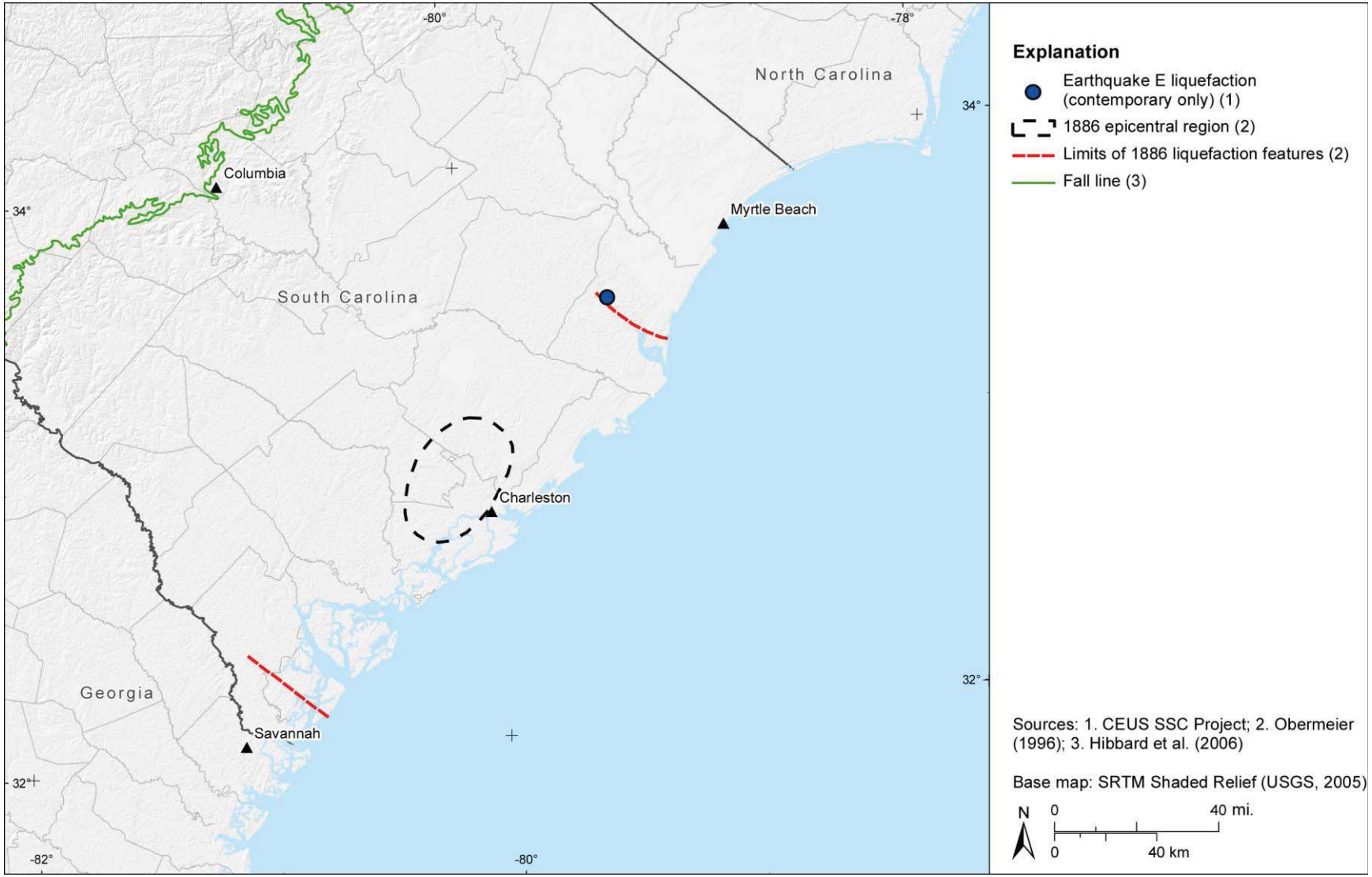

Figure 6.1.2-13
Distribution of liquefaction from earthquake E, contemporary-ages-only scenario

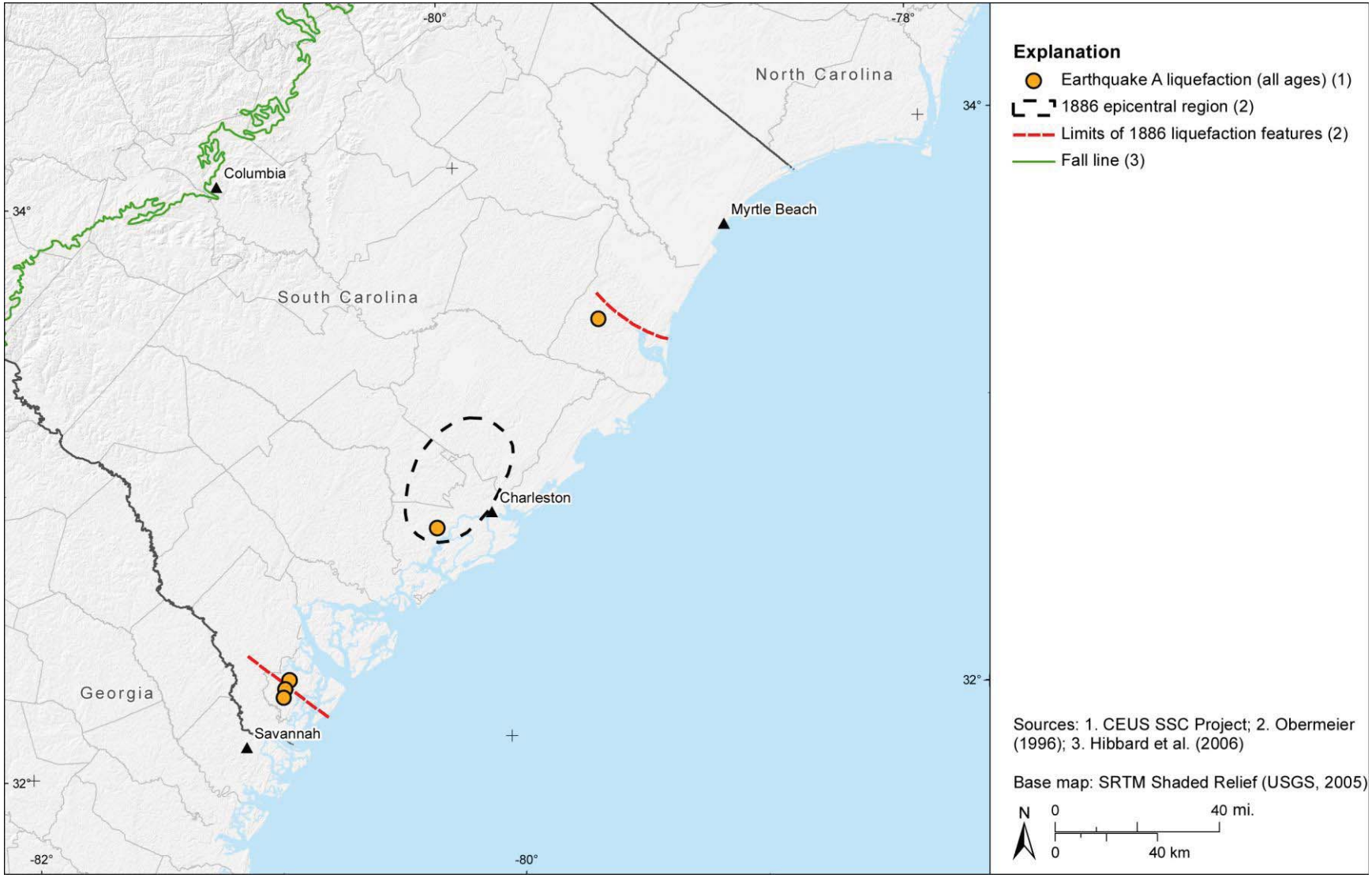

Figure 6.1.2-14
Distribution of liquefaction from earthquake A, all-ages scenario

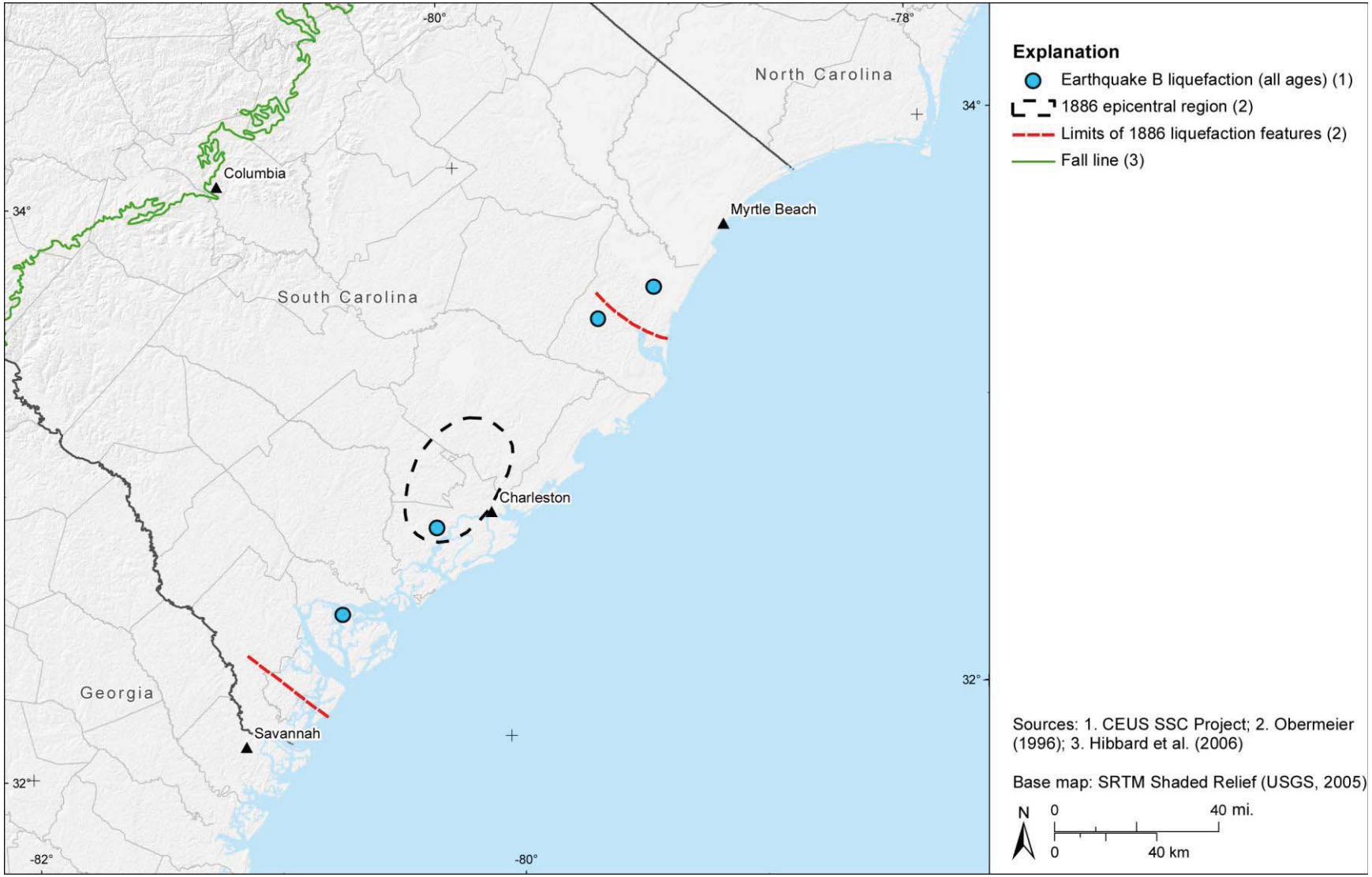

Figure 6.1.2-15
Distribution of liquefaction from earthquake B, all-ages scenario

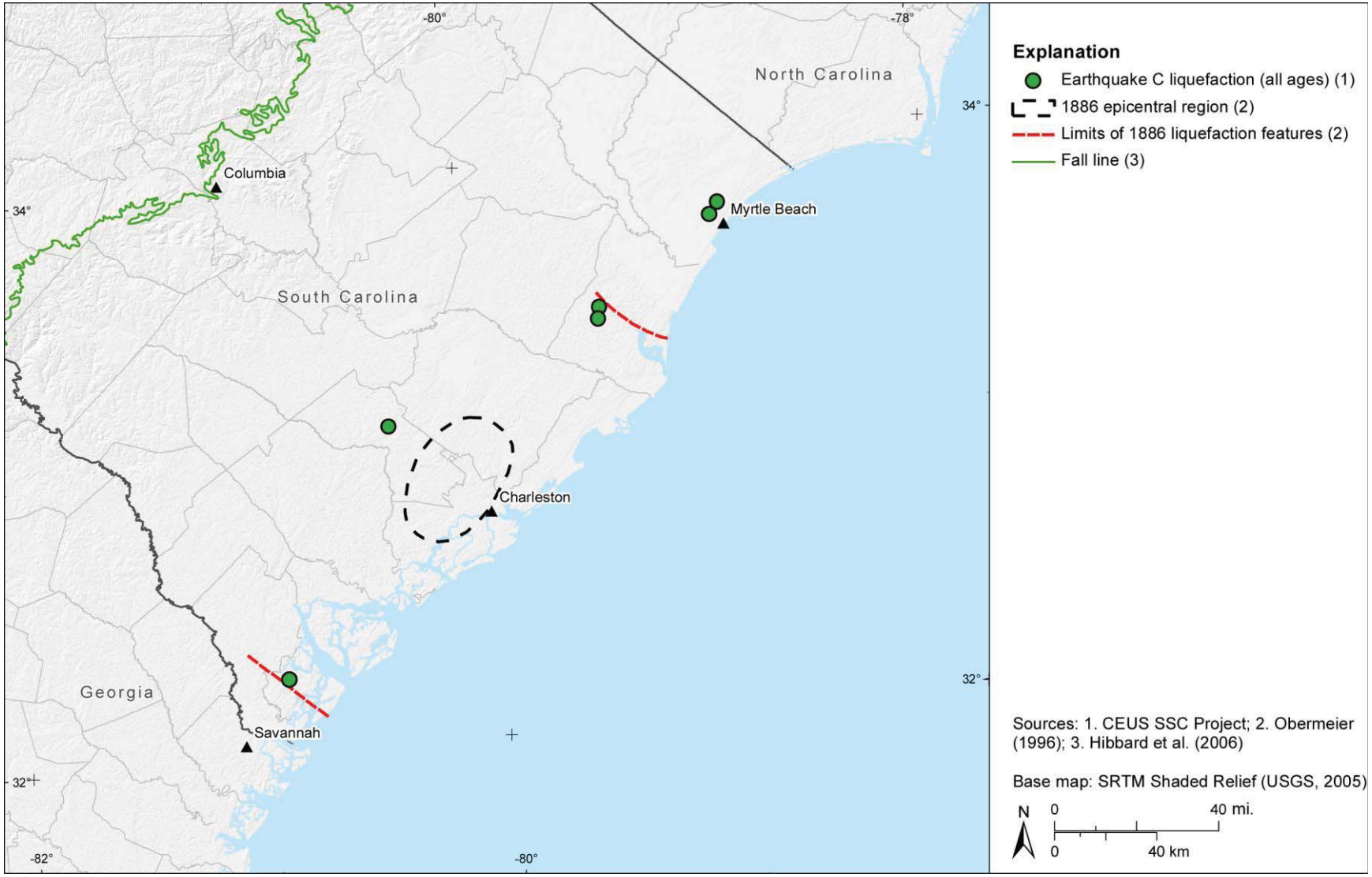

Figure 6.1.2-16
Distribution of liquefaction from earthquake C, all-ages scenario

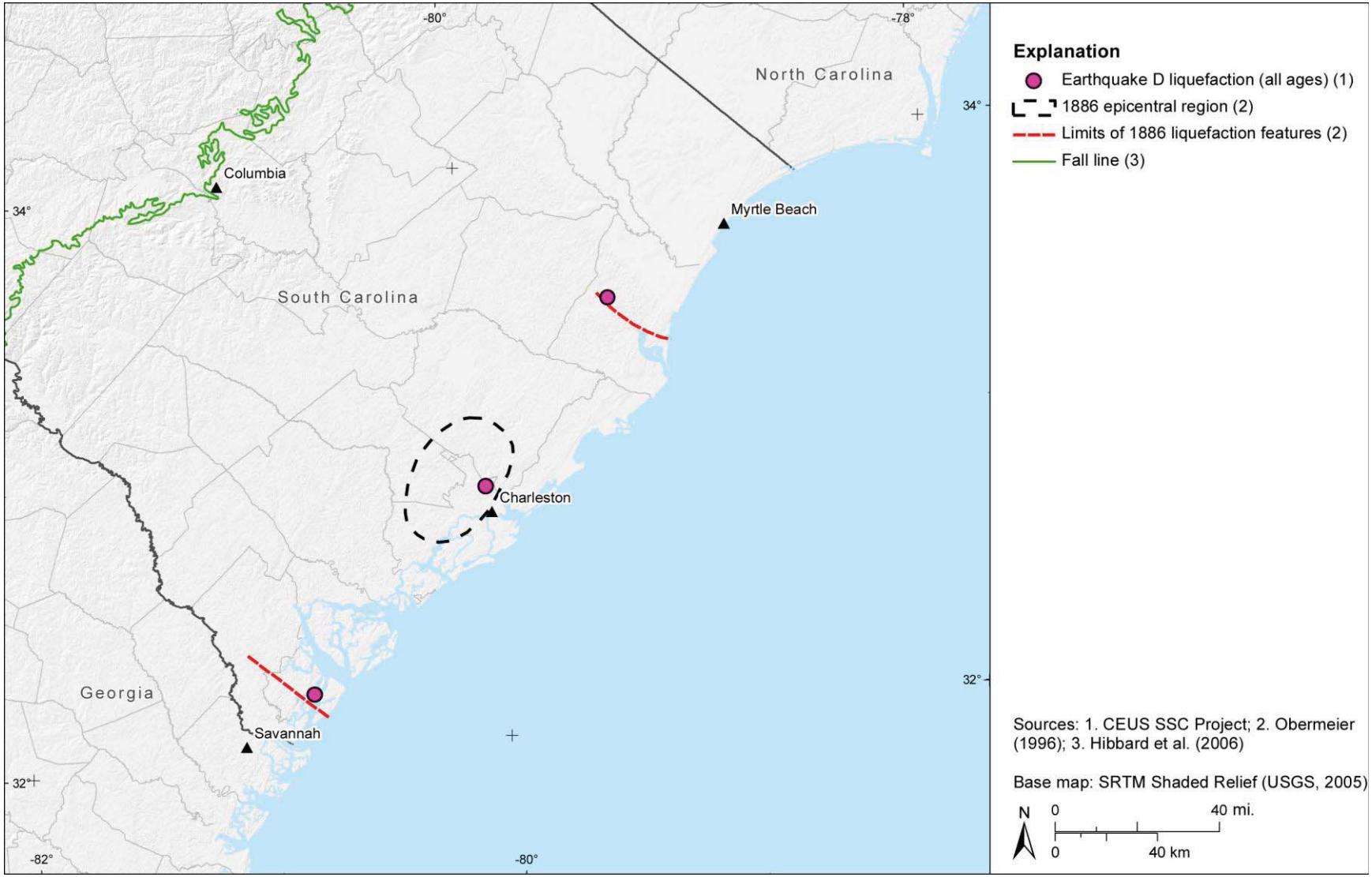

Figure 6.1.2-17
Distribution of liquefaction from earthquake D, all-ages scenario

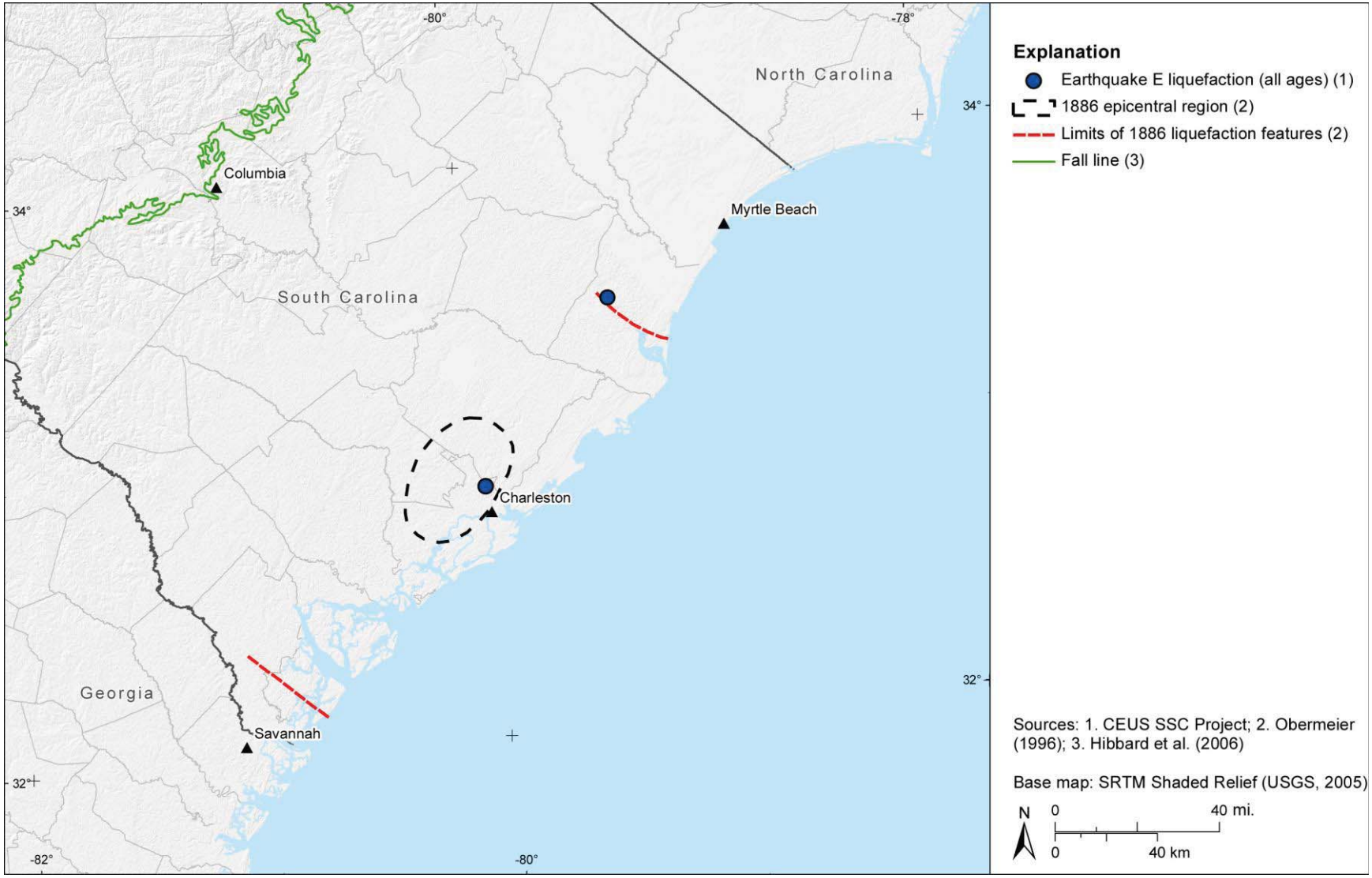

Figure 6.1.2-18
Distribution of liquefaction from earthquake E, all-ages scenario

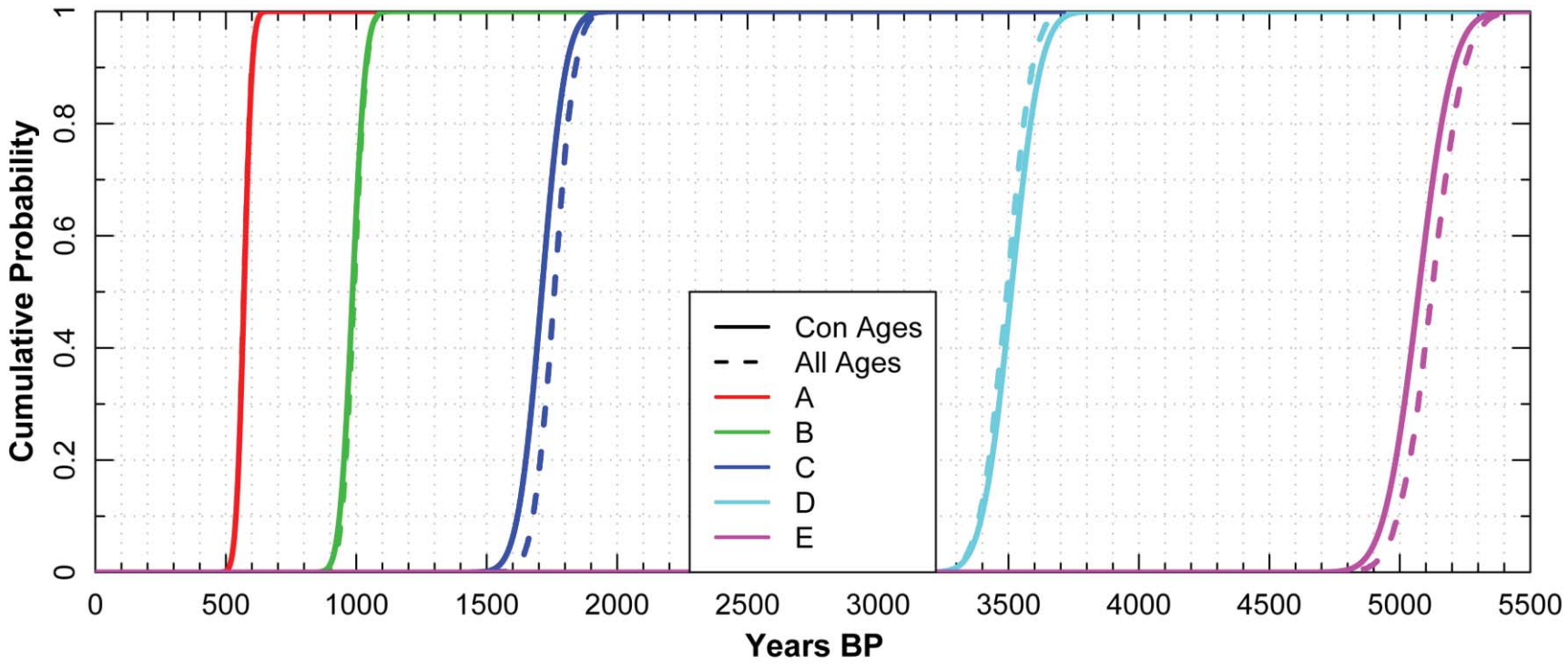

Figure 6.1.2-19
Uncertainty distributions for the age of Charleston RLMEs

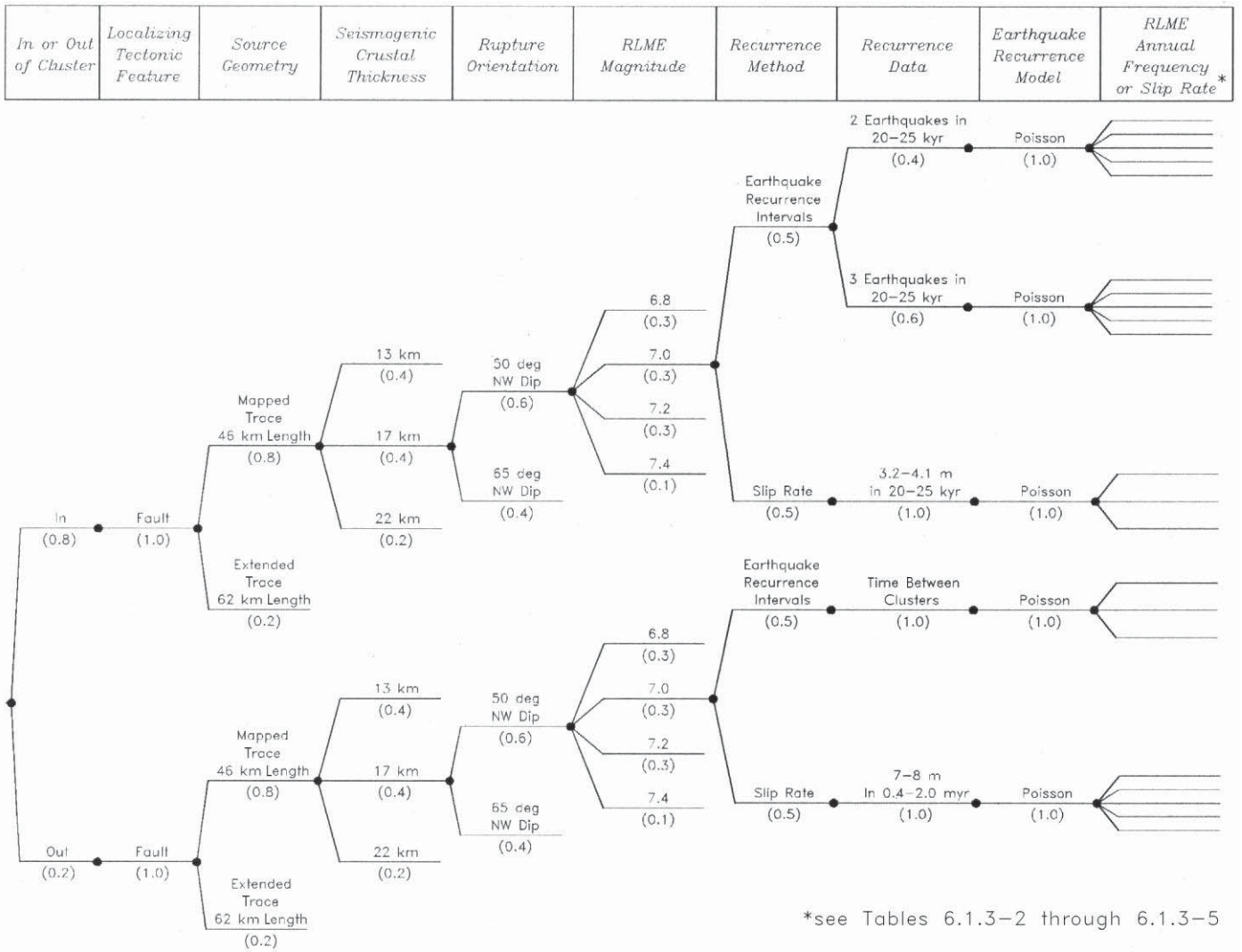

Figure 6.1.3-1
Logic tree for the Cheraw fault RLME source

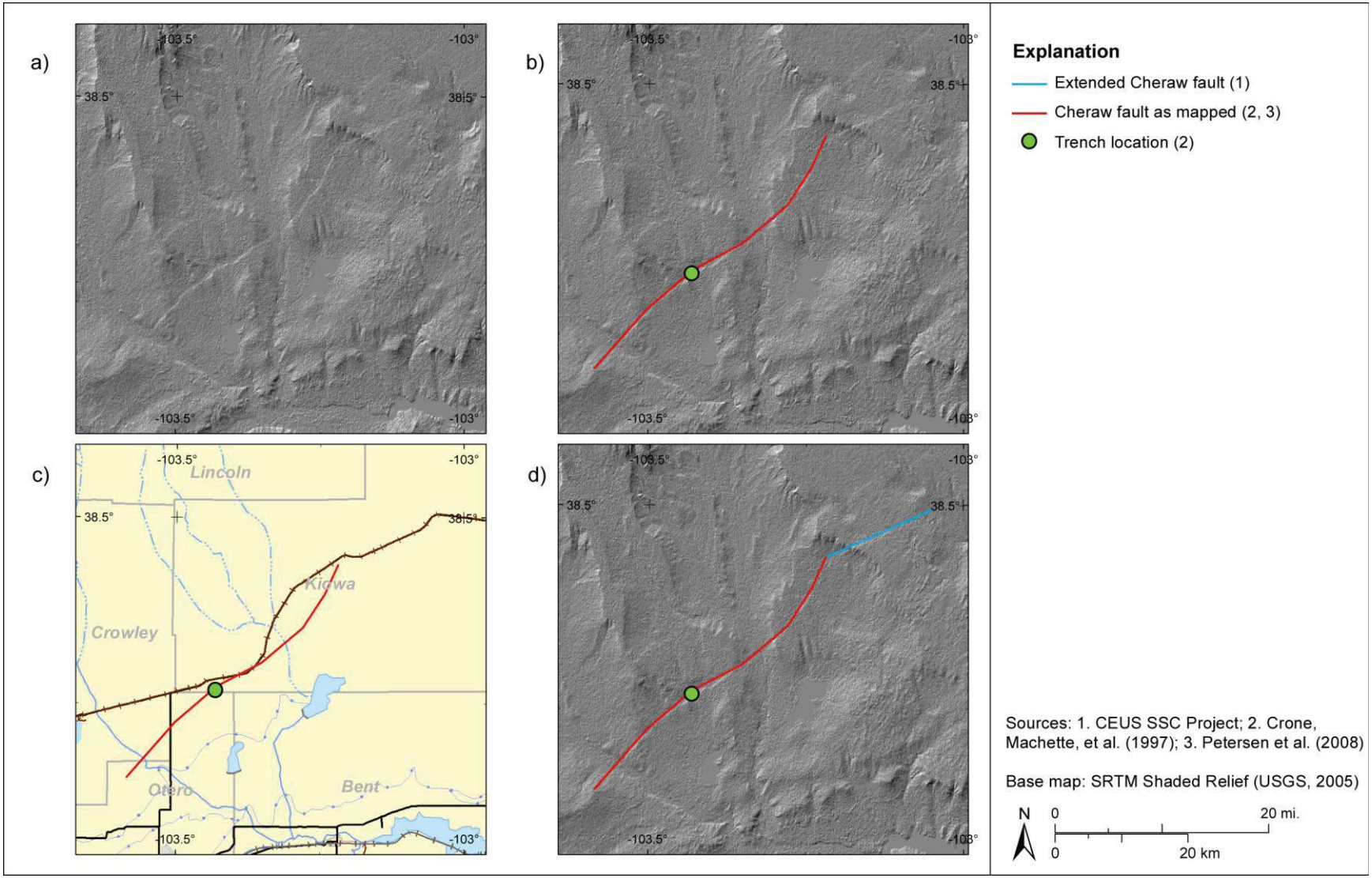

Figure 6.1.3-2
Map (c) and hillshade relief images (a, b, and d) showing location of mapped Cheraw fault, possible northeast extension, and paleoseismic locality

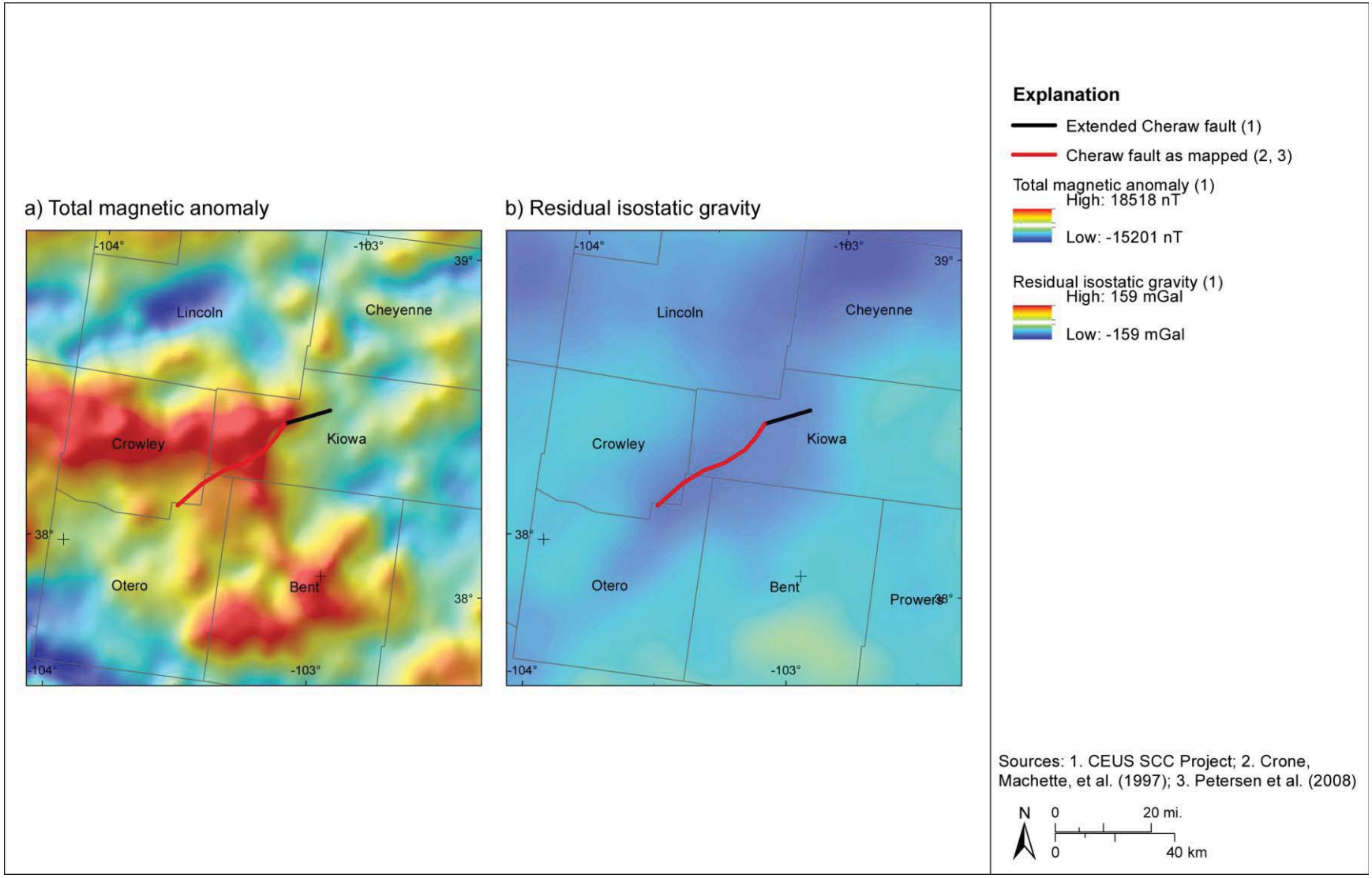

Figure 6.1.3-3
Cheraw RLME source relative to (a) total magnetic anomaly and (b) residual isostatic gravity data

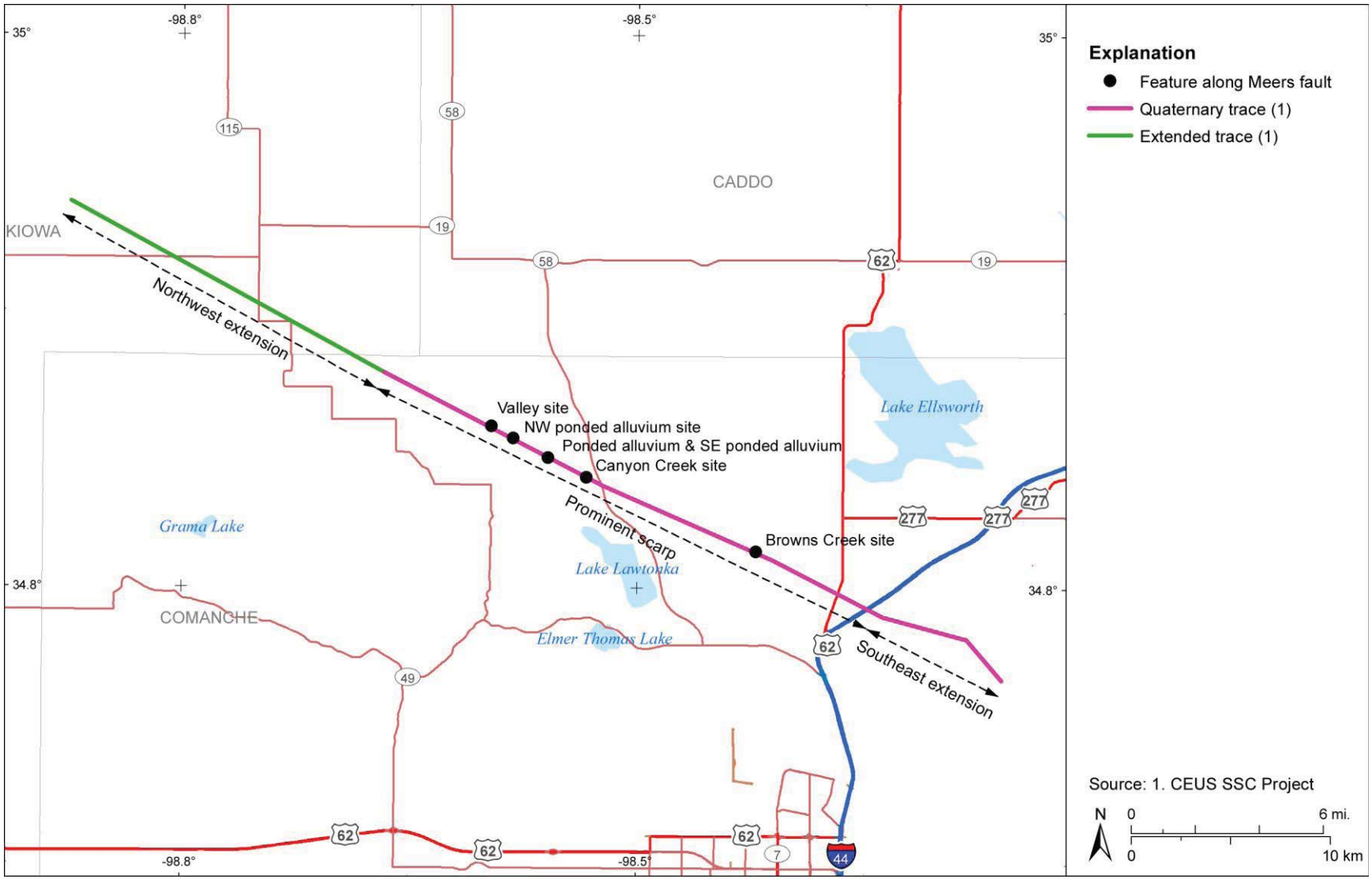

Figure 6.1.4-1
Meers fault location

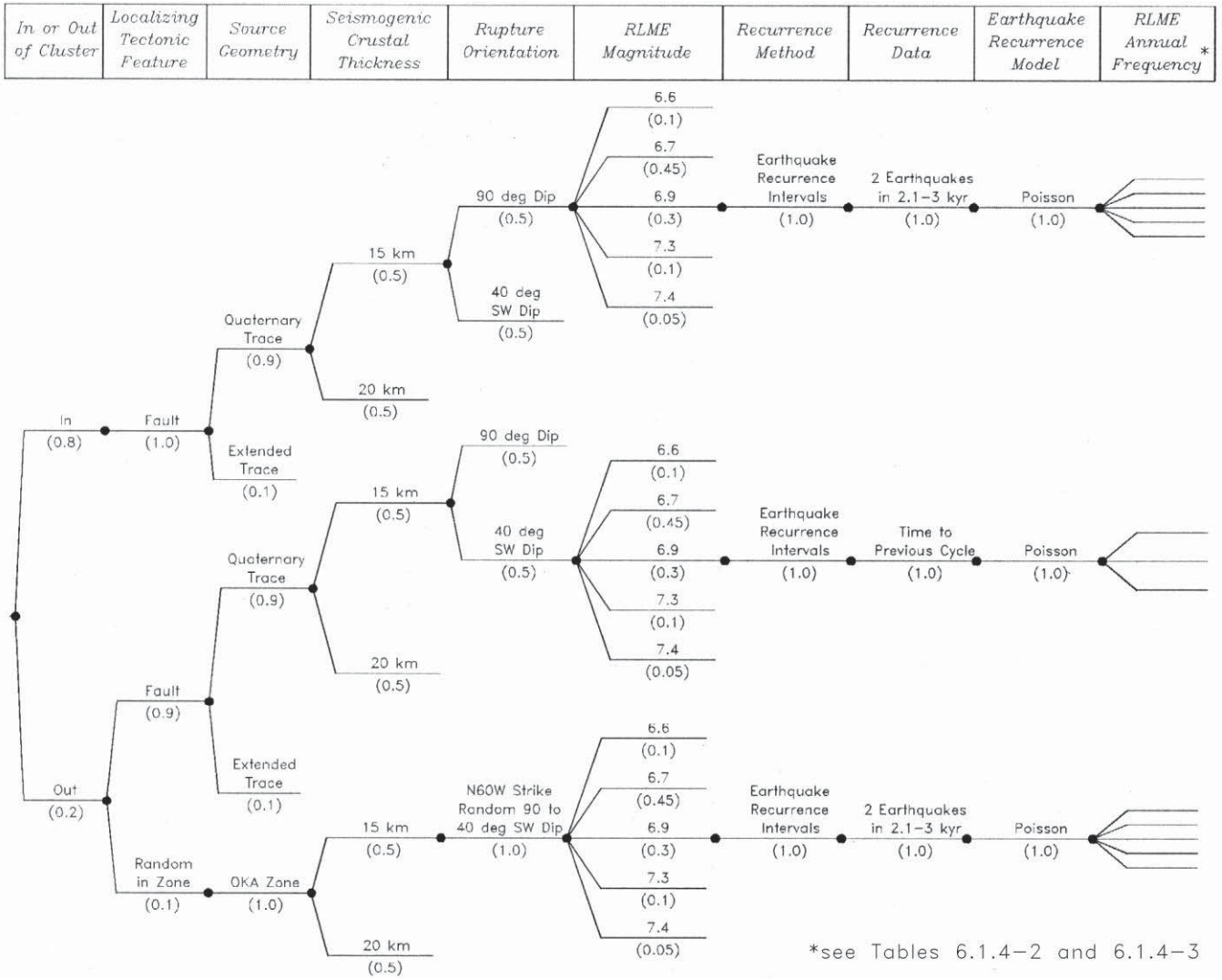

Figure 6.1.4-2
Logic tree for the Meers fault source

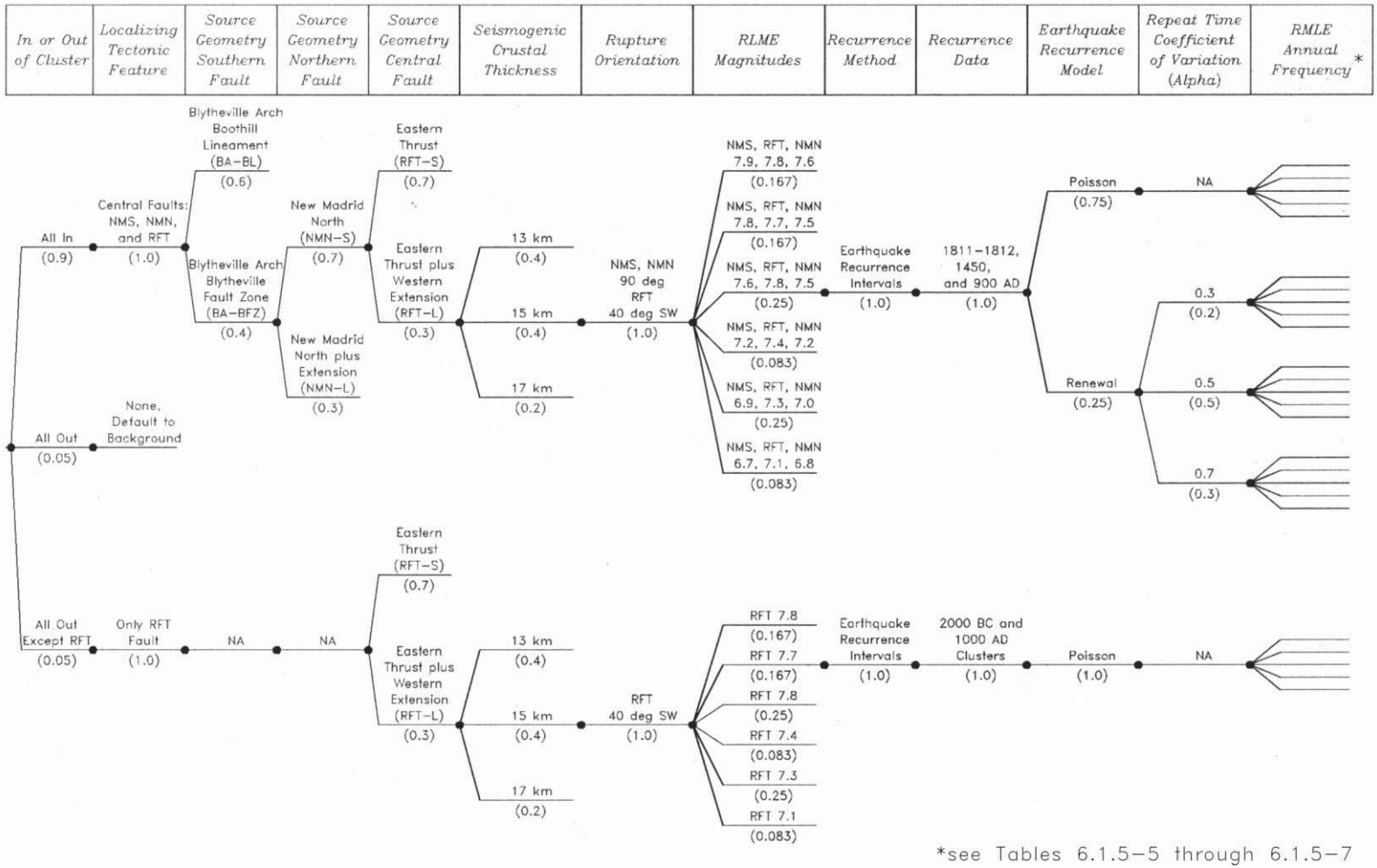

Figure 6.1.5-1
Logic tree for the NMFS RLME source

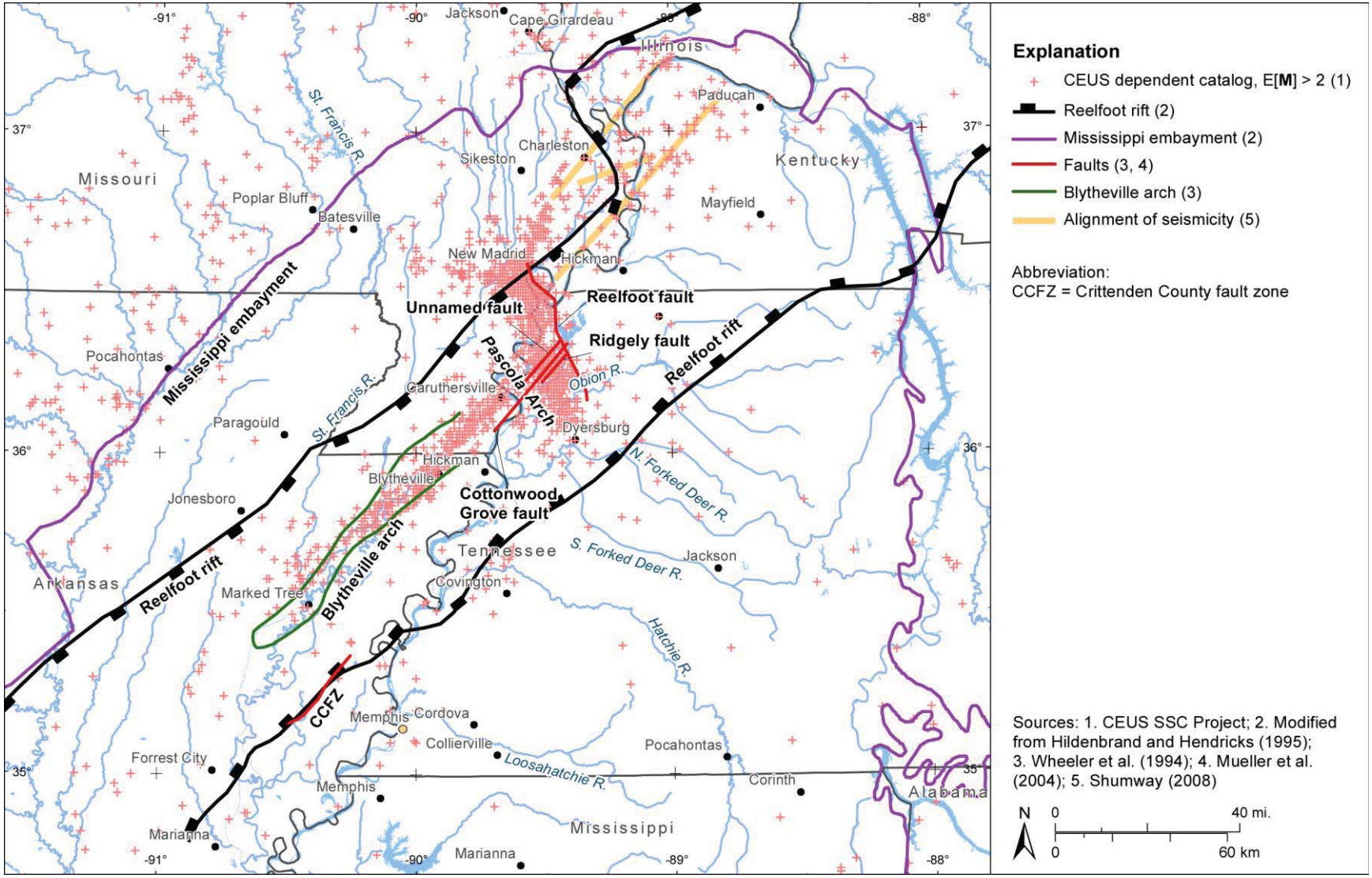

Figure 6.1.5-2
Map showing seismicity and major subsurface structural features in the New Madrid region

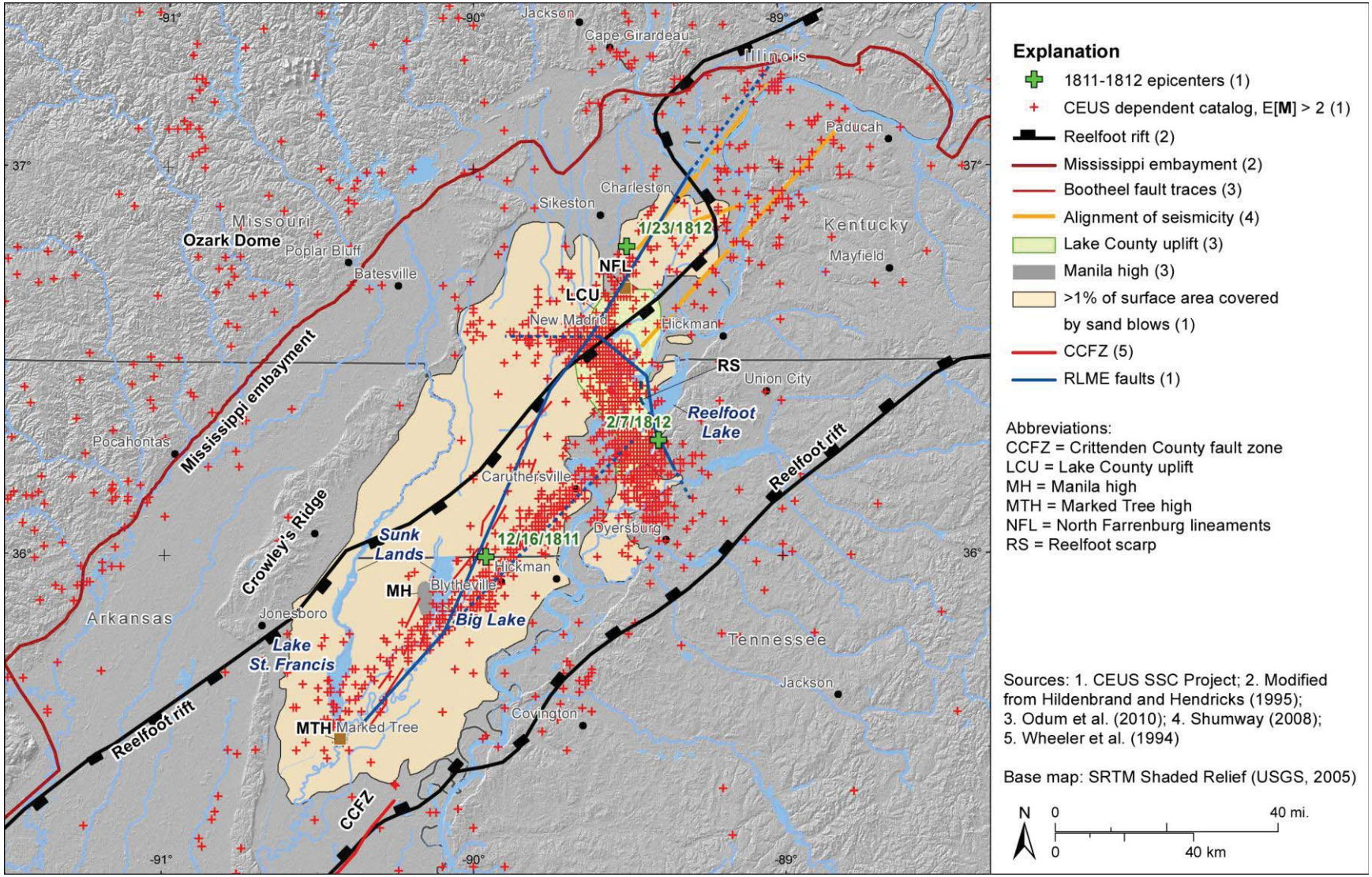

Figure 6.1.5-3
Map showing geomorphic and near-surface tectonic features in the New Madrid region and locations of NMFS RLME fault sources

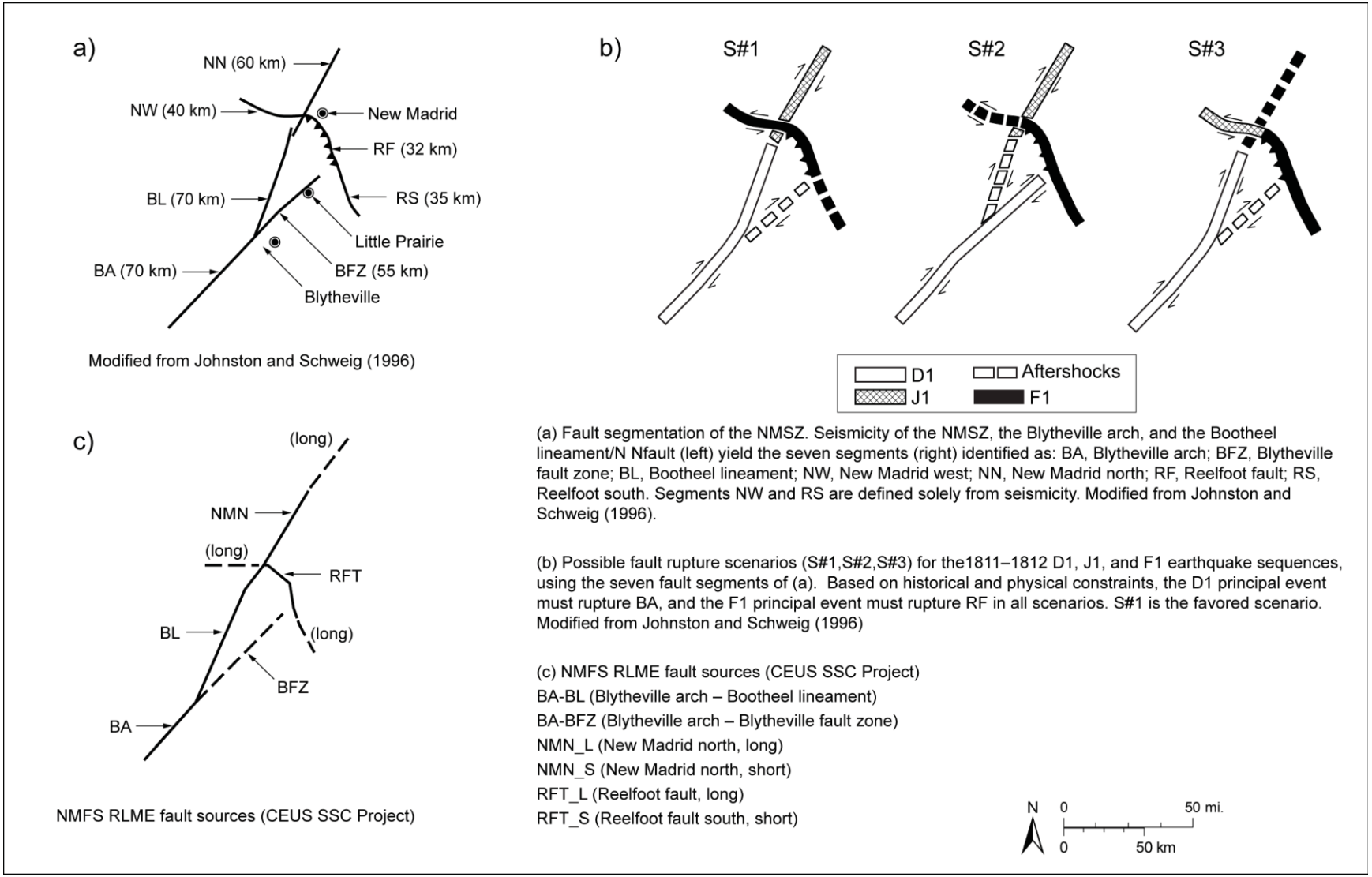

Figure 6.1.5-4
Rupture segments (a) and models (b) for the New Madrid faults from Johnston and Schweig (1996) and (c) the NMFS RLME fault sources

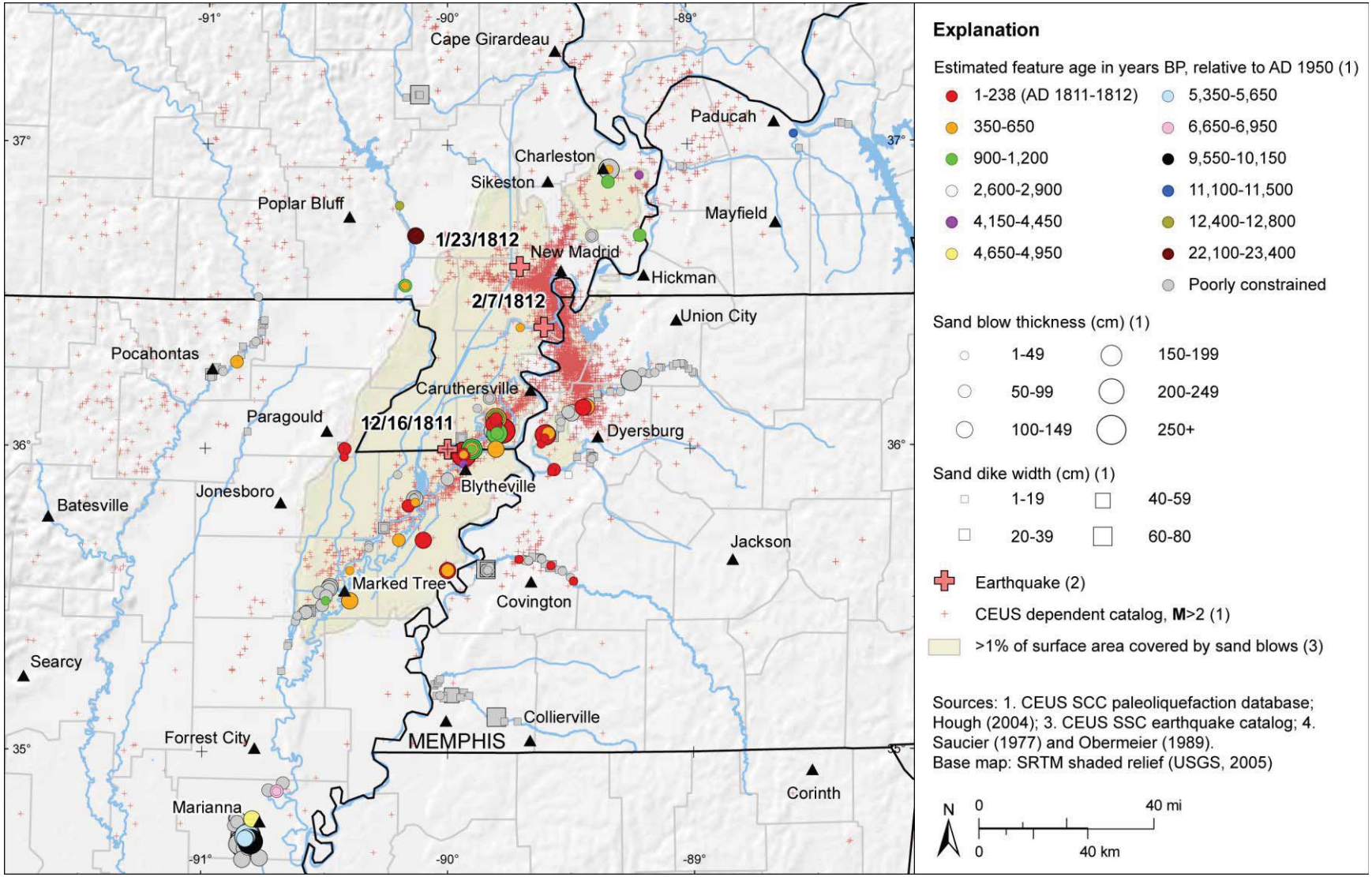

Figure 6.1.5-5
Map of NMSZ showing estimated ages and measured sizes of liquefaction features

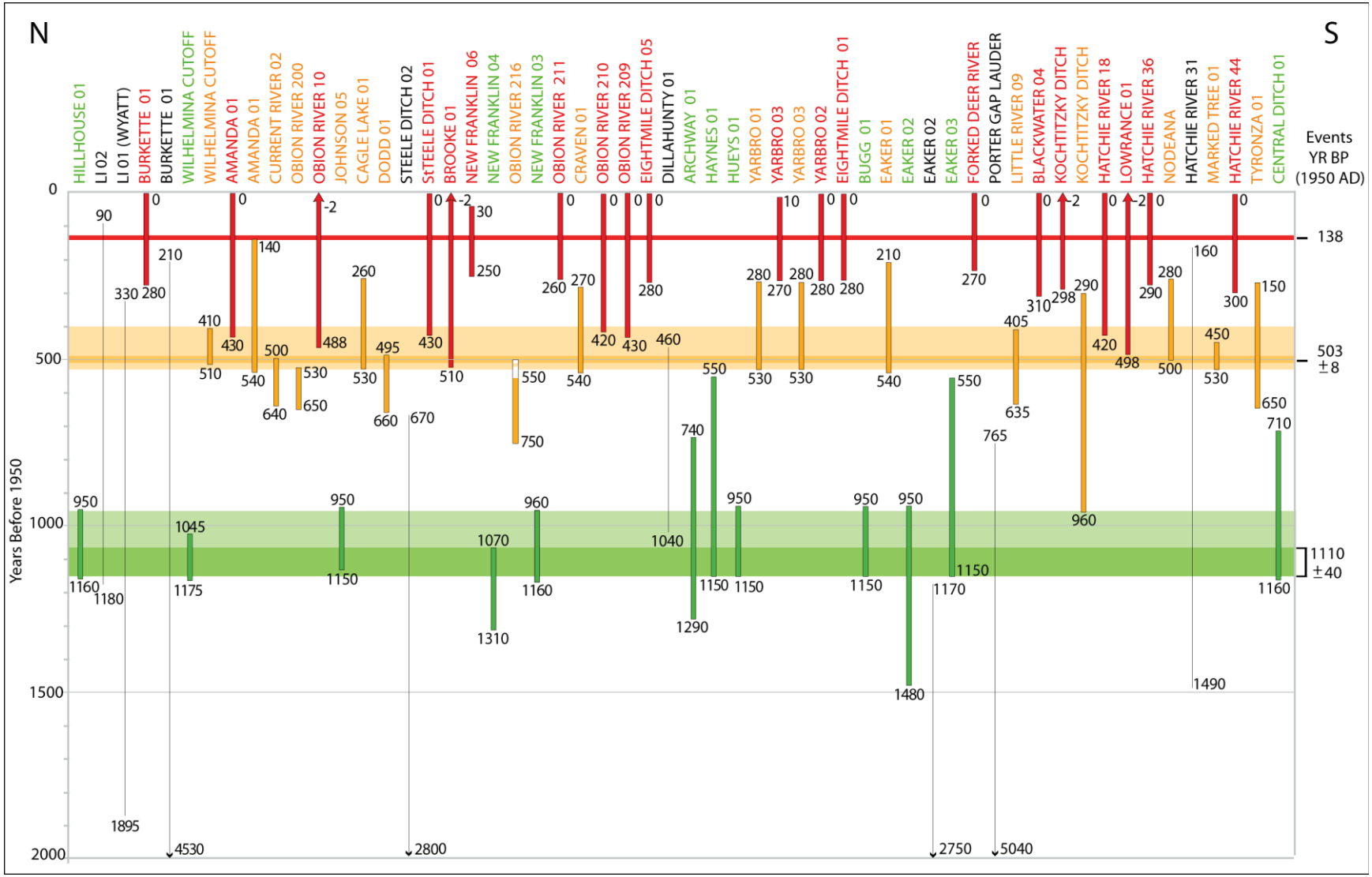

Figure 6.1.5-6
Earthquake chronology for NMSZ from dating and correlation of liquefaction features at sites (listed at top) along N-S transect across region

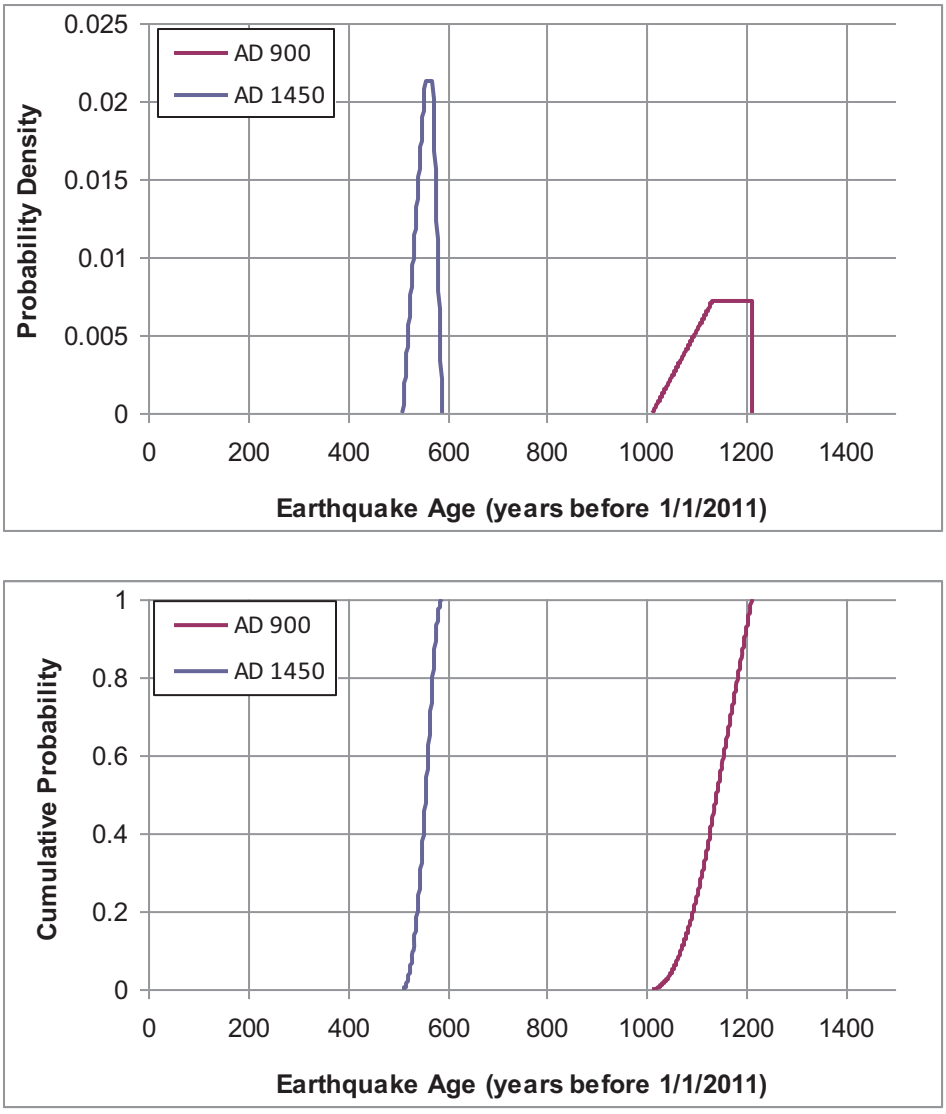

Figure 6.1.5-7
Probability distributions for the age of the AD 900 and AD 1450 NMFS RLMEs

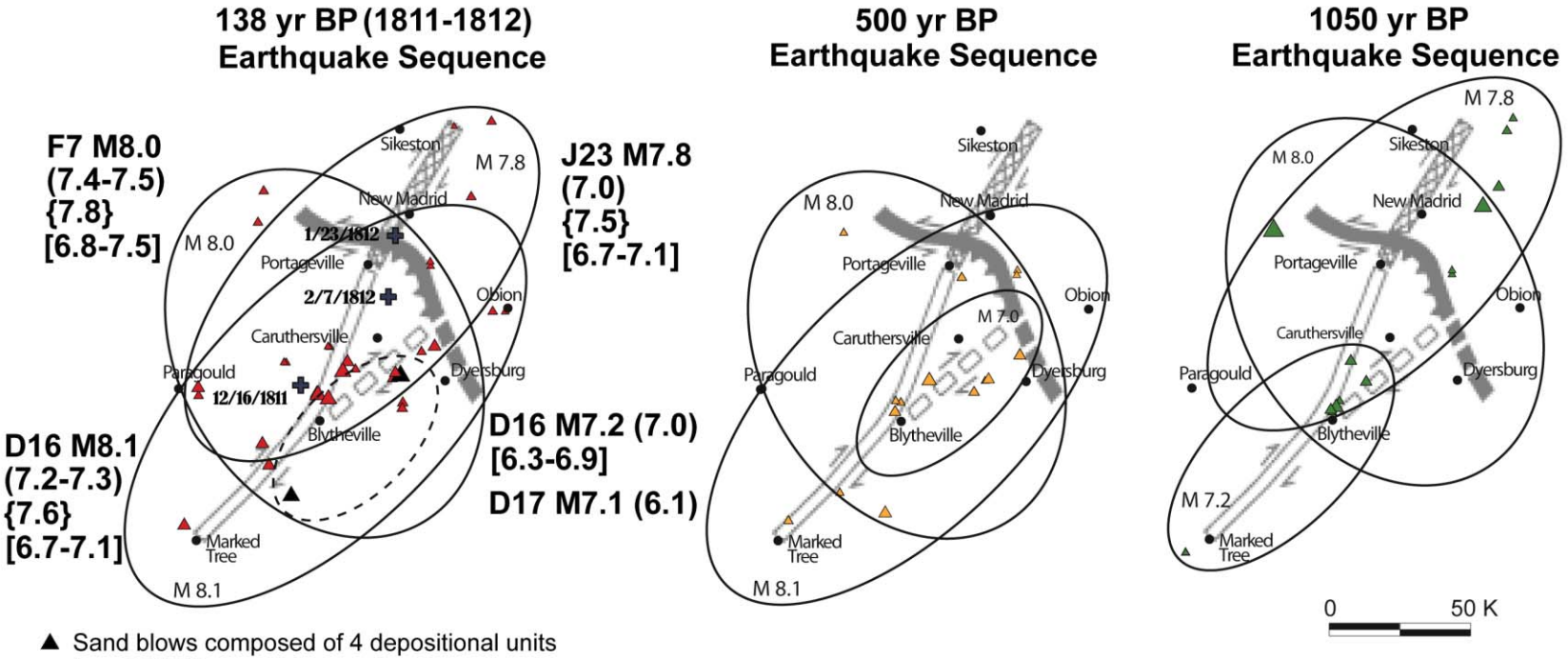

▲ Sand blows composed of 4 depositional units (as of 2001)

1811-1812 Main Shocks:
D16: December 16, 1811 earthquake
J23: January 23, 1812 earthquake
F7: February 7, 1812 earthquake

Estimated Magnitudes:
M 8.0 Johnston and Schweig (1996)
(7.4-7.5) Hough et al. (2000); Hough and Martin (2002)
{7.8} Bakun and Hopper (2004)
[6.8-7.5] Hough and Page (2011)

Source: Modified from Tuttle (2009)

Figure 6.1.5-8
Liquefaction fields for the 1811-1812, AD 1450, and AD 900 earthquakes as interpreted from spatial distribution and stratigraphy of sand blows

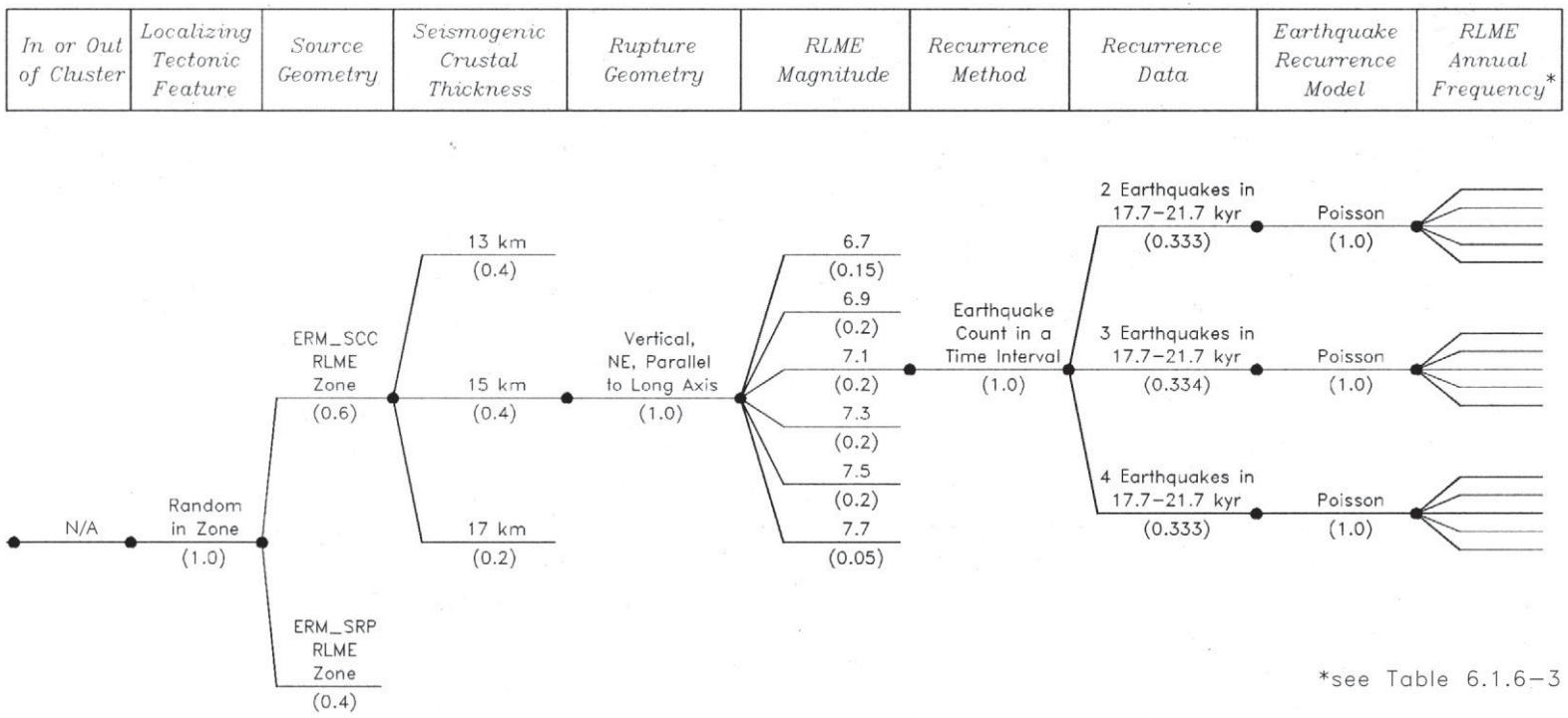

Figure 6.1.6-1a
Logic tree for the Reelfoot Rift–Eastern Rift Margin South RLME source. Two options for the southern extent of the ERM-S are considered: ERM-SCC includes the Crittenden County fault zone, and ERM-SRP includes the postulated zone of deformation based on fault picks identified in a high-resolution seismic profile along the Mississippi River.

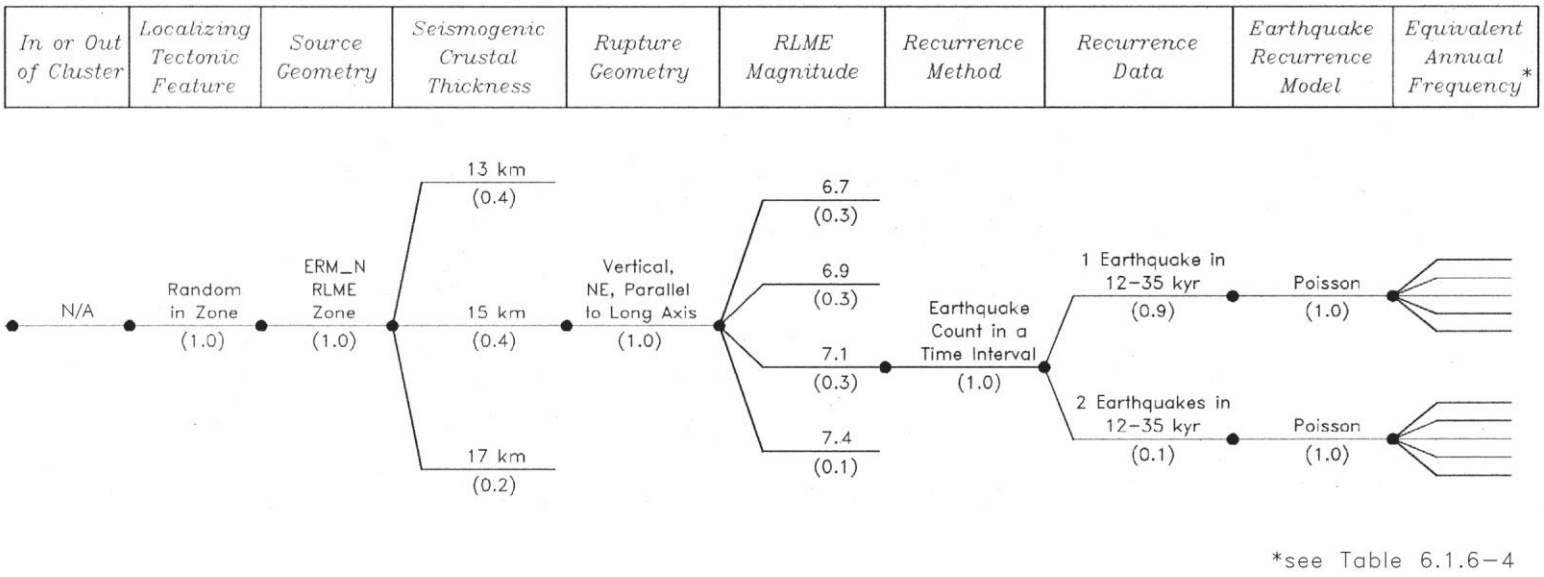

Figure 6.1.6-1b
Logic tree for the Reelfoot Rift–Eastern Rift Margin North RLME source

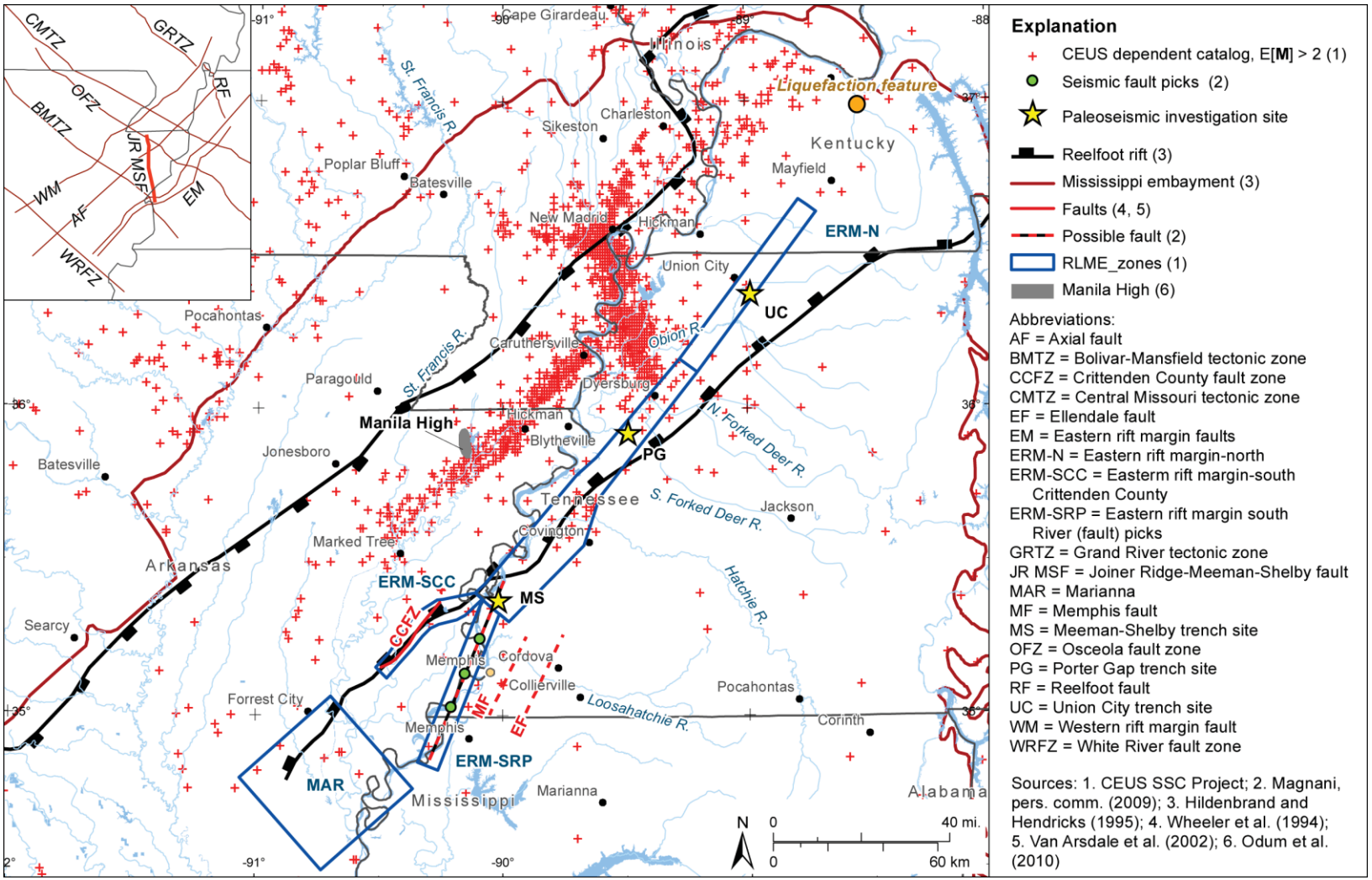

Figure 6.1.6-2
Map showing structural features and paleoseismic investigation sites along the eastern margin of the Reelfoot rift. The inset map shows the locations of inferred basement faults that border and cross the Reelfoot rift (Csontos et al., 2008) and the inferred Joiner Ridge–Meeman-Shelby fault (JR-MSF; Odum et al., 2010).

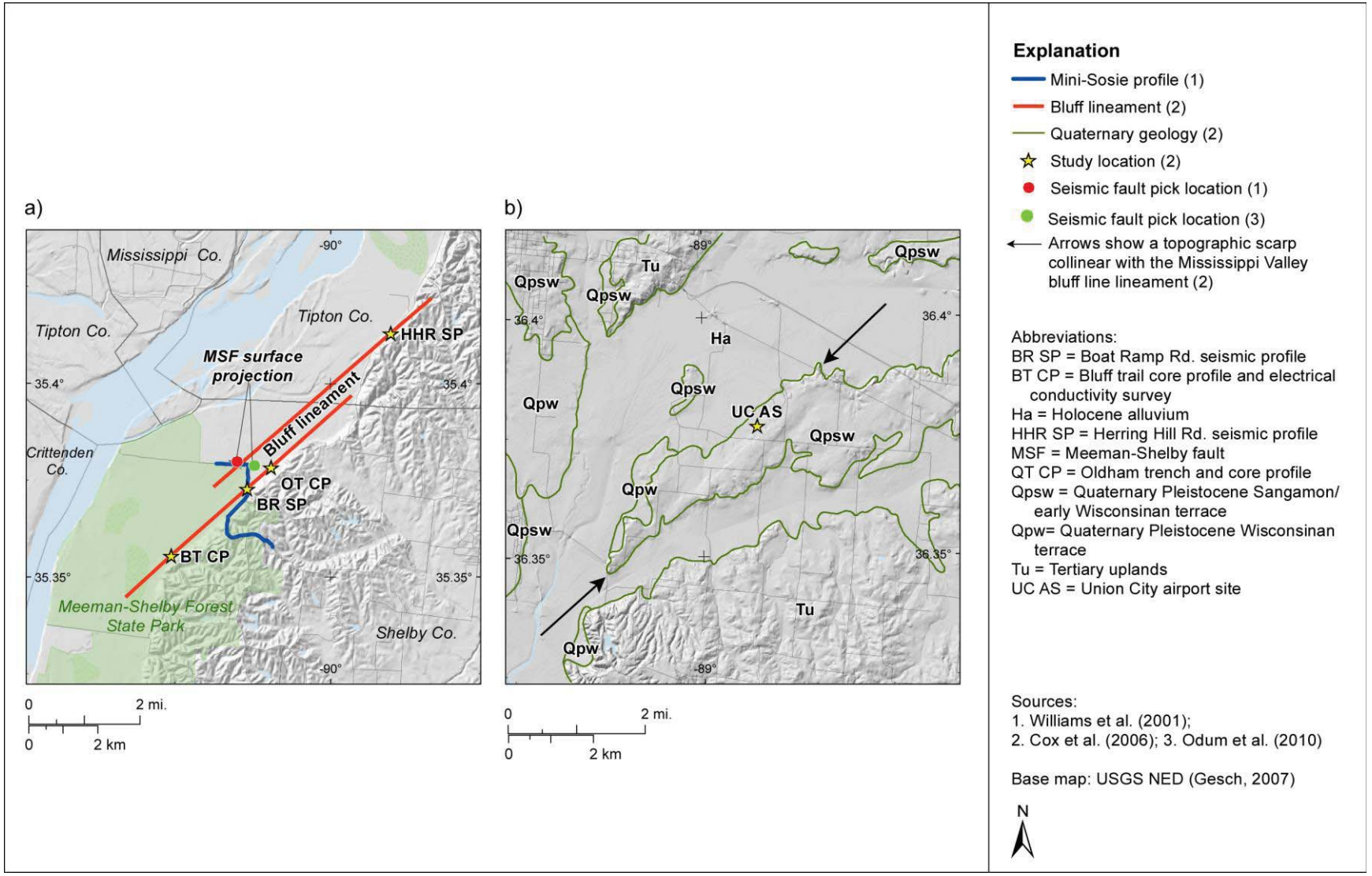

Figure 6.1.6-3
Maps showing surficial geology and locations of subsurface investigations at (a) Meeman-Shelby Forest State Park locality and (b) Union City site (MSF and UC on Figure 6.1.6-2). Modified from Cox et al. (2006) and Odum et al. (2010).

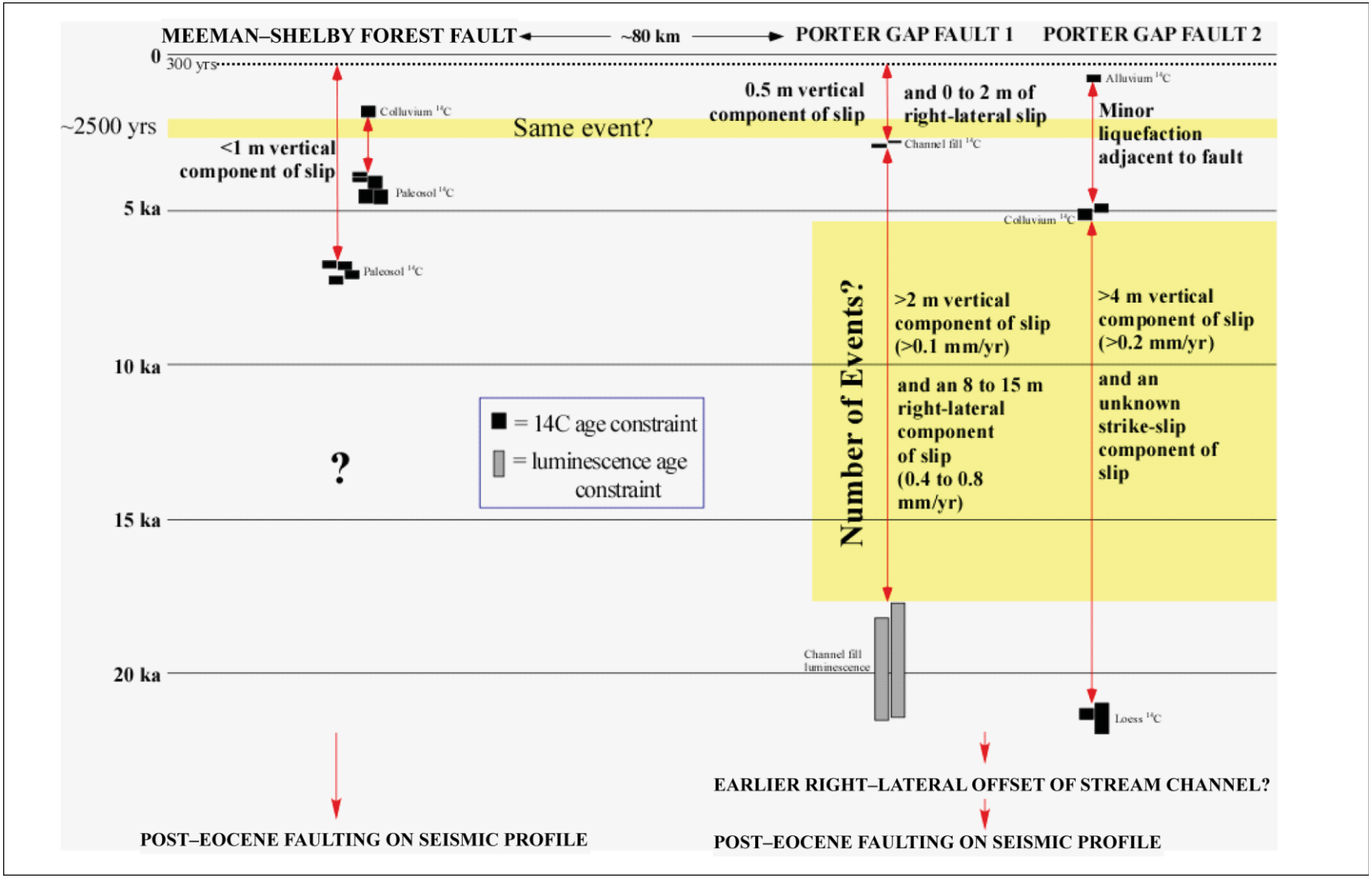

Figure 6.1.6-4
Figure showing the timing of events along the eastern Reelfoot rift margin. Modified from Cox (2009).

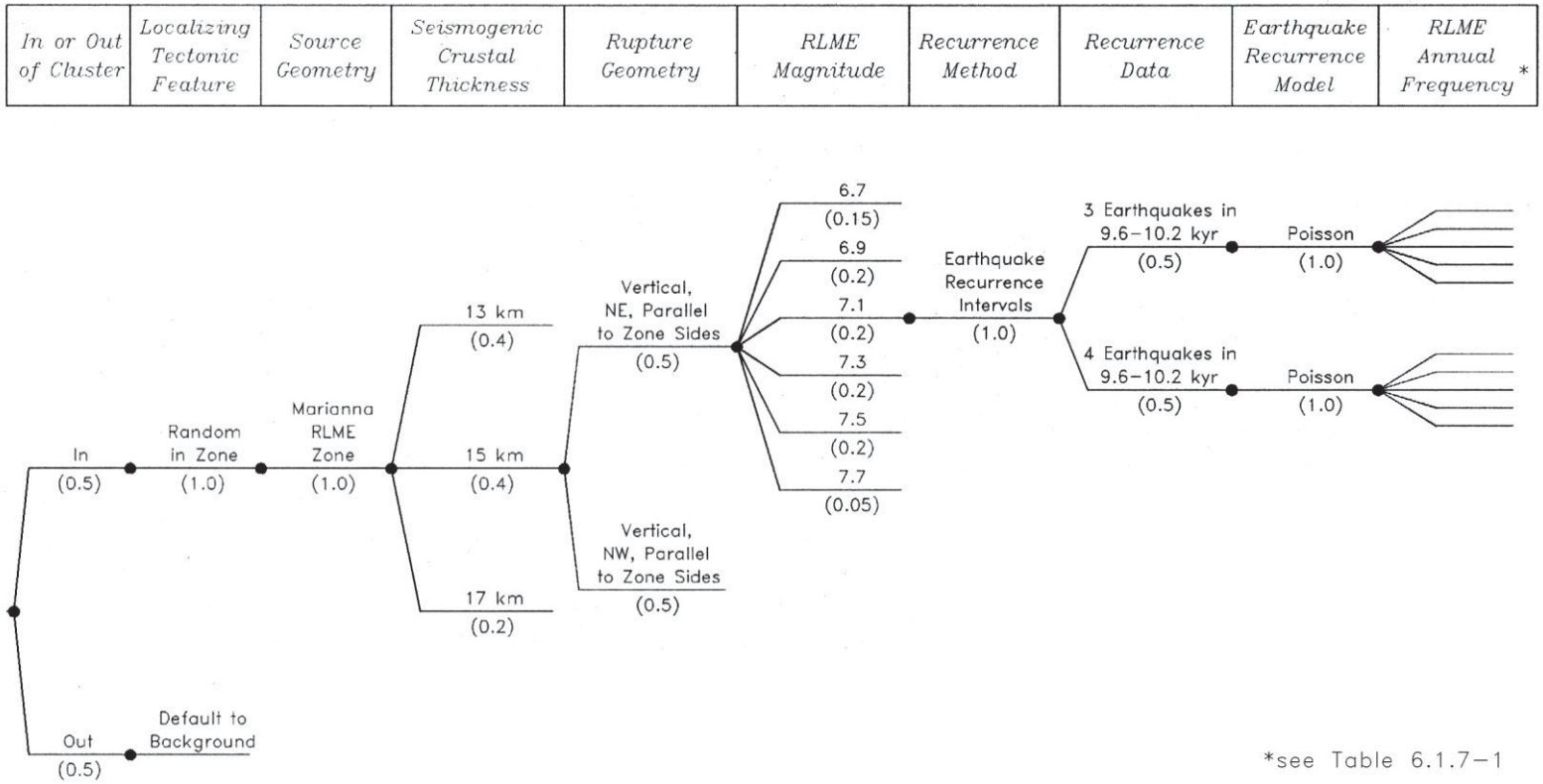

Figure 6.1.7-1
Logic tree for the Reelfoot rift–Marianna RLME source

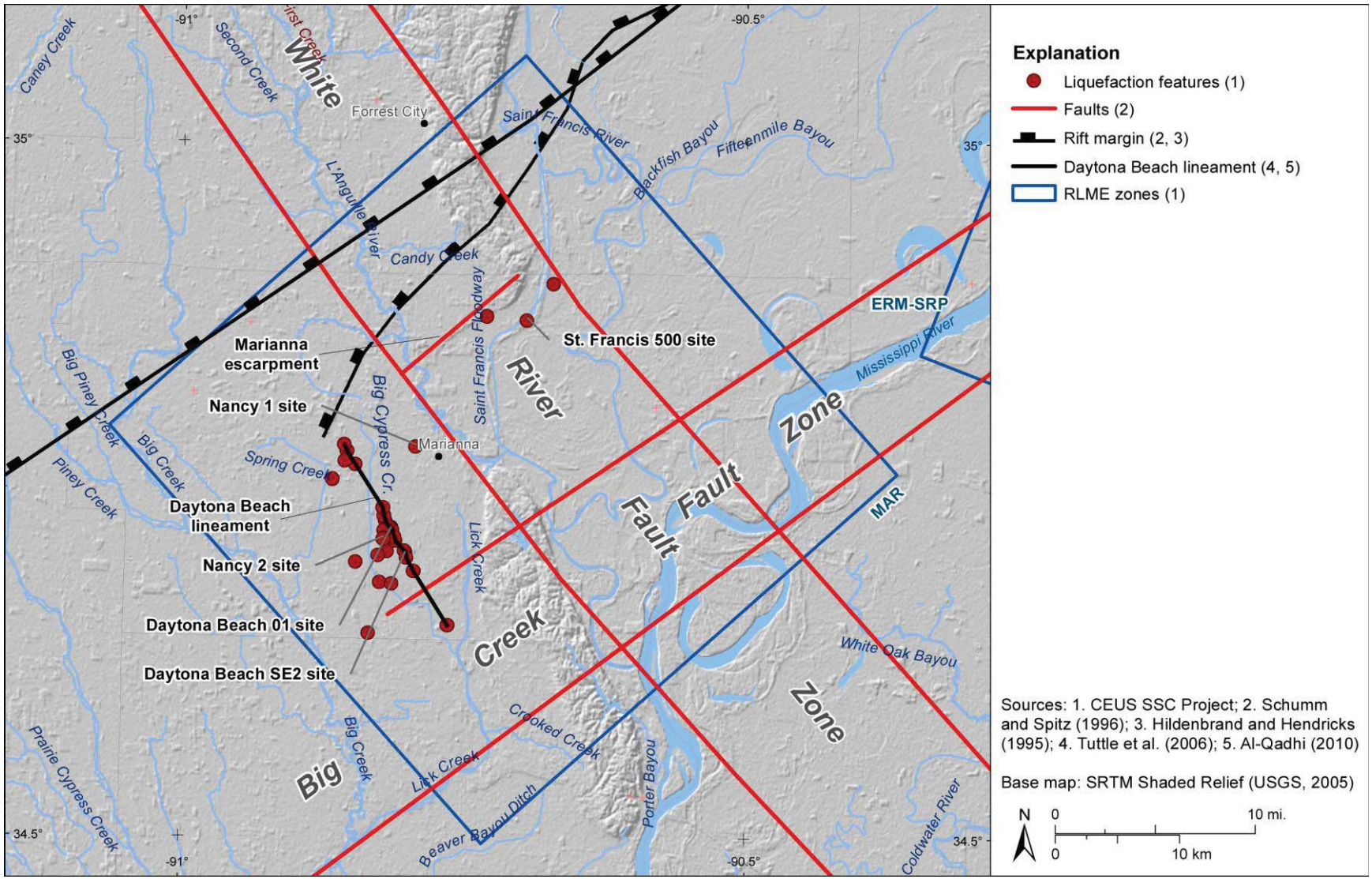

Figure 6.1.7-2
Map showing tectonic features and locations of paleoliquefaction sites in the vicinity of Marianna, Arkansas

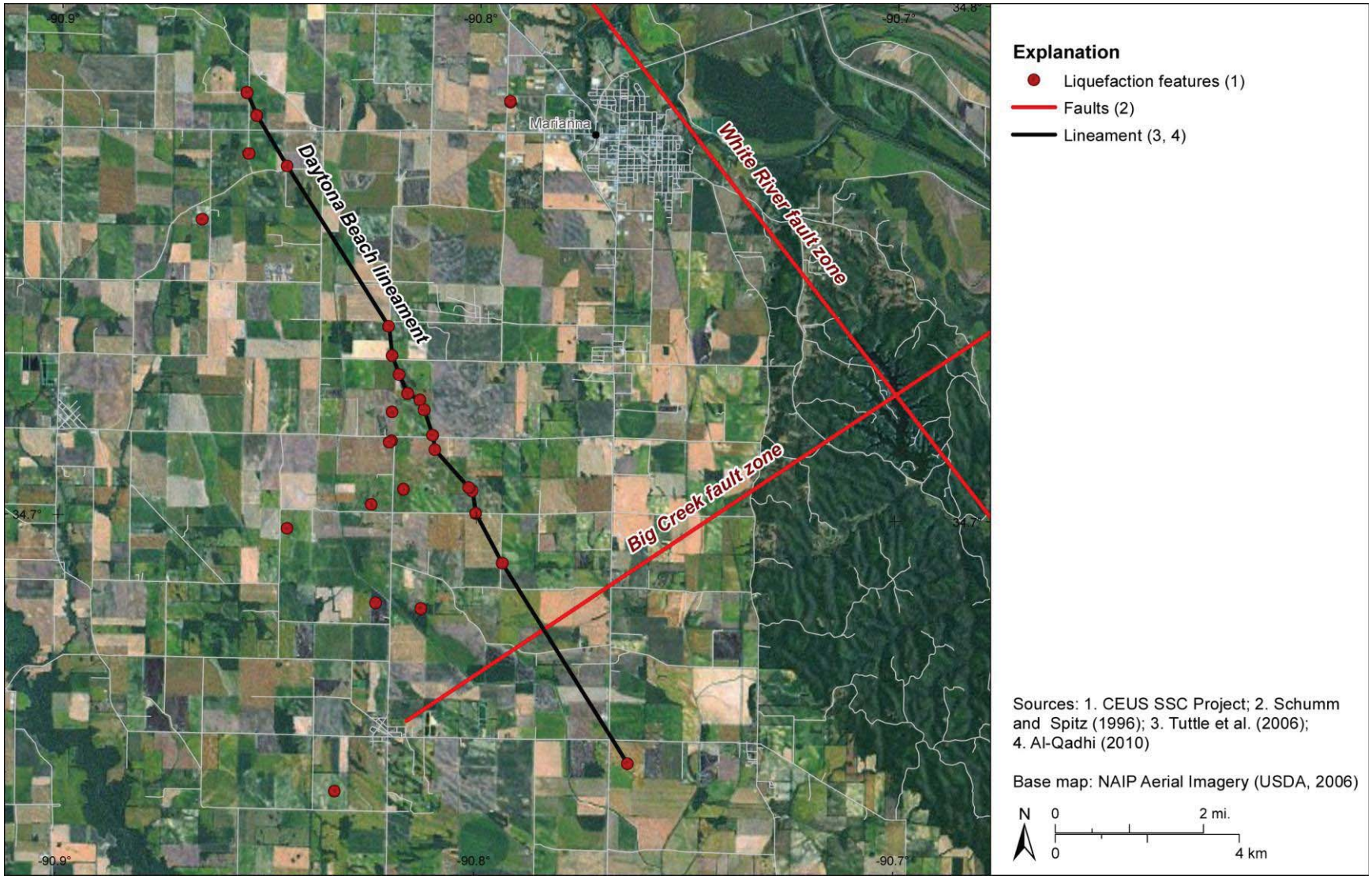

Figure 6.1.7-3
Map showing liquefaction features near Daytona Beach lineament southwest of Marianna, Arkansas

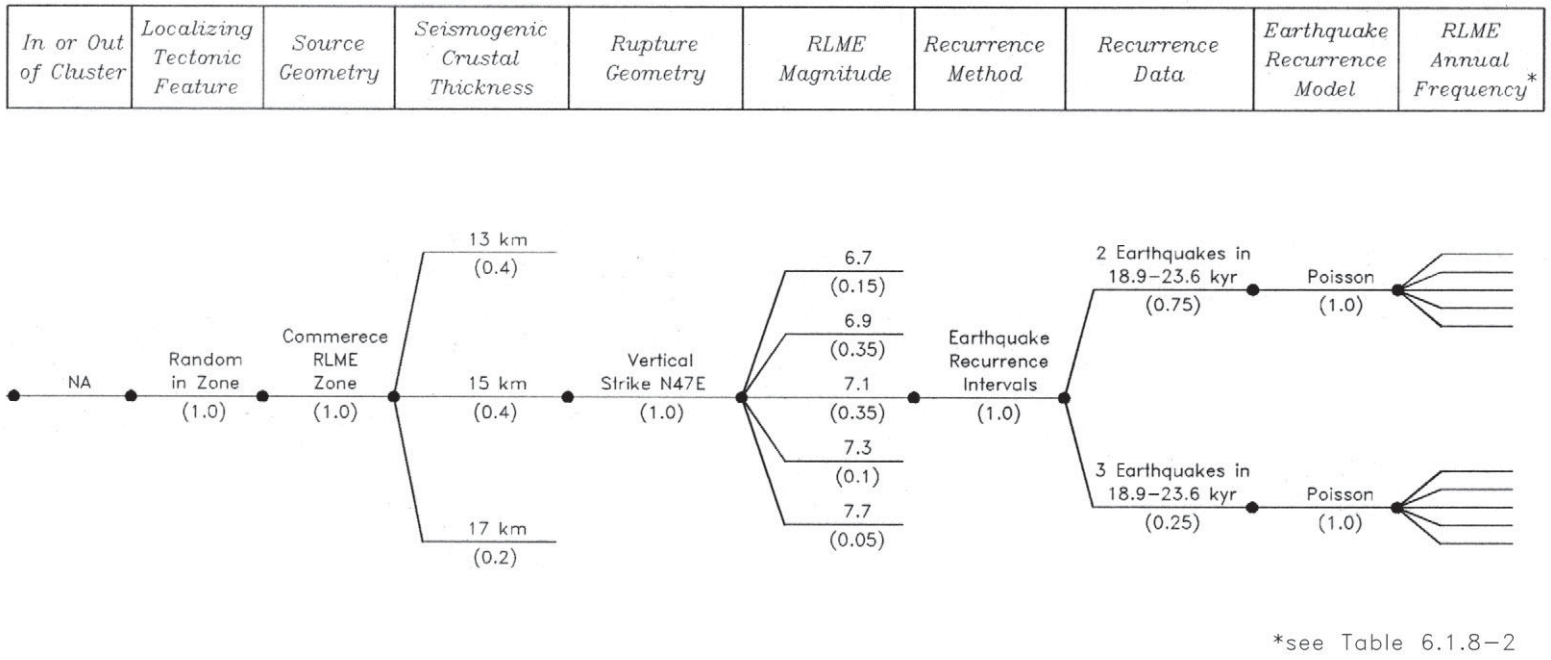

Figure 6.1.8-1
Logic tree for the Commerce Fault Zone RLME source

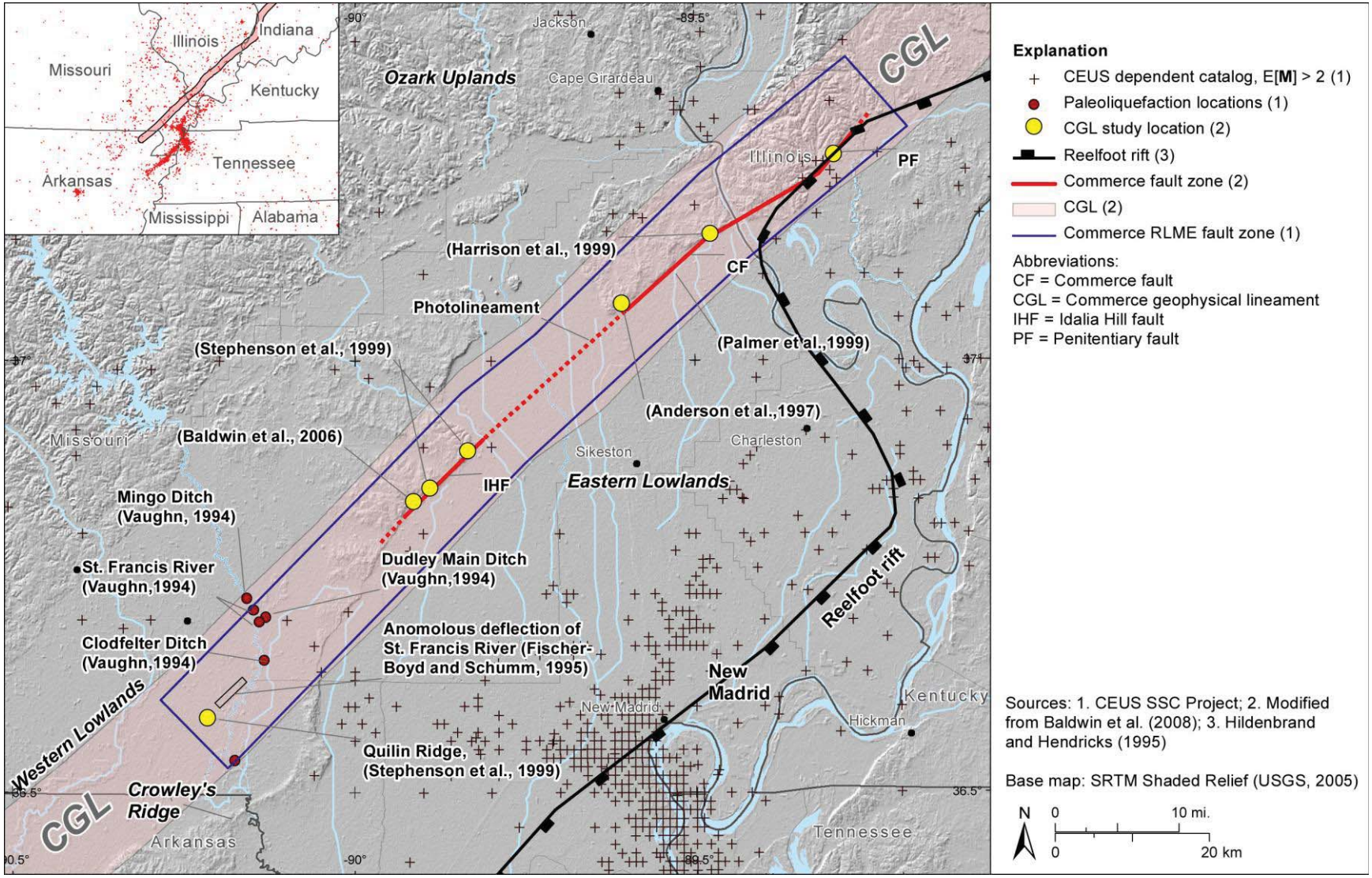

Figure 6.1.8-2
Map showing tectonic features, seismicity, and paleoseismic localities along the Commerce Fault Zone RLME source

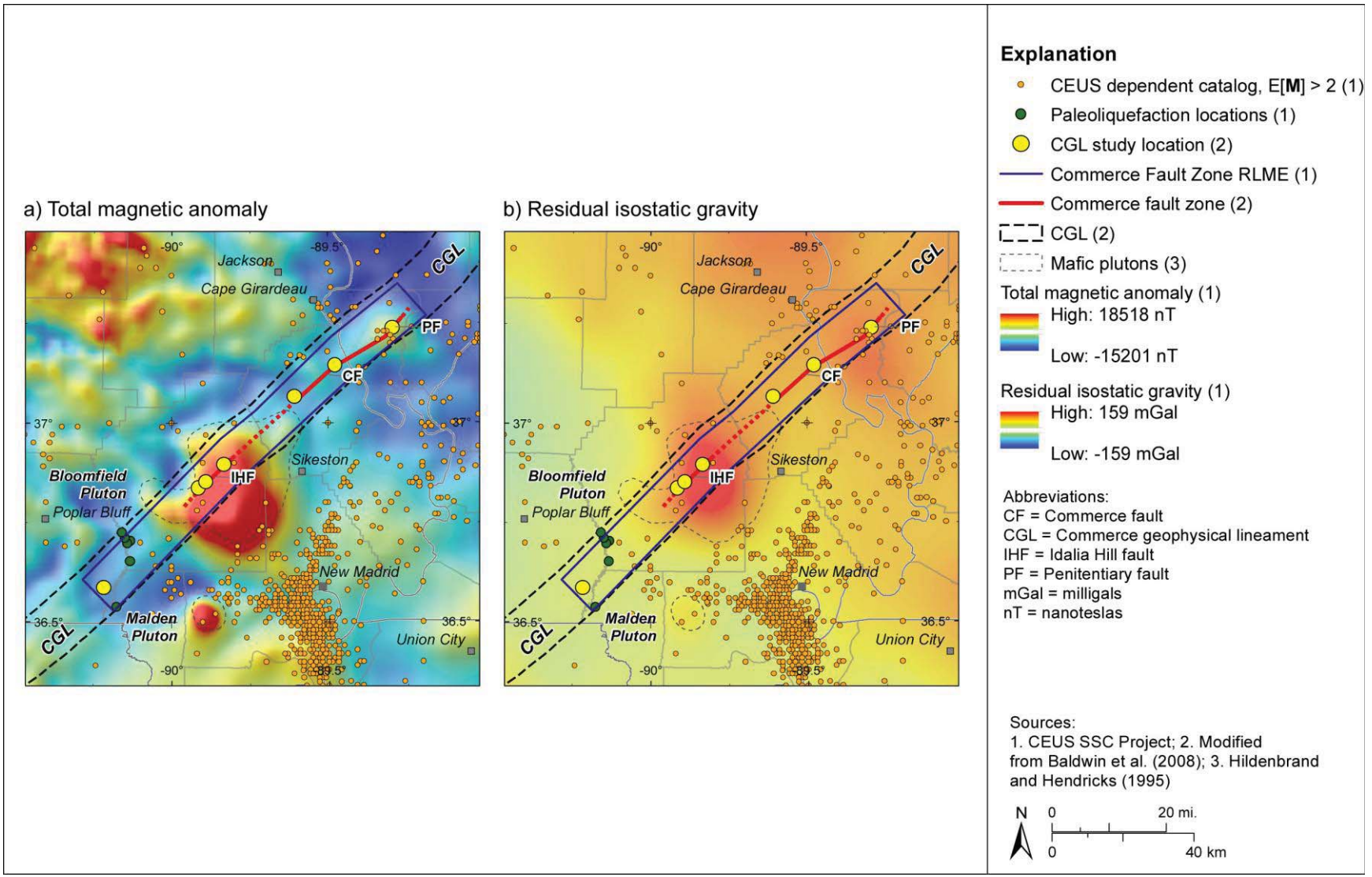

Figure 6.1.8-3
Location of the Commerce geophysical lineament and Commerce Fault Zone RLME source relative to the (a) regional magnetic anomaly map and (b) regional gravity anomaly map

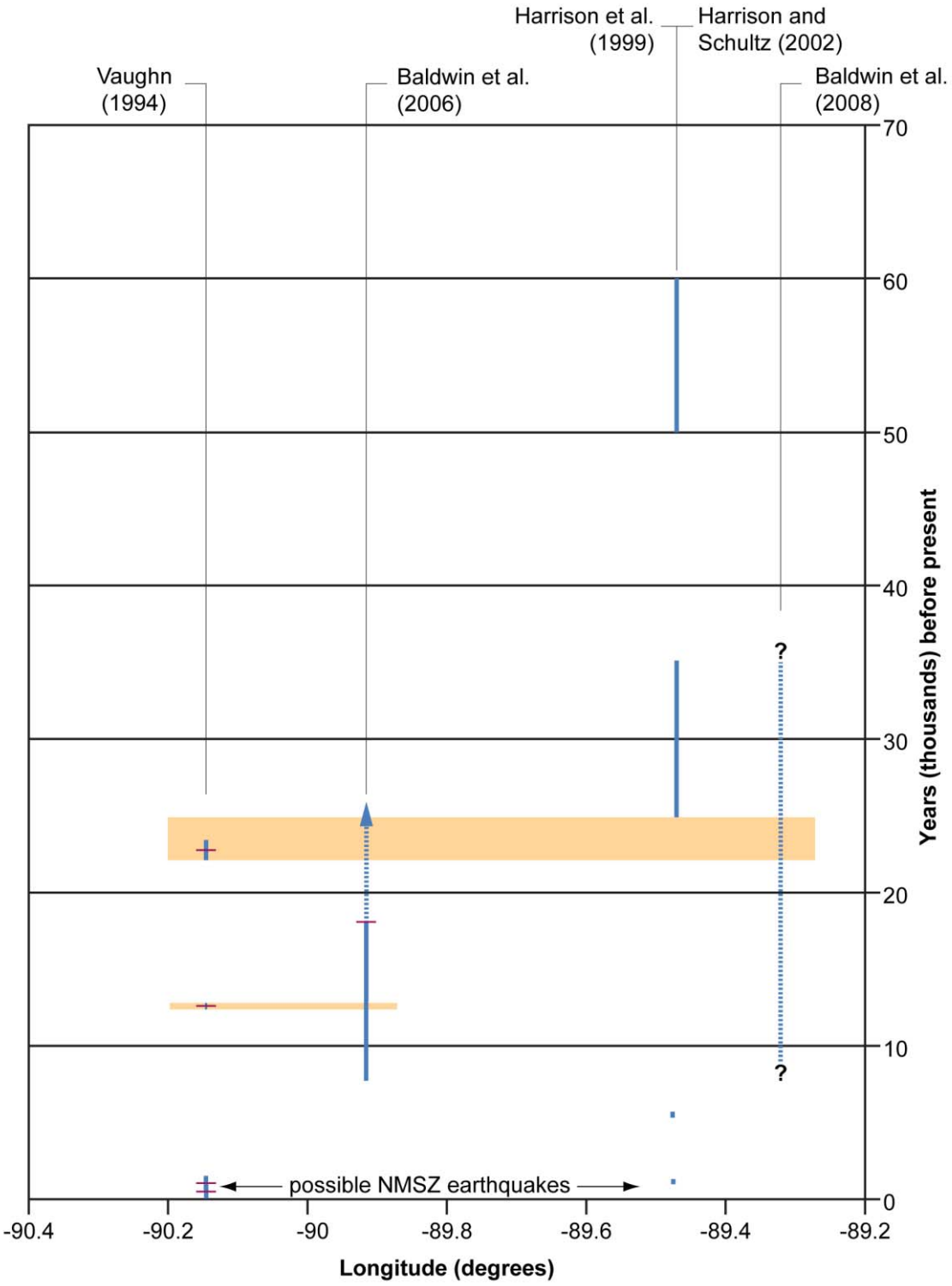

Figure 6.1.8-4
Space-time diagram showing constraints on the location and timing of late Pleistocene and Holocene paleoearthquakes that may be associated with the Commerce Fault Zone RLME source

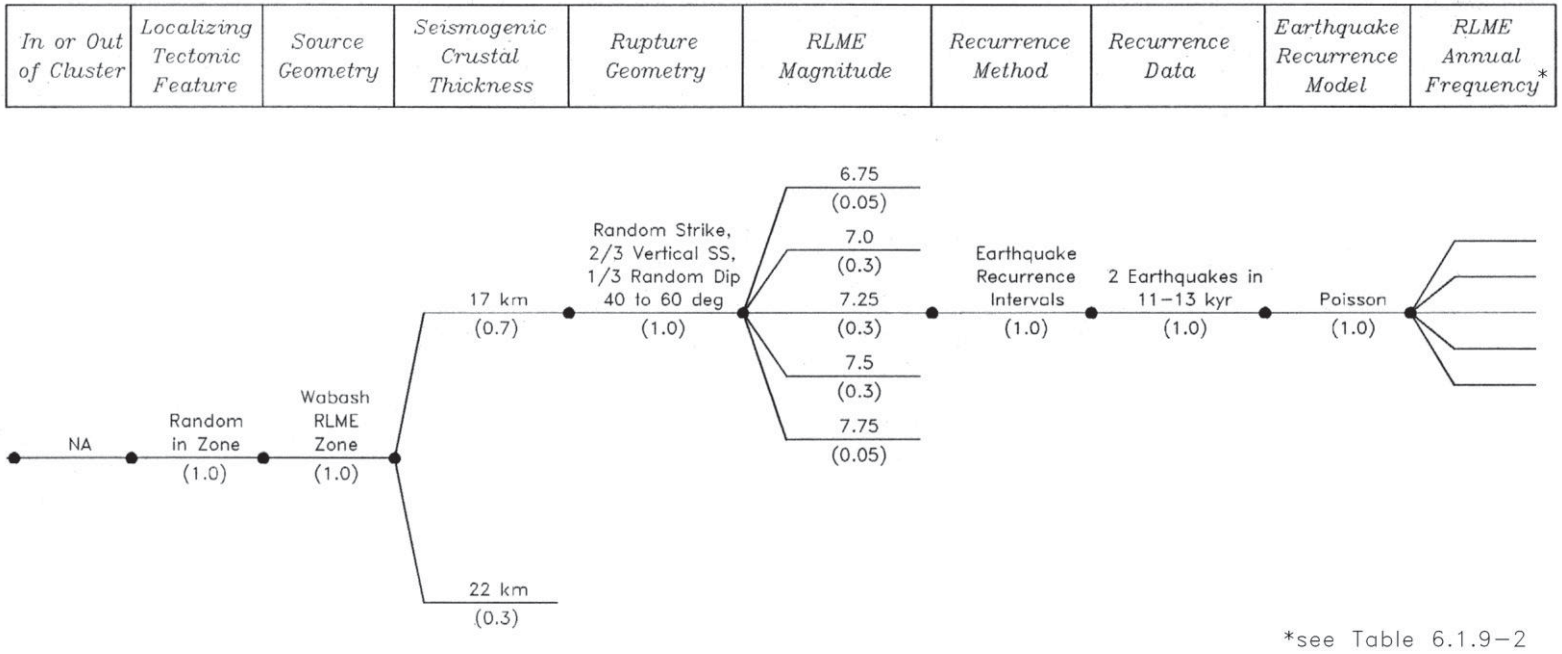

Figure 6.1.9-1
Logic tree for the Wabash Valley RLME source

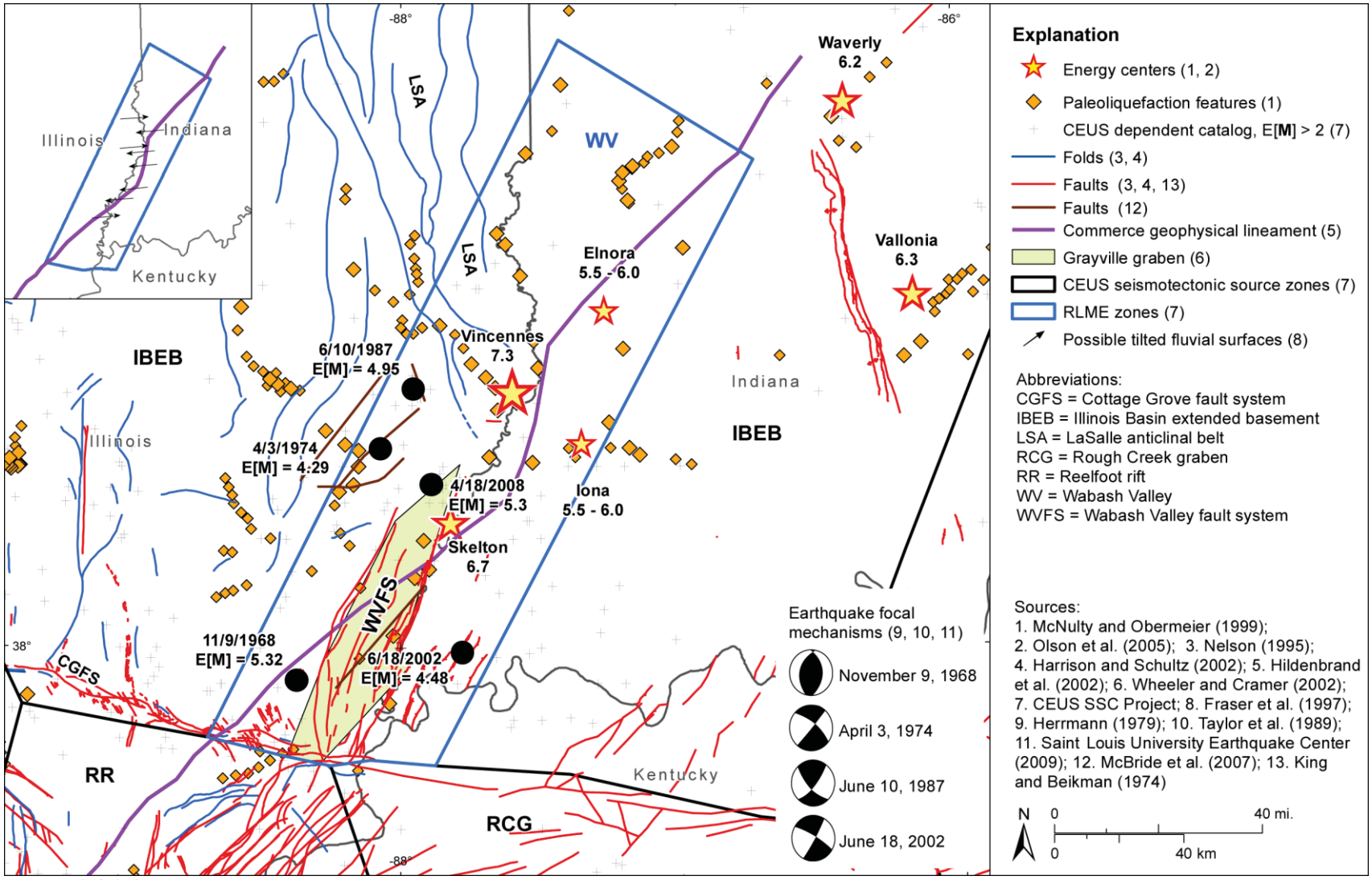

Figure 6.1.9-2
Map showing seismicity, subsurface structural features, paleoearthquake energy centers, and postulated neotectonic deformation in the Wabash Valley region of southern Illinois and southern Indiana

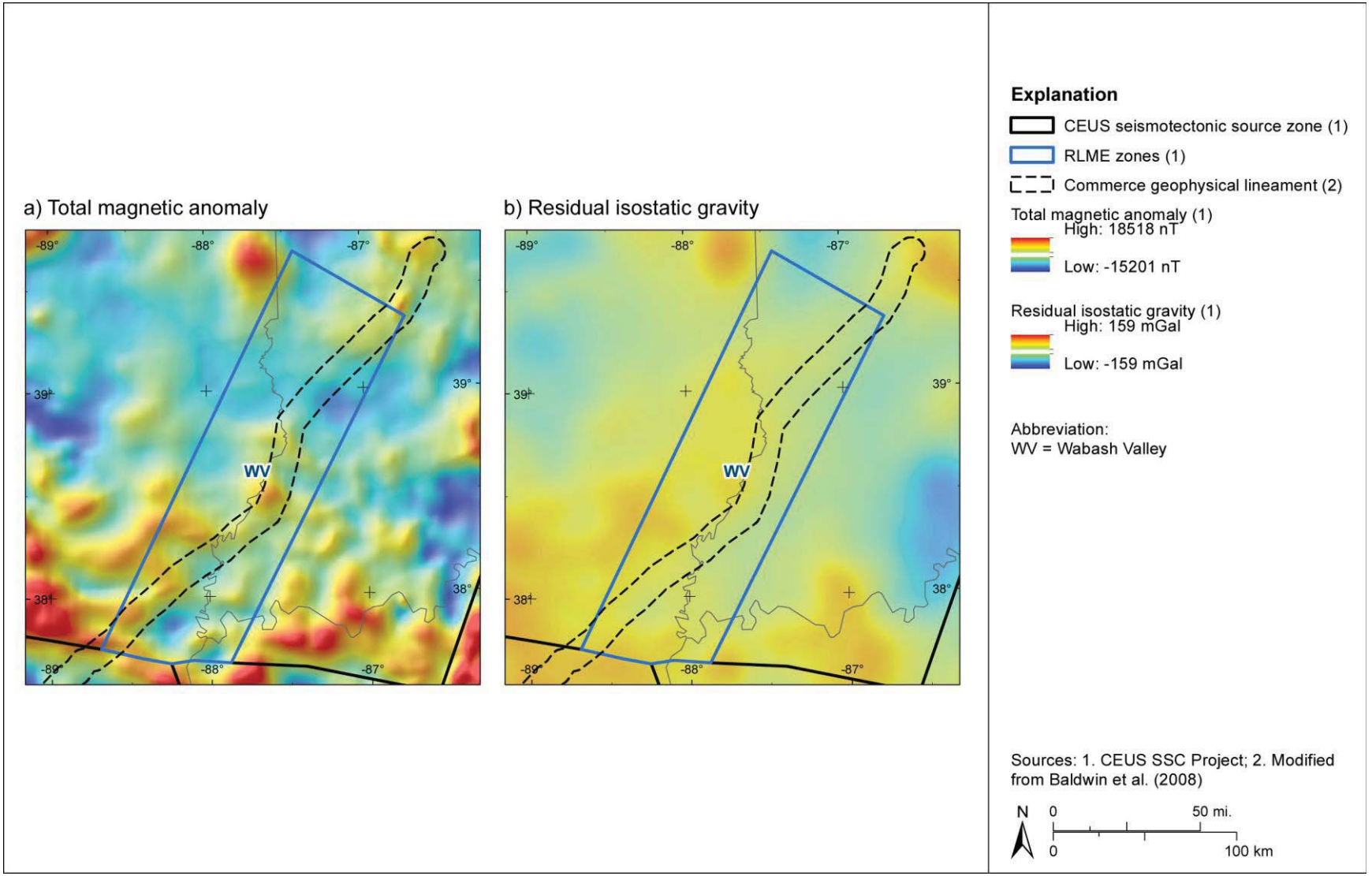

Figure 6.1.9-3
Wabash Valley RLME source relative to (a) magnetic anomaly, and (b) residual isostatic gravity data

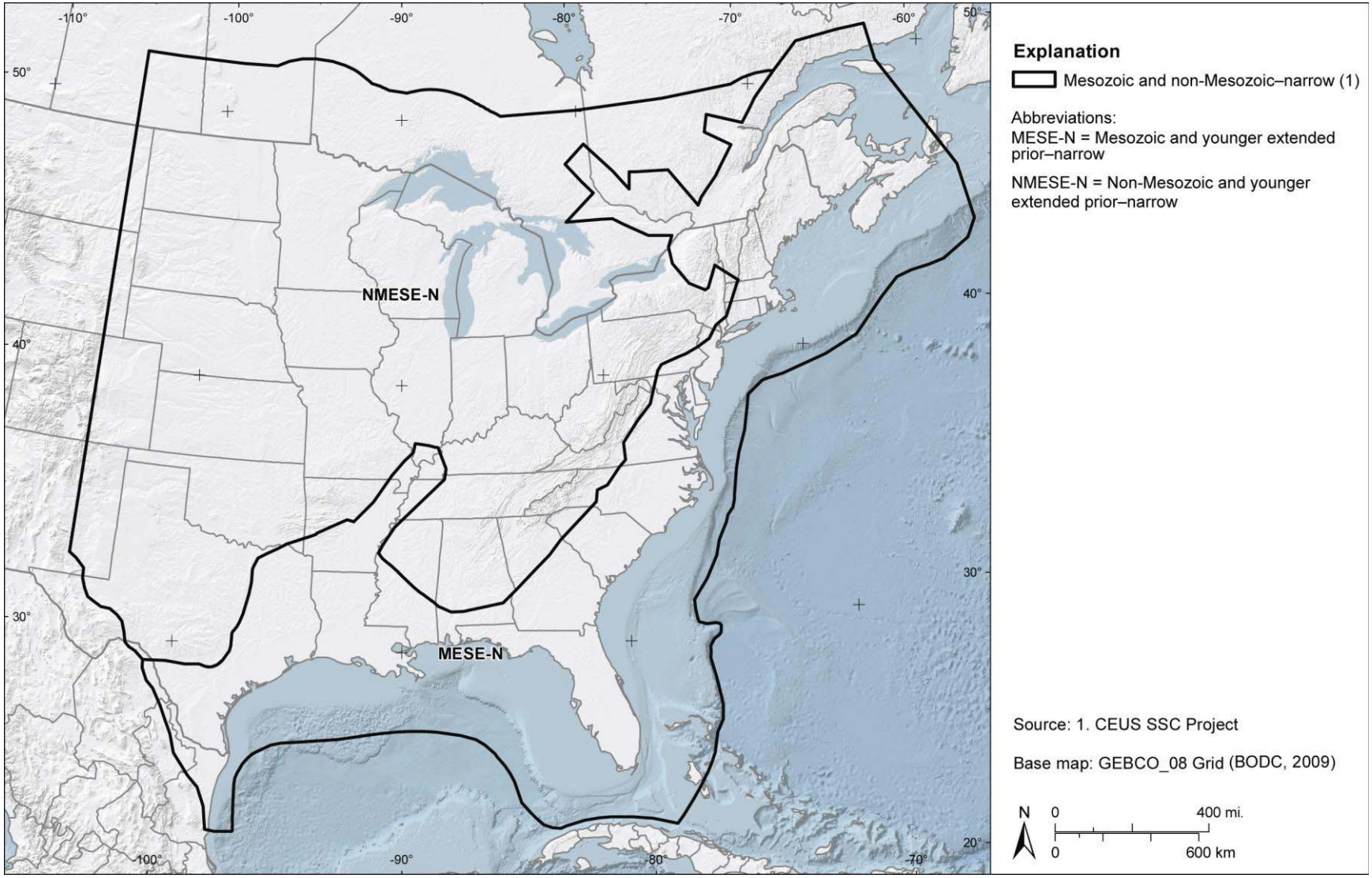

Figure 6.2-1
Map showing the two Mmax zones for the –narrow" interpretation of the Mesozoic-and-younger extended zone

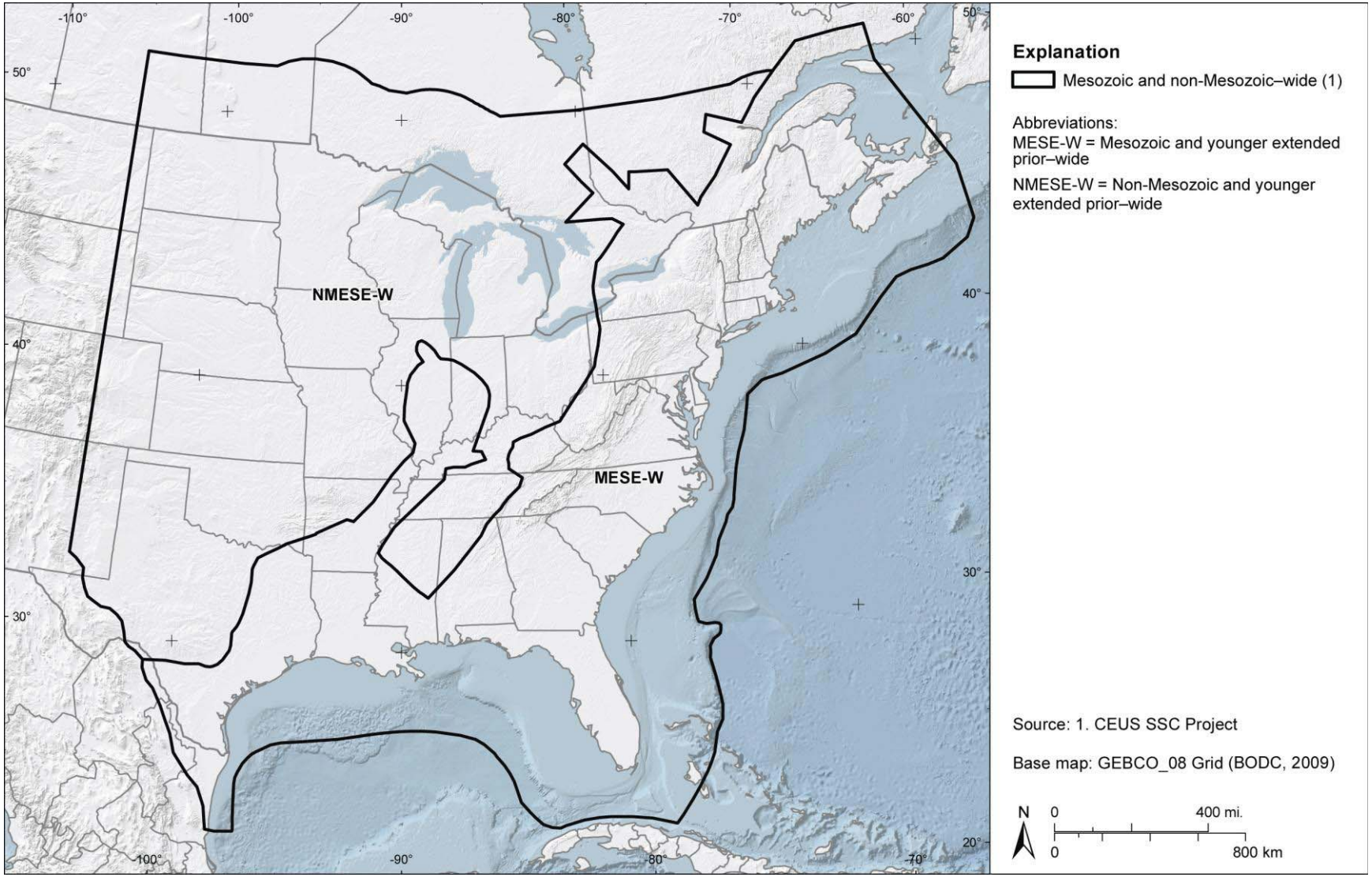

Figure 6.2-2
Map showing the two Mmax zones for the –wide" interpretation of the Mesozoic-and-younger extended zone

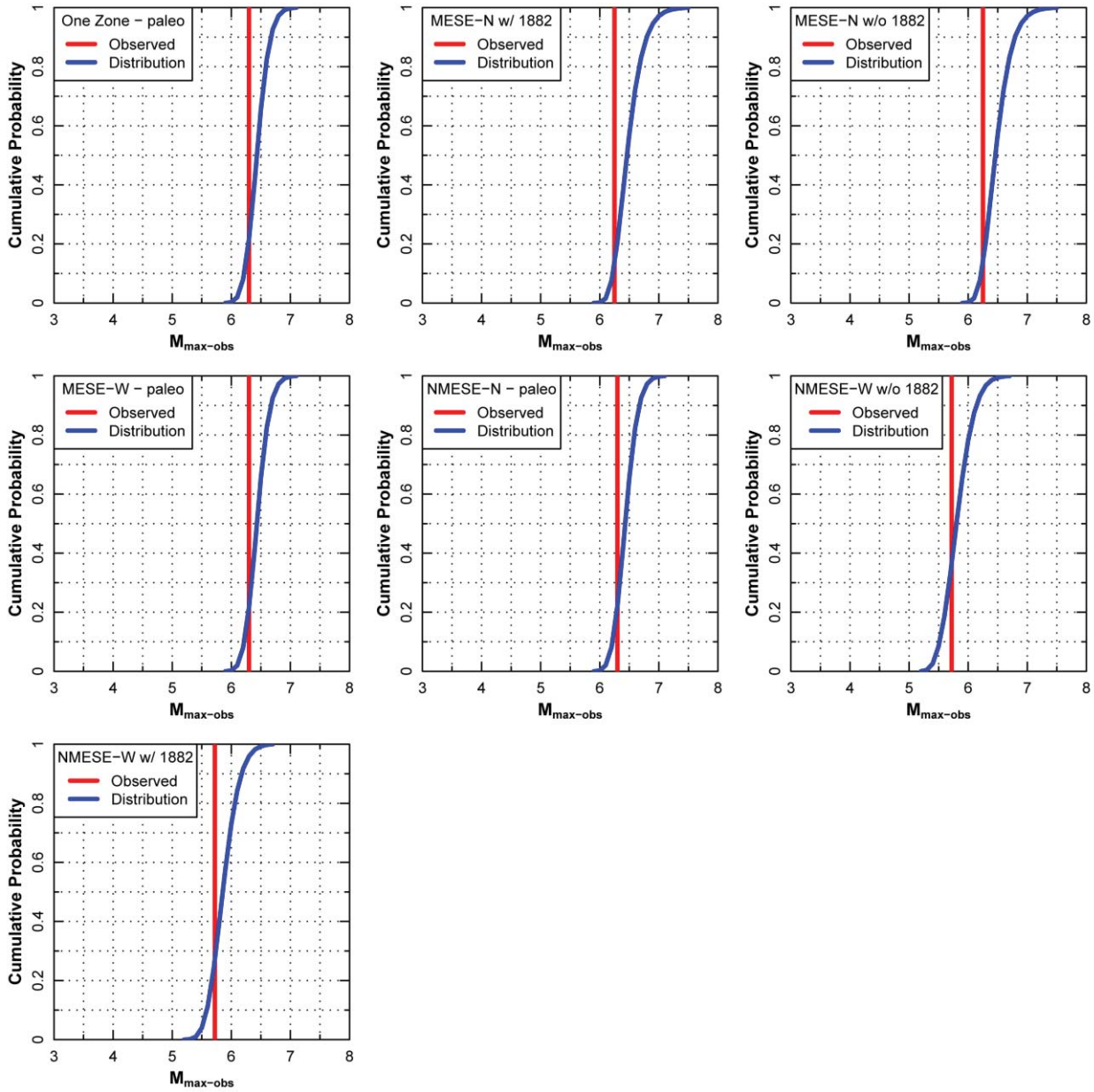

Figure 6.3.1-1
Distributions for $m_{\max-obs}$ for the Mmax distributed seismicity source zones

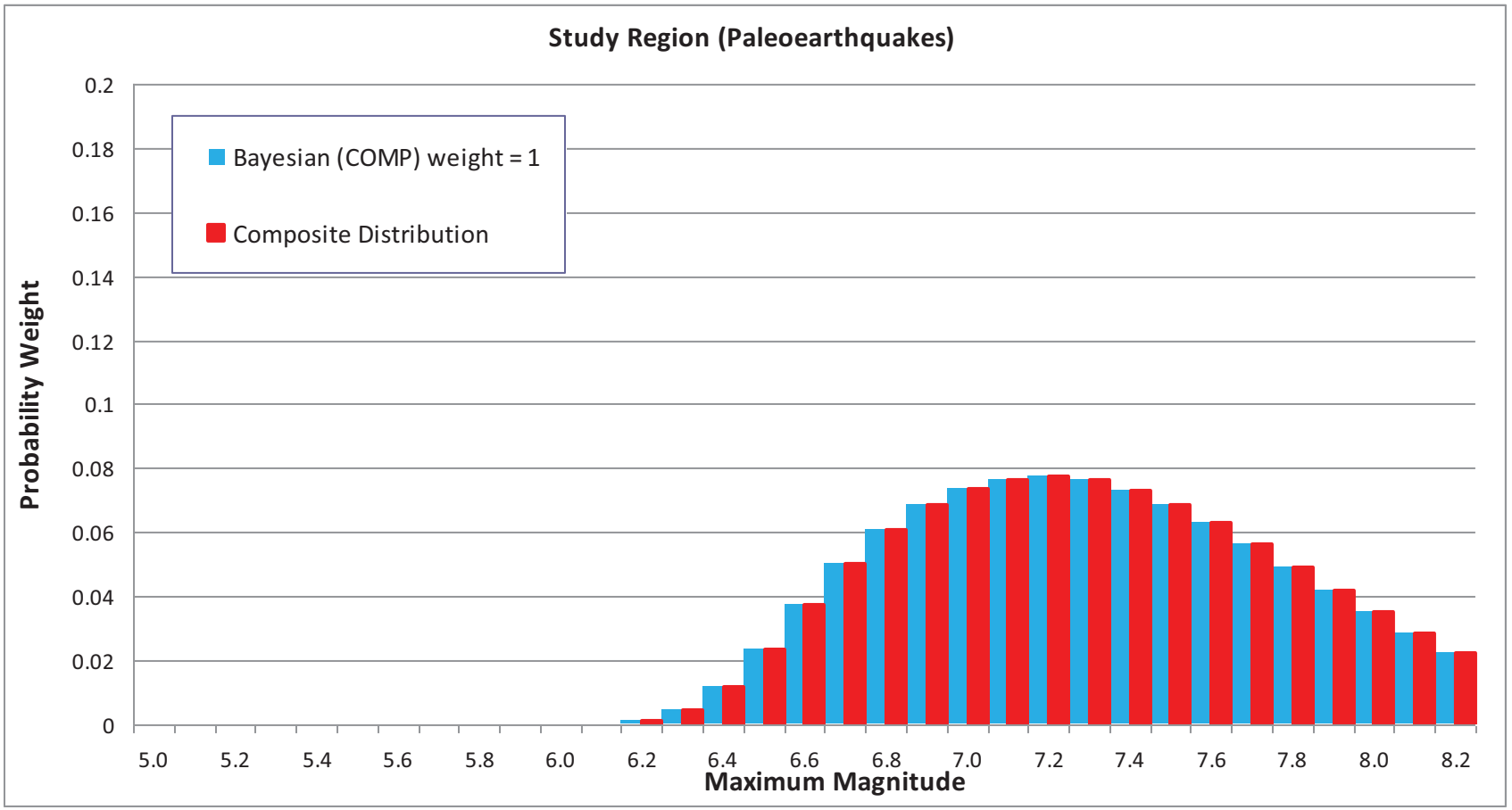

Figure 6.3.2-1
Mmax distributions for the study region treated as a single Mmax zone

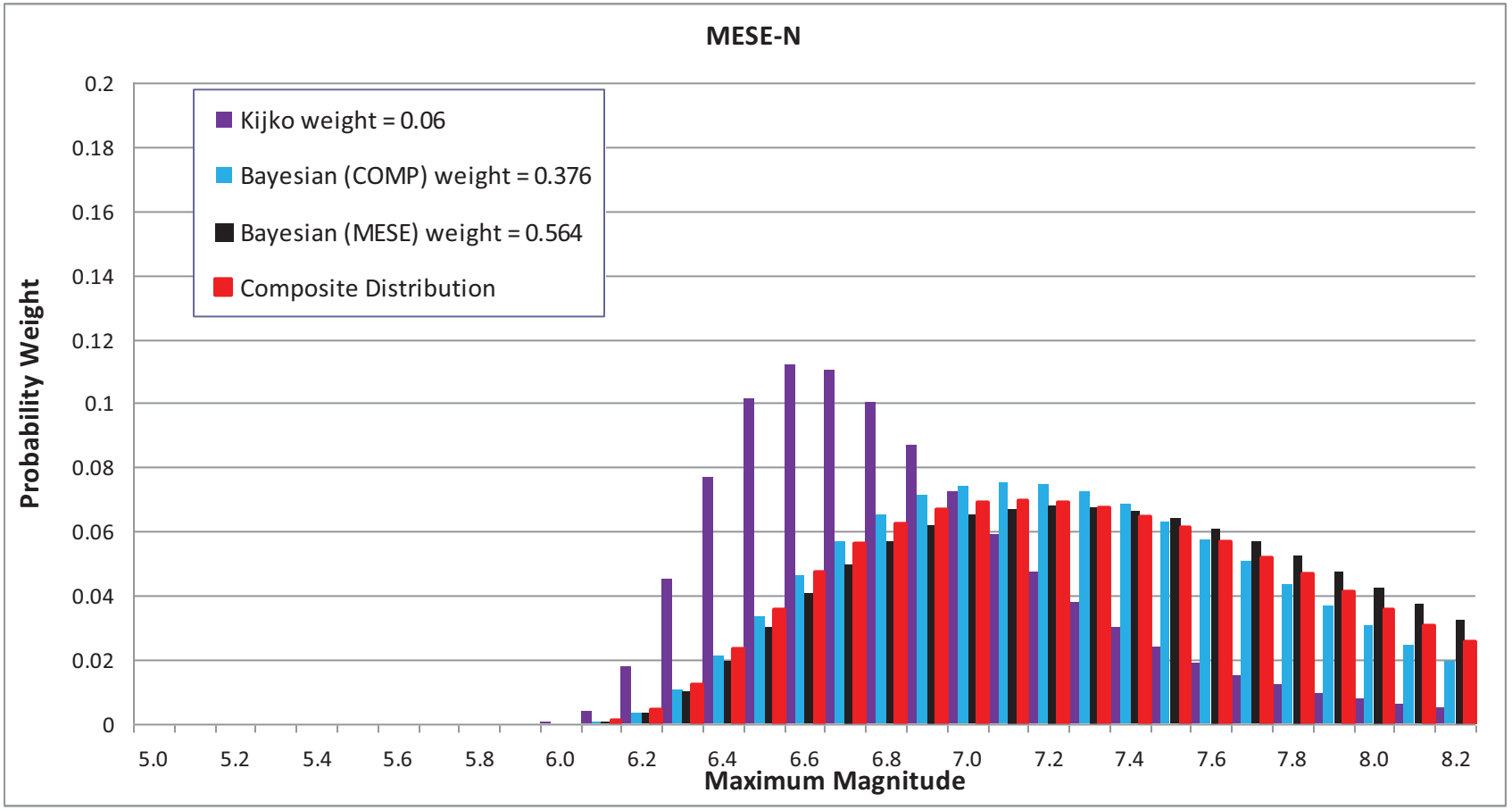

Figure 6.3.2-2
Mmax distributions for the MESE-N Mmax zone

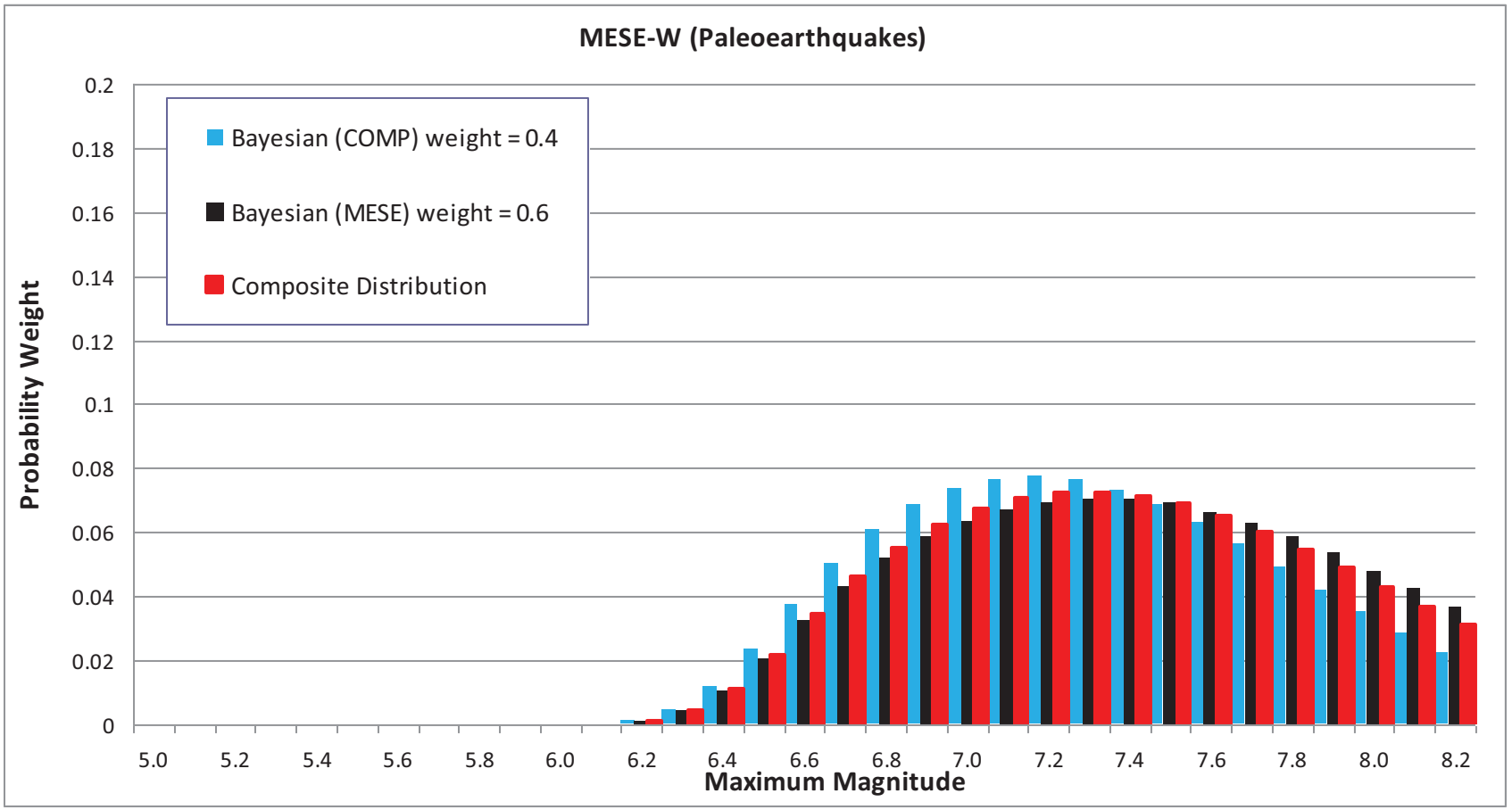

Figure 6.3.2-3
Mmax distributions for the MESE-W Mmax zone

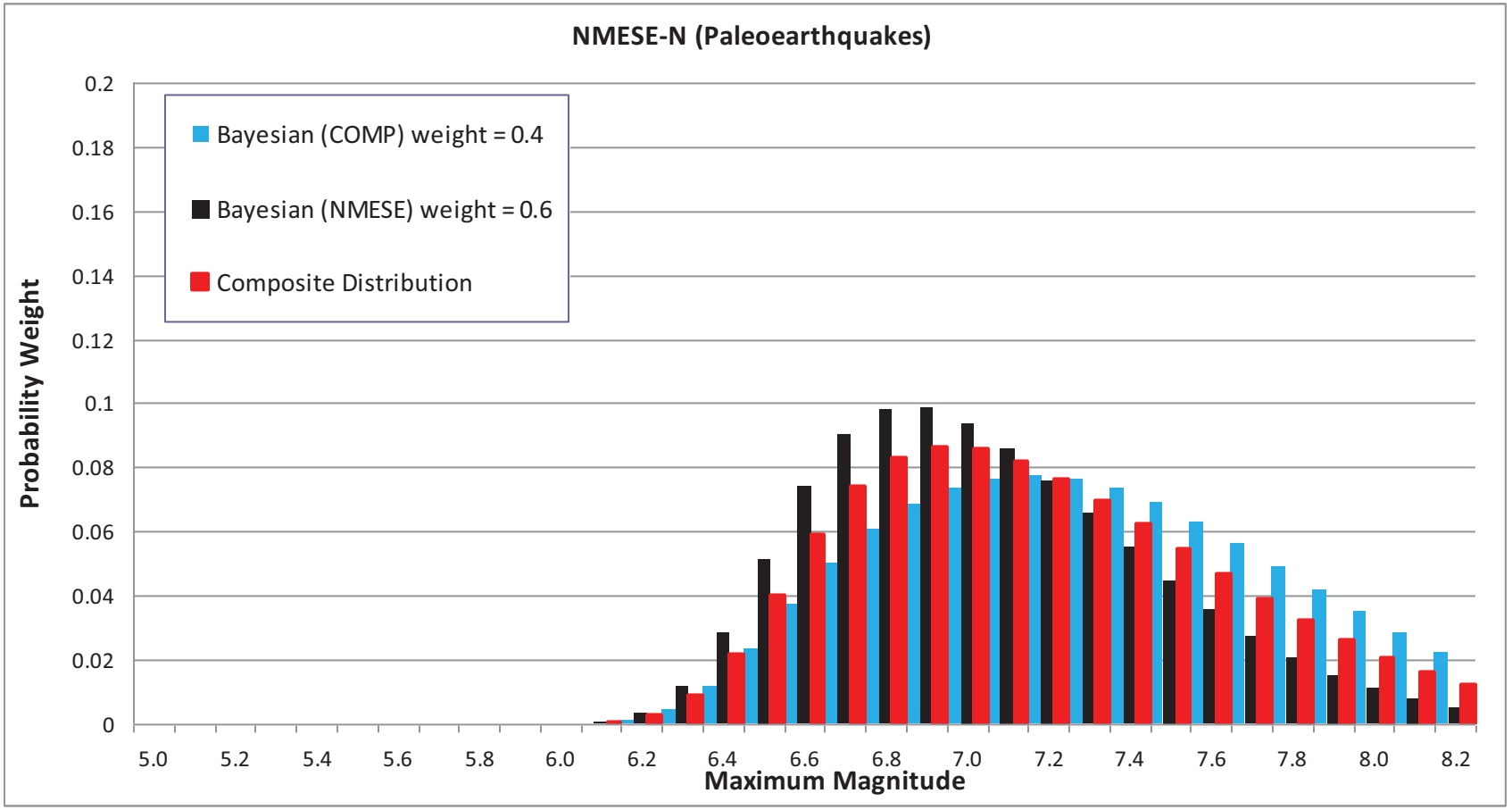

Figure 6.3.2-4
Mmax distributions for the NMESE-N Mmax zone

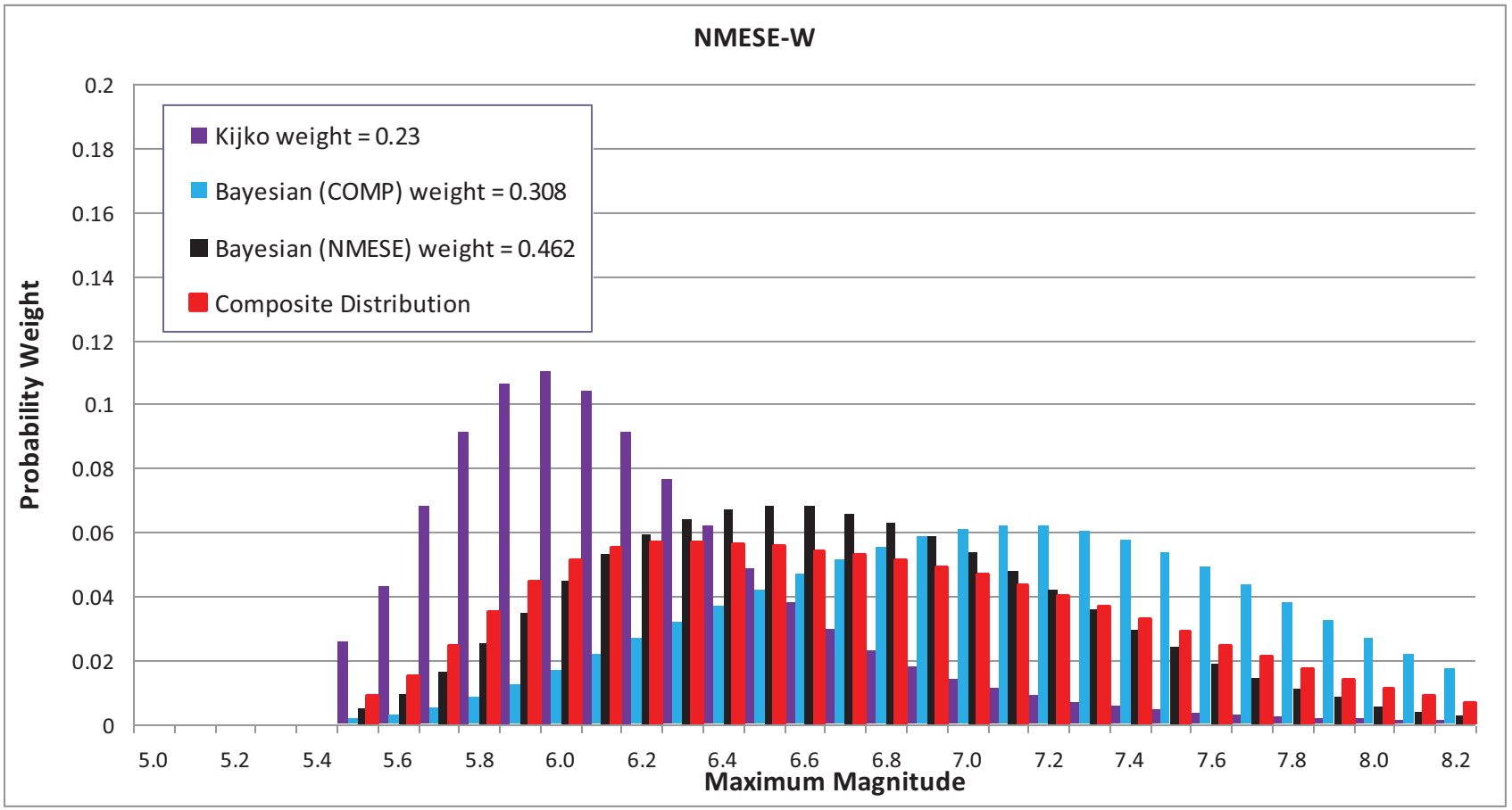

Figure 6.3.2-5
Mmax distributions for the NMESE-W Mmax zone

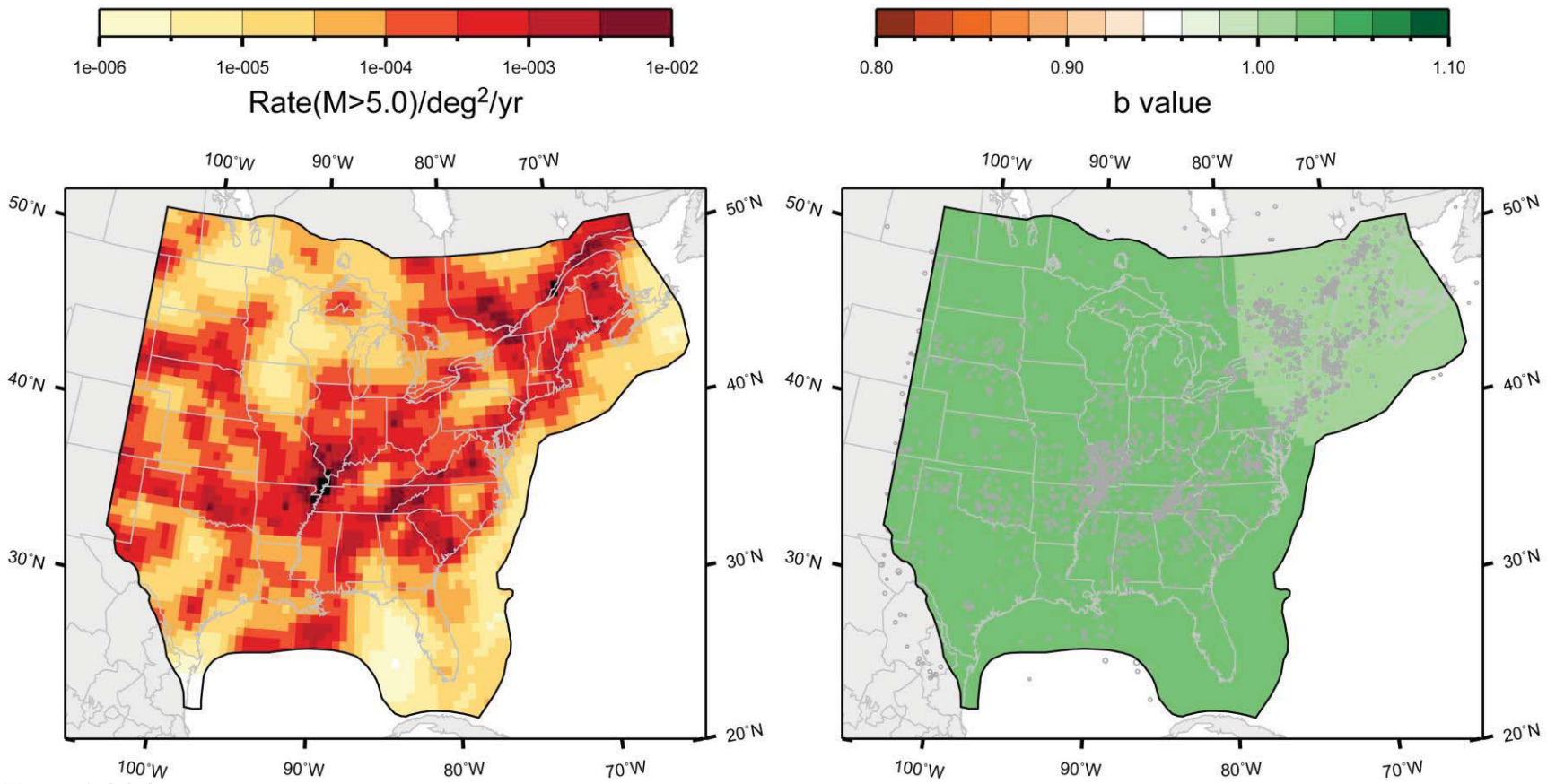

Figure 6.4.1-1
Mean map of rate and *b*-value for the study region under the source-zone configuration, with no separation of Mesozoic extended and non-extended; Case A magnitude weights

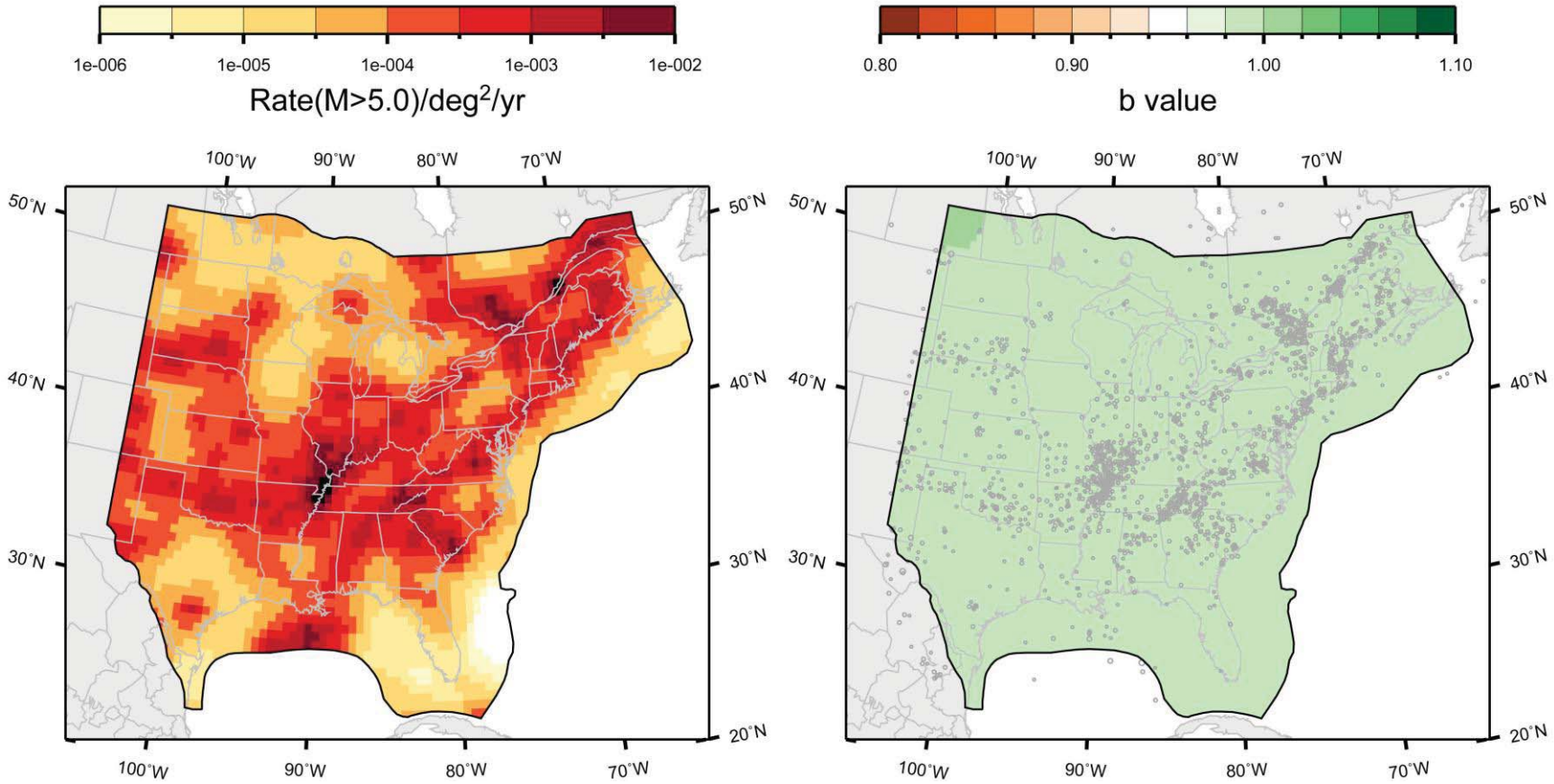

Figure 6.4.1-2
Mean map of rate and *b*-value for the study region under the source-zone configuration, with no separation of Mesozoic extended and non-extended; Case B magnitude weights

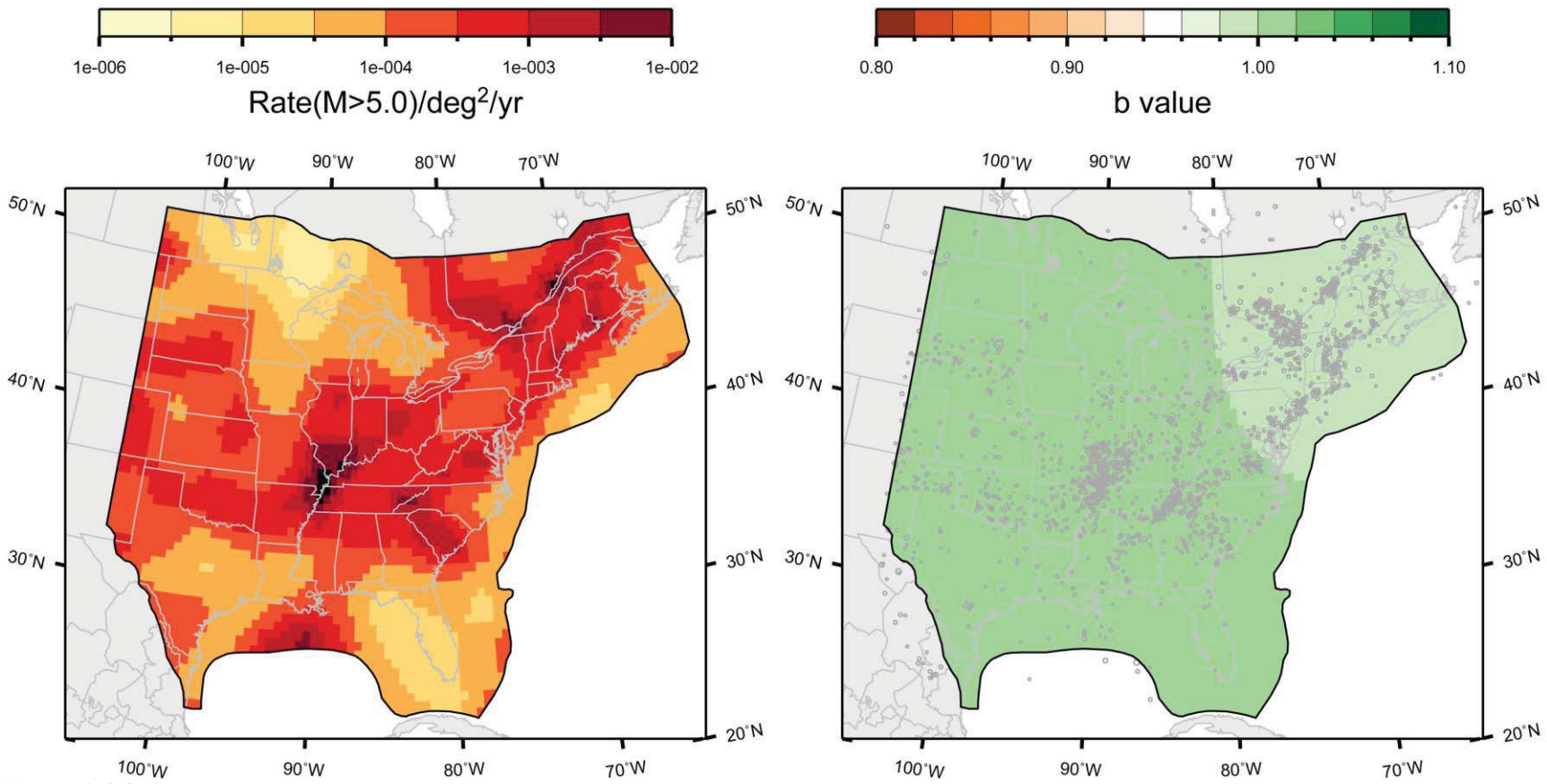

Figure 6.4.1-3
Mean map of rate and *b*-value for the study region under the source-zone configuration, with no separation of Mesozoic extended and non-extended; Case E magnitude weights

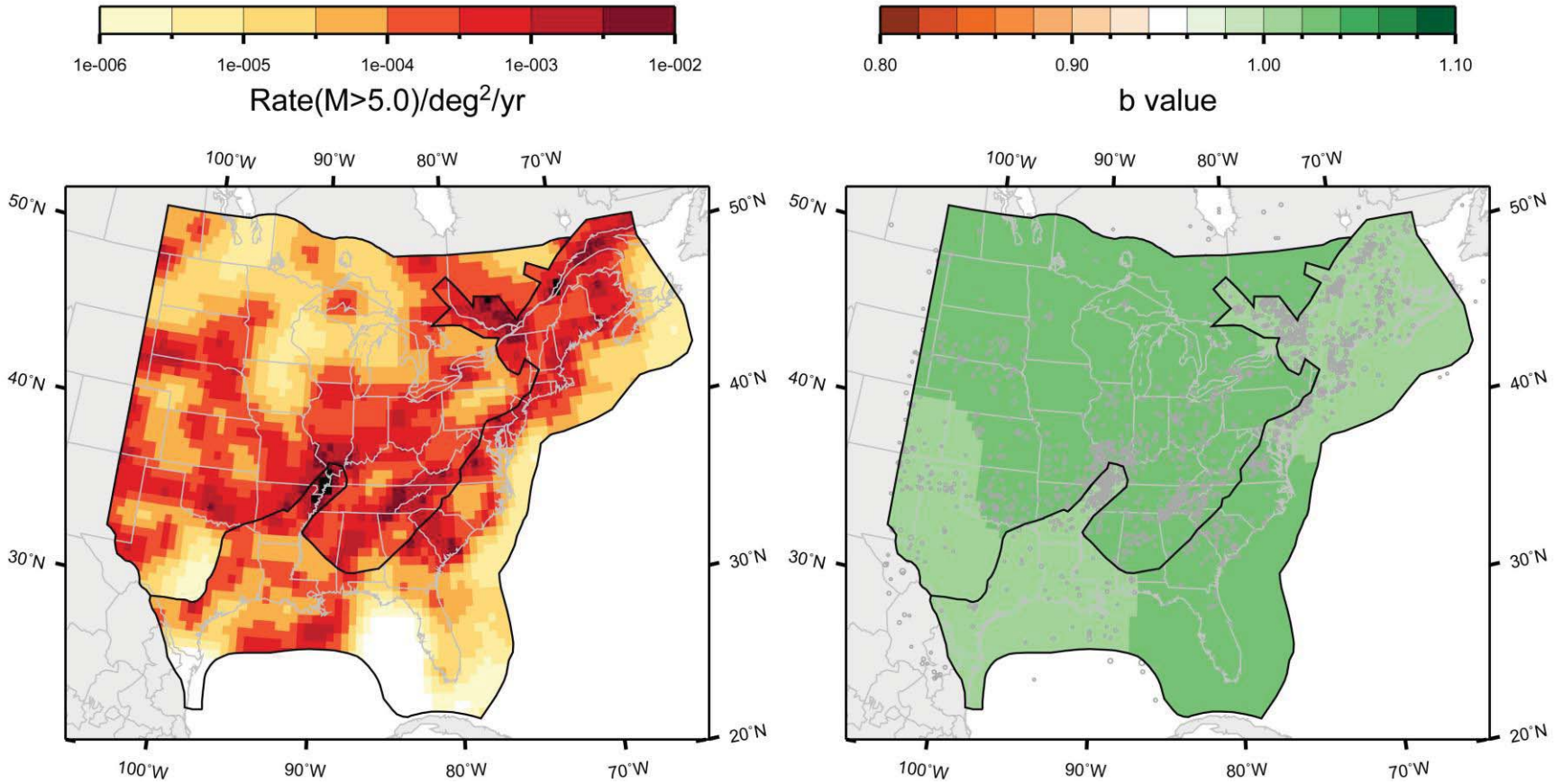

Figure 6.4.1-4
Mean map of rate and *b*-value for the study region under the source-zone configuration, with separation of Mesozoic extended and non-extended, narrow geometry for MESE; Case A magnitude weights

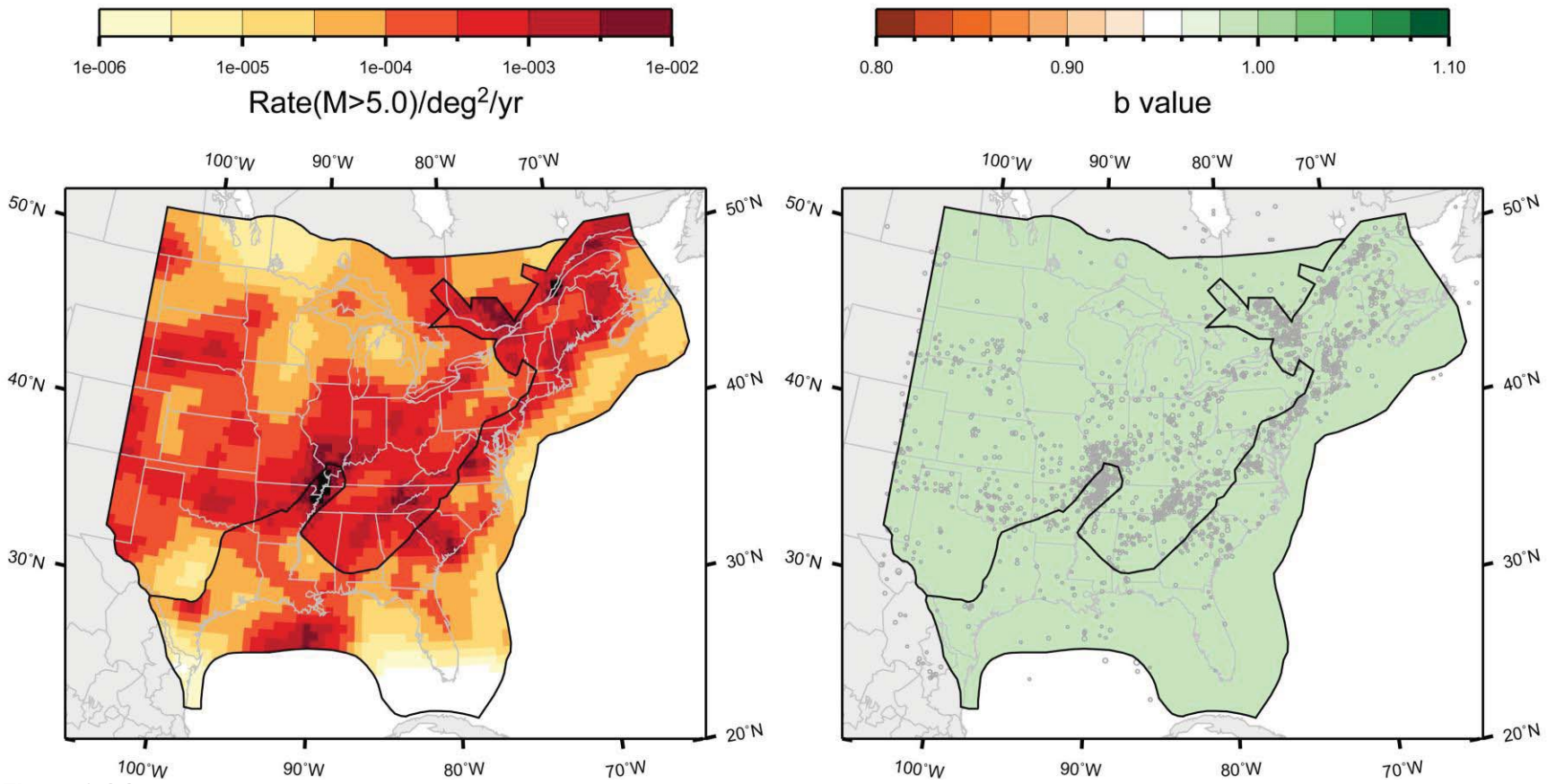

Figure 6.4.1-5
Mean map of rate and *b*-value for the study region under the source-zone configuration, with separation of Mesozoic extended and non-extended, narrow geometry for MESE; Case B magnitude weights

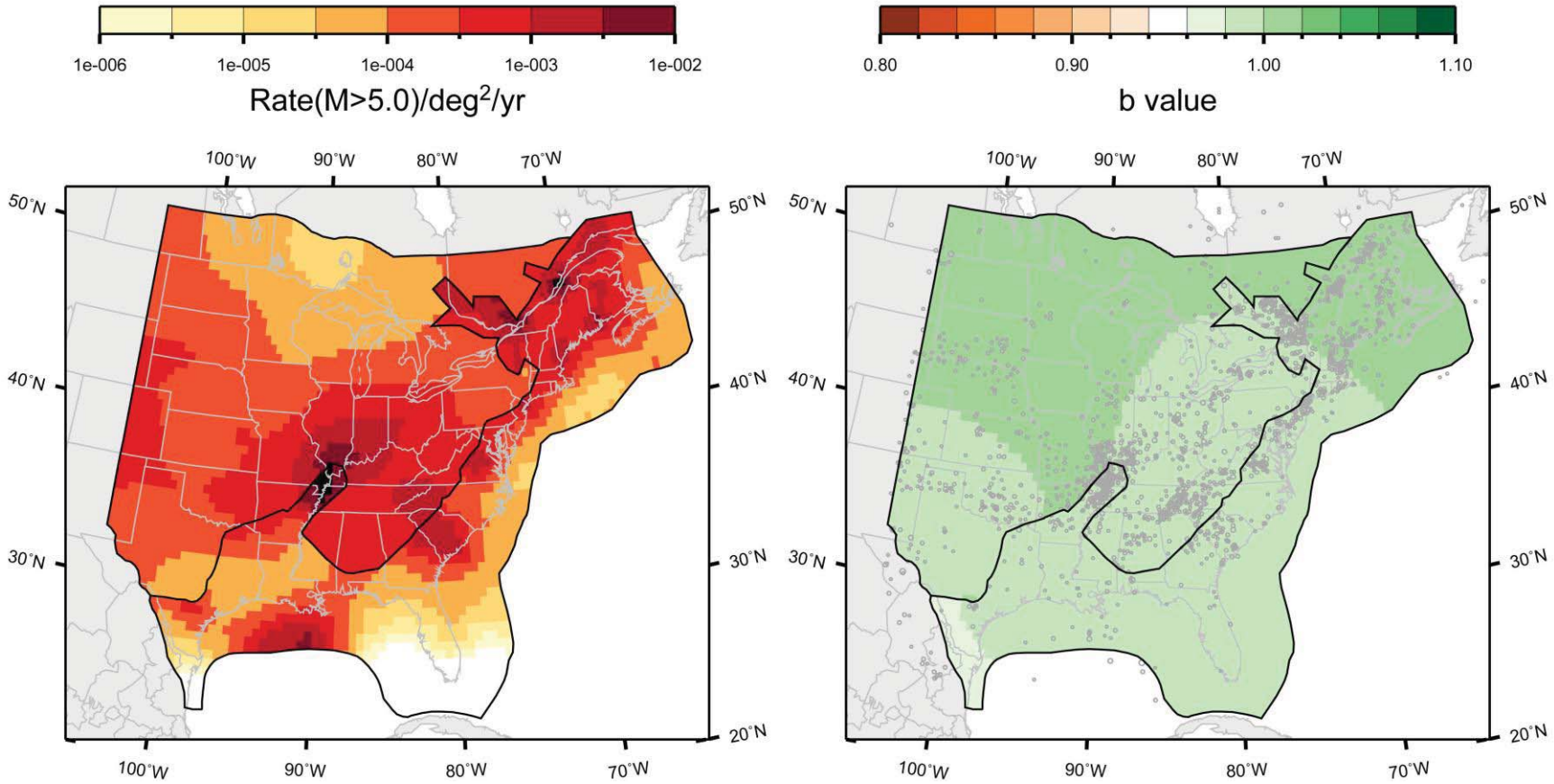

Figure 6.4.1-6
Mean map of rate and *b*-value for the study region under the source-zone configuration, with separation of Mesozoic extended and non-extended, narrow geometry for MESE; Case E magnitude weights

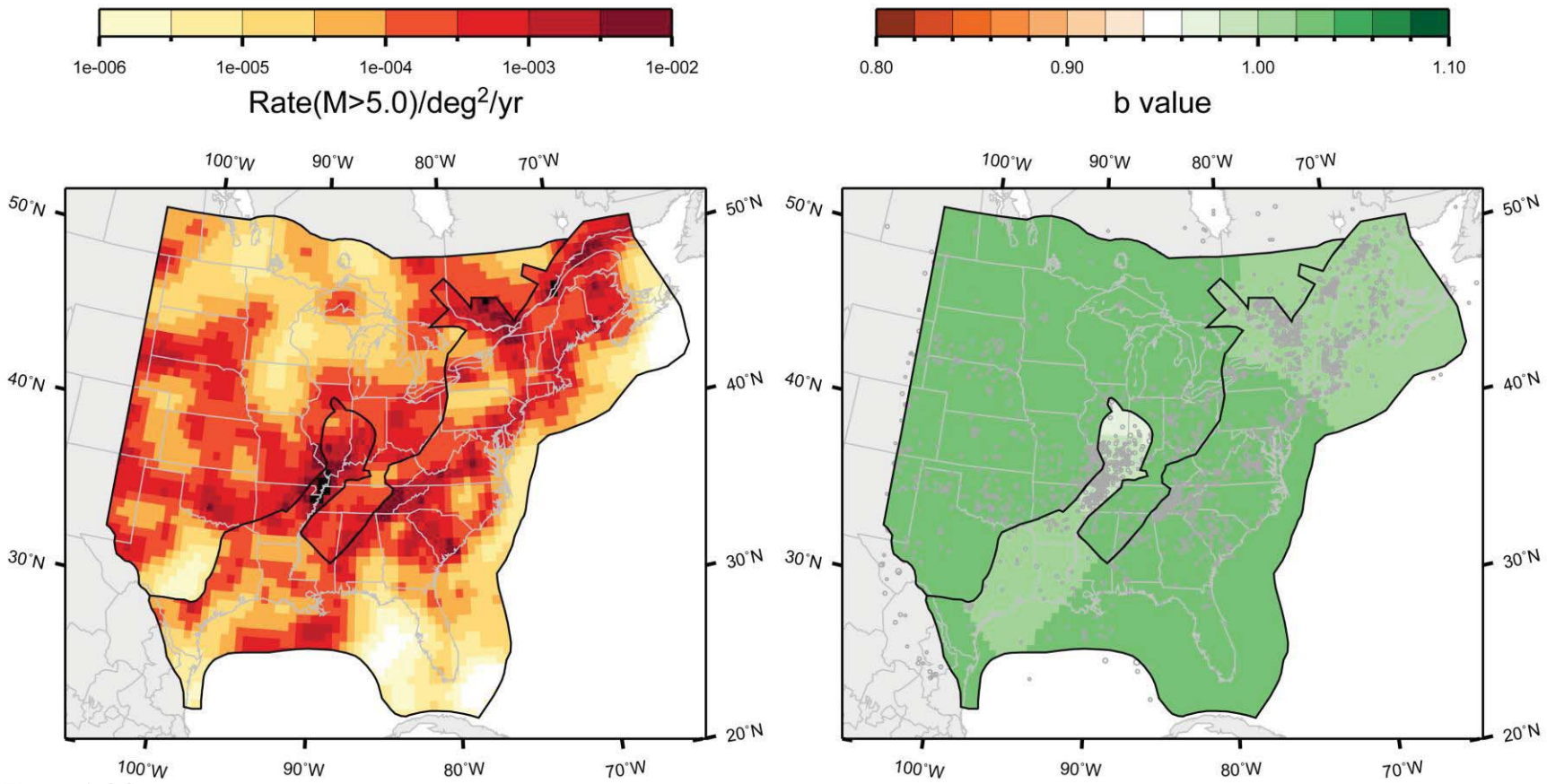

Figure 6.4.1-7
Mean map of rate and *b*-value for the study region under the source-zone configuration, with separation of Mesozoic extended and non-extended, wide geometry for MESE; Case A magnitude weights

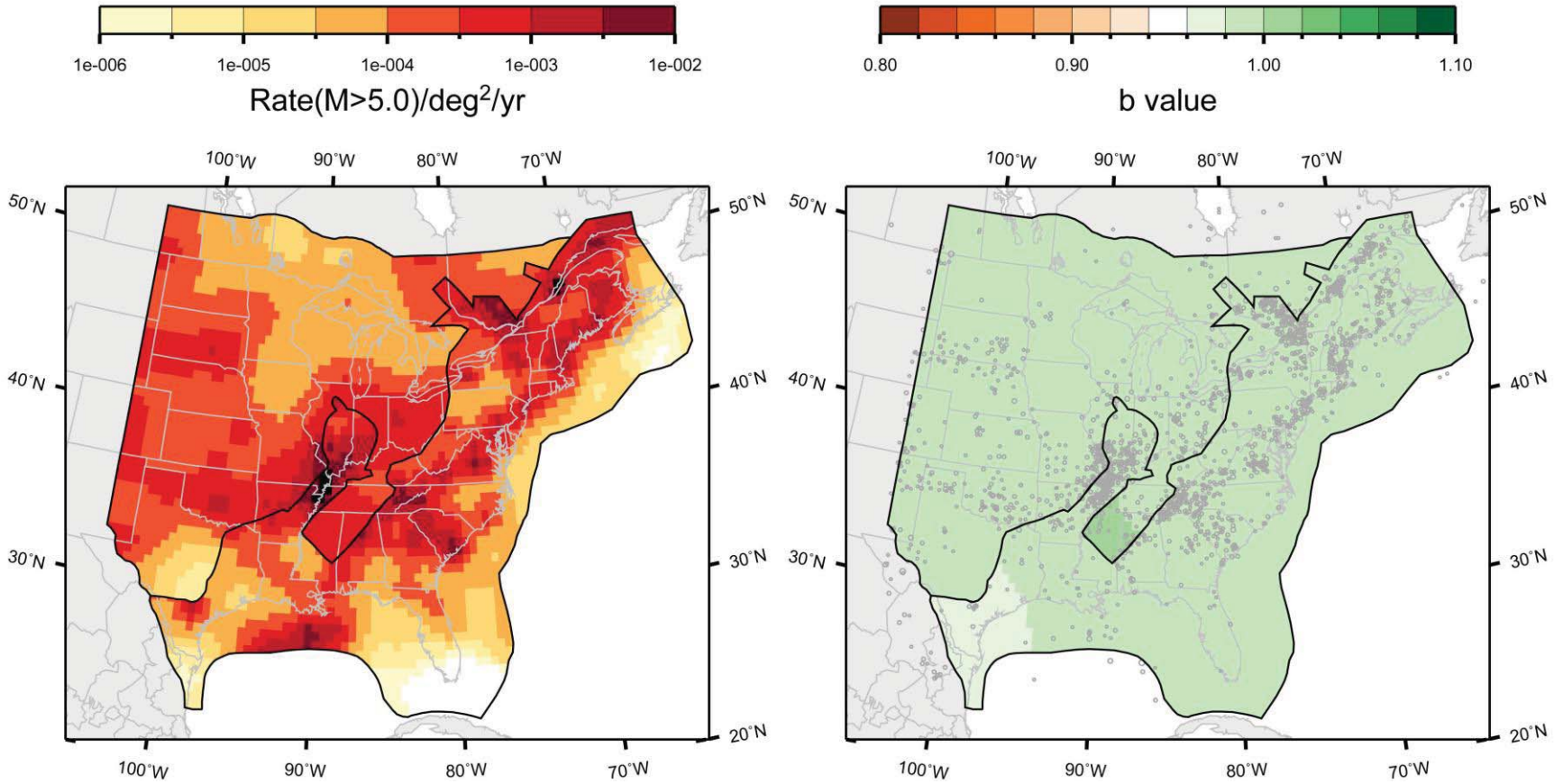

Figure 6.4.1-8
Mean map of rate and *b*-value for the study region under the source-zone configuration, with separation of Mesozoic extended and non-extended, wide geometry for MESE; Case B magnitude weights

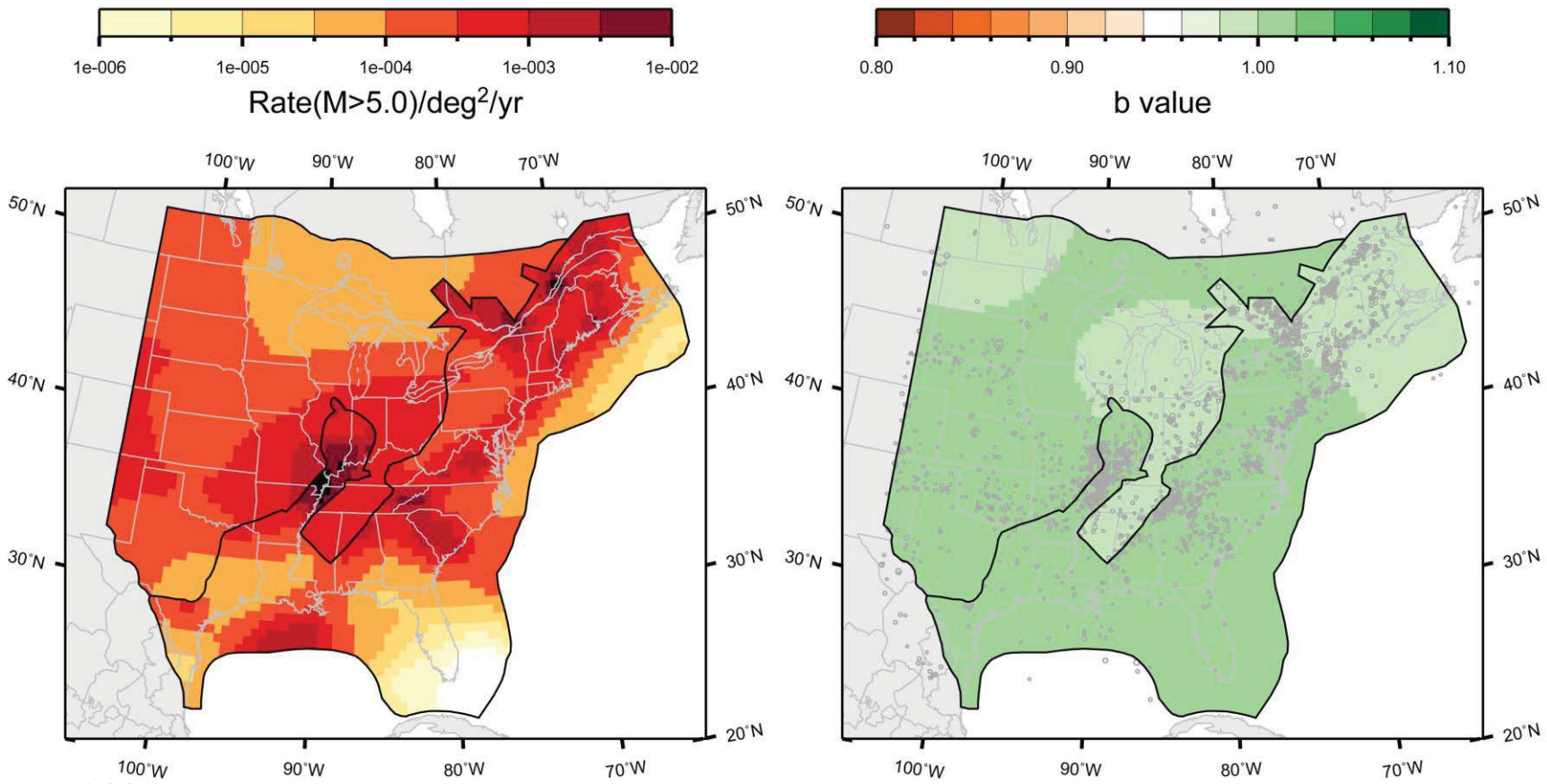

Figure 6.4.1-9
Mean map of rate and *b*-value for the study region under the source-zone configuration, with separation of Mesozoic extended and non-extended, wide geometry for MESE; Case E magnitude weights

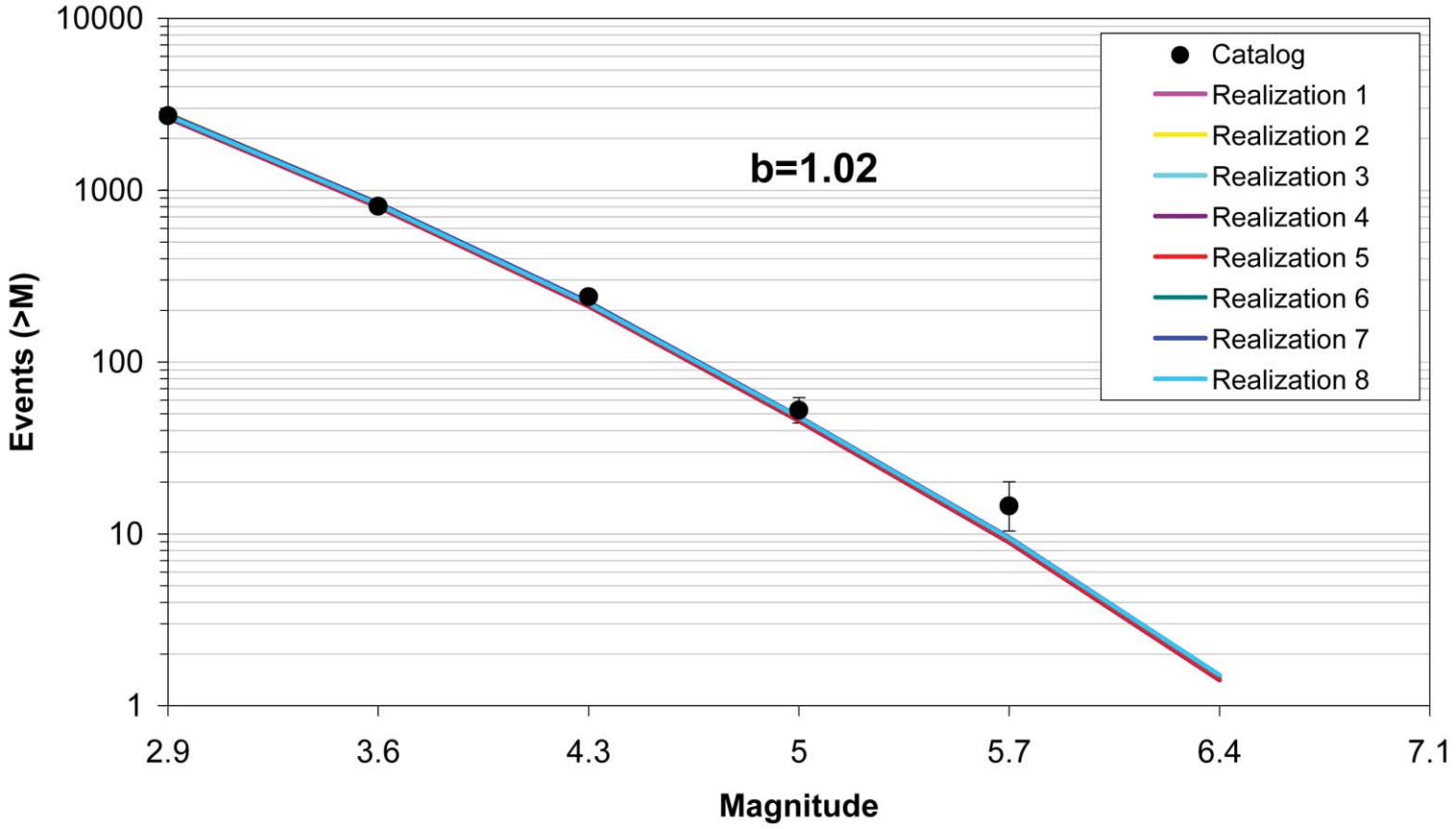

Figure 6.4.2-1
Comparison of model-predicted earthquake counts for study region using Case A magnitude weights. The error bars represent the 16%–84% uncertainty associated with the data, computed using the Weichert (1980) procedure.

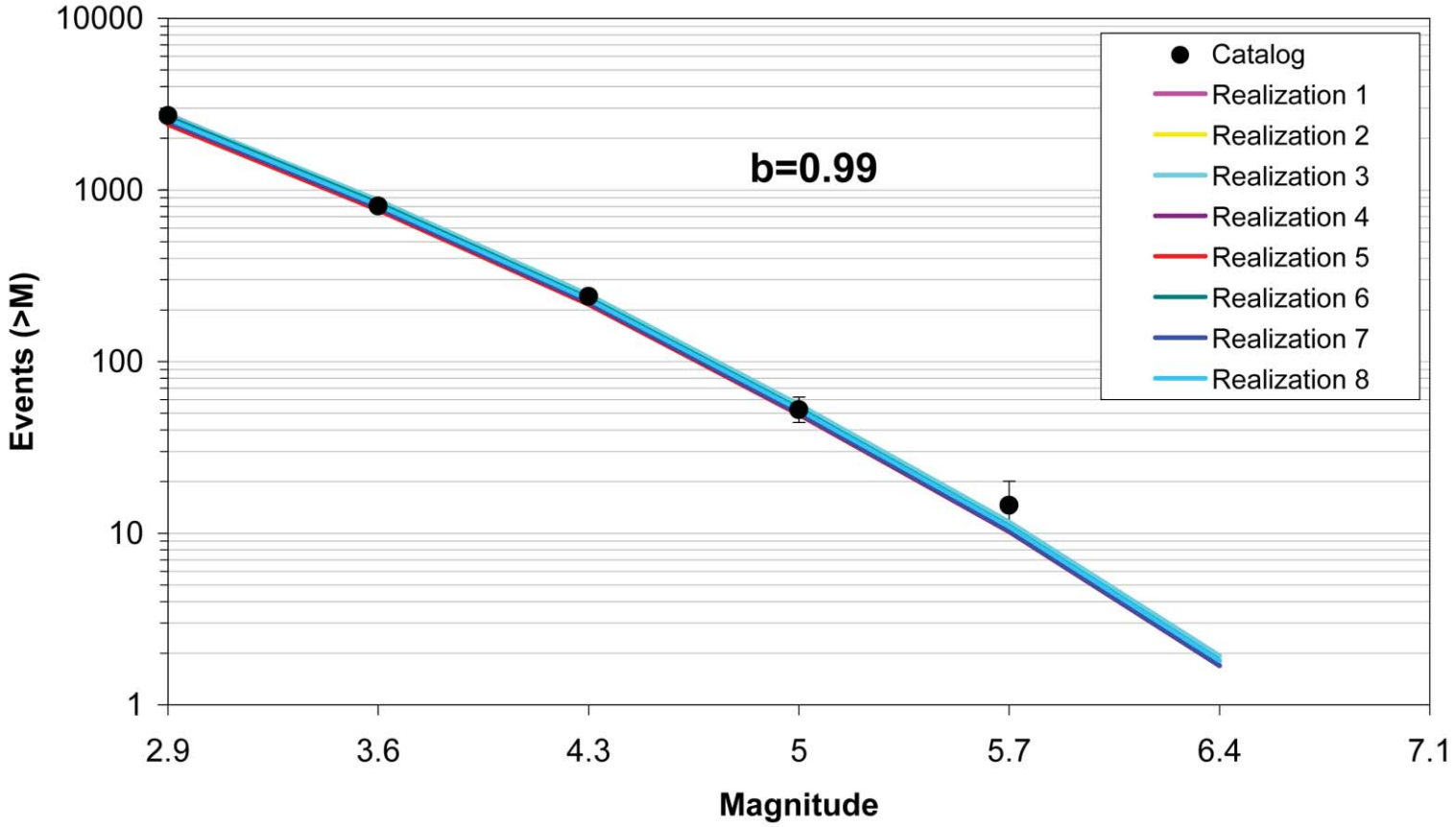

Figure 6.4.2-2
Comparison of model-predicted earthquake counts for study region using Case B magnitude weights. The error bars represent the 16%–84% uncertainty associated with the data, computed using the Weichert (1980) procedure.

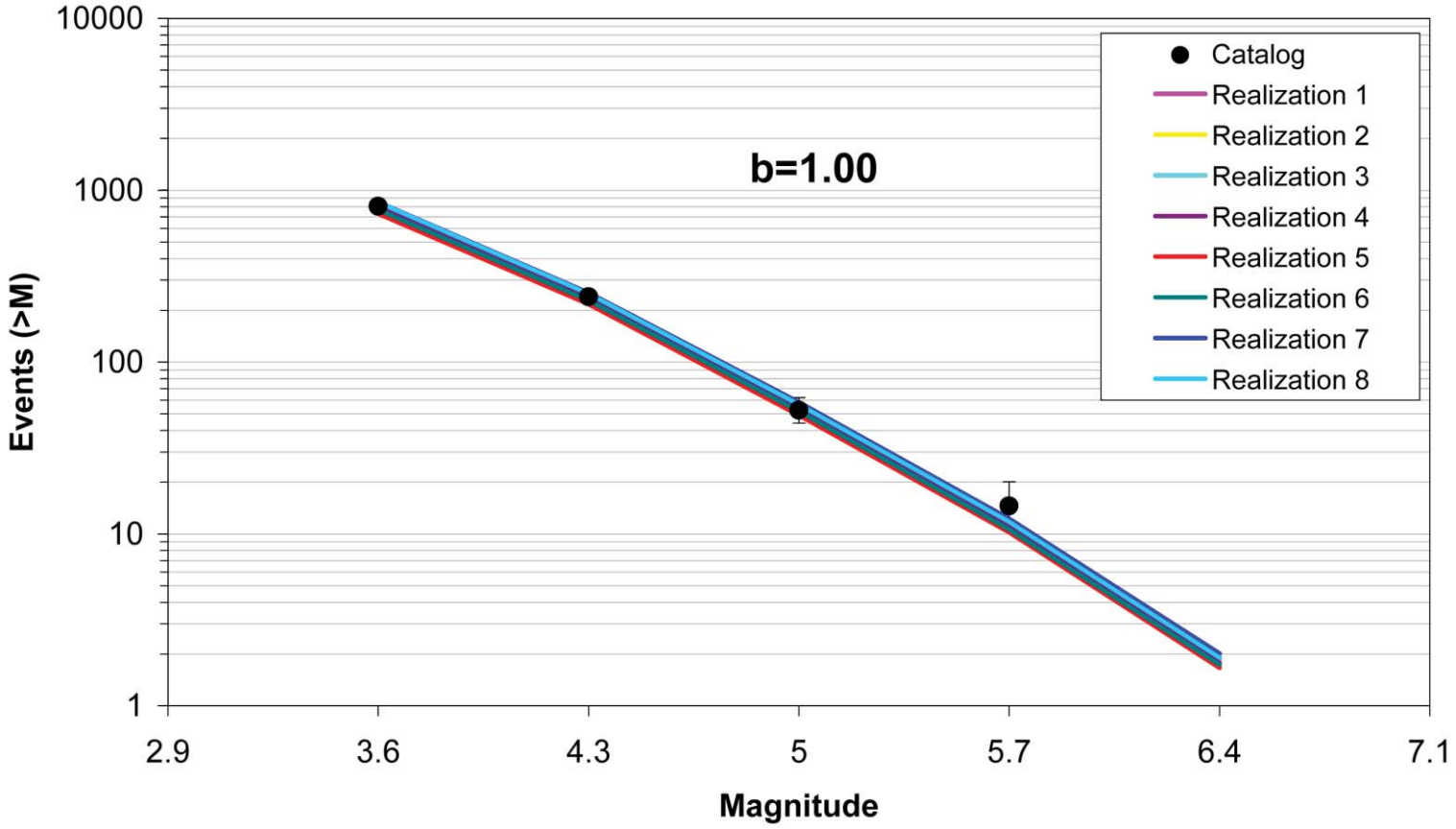

Figure 6.4.2-3
Comparison of model-predicted earthquake counts for study region using Case E magnitude weights. The error bars represent the 16%–84% uncertainty associated with the data, computed using the Weichert (1980) procedure.

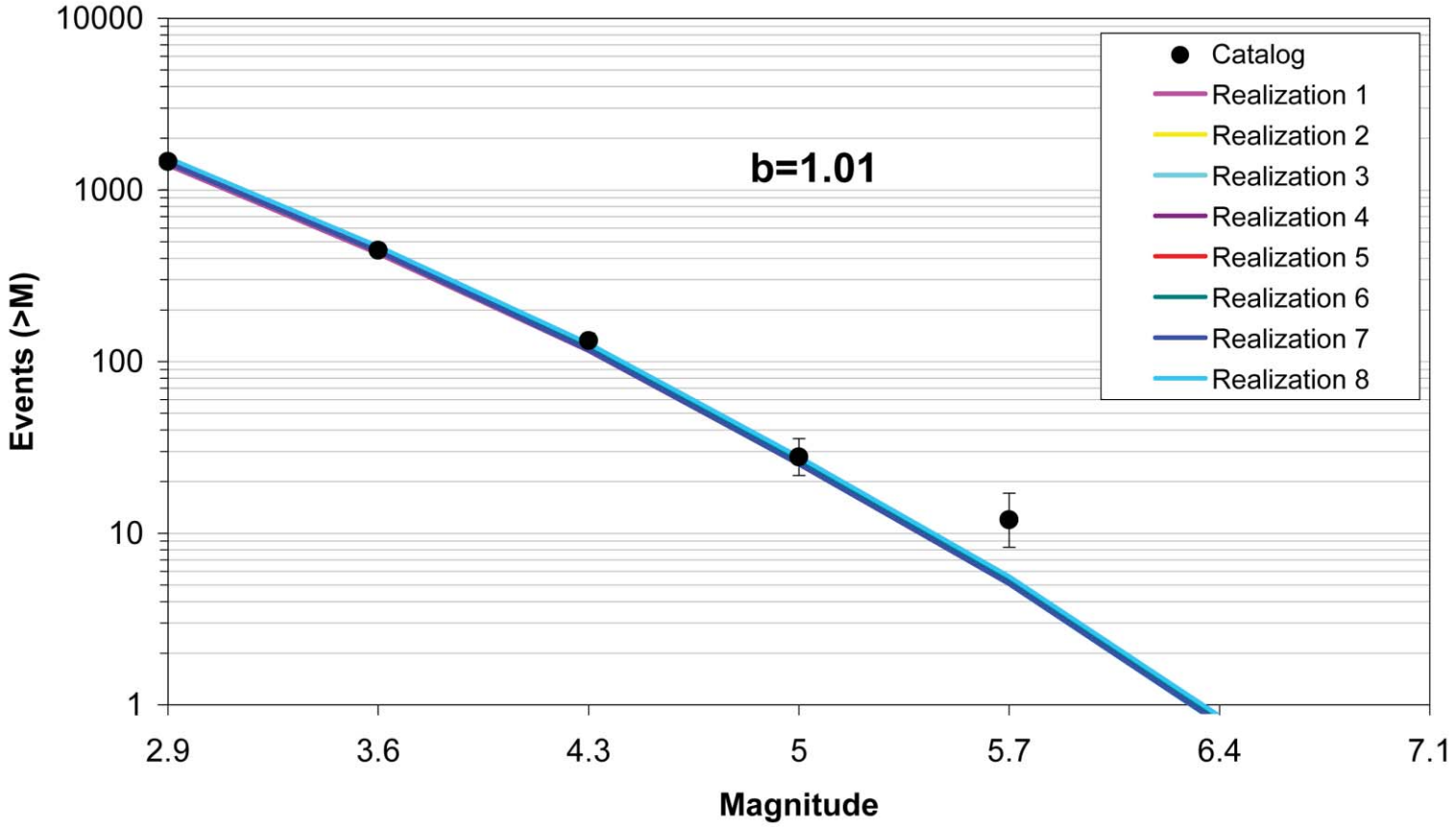

Figure 6.4.2-4
Comparison of model-predicted earthquake counts for MESE-N using Case A magnitude weights. The error bars represent the 16%–84% uncertainty associated with the data, computed using the Weichert (1980) procedure.

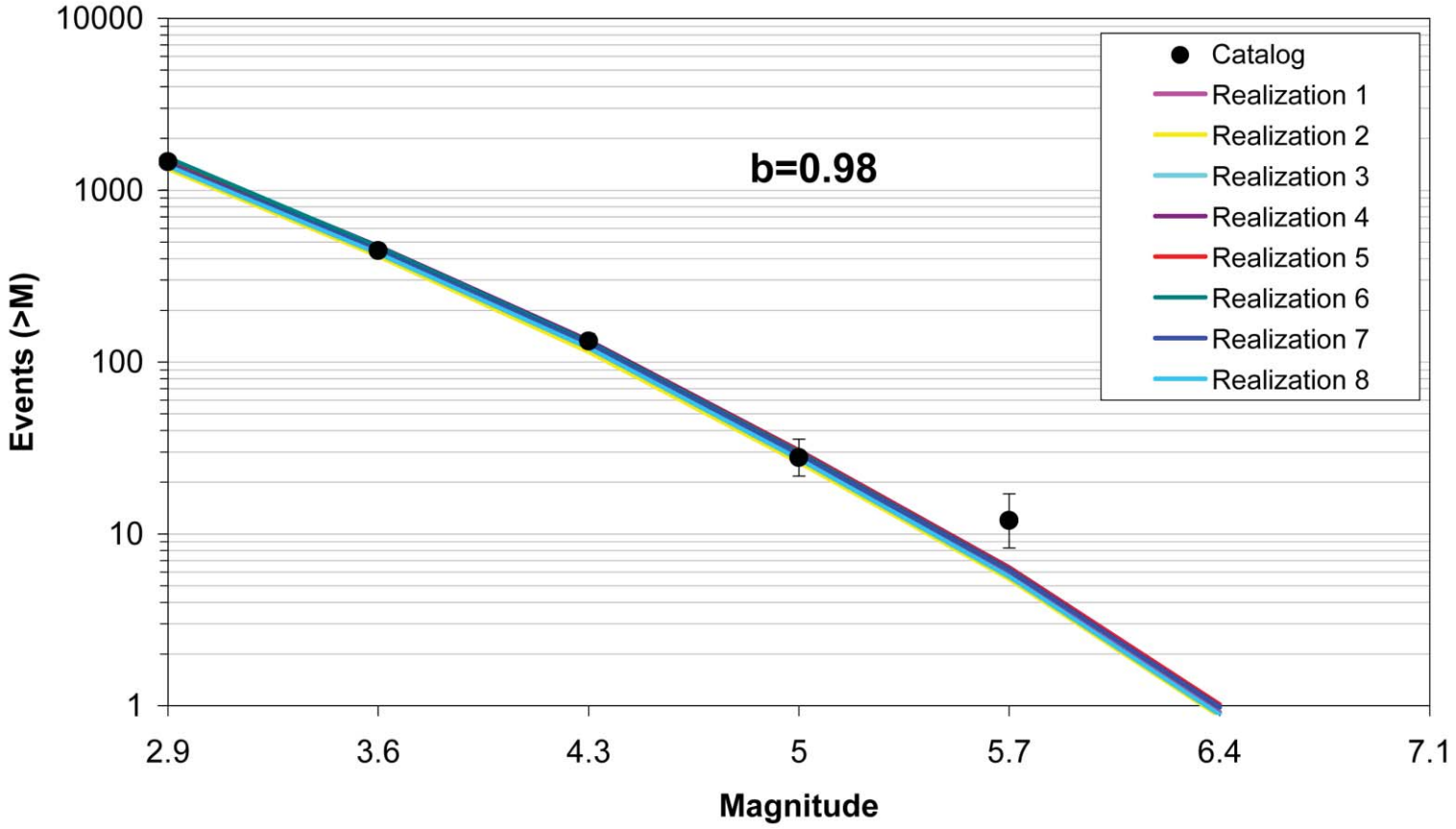

Figure 6.4.2-5
Comparison of model-predicted earthquake counts for MESE-N using Case B magnitude weights. The error bars represent the 16%–84% uncertainty associated with the data, computed using the Weichert (1980) procedure.

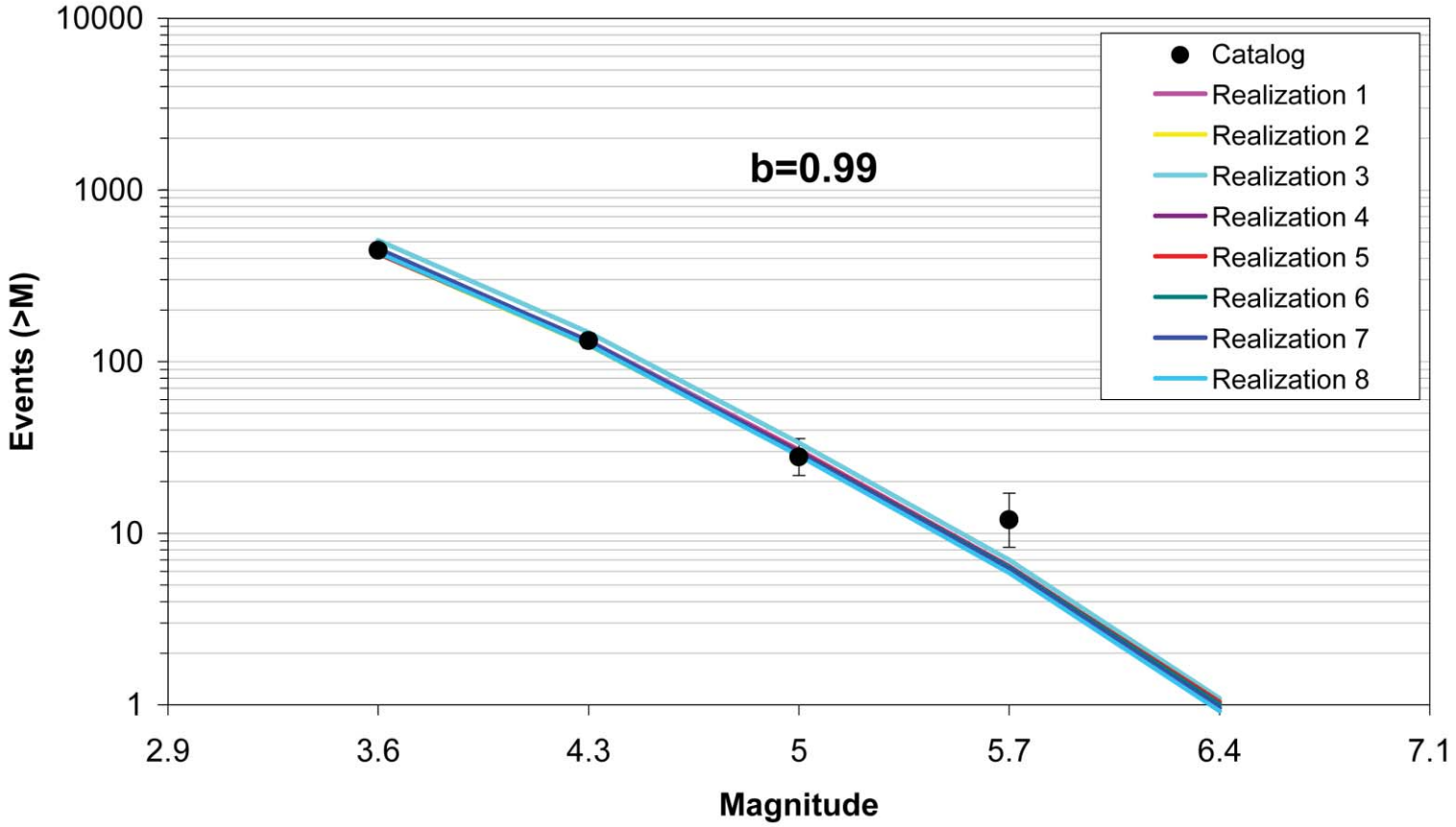

Figure 6.4.2-6
Comparison of model-predicted earthquake counts for MESE-N using Case E magnitude weights. The error bars represent the 16%–84% uncertainty associated with the data, computed using the Weichert (1980) procedure.

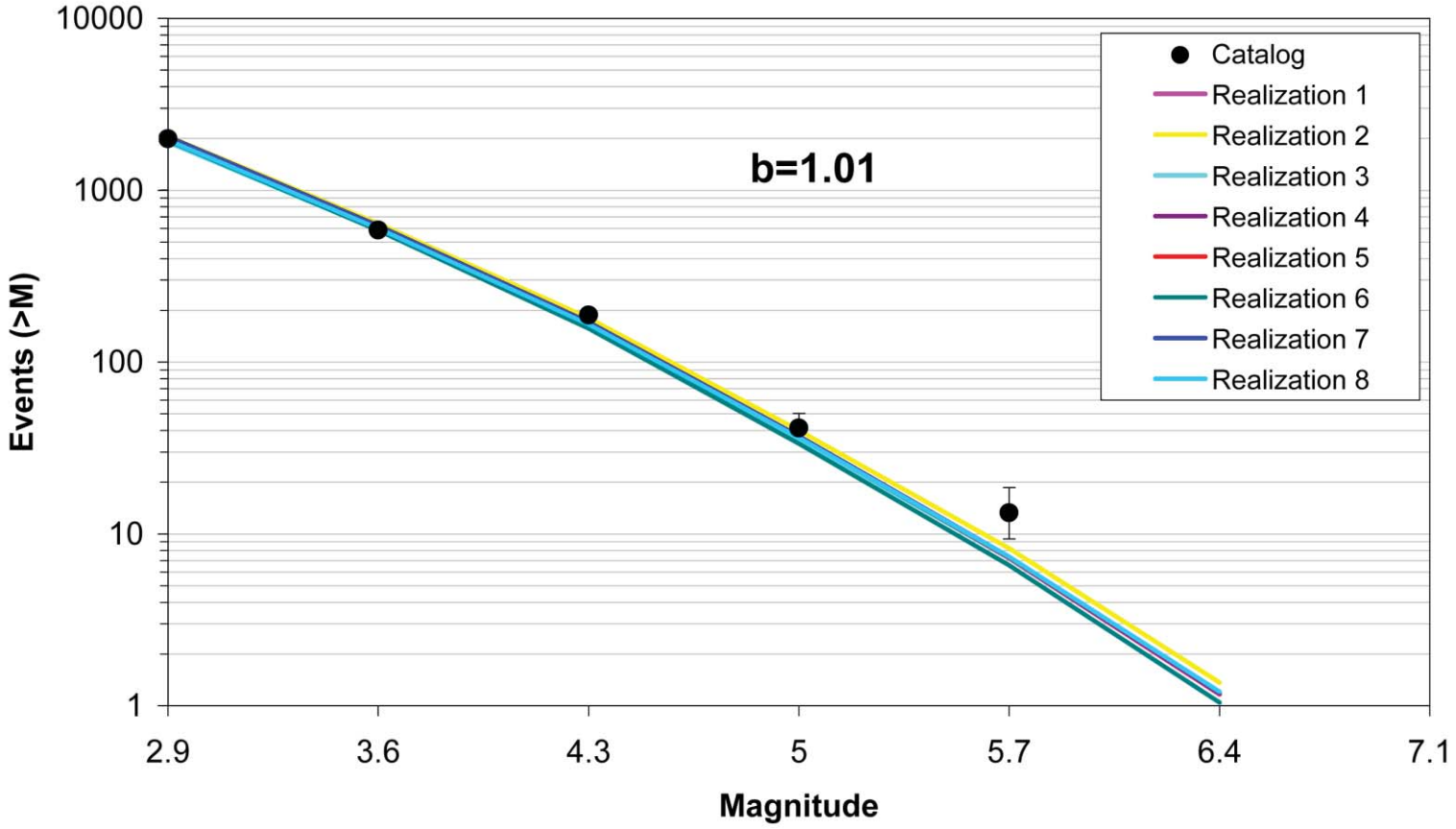

Figure 6.4.2-7
Comparison of model-predicted earthquake counts for MESE-W using Case A magnitude weights. The error bars represent the 16%–84% uncertainty associated with the data, computed using the Weichert (1980) procedure.

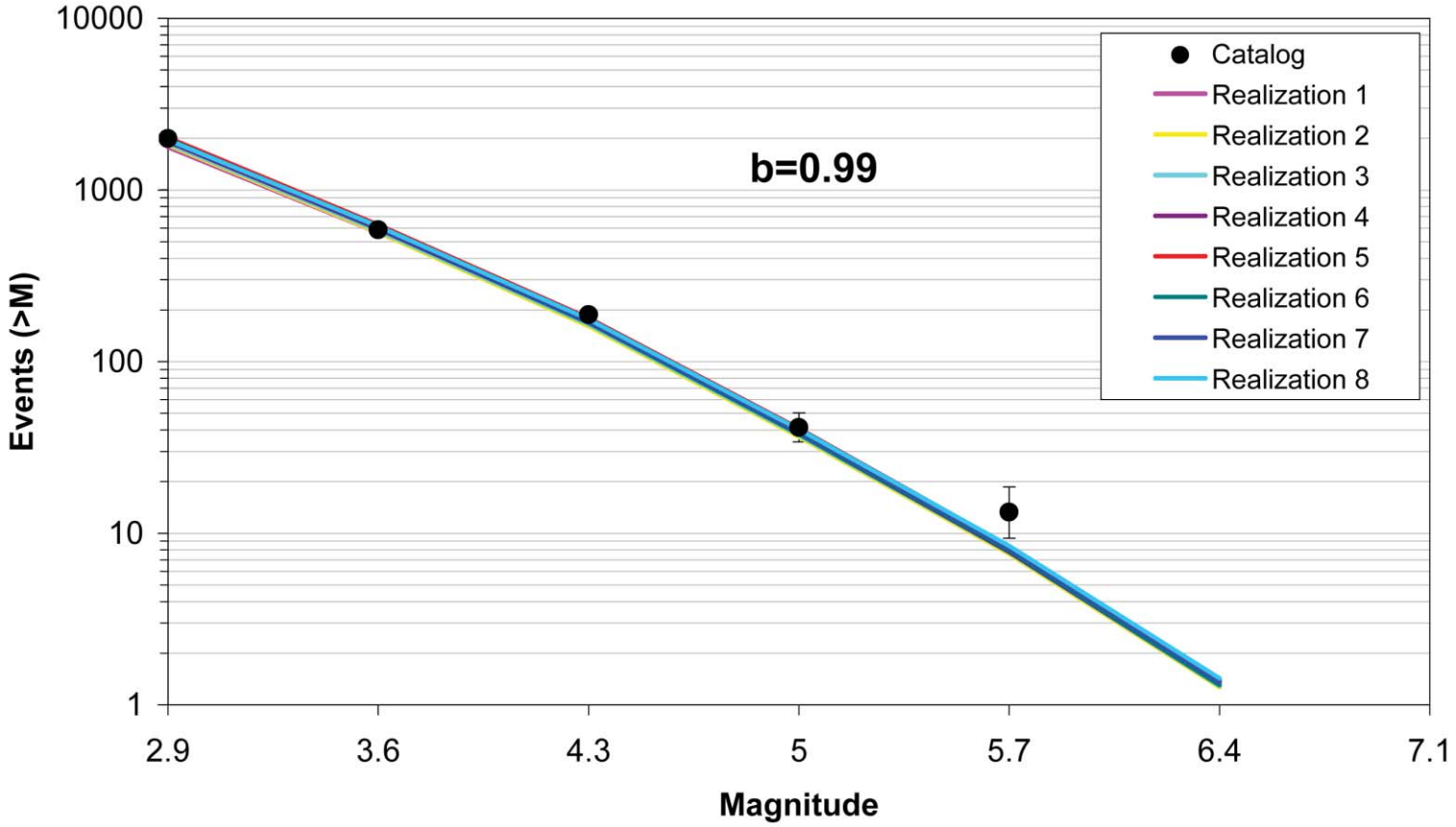

Figure 6.4.2-8
Comparison of model-predicted earthquake counts for MESE-W using Case B magnitude weights. The error bars represent the 16%–84% uncertainty associated with the data, computed using the Weichert (1980) procedure.

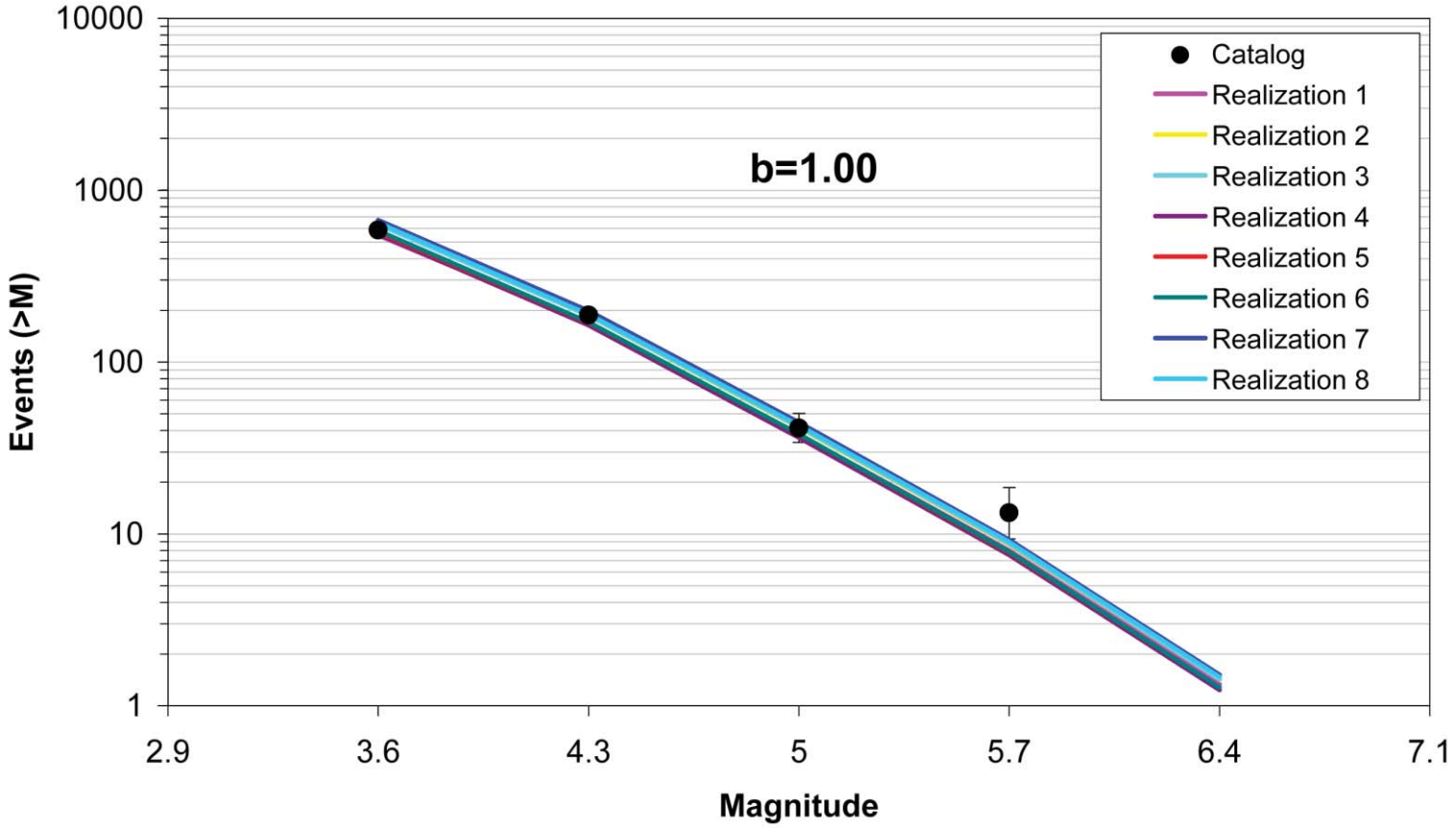

Figure 6.4.2-9
Comparison of model-predicted earthquake counts for MESE-W using Case E magnitude weights. The error bars represent the 16%–84% uncertainty associated with the data, computed using the Weichert (1980) procedure.

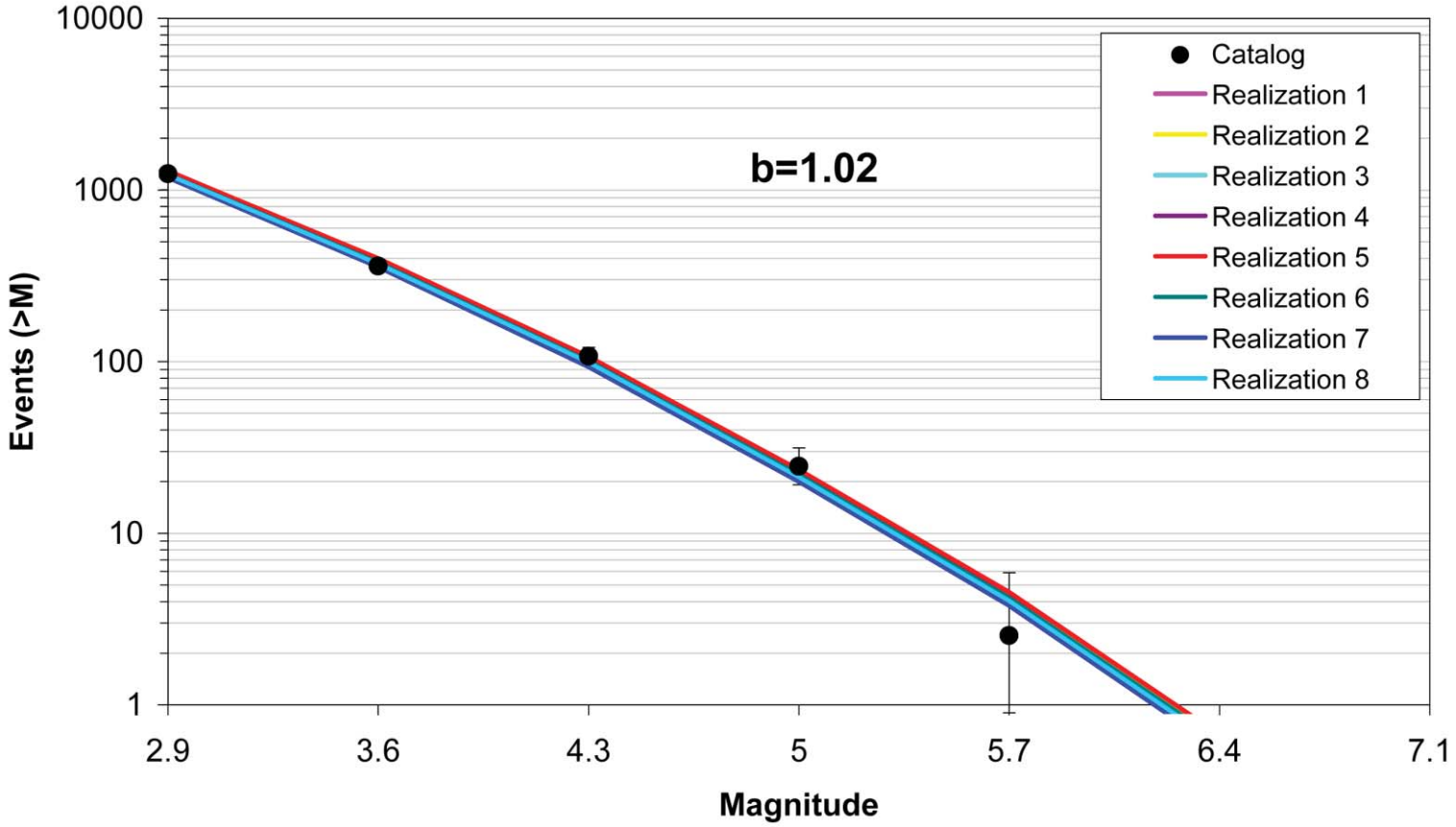

Figure 6.4.2-10
Comparison of model-predicted earthquake counts for NMESE-N using Case A magnitude weights. The error bars represent the 16%–84% uncertainty associated with the data, computed using the Weichert (1980) procedure.

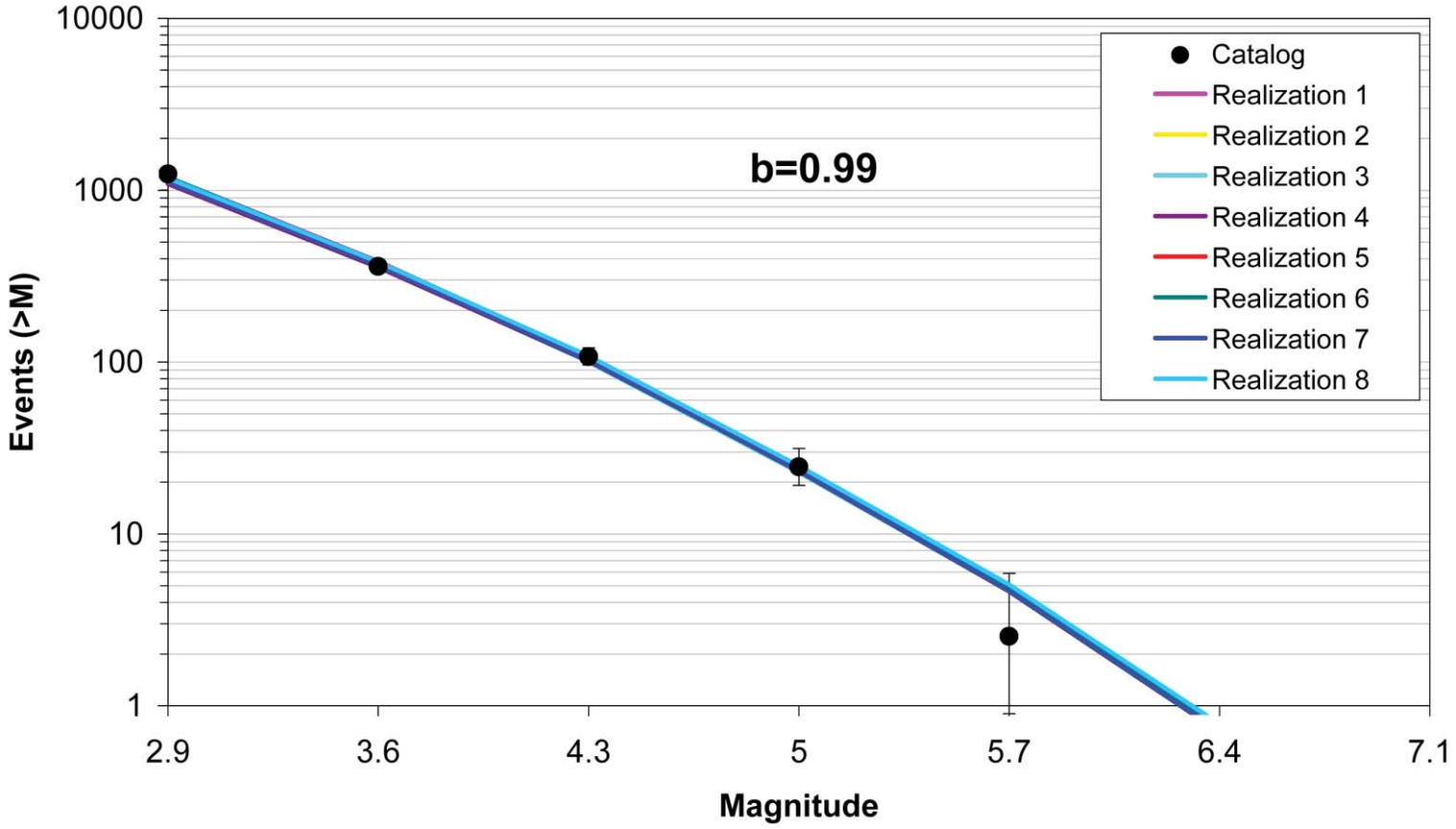

Figure 6.4.2-11
Comparison of model-predicted earthquake counts for NMESE-N using Case B magnitude weights. The error bars represent the 16%–84% uncertainty associated with the data, computed using the Weichert (1980) procedure.

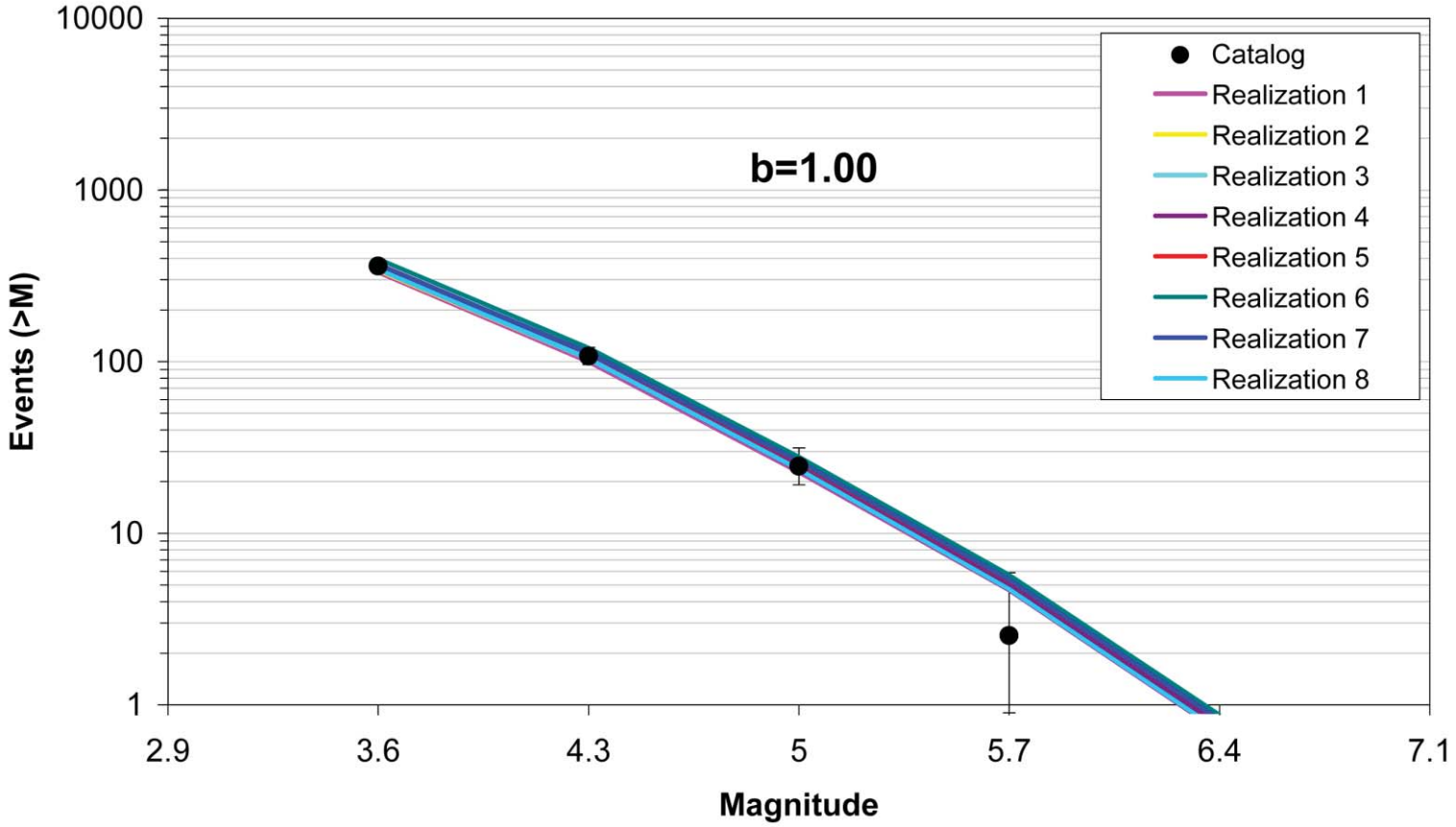

Figure 6.4.2-12
Comparison of model-predicted earthquake counts for NMESE-N using Case E magnitude weights. The error bars represent the 16%–84% uncertainty associated with the data, computed using the Weichert (1980) procedure.

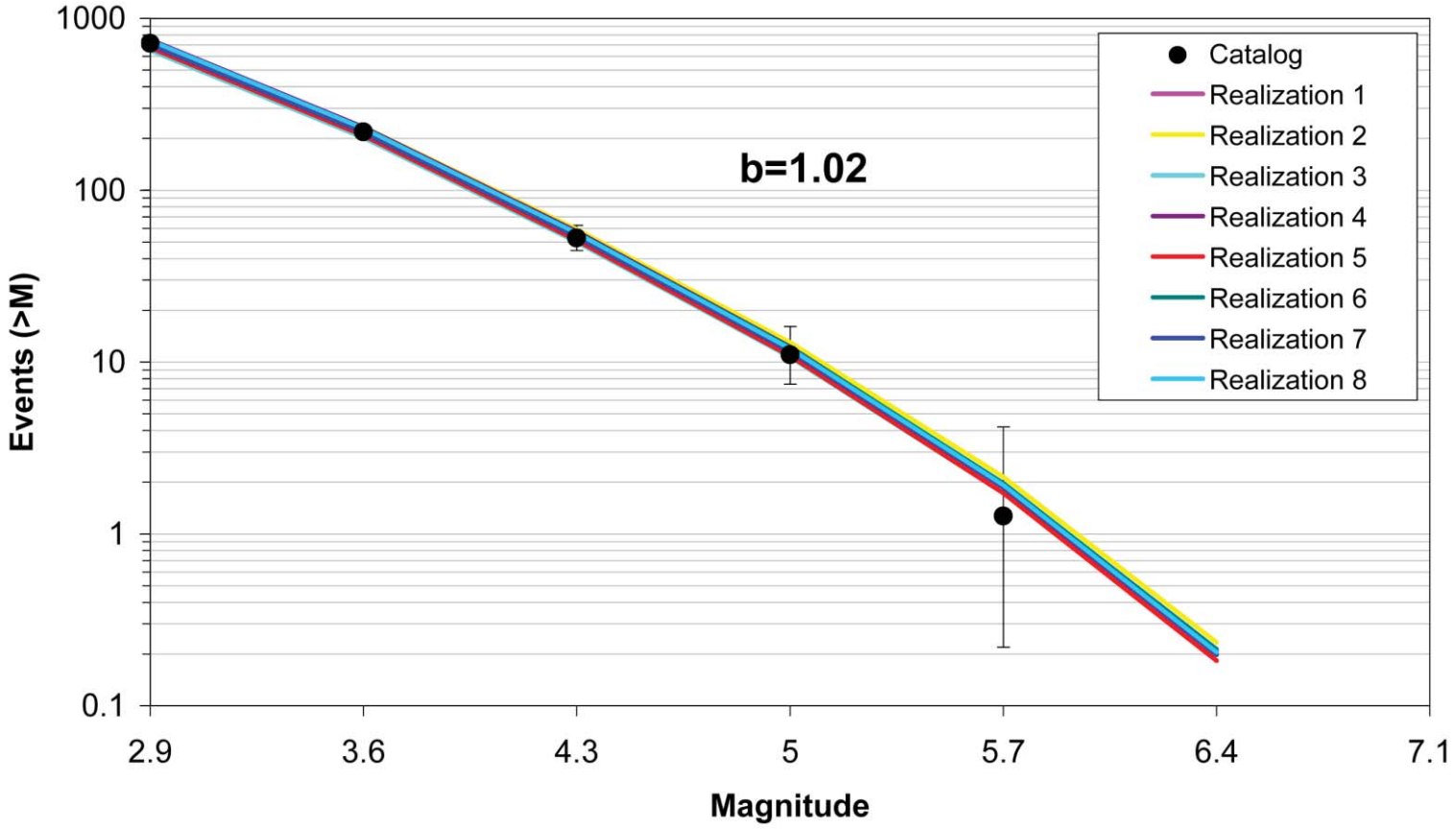

Figure 6.4.2-13
Comparison of model-predicted earthquake counts for NMESE-W using Case A magnitude weights. The error bars represent the 16%–84% uncertainty associated with the data, computed using the Weichert (1980) procedure.

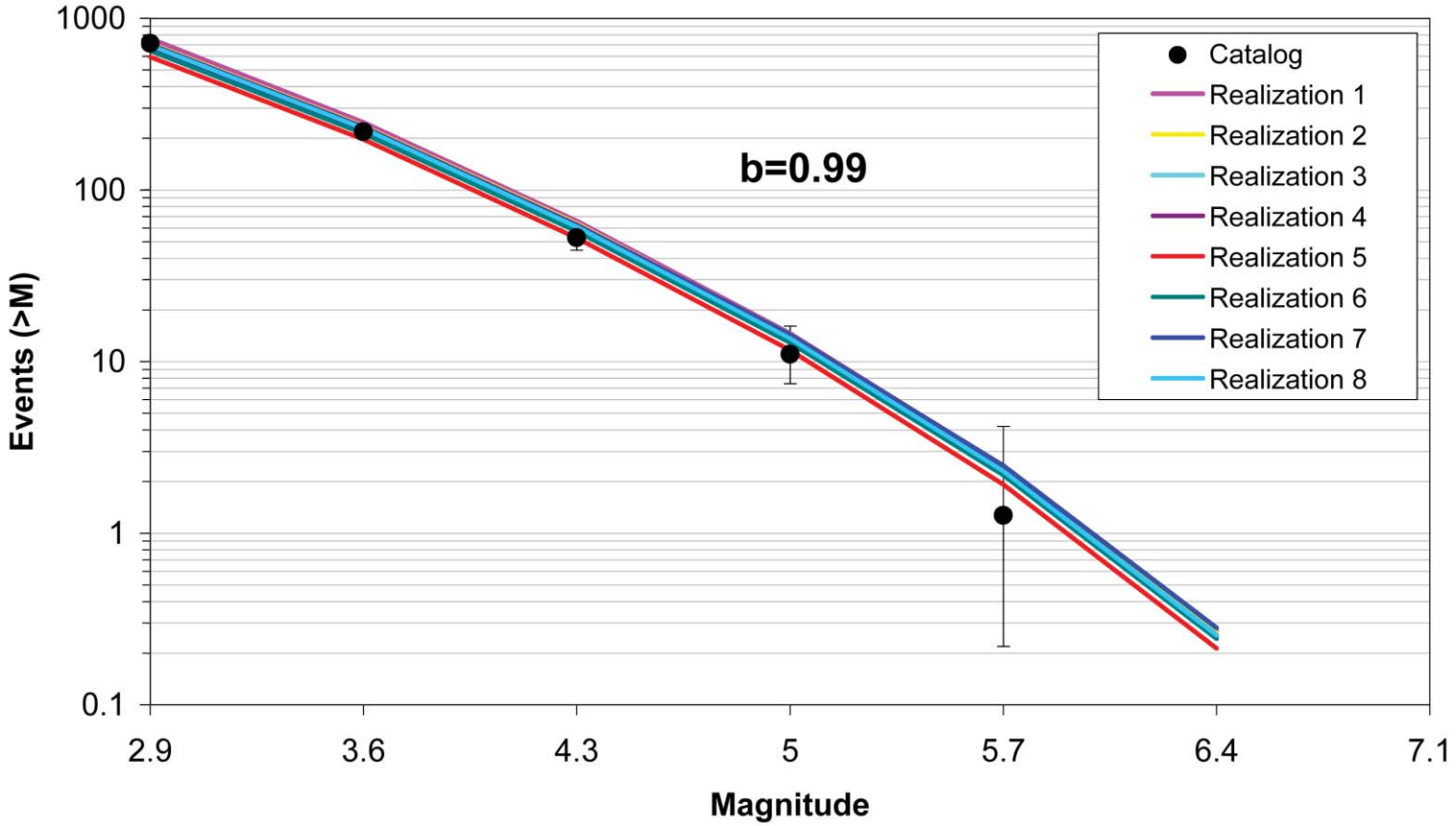

Figure 6.4.2-14
Comparison of model-predicted earthquake counts for NMESE-W using Case B magnitude weights. The error bars represent the 16%–84% uncertainty associated with the data, computed using the Weichert (1980) procedure.

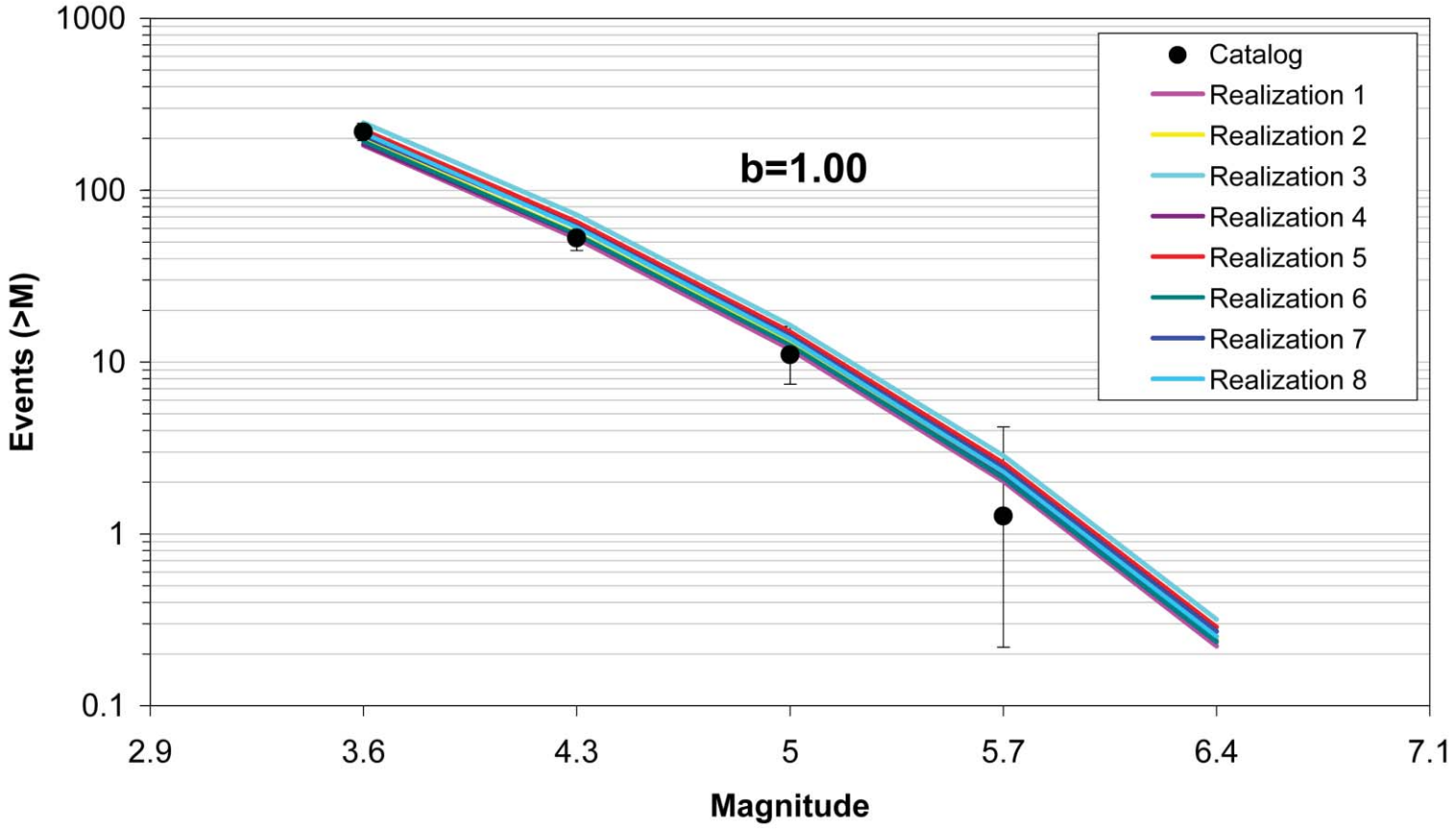

Figure 6.4.2-15
Comparison of model-predicted earthquake counts for NMESE-W using Case E magnitude weights. The error bars represent the 16%–84% uncertainty associated with the data, computed using the Weichert (1980) procedure.